UNIVERSITÉ PARIS-EST

École Doctorale Science Ingénierie et Environnement

Laboratoire Navier

Thèse

Présentée pour l'obtention du grade de Docteur ès Sciences

De l'Université Paris-Est

par

Hadrien Rattez

Couplages Thermo-Hydro-Mécaniques et localisation dans les milieux de Cosserat

Application à l'analyse de stabilité du cisaillement rapide des failles

---

Spécialité : Mécanique

Soutenue le 30/11/2017 devant un jury composé de :

Rapporteur	**Prof. Dmitry Garagash**	Dalhousie University
Rapporteur	**Prof. Samuel Forest**	École des Mines ParisTech
Président	**Prof. Renaud Toussaint**	Institut de Physique du Globe de Strasbourg
Examinateur	**Prof. Ahmed Benallal**	École Normale Supérieure Paris-Saclay
Examinateur	**Dr. Frédéric Collin**	Université de Liège
Examinateur	**Dr. Manolis Veveakis**	University of New South Wales
Directeur de thèse	**Prof. Jean Sulem**	École des Ponts ParisTech
Co-encadrant de thèse	**Dr. Ioannis Stefanou**	École des Ponts ParisTech

Thèse réalisée au sein du **Laboratoire Navier**
de l'École des Ponts ParisTech (UMR 8205), CNRS, IFFSTAR
6 / 8 avenue Blaise Pascal
Champs sur Marne
F-77455 Marne la Vallée Cedex 2
France

Résumé

Les matériaux soumis à de grandes déformations présentent pour la plupart l'apparition de déformations inélastiques. Ce phénomène est souvent accompagné d'une localisation des déformations dans une zone étroite, précurseuse de la rupture. Les bandes de cisaillement représentent un cas particulier mais très fréquent et apparaissent pour beaucoup de géomatériaux. Ces bandes peuvent être rencontrées à des niveaux allant de l'échelle kilométrique pour les zones de subduction à l'échelle micrométrique à l'intérieur des zones de faille. Étudier et modéliser la création de ces zones d'instabilité est fondamental pour décrire la rupture des géomatériaux et les phénomènes associés comme les glissements sismiques dans les zones de faille mature de la lithosphère. Les conditions de pression, de température, l'interaction de l'eau interstitielle avec un matériau finement broyé conduisent à l'apparition de multiples processus physiques impliqués dans les glissements sismiques.

Dans ce travail, nous modélisons la création de bandes de cisaillement à l'intérieur des gouges de faille par l'intermédiaire des milieux continus de Cosserat, ainsi que les couplages Thermo-Hydro-Mécaniques. L'utilisation de la théorie de Cosserat permet non seulement de régulariser le problème de localisation des déformations par l'introduction d'une longueur interne dans les lois constitutives, mais aussi de prendre en compte l'effet de la microstructure.

Deux approches sont employées pour étudier le système d'équations couplées aux dérivées partielles non linéaires : l'analyse de stabilité linéaire et la méthode des éléments finis. L'analyse de stabilité linéaire permet d'examiner les conditions d'apparitions d'instabilités pour un système mécanique avec des couplages multi-physiques. Par ailleurs, des considérations sur les perturbations appliquées dans ces analyses au système permettent aussi de déterminer l'épaisseur de la zone de cisaillement - un paramètre clé pour la compréhension du mécanisme des failles. Ces estimations sont confirmées par l'intégration numérique pour des déformations restant dans une gamme donnée. Elles sont confrontées aux observations expérimentales et *in situ* et présentent une bonne corrélation. D'autre part, les simulations numériques permettent d'obtenir la réponse mécanique de la gouge de faille et de donner des informations sur l'influence des différents couplages dans le budget énergétique d'un tremblement de terre.

Mots-clé : Localisation des déformations, mécanique des failles , couplages THM, Analyse de stabilité linéaire, éléments finis, microstructure, milieux continus de Cosserat.

Thermo-Hydro-Mechanical couplings and strain localization in Cosserat continuum

Application to stability analysis of rapid shear in faults

Abstract

When materials are subjected to large deformations, most of them experience inelastic deformations. It is often accompanied by a localization of these deformations into a narrow zone leading to failure. One particular case of localization is the shear bands and they are the most common patterns observed in geomaterials. They appear at very different scales, from kilometer scale for subduction zone, to micrometric scale inside fault cores. Studying and being able to model their creation is fundamental to describe the failure of geomaterials and understand phenomena that are associated with their existence such as seismic slip for mature crustal faults. The pressure and temperature conditions in these faults and the interaction with the pore water inside a highly fractured materials highlight the importance of different physical processes involved in the nucleation of earthquakes.

In this thesis, we model the creation of shear bands inside fault gouges taking into account the effect of microstructure by resorting to elastoplastic Cosserat continua and Thermo-Hydro-Mechanical couplings. The use of Cosserat theory not only enables to regularize the problem of localization by introducing an internal length into the constitutive equations, but at the same time it introduces informations about the microstructure.

Two approaches are used to study the coupled non-linear partial differential set of equations: linear stability analysis and finite element simulations. Linear stability analysis allows to study the occurrence of localized deformation in a mechanical system with multi-physical couplings. Considerations on the perturbations applied permit also to determine the width of the localized zone. It is confirmed by numerical integration in the post-localization regime for a certain range of deformation. The shear band thicknesses obtained, key parameters for understanding fault behavior, are in agreement with experimental and field observations. Moreover, numerical simulations enable to obtain the mechanical response of the gouge and give an insight into the influence of different couplings in the energy budget of a seismic slip.

Keywords:

Strain Localization, fault mechanics, THM couplings, linear stability analysis, Finite Element modelling, microstructure, Cosserat continuum.

Contents

List of Figures

List of Tables

Introduction

L'épaisseur de localisation des déformations dans les zones failles est un paramètre primordial pour la compréhension de leur dynamique. Dans cette thèse, on s'intéresse en particulier au rôle de la microstucture et des couplages Thermo-Hydro-Mécaniques dans le processus de localisation ainsi que dans la réponse du matériau. Pour cela, un modèle élasto-plastique pour les milieux continus de Cosserat avec couplages est développé.

Le présent manuscrit est divisé en quatre chapitres. Le premier constitue une introduction détaillée au sujet. La mécanique des failles y est expliquée ainsi que les différents phénomènes physiques se produisant au sein de la faille au cours d'un glissement sismique. Ceux-ci peuvent conduire à une diminution de la résistance de la faille au cours du glissement et engendrer ainsi un glissement dynamique à l'origine des tremblements de terre. La localisation des déformations est une conséquence de ces mécanismes d'affaiblissement de la zone de faille et son étude peut nous permettre de mieux appréhender le mécanisme des tremblements de terre. Les outils théoriques pour l'étude de la localisation sont également introduits. Dans le second chapitre, un modèle est développé pour lequel on applique une analyse de stabilité linéaire afin de déterminer l'influence des différents paramètres sur le déclenchement de la localisation et sur l'épaisseur de la bande de cisaillement. Le troisième chapitre présente l'implémentation numérique du modèle ainsi que la démarche suivie pour la validation du code. Le quatrième et dernier chapitre constitue une étude numérique de la localisation des déformations dans les zones de failles et de la réponse du matériau en termes de contraintes et déformations.

According to Kanamori and Brodsky (2004), the thickness of fault slip zones is the key parameter for understanding fault dynamics (see also Sibson (2003), Rice (2006a)).

In this Thesis we investigate the effect of the microstructure and of Thermo-Hydro-Mechanical (THM) couplings on the behavior of mature fault slip zones and the evolution of their thickness during pre- and co-seismic slip. Seismic slip is accompanied by extreme shear strain localization into a narrow, thin zone, which is often called Principal Slip Zone (PSZ). According to field observations, the PSZ has finite thickness (see for instance Punchbowl fault, San Andreas system (Chester and Chester, 1998), Big Hole normal fault, Utah (Shipton et al., 2006), Median Tectonic line, Japan (Wibberley and Shimamoto, 2003)) and varies from hundreds of microns to few centimetres (Sibson, 2003), depending on the size of the microstructure and of THM mechanisms. The PSZ lies within a zone of highly fragmented, granulated material called gouge (Ben-Zion and Sammis, 2003).

Theoretical and experimental research show that strain localization is caused and enhanced by weakening mechanisms that can either be of pure mechanical origin (e.g. geometrical and mechanical changes of the solid skeleton (Togo and Shimamoto, 2012), such as grain cataclasis, reorientation, debonding etc.) or of a combination of various physico-chemical couplings (Sulem and Stefanou, 2016). For instance, thermal pressurization of the pore fluid in saturated fault materials is a THM mechanism that plays a fundamental role in the weakening of fault zones (Viesca and Garagash, 2015, Lachenbruch, 1980). Thermal pressurization is a consequence of the contrast between the thermal expansion coefficient of the pore fluids and the solid matrix (Rice, 2006b) and leads to a decrease of the effective mean stress and consequently to a reduction of the shear strength of the gouge. This weakening is linked to the progressive development of the PSZ, whose thickness governs the temperature build-up and the overall energy budget. It is worth mentioning that the activation of additional multi-physical phenomena that involve chemical processes are precisely controlled by the thickness of the localization zone (Veveakis et al., 2013, Sulem and Stefanou, 2016, Brantut et al., 2011, Platt et al., 2015).

Models that are able to describe the localization thickness and its evolution have to take into account both the size of the microstructure of a fault gouge as well as the THM couplings that take place during seismic slip. The reason is that these features are central to the evolution of the PSZ thickness and, therefore, to the correct representation of the physics of the problem. Cosserat theory allows in a natural way to account for the aforementioned characteristics, leading to a shear band of finite thickness, even under low strain rates (Mühlhaus and Vardoulakis, 1987). The use of this theoretical framework is also justified by the fact that it offers a unified modeling environment as it can cover a large spectrum of strain rates, i.e. from very low (pre-seismic) to quite high (co-seismic). Notice that existing models for fault gouges based on the classical, Cauchy continuum (also called Boltzmann continuum (Vardoulakis, 2009)) lead to an infinitely small localized zone (slip on a mathematical plane) (Vardoulakis, 1985) unless rate-dependent constitutive behavior

is considered for high strain rates (Rice et al., 2014, Platt et al., 2014). Moreover, grain size can hardly be considered in the constitutive description of Cauchy continua, despite the fact that it has been recognized to play an important role on fault gouge behavior (Cashman et al., 2007, Anthony and Marone, 2005, Phillips and White, 2017).

Cosserat continuum (Cosserat and Cosserat, 1909) is a special case of micromorphic continua (Godio et al., 2016, Germain, 1973a), also called generalized or higher order continua. In addition to the translational degrees of freedom of the Cauchy continuum, Cosserat theory provides rotational degrees of freedom at the material point that allow for a better representation of the physics and the mechanical behavior of heterogeneous solids with non-negligible microstructure. Cosserat continuum theory naturally incorporates in the constitutive equations of the material one or several material lengths related to the microstructure .

The theory of Cosserat continuum has been previously applied for studying the behavior of fault gouges and strain localization (Sulem et al., 2011, Veveakis et al., 2013). In these works the conditions for the onset of localization were investigated under THM couplings with a microstructure of given size. In this Thesis, we extend the aforementioned works by studying:

(a) The evolution of the localization zone thickness and its dependency on various parameters such the size of the microstructure;

(b) The full stress-strain response of the fault gouge, which is related to the transition from seismic to aseismic slip (Scholz, 2002, Tse and Rice, 1986);

(c) The link between the shear band thickness evolution obtained from the linear stability and the one obtained from an numerical integration of the nonlinear set of equations.

It is worth emphasizing that computing the evolution of strain localization is a challenging task due to the difficulties that arise when dealing with softening behavior. It entails a loss of ellipticity of the governing equations in the classical continuum theory framework (Vardoulakis and Sulem, 1995, de Borst et al., 1993). The boundary value problem becomes mathematically ill-posed (Vardoulakis, 1986) and the results of classical finite element computations exhibit mesh dependency (as deformations localize in a band of thickness equal to the finite element size). Moreover, mesh refinement leads towards zero energy dissipation, which is nonphysical. However, the Cosserat Finite Element (FE) formulation followed herein does not suffer from the above limitations as it possesses a material parameter with dimension of length, which regularizes physically the numerical problem (see also (de Borst, 1991, Godio et al., 2016, Stefanou et al., 2017)).

The present manuscript is organized into four chapters. The first one gives a detailed introduction to the subject. The current state of knowledge in fault mechanics is briefly

summarized and the main physical phenomena taking place in the fault core during seismic slip are explained. These phenomena can lead to a weakening of the fault strength, which is accompanied by strain localization giving rise to dynamic slip, i.e. to earthquakes. The theoretical tools for studying strain localization are also introduced in this chapter. In the second chapter, a model of three-dimensional elasto-plastic Cosserat continuum with THM couplings is developed. Bifurcation theory and Linear Stability Analysis (LSA) is applied for this model to determine the influence of the various parameters on the onset of strain localization and on the the shear band thickness. In order to complete the investigation carried out with the LSA, in the third chapter the Cosserat THM model is implemented numerically in a parallel fully-coupled FE code. The strategy for integrating the nonlinear boundary value problem is presented in details and the tests carried out to verify thoroughly the implementation are described. The fourth and final chapter is devoted to the numerical study of strain localization in fault zones. The numerical results are compared to the ones obtained from the LSA. It also provides useful information regarding the complete response of the system, which is a key feature to determine the stability of a fault and study the transition from aseismic to seismic slip.

Chapter 1

Fault mechanics, instability and strain localization

Ce chapitre présente les éléments fondamentaux de la mécanique des failles permettant d'appréhender les mécanismes à l'origine du déclenchement des séismes. Les ondes qui se propagent au sein de la croûte terrestre et engendrent des dégats matériels ainsi que des pertes humaines sont généralement la conséquence d'une instabilité frictionelle le long d'une faille pré-existante.

Les observations in situ et en laboratoire montrent que les zones de failles sont très hétérogènes et possèdent une épaisseur non négligeable. En particulier, la couche de localisation des déformations au sein de la zone de faille a un rôle essentiel dans le déclenchement des séismes. Cette localisation des déformations fait intervenir de multiples couplages physiques liés notamment à la présence d'eau interstitielle dans les pores du matériau, la forte augmentation de température (engendrée par la vitesse considérable atteinte lors d'un glissement sismique) et l'activation de réactions chimiques.

La localisation peut être modélisée comme un phénomène de bifurcation. L'état de déformation homogène devient instable au sens de Lyapunov. Une analyse de stabilité linéaire permet alors de déterminer les conditions d'apparitions de la localisation.

Afin de suivre l'évolution de la taille de la zone localisée au cours du glissement, une méthode de régularisation doit être associée à l'intégration numérique du système d'équations non linéaires qui gouvernent le problème.

Contents

1.1 Fault mechanics

In this section, we describe the current understanding of the origin of earthquake in faults zones. The global mechanism of the unstable slip is first introduced in Section 1.1.1. In Section 1.1.2, the fault architecture and behavior is explained based on field observations and laboratory experiments. Finally, the different physical mechanisms involved and their couplings during the fault slipping process are presented in Section 1.1.3.

1.1.1 Mechanics of earthquake nucleation

The seismic waves that propagate through the earth's crust and cause dramatic deaths and structural damages are, in most cases, generated by a sudden slip along a fault. This explanation appeared in several publications, for instance Gilbert (1884) based on examinations of the Great Basin after the Owens Valley earthquake, but it became dominant after the 1906 San Francisco earthquake and the analysis of Reid (1910). Note that it was developed at the same time as the plate tectonics theory that has blossomed due to observations of the ocean floor and the development of a worldwide network of seismographs in the 1960s (Kramer, 1996).

The lithosphere, which is the rigid outermost shell of the Earth (the crust and upper mantle), is divided into tectonic plates, wich move with respect to each other. Their motion is principally driven by convective forces from the mantle (Coltice et al., 2017). As the upper portion of the mantle that is cooler and denser lies on top of a warmer and less dense material, the situation is unstable and leads to the creation of convection cells. However, it is not the only proposed mechanism to explain plate movement, ridge push and slab pull may also play a role (Hager, 1978).

One of the consequence of plate tectonics is the creation of earthquakes at the plate boundaries. The precise location of this seismic activity is one of the ways to determine the position of the plate boundaries. Moreover, volcanic activity, mountain-building, and oceanic trench formation also occur along these plate boundaries. Locally, the movement between two portions of the crust occurs on pre-existing or new offsets in the geologic structure called faults, which are by nature irregular.

The relative motion of the plates entails the storage of elastic energy in the material near the fault zones. It causes an increase of the shear stress until the shear strength is reached. The slip along the fault is then triggered, but this slip can be quasi-static or dynamic depending on the strength evolution during slippage. This mechanism is called the elastic rebound and can be illustrated by a simple spring-slider model (Fig. 1.1) (Scholz, 2002).

The sliding along the fault is frequently modeled by the motion of a block on an interface.

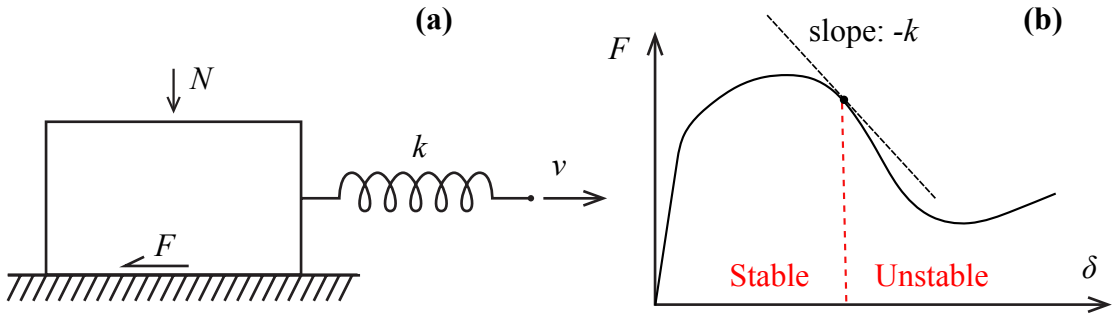

Figure 1.1: Simple spring-slider model to explain the origin of slip instability. (a) Sketch of the system studied. (b) Triggering of the instability when the strength decreases faster than the force applied by the spring.

F represents the fault strength and the spring of stiffness k represents the elasticity of the surrounding rock mass. The system is loaded by a constant velocity v applied at the extremity of the spring that simulates the tectonic motion at some distance from the fault. This velocity is of the order of some centimeters per year. If the strength of the fault increases with the slip δ, then the system is stable (no dynamic propagation occurs). However, if the strength decreases with the slip, two configurations are possible. If the slope of the load-displacement diagram is less steep than the spring stiffness, the system is also stable. If, on the contrary, the slope of the load-displacement diagram is steeper than the spring stiffness, the forces applied to the block cannot be balanced and the system is unstable, in the sense that the block slips dynamically. The condition for the instability of the system can be expressed as $\frac{dF}{d\delta} < -k$.

This instability results in stick-slip motions as observed by Brace and Byerlee (1966) in the frictional sliding of rocks. These observations led these authors to propose it as an explanation for the mechanism of earthquakes. Indeed, most of earthquakes are created by a friction instability along a pre-existing fault in the brittle part of the lithosphere (usually between 3 and 14 km depth (Marone and Scholz, 1988)). Moreover, this simple example shows the key importance of the strength evolution of the fault to assess the stability of its motion and its capacity to generate earthquakes.

Many studies since the publication of Brace and Byerlee (1966) have focused on the frictional behavior of rocks and in particular the effect of velocity (Dieterich, 1979). Ruina (1983) showed theoretically that for a velocity-strengthening material, the unstable sliding is quickly damped, whereas a velocity-weakening material always exhibits growing oscillations and presents a stick-slip behavior. This phenomenon can be captured by using the empirical rate-and-state friction laws that also apply to a wide range of materials such as plastic or glass (Baumberger et al., 1999). Nevertheless, these laws are phenomenological and describe the behavior of an interface by introducing a state variable that represents

the average age of contact for asperities. However, a mature fault that has accommodated meters of slip is composed of highly crushed granular material that presents a shear zone of finite width. It is, thus, likely that this representation by an interface does not systematically reflect the real physical mechanisms (Brantut, 2010).

In the framework of a fault zone with a finite thickness, many parameters can strongly affect the mechanical strength during slip and consequently the slippage stability, like the pore fluid pressure, the temperature or the confining pressure. Moreover, the thickness is of major importance for the energy efficiency of an earthquake as only a part of the elastic energy is radiated by elastic waves and the thickness controls the temperature rise during the coseismic slip (Kanamori and Rivera, 2006, Sibson, 2003).

1.1.2 In situ observations and laboratory experiments

To understand the physical mechanism of earthquakes, we need to examine the source, where rupture initiates and propagates. Many drilling projects were undertaken to investigate the properties of fault zones directly. Examples are for the Aigion fault in the Corinthian Gulf (Cornet et al., 2004), the San Andreas fault in California at different locations (Zoback et al., 1988, 2011) and the Nojima fault in Japan (Ando, 2001) among others. These inland drilling projects were completed by offshore subduction drilling projects (Losh et al., 1999, Vannucchi and Leoni, 2007, Sakaguchi et al., 2011). These cores enable us to obtain valuable informations about the fault zone structure, material and the stress conditions at the depth of the fault. However, the information is obtained only at a single point of the fault zone, so it is difficult to generalize the obtained features, as the fault is usually not planar but has many kinks, joints, jogs, steps, and branches (Fukuyama, 2009). Furthermore, the depths of drilling remain shallow (less than 3 kilometers) compared to the seismogenic zone (3 to 14 kilometers) and, thus, the conditions of temperature and pressure may be significantly different.

To overcome these problems, field investigations have been conducted on exhumed faults, on which earthquakes occurred long time ago at greater depth and are presently exposed on the surface. Based on the observation of these outcrops, it could be assessed that fault slip occurred within a very thin region of the fault (Poulet et al., 2014, Chester and Chester, 1998, Collettini et al., 2014), that has accommodated several kilometers of slip. The slip zone is surrounded by a broader damage zone.

From field observations, the fault zone structure and its evolution can be tracked. First, a set of fractures appears due to the shear stresses within the rock mass (Riedel shear (Riedel, 1929)). This network of fractures enlarges and becomes denser until the emergence of several dominant slip planes in which all the deformations are concentrated, forming the fault zone core. Around this core, lies a complex zone of damaged and fractured rocks. Then, with increasing deformations, severe fracturing and damage of core rocks

continues until the formation of a gouge, which composed of ultra-cataclasite materials (highly crushed particles) (Rafini, 2008). Further investigations reveal a zone of highly localized shear of the order of 10μm to a few centimeters wide nested within the fault gouge called the Principal Slip Zone (PSZ) (Poulet et al., 2014, Sibson, 2003, De Paola et al., 2008, Shipton et al., 2006, Heermance et al., 2003). A map of a fault zone is shown in Fig. 1.2 as well as pictures of the PSZ in the Glarus thrust fault in Switzerland in Fig. 1.3 .

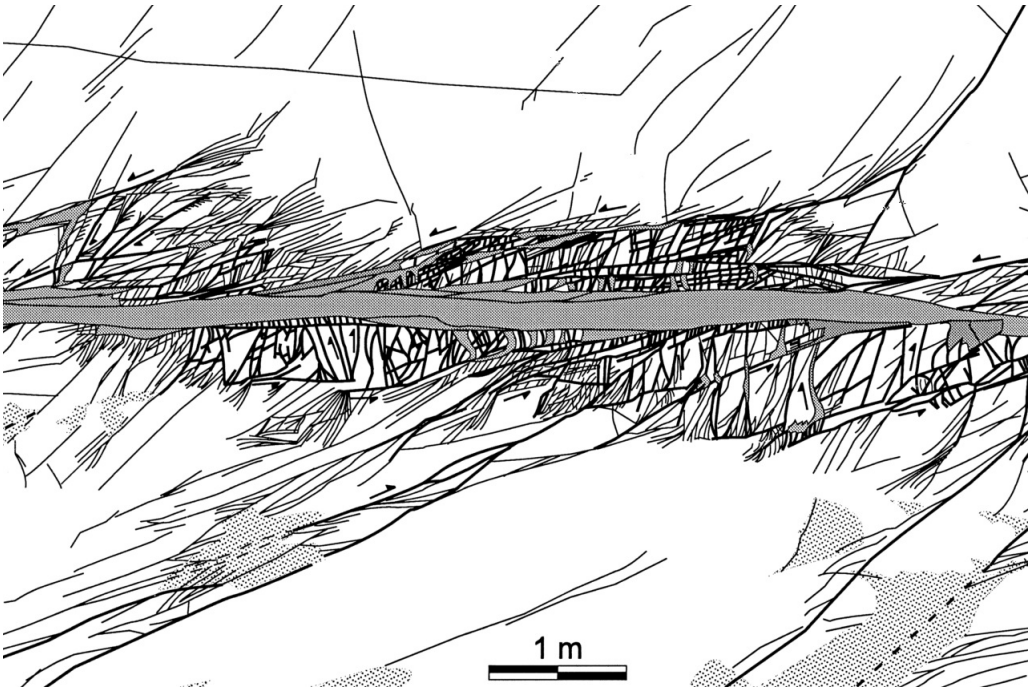

Figure 1.2: Detailed map of a fault gouge and the surrounding fracture network realized digitally from photographs of outcrops in the Valley of Fire State Park, southern Nevada, USA (Myers and Aydin, 2004)

Many investigations have been carried out in the laboratory to understand the behavior of fault gouges (see Marone (1998) for a review) using drilling core specimens (Sulem et al., 2004, Brantut et al., 2008, Boulton et al., 2017, Ujiie and Tsutsumi, 2010, Scuderi et al., 2013) or simulated fault gouges (Ikari et al., 2009, Samuelson and Spiers, 2012, Verberne et al., 2013). In these experiments, a fine granular materials is sheared using either a double direct shear device, a triaxial cell or a rotary shear apparatus, both in wet and dry conditions. The experiments show the development of a localization zone, which is usually characterized by a grain cataclasis (see Fig. 1.4). Most of the laboratory tests are performed under a low slip velocity (< 0.1 m/s) and small displacements only (on the order of centimeters). In these conditions, the rate-and-state friction laws seem appropriate to model the layer's behavior. However, the recent technical development of a new generation of rotary shear apparatus has enabled researchers to reach coseismic slip velocities (a few m/s) together with normal stresses and temperature at seismogenic depths (Tsutsumi and

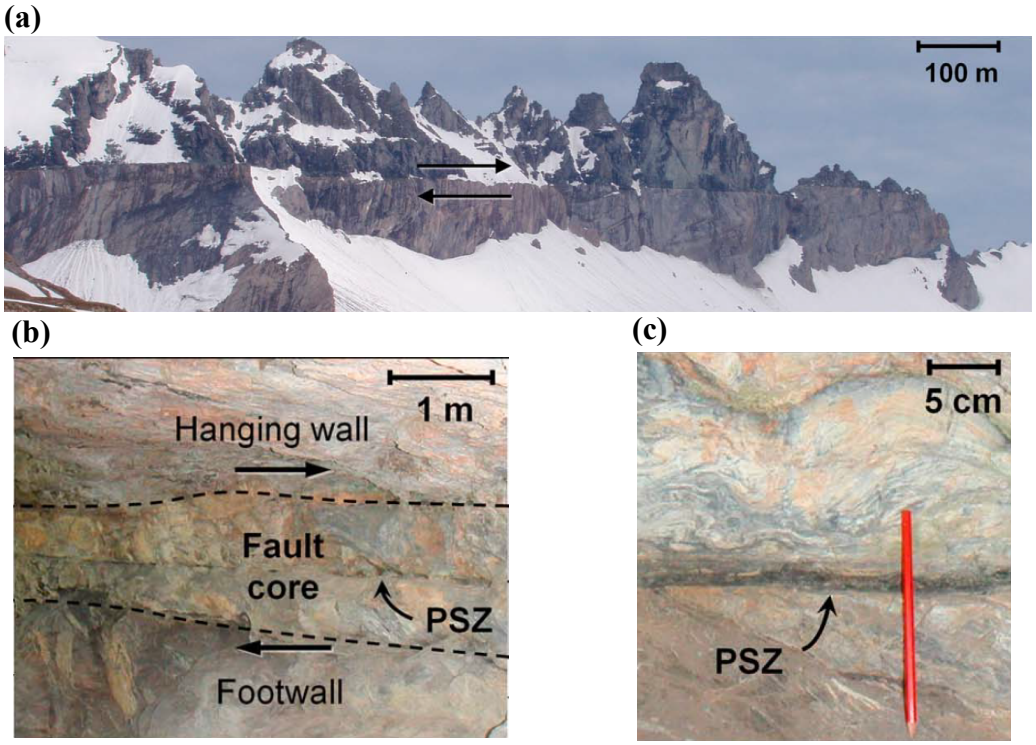

Figure 1.3: Photos from the Glarus thrust outcrop (Switzerland) illustrating the structure of a fault zone on three different scales: (a) The fault has moved on a very sharp boundary at the kilometer scale. (b) A closer look reveals a meter-wide fault core, at the (c) center of which an ultralocalized centimeter-thick most recent PSZ is clearly visible. (Poulet et al., 2014)

Shimamoto, 1997, Di Toro et al., 2010). These high-velocity rotary-shear experiments showed that rocks weaken dramatically at seismic slip rates and the rate-and-state laws do not adequately describe this weakening (Rempe, 2015). Several thermally and mechanically activated weakening mechanisms were proposed to understand the experimental results at seismic slip rates (Di Toro et al., 2011), but it remains an open problem. Some of the most important weakening mechanisms are presented in the next section.

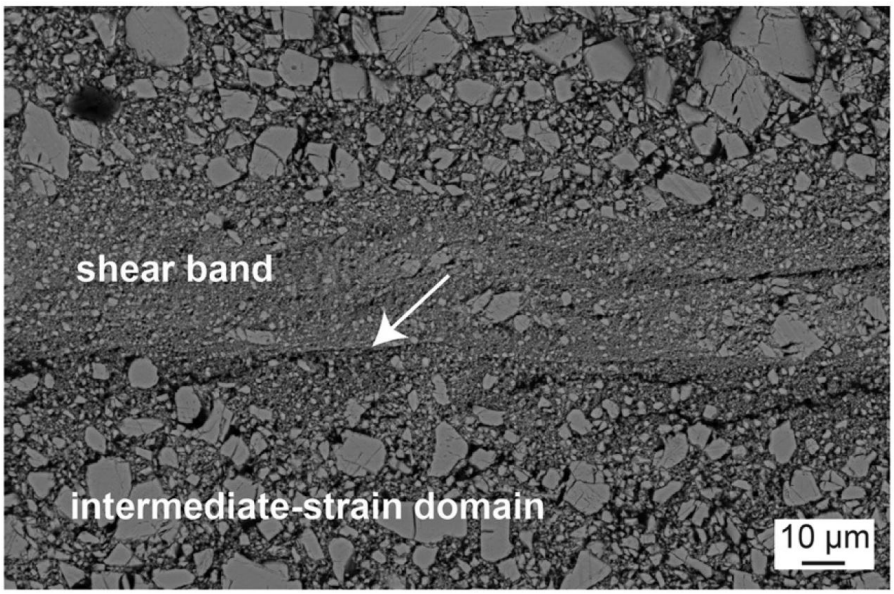

Figure 1.4: Scanning Electron Microscope image of a high-strain shear band obtained in a rotary shear apparatus for calcite with a normal stress applied of 17.3 MPa and a maximum applied shear velocity of 0.4 m.s^{-1} (Smith et al., 2015)

1.1.3 Multi-physical couplings and the role of the microstructure

Poromechanical theories and experiments have shown that the presence of a fluid inside the pore space of rocks has a fundamental effect on their behavior (Coussy, 2004). This is also the case in fault zones that are saturated with water. This effect can be addressed in a first approach by Terzaghi's principle for frictional materials. This principle states that the maximum applied shear stress τ_F is proportional to the applied effective normal stress σ': $\tau_F = \mu.\sigma' = \mu.(\sigma + p)$ (where μ is the friction coefficient, σ is the total normal stress and p the pore pressure; compression negative). This equation is central for the study of earthquake nucleation: If the pore pressure increases, the shear strength decreases and the slip is triggered. It is widely used to explain the mechanism of induced seismicity as the injection of a fluid (e.g. water or CO_2) induces a pore pressure change and, thus, a shear strength decrease (Simpson, 1976, Ando, 2001, Cappa, 2012, Gan and Frohlich, 2013). High pore pressure might also explain the apparent weakness of the San Andreas fault (Rice, 1992).

Pore pressure not only influences the slip nucleation but also the stability of the fault as it can evolve with deformation. During slip, an increase of the porosity (dilatant behavior) or a decrease (compaction) can occur. In the former case, the pore pressure decreases, whereas in the latter it increases affecting, thus, the slip behavior (see Fig. 1.1). Field observations confirmed the influence of pore pressure changes with slip. Sibson (1981) describes the effusions and the hydrothermal vein systems found in exhumed fault zones due to the intermittent channel flow of fluids that accompanies slip. This hydraulic fracturing of the rock is due to the modification of pore water pressure. In addition, experimental works were also conducted to investigate the effect of water on the friction properties (Scuderi et al., 2014, Verberne et al., 2014).

The large slip rates developed during seismic slip, which are of the order of 1m/s (Scholz, 2002), induce an important shear heating. As a result, the temperature increase can be very large and can induce various mechanisms. One of them is thermal pressurization of the pore fluid: high pore-fluid pressure is generated due to frictional heating during seismic slip (Sibson, 1973) as the thermal expansion of water is larger than the thermal expansion of the solid grains (Lachenbruch, 1980, Garagash and Rudnicki, 2003, Rice, 2006b, Segall and Rice, 2006, Ghabezloo and Sulem, 2009). Recently, Viesca and Garagash (2015) showed that this phenomenon is a potentially ubiquitous weakening mechanism, compatible with earthquake data over a wide range of magnitudes. Advances in experimental setups have also enabled observation of this phenomenon in the laboratory within seismic slip conditions (Ujiie et al., 2011).

A micro-mechanical consequence of the high-velocity slip is the intense heating at micro-asperity contacts, called flash heating. This weakening mechanism was first studied in tribology for metals and then applied to fault zones by Rice (1999). The increase of temperature for highly stressed frictional microcontacts between grains with rapid slip induces a reduction of the friction coefficient (Rice, 2006a). Flash heating provides a consistent explanation for the observed dynamic weakening in laboratory experiments for small displacements (less than a millimeter) (Brantut and Viesca, 2017). This weakening is triggered prior to macroscopic melting and is one of the possible explanations for rapidly diminishing fault strength as slip accumulates. Indeed, evidences for narrowness of the zone where frictional work is dissipated imply temperature rises, which far exceed those for onset of melting (around $1000/^{o}$C for wet granitic materials) if no weakening is considered (Rice, 2006a).

The only clear evidence of melting in some fault zone outcrops is the presence of Pseudotachylytes (Sibson, 1975). Pseudotachylyte is a glassy looking rock embedding survivor clasts of the host rock and is the result of solidification of friction-induced melt produced during seismic slip (Di Toro et al., 2009). These rocks are rarely observed in the field (Rice, 2006a), which means that the temperature increase is precluded in much of the seismogenic zone. This assertion is qualitatively consistent with low heat outflow measured from major

faults (Lachenbruch and Sass, 1980).

A potential mechanism that would cap the temperature increase is the triggering of endothermic chemical reactions like the decomposition of carbonates (Collettini et al., 2014, Hirono et al., 2007, Sulem and Famin, 2009a) or dehydration reactions (Veveakis et al., 2010, Brantut et al., 2011, 2017). These reactions have an activation temperature that is lower than the melting point of the minerals and act as a sink in the energy balance equation. Thermo-Chemical mechanisms can also alter the mechanical properties of the material and lead to weakening (Wibberley, 2005, Brantut and Sulem, 2012a).

At high confinement, like in seismogenic faults, we observe a substantial grain size reduction or grain cataclasis (Sammis and Ben-Zion, 2008). This is usually used as a marker to identify the principal slip zone. However, the microstructure change has an effect on many physical mechanisms. The production of fine particles can significantly weaken the material. Some studies have shown that the addition of nanograins to slip surfaces reduces the friction coefficient due to the rolling of the grains (Han et al., 2010, Di Toro et al., 2011). Anthony and Marone (2005) have shown that the grain size in the gouge affects the its frictional behavior. Grain size also has an effect on the strength of the gouge (Dieterich, 1981) and on the chemical reactions kinetics as it depends on the specific surface: crushing a solid into smaller parts means that more particles are present at the surface, and the frequency of collisions between these and reactant particles, if they are present in the pore space, increases, so that the chemical reaction occurs more rapidly.

A fault zone is, thus, a complex system where various physical mechanisms occur and are coupled together. Many studies have been devoted to the understanding of the weakening mechanisms that accompany the pre- and coseismic slip. A key parameter to study the slippage is the formation and the evolution of the zone of localized deformation. The thickness of this deforming zone is, on one side, determined by the weakening processes and the microstructure, but on the other side, it also controls the magnitude of the multi-physical couplings as, for example, the temperature rise is determined by the shear band width.

1.2 Strain localization analysis

In this section, we introduce the theoretical concepts useful for studying strain localization. A brief introduction to the bifurcation theory is given with an application to strain localization.

1.2.1 Instability and bifurcation

From an engineering point of view the stability of a system can be seen as a sensitivity to small perturbations for a given state of equilibrium. It is stable if small changes in the input (disturbances in the loading system, material imperfections, etc...) do not induce catastrophic consequences for the system (Chambon et al., 2004). This conception of stability is simplistic but it can be linked with the theoretical definitions of stability.

Stability was rigorously defined by Lyapunov in a paper published in 1892 and translated into English one century later (Lyapunov, 1992). It is worth mentioning that a french translation was published in 1907 by Edouard Davaux, son in law of François Cosserat (Chatzis and Brocato, 2009).

Lyapunov stability depends on the points considered. A system can have several fixed points and some can be stable and other not. If the system starts sufficiently close to the fixed point, then it will stay arbitrarily close to the fixed point forever. It means that the state of the system will not run away but it does not mean that the state of the system will come back to the fixed point.

To express it in a mathematical manner, we have to introduce some definitions and for that we take the same notations as Pac (2012). We consider a system, whose evolution is described by an ordinary differential equation in the form: $\dot{\mathbf{x}} = \mathbf{f}(\mathbf{x})$, where $\mathbf{x}$ is a vector that describes the state of a system, $\dot{\mathbf{x}}$ its time derivative, and $f \in C^1(\mathbb{R}^n, \mathbb{R}^n)$.

Definition x_0 is an equilibrium point (also called fixed point or stationary point) if and only if $f(x_0) = 0$.

x_1 is a regular point if it is not an equilibrium point, i.e. if and only if $f(x_1) \neq 0$.

One may note that the system is linear if there is an endomorphism $\boldsymbol{A}$ of $\mathbb{R}^n$ such as $\mathbf{f}(\mathbf{x}) = \boldsymbol{A}(\mathbf{x})$. $\mathbf{0}$ is an equilibrium point for all linear systems and if $\boldsymbol{A}$ is injective it is the only one (otherwise it is a vector subspace of $\mathbb{R}^n$).

Definition The point x_0 is Lyapunov stable if and only if

$$\forall R > 0,\ \exists \epsilon > 0,\ \|\mathbf{x}(t=0) - \mathbf{x}_0\| < \epsilon \Longrightarrow \forall t > 0\ \|\mathbf{x}(t) - \mathbf{x}_0\| < R$$

With this definition we remark that a stable system can present persistent small oscillations around the fixed point. For engineers it would be ideal for these oscillations to disappear in the long term, which is called *asymptotic stability* and is defined below. According to A. T. Fuller in the guest editorial of the English translation of Lyanpunov's manuscript (Lyapunov, 1992), Lyapunov paid more attention to this definition of stability because he was mainly concerned with astronomical problems. This class of problems is mathematically described without any dissipation, so that *asymptotic stability* is not possible. Indeed the best we can expect for the bodies is that they perform small oscillations around

their nominal motions. To address the concept of asymptotic stability, we introduce the definition of an attracting point. If the system starts sufficiently close to an attracting point, it will converge to it.

Definition The point x_0 is attracting if and only if

$$\exists \epsilon > 0,\ \|\mathbf{x}(t=0) - \mathbf{x}_0\| < \epsilon \Longrightarrow \lim_{t\to\infty} \|\mathbf{x}(t) - \mathbf{x}_0\| = 0$$

None of the definitions above is included in the other. A point can be Lyapunov stable and not attracting (as mentioned above, it can exhibit persistent small oscillations around the fixed point) and conversely it can be attracting and not Lyapunov stable as shown in the following example.

Example Consider the equation $\dot{\theta} = 1 - \cos(\theta)$. We can draw the phase diagram for this equation and we observe that the origin is half-stable, so if we perturb the system such as $\theta(t=0) > 0$, θ increases from $\theta(t=0)$ *to* π and then from $-\pi$ *to* 0 (it travels around a circle), so it reaches the fixed point, which is thus an attracting point, but it has diverged first before coming back, which means it is not Lyapunov stable.

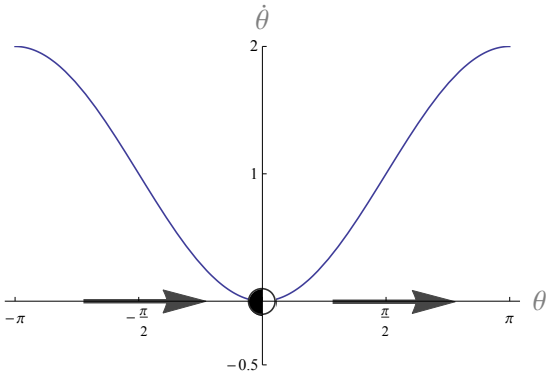

Figure 1.5: Phase diagram for the equation $\dot{\theta} = 1 - \cos(\theta)$

A fixed point is considered *asymptotically stable* if it is at the same time Lyapunov stable and attracting. This property is due to the ability of the system to damp the effects of perturbations acting on it. If it is only Lyapunov stable and not attracting, it is called *marginally* or *neutrally stable*. A basic example of this behavior is the simple pendulum with small angle approximation and no dissipation. The amplitude of oscillations can be limited by choosing appropriate initial conditions.

Thus, asymptotic stability implies Lyapunov stability by definition. On the contrary, the attraction causes asymptotic stability only if the system is linear (see the example of equation $\dot{\theta} = 1 - \cos(\theta)$ which is non-linear).

In Fig. 1.5, a phase diagram is shown. This graph is very convenient for understanding the behavior of linear or non-linear systems, but the pattern of the figure can change as parameters vary. For example a fixed point can disappear, a new one can be created or

their stability can change. These modifications not only modify the values of fixed points, they affect the complete behavior of the system. These qualitative changes are called *bifurcations* (Strogatz, 1994) and the parameter's values for which this change occurs are called bifurcation points. We will not give the mathematical definition of this concept because it involves topological considerations that are not useful to our study.

In Fig. 1.6, we present an idealized diagram of bifurcation, with a governing parameter in the horizontal axis and the equilibrium state in the vertical axis. This kind of diagram can be found in May (1976), where the authors studied the evolution of an insect population. Here the state is the population and the parameter is the rate of growth for this population. We observe that beyond λ_1 the population has several states available, which means that its numbers will oscillate between these values, and beyond a critical value of the parameter the behavior can become chaotic and the number of states available becomes infinite.

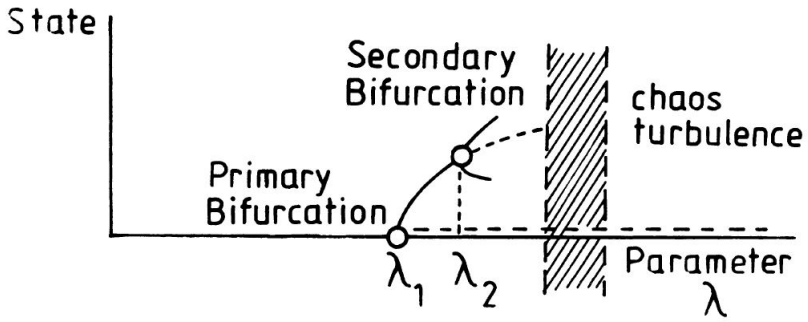

Figure 1.6: Example of bifurcation diagram from Prigogine (Prigogine and Nicolis, 1985)

The dashed lines represent unstable states, whereas the solid lines for stable ones. The state for $\lambda < \lambda_1$ is stable and the population is equal to 0. When $\lambda > \lambda_1$, this aforementioned state is no longer stable and new stable states appear. In that case the loss of uniqueness is accompanied with an exchange of stability. The previous solution becomes unstable while the new ones are stable.

For localization phenomena in geomaterials, we look for alternative solutions presenting heterogeneous deformation. It is also possible to have alternative solutions that are homogeneous (Lesniewska and Wood, 2011). The localized zone is called a deformation band, which can be a compaction, dilation or shear band. These different bands influence the strength of the body as deformation localizes and, thus, the persistence of the heterogeneous deformation pattern.

The softening behavior of a material favors a localization of deformation (Molinari and Leroy, 1991, Molinari and Clifton, 1986) (see Fig. 1.7 for an example of material with softening). However, it is not a necessary condition as we can observe strain localization even for materials with a strain-hardening behavior (e.g. materials presenting non-associative or non-coaxial plastic response (Rudnicki and Rice, 1975b, Issen and Rudnicki, 2000)).

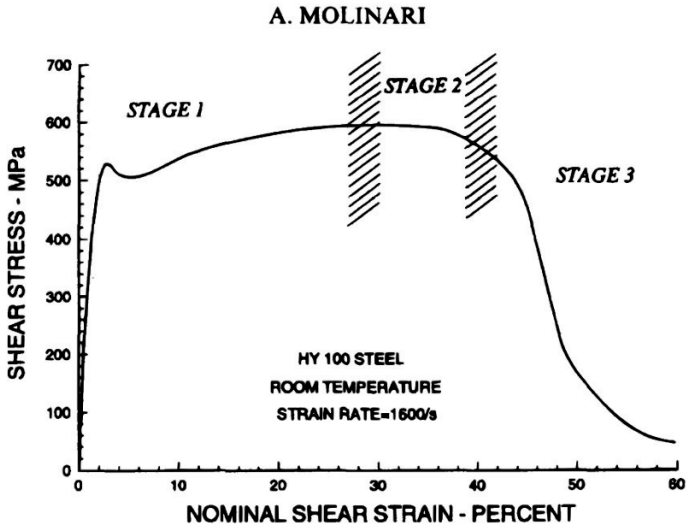

Figure 1.7: Stress-strain torsion response of a steel that presents a strain-softening (Molinari, 1997)

1.2.2 Localization conditions

To explore under which condition a homogeneous solution is stable/unstable, we perform a stability analysis of the homogeneous state, which is considered as a fixed point according to the above terminology. This analysis corresponds to the first method developed by Lyapunov in his manuscript (Lyapunov, 1992).

As an example, the method is applied to a Cauchy continuum to determine the classical condition of localization (Stefanou and Alevizos, 2016).

The momentum balance equation for this problem is:

$$\sigma_{ij,j} = \rho \ddot{u}_i \tag{1.1}$$

where σ_{ij} is the stress tensor in a Cauchy continuum, ρ is the density of the material and u_i are the displacements defined at each point of the continuum.

Considering a reference homogeneous state, which is in equilibrium, we obtain:

$$\sigma^0_{ij,j} = 0 \tag{1.2}$$

where σ^0_{ij} is the stress tensor of the homogeneous state. We consider that for the class of material studied and for a small increment, the constitutive law can be linearized around the homogeneous state as follows:

$$\Delta\sigma_{ij} = C_{ijkl}\Delta u_{k,l} \tag{1.3}$$

where Δu_i is an increment of displacements from the homogeneous solution u_i^0. Inserting the constitutive law into Eq. 1.1, we get:

$$C_{ijkl}\Delta u_{k,lj} = \rho\Delta\ddot{u}_i \tag{1.4}$$

The method of separation of variables is used to find the solution of this linearized system $\Delta u_i = X(x_k)U_i(t)$, which results to:

$$C_{ijkl}X_{,lj}U_k = \rho X\ddot{U}_i \tag{1.5}$$

The solutions for X are sinusoidal functions and as we are looking for solutions in the form of deformation bands, which are planar, they can be written as $X(x_k) = e^{i\xi n_j x_j}$, where n_i is the unit vector normal to the band, ξ is the wave number of the perturbation and $i^2 = -1$. This expression of X is inserted in Eq. 1.5 and by setting $\dot{U}_i = V_i$, we obtain the following system of Ordinary Differential Equations of first order in V_i and U_i:

$$\begin{aligned}\rho\dot{V}_i &= -C_{ijkl}\xi^2 n_l n_j U_k \\ \dot{U}_i &= V_i\end{aligned} \tag{1.6}$$

A particular solution of this system is $U_j(t) = g_j e^{st}$ and $V_j(t) = f_j e^{st}$, where g_j and f_j are non-zero constant vectors and s is the so-called "Lyapunov exponent" or "growth coefficient" of the perturbation. After some algebra, the system becomes:

$$[C_{ijkl}n_l n_j + \rho(\frac{s}{\xi})^2\delta_{ik}]g_k = 0 \tag{1.7}$$

where δ_{ik} is the Kronecker symbol. Thus, a non-zero solution for g_k is possible only if the determinant of the second order tensor between the brackets vanishes. This condition yields a polynomial equation for the growth coefficient s (characteristic polynomial). If a solution of this polynomial has a positive real part, then the corresponding perturbation grows exponentially in time and the homogeneous solution is unstable, leading to a localization. This condition coincides with Hadamard's stability condition (Hadamard, 1903) by setting $c = \frac{s}{\xi}i$. The second order tensor $C_{ijkl}n_l n_j$ is usually called the acoustic tensor.

As we are looking for the change of sign of the real part of s to determine the bifurcation condition for the triggering of localization, a necessary condition for the onset is that the determinant of the acoustic tensor is zero. This localization condition can also be obtained considering a thin layer bounded by two discontinuities (Mandel, 1966, Rudnicki and Rice,

1975a).

The inner product of the unit vector to the band n_j and the vector for the direction of perturbation increment g_j determine the nature of the deformation band:

$$\begin{cases} n_j g_j = 1 \ : \ \text{pure dilation band} \\ 0 < n_j g_j < 1 \ : \ \text{dilatant shear dilation band} \\ n_j g_j = 0 \ : \text{simple shear band} \\ -1 < n_j g_j < 0 \ : \ \text{compactive shear band} \\ n_j g_j = -1 \ : \ \text{pure compaction band} \end{cases} \tag{1.8}$$

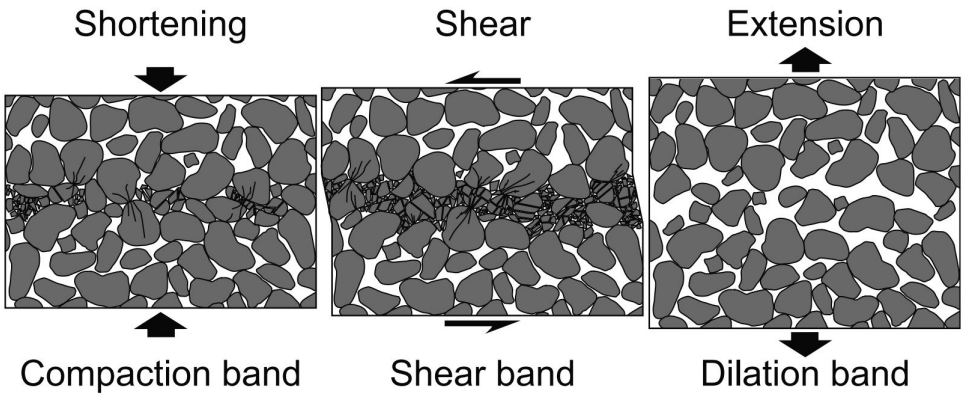

Figure 1.8: Illustration of the different deformation bands in granular media from Du Bernard et al. (2002)

For elasto-plastic materials, the threshold for the bifurcation condition is usually expressed in terms of the hardening modulus. The orientation n_j, for which the hardening modulus is maximum, is sought (Rudnicki and Rice, 1975a). Nevertheless, in the case of a fault gouge, as it is modeled as a shear band, the polarization vector g_j and the normal to the band n_j are already determined. Therefore we search only for the critical hardening modulus.

This condition for a purely mechanical system has been applied for various constitutive models (Bardet, 1990, Bigoni and Hueckel, 1991) and the methodology presented here is general enough to be applied to many problems. For instance, it has been applied to mechanical system taking into account different couplings: Hydro-mechanical couplings (Rice, 1975, Benallal and Comi, 2003, Loret and Prevost, 1991), Thermo-Mechanical couplings (Benallal and Bigoni, 2004, Armero and Park, 2003) or Thermo-Hydro-Mechanical couplings (Rice et al., 2014, Benallal, 2005, Sulem et al., 2011). Furthermore, despite considering a Cauchy continuum, the same approach can also be applied to higher order continua (Mühlhaus and Vardoulakis, 1987, Veveakis et al., 2012).

1.3 Post-bifurcation analysis

A first approach to study a localization problem consists at looking at the possible critical conditions for which the constitutive equations of the material allow a bifurcation point as explained above. But in some cases, we would like to know the evolution of the system after the onset of localization. For instance, the study of the principal slip zone evolution enables to extract information about seismic slip. For that, we need to approximate the solution of a nonlinear boundary value problem numerically. It is a challenging task due to the complications that arise while dealing with a softening behavior. Indeed, the classical continuum theory cannot be used because the governing system of equations is ill-posed (Vardoulakis, 1985) and a regularization of the problem is needed.

1.3.1 Regularization methods

This ill-posedness of the localization problem in the Cauchy continuum can be tracked back to the fact that constitutive models do not contain material parameters with the dimension of length and, thus, the size of the localized zone is zero. This phenomenon is observed numerically by *mesh dependency* of the numerical results. The deformation localizes in only one element of the mesh and the behavior of the system depends therefore on the mesh size. The non-objectivity can lead to nonphysical results and this pathological issue has to be addressed by resorting to appropriate theories that enable a *regularization* of the problem.

The need to introduce a length scale into the constitutive description can be explained by the fact that when the localization process occurs, the macroscopic mechanical characteristic scale becomes of the same magnitude as the microstructural length scale. Therefore, the hypothesis of scale separation to derive a homogenized classical continuous material is no longer valid (Forest and Lorentz, 2004). The scale of heterogeneities of the microstructure and the scale of interactions of closed points have to be taken into account.

A number of theories have been proposed which set out to enrich the continuum description with more physics such that localization can develop while ellipticity of the equations is preserved:

- Viscous regularization by considering strain rate hardening/softening together with inertia terms (Needleman, 1988, Wang et al., 1996).

- Generalized continua with microstructure, such as the Cosserat continuum (de Borst, 1991, Mühlhaus and Vardoulakis, 1987) or second gradient models (Collin et al., 2006).

- Non-local models of the integral type (Jirasek, 2015, Pijaudier and Bazant, 1987) for which integral relations relate stress and strain evolution.

However, enhanced models restore the mesh objectivity of the solution, but not the the

uniqueness of the solution.

1.3.2 Numerical methods

In order to integrate the nonlinear set of equations considering a higher-order theory, an efficient numerical method has to be considered. Most of the numerical methods are based on a discretization of the continuous system of equations in time and space.

The most intuitive one is the method of Finite Differences (FDM), which is based on Taylor's expansions of the derivatives (Taylor, 1715). The method was developed in the 18th century and was applied for the first time for approximating the solution of an engineering problem for dams by Richardson (1911). Many variants of this method have emerged since, improving the stability and convergence of the method (e.g. Runge-Kutta (Butcher, 1996) or Crank-Nicolson (Crank et al., 1947)). Nowadays, FDM is mainly used for the discretization of the time derivatives of the Partial Differential Equations (PDE) to solve. This strategy, is also applied in this Thesis, for the time derivatives. In particular, a backward Euler method is applied for the time integration.

As far as it concerns the spatial discretization of our mathematical problem, we use the Finite Element Method (FEM) in this Thesis. FEM blossomed in the 60s after the pioneer works of A. Hrennikoff, R. Courant and I. Argyris in the 40s and 50s. The method consists in calculating the solution of the variational form of the mathematical problem (Zienkiewicz and Taylor, 1994). The Finite Element implementation is presented in details in Chapter 3.

An alternative for the spatial discretization of our PDEs is, between others, the pseudo-spectral method. This method is strongly related to spectral methods, as the Chebyshev polynomials usually used for interpolating the functions are Fourier series in disguise. Indeed, a change of variables turn the cosines and sines of the Fourier series into a Chebyshev polynomial. Thus, most of the properties demonstrated for the Fourier series are true for these polynomials, such as completeness or convergence. The spectral methods developed by Fourier in 1822 to solve the heat equation (Fourier, 1822) consists of projecting the solution on to a finite family of trigonometric functions.

This method knew a great development through the algorithm of Fast Fourier Transform by Cooley and Tukey in 1965 which speed up significantly the calculation of the coefficients (Cooley and Tukey, 1965). Pseudo-spectral methods appear to be very efficient for simple geometries, but as the interpolation functions are defined over the whole domain, difficulties appear in the integration of complex geometries (see Boyd (2000) for a detailed description). Moreover, there are might be other problems related to Aliasing, Spectral Blocking and Blow-up, which hinder the direct application of the method in highly non-linear, fully coupled problems. This is why we preferred to stick to the classical FEM.

Chapter 2

Theory and linear stability analysis of strain localization in a 3D continuum with microstructure and multi-physical couplings

Un modèle Thermo-Hydro-Mécanique (THM) dans les milieux de Cosserat est développé dans ce chapitre afin de montrer l'influence de l'échauffement par frottement et de la pressurisation thermique de l'eau dans les pores sur le phénomène de localisation des déformations. Cette localisation est considérée comme le résultat d'une instabilité de l'état de déformations homogènes. Un cadre général est présenté pour mener une analyse de bifurcation dans les milieux élasto-plastiques de Cosserat présentant des couplages THM et, ainsi, prédire le déclenchement de l'instabilité. D'autre part, la présence d'une longueur au sein de la loi constitutive permet une estimation de l'épaisseur de localisation. En effet, cela conduit à la sélection d'une longueur d'onde préférentielle du mode instable correspondant au mode dont le coefficient d'accroissement est le plus élevé. Un lien est établi entre la microstructure du matériau et la longueur interne de la loi constitutive. Ces concepts sont ensuite appliqués pour comprendre le mécanisme des failles qui créent des séismes. Pour ce faire, nous considérons le modèle d'une couche granulaire infinie saturée et cisaillée. L'influence des couplages THM sur la bifurcation et la taille de bande est analysée. En considérant des paramètres représentatifs d'une gouge de faille à une profondeur centrale de la partie fragile de la lithosphère, l'évolution de la taille de la bande de cisaillement est obtenue. Une analyse de l'influence des principaux paramètres sur les résultats est aussi menée. Finalement, l'effet de l'écrasement des grains au sein de la bande est exploré en modifiant la valeur de la longueur interne.

Contents

2.1 Introduction

In this chapter, we focus on the thermal pressurization process. It has been recognized to play ubiquitous role in the weakening of fault zones (Viesca and Garagash, 2015, Lachenbruch, 1980). This phenomenon is a consequence of the discrepancy between the thermal expansion of pore water and the solid matrix (Rice, 2006b). It results in a decrease of the effective mean stress and consequently of the shear strength. To determine the thickness of the localized zone, the frame of classical continuum theory is not appropriate as it leads to an infinitely small localized zone (Vardoulakis, 1985). A rate dependent constitutive behavior is a common procedure to overcome this issue (Rice et al., 2014), but it is rather empirical. Another approach is to consider continua with microstructure, like Cosserat continua. They also enable us to introduce the effect of the microstructure into the constitutive relationships. A major asset as the microstructure has been recognized to play an important role on gouge behavior (Phillips and White, 2017, Anthony and Marone, 2005).

Cosserat continua (Cosserat and Cosserat, 1909) is a theory that considers more degrees of freedom than the classical Cauchy continuum and provides a better representation of the physics and the mechanical behavior of continua with microstructure. This microstructure is related naturally to the model by the presence of several characteristic lengths (see A.2).

In this chapter, we focus mainly on using bifurcation theory and Linear Stability Analysis (LSA). The approach is analytical and it allows us to explore qualitatively the influence of the evolution of the hardening parameter and of the grain size on the thickness of the localized zone. In Sections 2.2 and 2.3 we present the momentum, mass and energy balance equations of the problem and the full constitutive equations for general Cosserat elastoplastic continua. The bifurcation analysis in this framework is presented in Section 2.4 and linked with classical results like the singularity of the acoustic tensor. Finally, the bifurcation analysis is applied to the problem of slip in a fault zone (Section 2.5) and the influence of the main parameters of the model is investigated as far it concerns the onset of localization and the shear band thickness evolution.

2.2 Basic concepts of three-dimensional Cosserat continuum mechanics and balance equations

The Cosserat continuum is a special case of first order micromorphic continua, for which the particle is considered rigid (Godio et al., 2016, Stefanou et al., 2010). In the frame of Cosserat theory the kinematics of a material point in three-dimensional (3D) space is described by six degrees of freedom, which are three translations u_i and three rotations

$\omega_i^c (i = 1, 2, 3)$. In this section, the basic concepts of Cosserat theory are outlined.

2.2.1 Cosserat kinematics

Compared to a Cauchy continuum formed by a set of particles identified by their coordinates x_i, we attach to every particle a system of axes parallel to the Cartesian one and with M, the center of mass of the particle, as origin.

If we consider a point M', in the particle of center M, defined by its coordinates x'_i, the displacement field in M', u'_i, can be written as follows, considering only terms of first order.

$$u'_i = u_i + \chi_{ij}\ x'_j \tag{2.1}$$

Einstein summation convention is followed herein. χ_{ij} is the micro-deformation tensor. As the microstructure is considered rigid in Cosserat theory, the micro-volume cannot deform and can only rotate. Thus, the micro-deformation tensor χ_{ij} is antisymmetric and is called the Cosserat rotation ω_{ij}^c. As ω_{ij}^c is antisymmetric, we can write :

$$\omega_{ij}^c = -e_{ijk}\ \omega_k^c \tag{2.2}$$

where e_{ijk} is the Levi-Civita symbol.

The following kinematic fields are introduced:: the deformation tensor γ_{ij} - which is split into its symmetric ε_{ij} and antisymmetric part $\gamma_{[ij]}$ - and the curvature tensor κ_{ij} - also split into its symmetric $\kappa_{(ij)}$ and antisymmetric part $\kappa_{[ij]}$.

$$\begin{aligned} \varepsilon_{ij} = \frac{1}{2}(u_{i,j} + u_{j,i}) \qquad \Omega_{ij} = \frac{1}{2}(u_{i,j} - u_{j,i}) \\ \gamma_{[ij]} = \Omega_{ij} - \omega_{ij}^c \qquad \kappa_{ij} = \omega_{i,j}^c \\ \gamma_{ij} = \varepsilon_{ij} + \gamma_{[ij]} = u_{i,j} - \omega_{ij}^c = u_{i,j} + e_{ijk}\ \omega_k^c \end{aligned} \tag{2.3}$$

The macroscopic strain and rotation tensors (ε_{ij} and Ω_{ij}) are the symmetric and antisymmetric parts of the displacement gradient as in a classical Cauchy continuum. $\gamma_{[ij]}$ is the difference between the macroscopic rotation Ω_{ij} and the rotation of the microstructure ω_{ij}^c. The curvature tensor κ_{ij} is defined as the gradient of Cosserat rotations.

2.2.2 Momentum and angular momentum balance equations

Correspondingly the stress tensor τ_{ij} is also divided into its symmetric σ_{ij} and antisymmetric part $\tau_{[ij]}$. The symmetric part corresponds to the macroscopic stresses (the ones that are considered in Cauchy continuum), the antisymmetric one is nonzero in general. A tensor for the couple-stress is defined by μ_{ij} linked to the curvature.

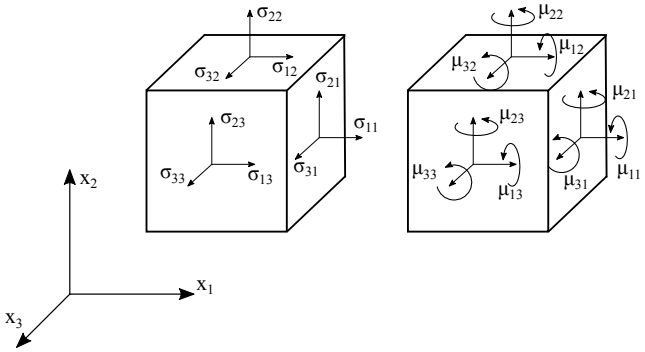

Figure 2.1: Representation of stress and couple-stress components.

The momentum balance equations can be written as follows (assuming no body forces acting on the medium)(Vardoulakis and Sulem, 1995, Stefanou et al., 2017):

$$\tau_{ij,j} - \rho \frac{\partial^2 u_i}{\partial t^2} = 0 \tag{2.4}$$

$$\mu_{ij,j} - e_{ijk}\ \tau_{jk} - \rho I \frac{\partial^2 \omega_i^c}{\partial t^2} = 0 \tag{2.5}$$

where ρ is the density, I is the micro-inertia, which is considered isotropic here. For example, $I = \frac{2}{5}R^2$ if we identify the particle as spherical grains with radius R ($I = \frac{1}{2}R^2$ in 2D) (Vardoulakis and Sulem, 1995).

2.2.3 Energy balance equation

The energy and mass balance equations as classically derived for a saturated Cauchy continuum are extended here to a saturated Cosserat continuum.

The energy conservation in a quasi-static transformation is expressed as follows:

$$\rho C \frac{\partial \mathrm{T}}{\partial t} = P_H - j^Q_{i,i} \tag{2.6}$$

where ρC is the specific heat per unit volume of the material in its reference state and j_i^Q represents the heat flux density. It is assumed here that the rate of heat produced P_H is

due to plastic dissipation, thus, $P_H = \sigma_{ij}\dot{\varepsilon}^p_{ij} + \tau_{[ij]}\dot{\gamma}^p_{[ij]} + \mu_{ij}\dot{\kappa}^p_{ij}$. This expression is the sum of three terms, one corresponding to the plastic work due to the symmetric part of the stress tensor (Cauchy), $\sigma_{ij}\dot{\varepsilon}^p_{ij}$, and the two others are due to Cosserat effects (Vardoulakis and Sulem, 1995). $\dot{\varepsilon}^p_{ij}$, $\dot{\gamma}^p_{[ij]}$ and $\dot{\kappa_{ij}}^p$ are the plastic symmetric deformation rate, plastic antisymmetric deformation rate and the plastic curvature rate tensors respectively. The heat flux is linked to the temperature gradient by Fourier's law:

$$j^Q_i = -k_T\ T_{,i} \tag{2.7}$$

where k_T is the thermal conductivity of the material which is assumed homogeneous here. Substituting these two expressions gives the energy balance equation.

$$\rho \mathrm{C}(\frac{\partial \mathrm{T}}{\partial t} - c_{th}T_{,ii}) = \sigma_{ij}\dot{\varepsilon}^p_{ij} + \tau_{[ij]}\dot{\gamma}^p_{[ij]} + \mu_{ij}\dot{\kappa}^p_{ij} \tag{2.8}$$

where $c_{th} = \frac{k_T}{\rho C}$ is the thermal diffusivity.

2.2.4 Mass balance equation

We consider a porous medium consisting of two phases, i.e. the solid skeleton and the fluid contained in the pores. The conservation of the mass of the skeleton and the fluid, when no mass exchange occurs is:

$$\begin{aligned} \frac{d^s m^s}{dt} &= 0 \\ \frac{d^f m^f}{dt} &= 0 \end{aligned} \tag{2.9}$$

where $\frac{d^\pi}{dt}$ refers to the particle derivative with respect to particle π $(= s\ or\ f)$ (Coussy, 2004). m^f and m^s are respectively the fluid mass and the skeleton mass per unit volume of the medium. If ρ_s and ρ_f are the skeleton and fluid mass densities so that $\rho_s\ (1-n)\ d\Omega^t$ and $\rho_f\ n\ d\Omega^t$ are respectively the skeleton mass and the fluid mass currently contained in the material volume with an Eulerian porosity n, we obtain:

$$\begin{aligned} \frac{d^s m^s}{dt} = \frac{d^s(\rho^s\ (1-n)\ d\Omega^t)}{dt} &= \frac{d^s(\rho^s\ (1-n))}{dt}\ d\Omega^t + \rho^s\ (1-n)\frac{d^s d\Omega^t}{dt} \\ \frac{d^f m^f}{dt} = \frac{d^f(\rho^f\ n\ d\Omega^t)}{dt} &= \frac{d^f(\rho^f\ n)}{dt} d\Omega^t + \rho^f\ n\frac{d^f d\Omega^t}{dt} \end{aligned} \tag{2.10}$$

By applying the Eulerian continuity conditions and using the expression of the particle derivative (Coussy, 2004) we get:

$$\frac{\partial(\rho^s\ (1-n))}{\partial t} + ((\rho^s\ (1-n))V_i^s)_{,i} = 0$$
$$\frac{\partial(\rho^f\ n)}{\partial t} + (\rho^f\ n\ V_i^f)_{,i} = 0 \tag{2.11}$$

where V_i^s and V_i^f are the velocity fields of the solid and fluid phase respectively. $()_{,i}$ represents the divergence operator applied to the current state. However, we keep a small strain framework and therefore no distinction will be made in the following between the reference and the deformed configuration.

If we neglect the gradient of the density of the fluid and solid phases, Eq. 2.11 becomes

$$-\rho^s\frac{\partial n}{\partial t} + (1-n)\frac{\partial \rho^s}{\partial t} + \rho^s\ ((1-n)V_i^s)_{,i} = 0 \tag{2.12}$$
$$\frac{n}{\rho^f}\frac{\partial \rho^f}{\partial t} + \frac{\partial n}{\partial t} + n\ V_{i,i}^f = 0 \tag{2.13}$$

Finally, adding Eq. 2.12 divided by ρ^s and Eq. 2.13 yields:

$$\frac{n}{\rho^f}\frac{\partial \rho^f}{\partial t} + \frac{1-n}{\rho^s}\frac{\partial \rho^s}{\partial t} + V_{i,i}^s + \ (n(V_i^f - V_i^s))_{,i} = 0 \tag{2.14}$$

If we assume that the density of the fluid ρ^f and of the solid ρ^s only depend on the pressure and temperature (Rice, 2006b), we obtain:

$$\frac{\partial \rho^f}{\partial t} = \rho^f\ \beta^f\frac{\partial p}{\partial t} - \ \rho^f\ \lambda^f\frac{\partial T}{\partial t}$$
$$\frac{\partial \rho^s}{\partial t} = \rho^s\ \beta^s\frac{\partial p}{\partial t} - \ \rho^s\ \lambda^s\frac{\partial T}{\partial t} \tag{2.15}$$

where β^f and β^s are the compressibilities per unit volume of the pore fluid and the solid phase respectively and λ^f, λ^s the thermal expansivities per unit volume. The fluid mass flux is assumed to obey the isotropic Darcy's law (for a quasi-static flow without any body force).

$$n(V_i^f - V_i^s) = -\frac{\chi}{\eta^f}\ p_{,i} \tag{2.16}$$

where χ is the intrinsic permeability of the porous medium, and η^f is the viscosity of the pore fluid. Inserting Eqs. 2.15, 2.16 in Eq. 2.14 we obtain

$$\frac{\partial p}{\partial t} = c_{hy}\ p_{,ii} + \frac{\lambda^*}{\beta^*}\frac{\partial \mathrm{T}}{\partial t} - \frac{1}{\beta^*}\frac{\partial \varepsilon_v}{\partial t} \tag{2.17}$$

where $c_{hy} = \chi/(\eta^f \beta^*)$ is the hydraulic diffusivity, $\beta^* = n\beta^f + (1-n)\beta^s$ is the mixture compressibility, $\lambda^* = (n\lambda^f + (1-n)\lambda^s)$ is the coefficient of thermal expansion of the soil-water mixture (Vardoulakis, 1986). This formulation differs from Sulem et al. (2011) and Rice (2006b), where the authors introduce the mechanical constitutive equation through the variation of porosity. Therefore, instead of having the term depending on total volumetric deformation ε_v, they have one depending on plastic volumetric deformation ε_v^p. In Eq. 2.17, we keep the volumetric deformation without assuming any particular constitutive equation (Lachenbruch, 1980). Its evolution can be controlled by damage, plastic deformation or evolution of the porous space. The link between the two formulations in the case of an elasto-plastic constitutive model is shown in Appendix A.1.

2.3 Thermo-Hydro elasto-plastic model for fluid-saturated isotropic Cosserat materials

For simplicity, constitutive equations are written in terms of the Terzaghi effective stress for both the elastic and plastic strains. However the underlying assumption of elastically incompressible grains can be overcome without difficulty by resorting to Biot's theory of poromechanics (Biot and Willis, 1957).

2.3.1 Isotropic elastic constitutive law

The general constitutive equations for a linear isotropic elastic Cosserat continuum are defined by six coefficients. The two classical deformation moduli, K and G, and four additional coefficients, G_c, L, M, and M_c (Mindlin, 1964).

$$\tau_{ij} = K\gamma^e_{kk}\ \delta_{ij} + 2G(\varepsilon^e_{ij} - \frac{1}{3}\gamma^e_{kk}) + 2G_c\gamma^e_{[ij]} \tag{2.18}$$

$$\mu_{ij} = L\kappa^e_{kk}\ \delta_{ij} + 2M(\kappa^e_{(ij)} - \frac{1}{3}\kappa^e_{kk}) + 2M_c\kappa^e_{[ij]} \tag{2.19}$$

$(.)^e$ denotes elastic quantities. In comparison with the classical Cauchy continuum four additional moduli are used for an isotropic, centrosymmetric linear elastic Cosserat continuum. The first one is G_c, which has a dimension of stress and relates the antisymmetric

parts of the stress and deformation tensors, which are conjugate in energy. The other moduli, L, M and M_c have the dimension of length squared times stress. Any ratio of L, M or Mc to K, G or G_c results in a material parameter of dimension of length squared (Cowin, 1970).

In the analyses of simple shearing of an infinite layer presented in Section 2.5 the choice of L does not have any influence due to invariance in x_1 and x_3 directions. Moreover, setting $M_c = M = \frac{GR^2}{h_3}$, where h_3 a coefficient defined in A.2, we assure that no out-of-plane moments are developed (see Fig. 2.1 and Eq. 2.19).

The generalized elastic stress-strain relationships are written as:

$$\begin{aligned} \tau_{ij} &= C^e_{ijkl}\ \gamma_{kl} \\ \mu_{ij} &= M^e_{ijkl}\ \kappa_{kl} \end{aligned} \tag{2.20}$$

where the elastic stiffness tensors C^e_{ijkl} and M^e_{ijkl} are derived from (Eqs. 2.18 - 2.19).

$$C^e_{ijkl} = (K - \frac{2}{3}G)\delta_{ij}\delta_{kl} + (G + G_c)\delta_{ik}\delta_{jl} + (G - G_c)\delta_{il}\delta_{jk} \tag{2.21}$$

$$M^e_{ijkl} = (L - \frac{2}{3}M)\delta_{ij}\delta_{kl} + (M + M_c)\delta_{ik}\delta_{jl} + (M - M_c)\delta_{il}\delta_{jk} \tag{2.22}$$

2.3.2 Thermo-elasto-plastic incremental constitutive relationship

Following Mühlhaus and Vardoulakis (1987), a flow theory of plasticity for granular media with Cosserat microstructure can be derived by keeping the same definitions for the yield surface and the plastic potential as in the classical theory and by generalizing the stress and strain invariants for Cosserat continua. We decompose the deformation rate tensor and the curvature rate tensor into elastic, plastic and thermal parts (Lemaitre et al., 2009):

$$\dot{\gamma}_{ij} = \dot{\gamma}^e_{ij} + \dot{\gamma}^p_{ij} + \dot{\gamma}^{th}_{ij} \quad and \quad \dot{\kappa}_{ij} = \dot{\kappa}^e_{ij} + \dot{\kappa}^p_{ij} \tag{2.23}$$

$\dot{(.)}$ denotes the time derivative. Thermal strains are written as: $\dot{\gamma}^{th}_{ij} = \alpha\dot{T}\ \delta_{ij}$ where α is the coefficient of thermal expansion. No thermal part for the curvature is considered as the thermal expansion for isotropic solids does not have a direct effect on the rotations inside the medium.

Denoting F the yield function and assuming that F depends on the stress invariants and on accumulated plastic strains $F = F(\tau, \sigma, \gamma^p, \varepsilon^p_v)$, we obtain

$$\dot{F} = \frac{\partial F}{\partial \tau}\dot{\tau} + \frac{\partial F}{\partial \sigma}\dot{\sigma} + \frac{\partial F}{\partial \gamma^p}\dot{\gamma}^p + \frac{\partial F}{\partial \varepsilon^p_v}\dot{\varepsilon_v}^p = 0 \tag{2.24}$$

An example of generalized invariants used for Cosserat media is presented in detail in part

2.4.

Denoting Q the plastic potential and $\dot{\lambda}$ the plastic multiplier, we have

$$\begin{aligned} \dot{\gamma}^p_{ij} &= \dot{\lambda}\ \frac{\partial Q}{\partial \tau_{ij}} \\ \dot{\kappa}^p_{ij} &= \dot{\lambda}\ \frac{\partial Q}{\partial \mu_{ij}} \end{aligned} \tag{2.25}$$

The hardening modulus H_s is defined by:

$$H_s = -\frac{\partial F}{\partial \gamma^p} \tag{2.26}$$

We assume the following equalities that can be proven for several yield functions that have a linear dependence in τ and σ (see for example Drucker-Prager in the following):

$$\dot{\lambda} = \dot{\gamma}^p \qquad and \qquad \dot{\varepsilon}^p_v = \beta\ \dot{\gamma}^p \tag{2.27}$$

The consistency condition gives

$$\dot{\lambda} = \frac{< 1 >}{H_p}(\frac{\partial F}{\partial \tau_{ij}} C^e_{ijkl}(\dot{\gamma}_{kl} - \alpha\ \dot{T}\ \delta_{kl})) + \frac{\partial F}{\partial \mu_{ij}} M^e_{ijkl}\dot{\kappa}_{kl} \tag{2.28}$$

or,

$$\dot{\lambda} = \frac{< 1 >}{H_p}(b^F_{kl}\ (\dot{\gamma}_{kl} - \alpha\ \dot{T}\ \delta_{kl}) + b^{FM}_{kl}\ \dot{\kappa}_{kl}) \tag{2.29}$$

with

$$H_p = \frac{\partial F}{\partial \tau_{ij}} C^e_{ijkl} \frac{\partial Q}{\partial \tau_{kl}} + \frac{\partial F}{\partial \mu_{ij}} M^e_{ijkl} \frac{\partial Q}{\partial \mu_{kl}} + H_s \tag{2.30}$$

$$< 1 >= \begin{cases} 1 & \text{if } F = 0 \ \text{ and } \ \dot{\lambda} > 0 \text{ (plastic loading)} \\ 0 & \text{otherwise} \end{cases} \tag{2.31}$$

and,

$$b^F_{kl} = \frac{\partial F}{\partial \tau_{ij}} C^e_{ijkl} \tag{2.32}$$

$$b^Q_{ij} = C^e_{ijkl} \frac{\partial Q}{\partial \tau_{kl}} \tag{2.33}$$

$$b^{FM}_{kl} = \frac{\partial F}{\partial \mu_{ij}} M^e_{ijkl} \tag{2.34}$$

$$b^{QM}_{ij} = M^e_{ijkl} \frac{\partial Q}{\partial \mu_{kl}} \tag{2.35}$$

Using Eqs. 2.25 and 2.29, the incremental constitutive equations can be expressed as:

$$\begin{aligned}\dot{\tau}_{ij} &= (C^e_{ijkl} - \frac{<1>}{H_p} b^Q_{ij} b^F_{kl})\dot{\gamma}_{kl} - \alpha\dot{T}(C^e_{ijkl} - \frac{<1>}{H_p} b^Q_{ij} b^F_{kl})\delta_{kl} - \frac{<1>}{H_p} b^Q_{ij} b^{FM}_{kl}\dot{\kappa}_{kl} \\ \dot{\mu}_{ij} &= (M^e_{ijkl} - \frac{<1>}{H_p} b^{QM}_{ij} b^{FM}_{kl})\ \dot{\kappa}_{kl} - \frac{<1>}{H_p} b^{QM}_{ij} b^F_{kl}\ \dot{\gamma}_{kl} - \alpha\dot{T}\frac{<1>}{H_p} b^{QM}_{ij} b^F_{kl}\ \delta_{kl}\end{aligned} \tag{2.36}$$

These constitutive relationships can be written in the general form.

$$\begin{aligned}\dot{\tau}_{ij} &= C^{ep}_{ijkl}\ \dot{\gamma}_{kl} + D^{ep}_{ijkl}\ \dot{\kappa}_{kl} + E^{ep}_{ijkl}\ \dot{T}\ \delta_{kl} \\ \dot{\mu}_{ij} &= M^{ep}_{ijkl}\ \dot{\kappa}_{kl} + L^{ep}_{ijkl}\ \dot{\gamma}_{kl} + N^{ep}_{ijkl}\ \dot{T}\ \delta_{kl}\end{aligned} \tag{2.37}$$

with,

$$\begin{aligned} C^{ep}_{ijkl} &= C^e_{ijkl} - \frac{<1>}{H_p} b^Q_{ij} b^F_{kl} & D^{ep}_{ijkl} &= -\frac{<1>}{H_p} b^Q_{ij} b^{FM}_{kl} \\ E^{ep}_{ijkl} &= -(C^e_{ijkl} - \frac{<1>}{H_p} b^Q_{ij} b^F_{kl}) & L^{ep}_{ijkl} &= -\frac{<1>}{H_p} b^{QM}_{ij} b^F_{kl} \\ M^{ep}_{ijkl} &= M^e_{ijkl} - \frac{<1>}{H_p} b^{QM}_{ij} b^{FM}_{kl} & N^{ep}_{ijkl} &= \frac{<1>}{H_p} b^{QM}_{ij} b^F_{kl} \end{aligned} \tag{2.38}$$

2.3.3 Drucker-Prager yield surface

The classical Drucker-Prager plastic model for cohesionless materials was extended to Cosserat media by Mühlhaus and Vardoulakis (1987) for a 2D continuum. Herein, we follow the same approach to develop a 3D THM model for Cosserat continua.

$$F = \tau + \mu\ \sigma \quad \text{and} \quad Q = \tau + \beta\ \sigma \tag{2.39}$$

The generalized stress invariants are defined as:

$$\sigma = \frac{\tau_{kk}}{3} \tag{2.40}$$

$$\tau = \sqrt{h_1\, s_{ij}\, s_{ij} + h_2\, s_{ij}\, s_{ji} + \frac{1}{R^2}(h_3\, m_{ij}\, m_{ij} + h_4\, m_{ij}\, m_{ji})} \tag{2.41}$$

Similarly, the generalized plastic deviatoric strain rate is written as:

$$\dot{\gamma}_p = \sqrt{g_1\, \dot{e}^p_{ij}\, \dot{e}^p_{ij} + g_2\, \dot{e}^p_{ij}\, \dot{e}^p_{ji} + R^2(g_3\, \dot{k}^p_{ij}\, \dot{k}^p_{ij} + g_4\, \dot{k}^p_{ij}\, \dot{k}^p_{ji})} \tag{2.42}$$

where s_{ij}, m_{ij}, e_{ij} and k_{ij} are the deviatoric parts of the stress, couple-stress, strain and curvature respectively. The evaluation of the parameters h_i and g_i is discussed in A.2 based on micro-mechanical considerations. Some values are summarized in Table 2.1.

	2D model	3D model
static model	$\{h_i\} = \{3/4, -1/4, 1, 0\}$ $\{g_i\} = \{3/2, 1/2, 1, 0\}$	$\{h_i\} = \{2/3, -1/6, 2/3, -1/6\}$ $\{g_i\} = \{8/5, 2/5, 8/5, 2/5\}$
Kinematic model	$\{h_i\} = \{3/8, 1/8, 1/4, 0\}$ $\{g_i\} = \{3, -1, 4, 0\}$	$\{h_i\} = \{2/5, 1/10, 2/5, 1/10\}$ $\{g_i\} = \{8/3, -2/3, 8/3, -2/3\}$

Table 2.1: Values for the coefficients in the stress and strain deviatoric generalized invariants for a Cosserat continuum from Mühlhaus (1986), Mühlhaus and Vardoulakis (1987), Sulem and Vardoulakis (1990), Unterreiner (1994)

The hardening shear modulus is:

$$-H_s = \frac{\partial F}{\partial \gamma^p} = \frac{\partial \mu}{\partial \gamma^p}\ \sigma \tag{2.43}$$

and the hardening coefficient is:

$$h_s = \frac{\partial \mu}{\partial \gamma^p} \tag{2.44}$$

The gradient terms of the yield function and plastic potential are expressed as :

$$\frac{\partial F}{\partial \tau_{ij}} = \frac{1}{\tau}(h_1\ s_{ij} + h_2\ s_{ji}) + \frac{\mu}{3}\delta_{ij} \tag{2.45}$$

$$\frac{\partial Q}{\partial \tau_{ij}} = \frac{1}{\tau}(h_1\ s_{ij} + h_2\ s_{ji}) + \frac{\beta}{3}\delta_{ij} \tag{2.46}$$

$$\frac{\partial F}{\partial \mu_{ij}} = \frac{\partial Q}{\partial \mu_{ij}} = \frac{1}{\tau R^2}(h_3\ \mu_{ij} + h_4\ \mu_{ji}) \tag{2.47}$$

It is easily shown that $\dot{\lambda} = \dot{\gamma}^p$ and $\dot{\varepsilon}^p_v = \beta\ \dot{\gamma}^p$ by decomposing $\dot{\gamma}^p_{ij}$ (obtained from the plastic flow rule) into its deviatoric and volumetric part and then replacing them into the expression for $\dot{\gamma}^p$. Moreover, we have

$$b^F_{kl} = K\mu\ \delta_{kl} + \frac{s_{kl}}{q}\big((G+G_c)h_1 + (G-G_c)h_2\big) + \frac{s_{lk}}{q}\big((G+G_c)h_2 + (G-G_c)h_1\big) \tag{2.48}$$

$$b^Q_{ij} = K\beta\ \delta_{ij} + \frac{s_{ij}}{\tau}\big((G+G_c)h_1 + (G-G_c)h_2\big) + \frac{s_{ji}}{\tau}\big((G+G_c)h_2 + (G-G_c)h_1\big) \tag{2.49}$$

$$b^{FM}_{kl} = b^{QM}_{kl} = \frac{1}{\tau R^2}\Big[m_{kl}\ \big((M+M_c)h_3 + (M-M_c)h_4\big) + m_{lk}\ \big((M-M_c)h_3 + (M+M_c)h_4\big)\Big] \tag{2.50}$$

$$\frac{\partial F}{\partial \sigma_{ij}} C_{ijkl} \frac{\partial Q}{\partial \sigma_{kl}} = K\ \mu\ \beta\ +\ \frac{s_{kl} s_{kl}}{\tau^2}\big((G+G_c)(h_1^2+h_2^2)+2(G-G_c)h_1h_2\big) + \frac{s_{kl} s_{lk}}{\tau^2}\big((G-G_c)(h_1^2+h_2^2)+2(G+G_c)h_1h_2\big) \tag{2.51}$$

$$\frac{\partial F}{\partial \mu_{ij}} M_{ijkl} \frac{\partial Q}{\partial \mu_{kl}} = \frac{1}{\tau^2 R^4}\Big[m_{kl}\ m_{kl}\ ((M+M_c)(h_3^2+h_4^2)+2(M-M_c)h_3h_4) + m_{kl}\ m_{lk}\ ((M-M_c)(h_3^2+h_4^2)+2(M+M_c)h_3h_4)\Big] \tag{2.52}$$

2.4 Bifurcation analysis

Let us consider an evolution problem described by Eqs. 2.4, 2.5, 2.8 and 2.17. This set of equations presents a homogeneous steady state without Cosserat effects if adiabatic, undrained and prescribed total stresses as boundary conditions are applied. This steady state is defined by $T = T_s$, $p = p_s$, $\tau_{ij} = \tau_{ij}^0$, $\gamma_{ij} = \gamma_{ij}^0$, $\mu_{ij} = 0$ and $\kappa_{ij} = 0$, where T_s and p_s are a reference temperature and pressure respectively,τ_{ij}^0 and γ_{ij}^0 are the homogeneous stress and deformation tensors that depend on the geometry and boundary conditions. We denote all the fields corresponding to this steady state with a superscript 0.

We are interested in determining the conditions for which the above homogeneous solutions become unstable in the Lyapunov sense (Lyapunov, 1892, Stefanou and Alevizos, 2016). The relevant variables of the problem are expressed as follows:

$$\begin{aligned} T(x_i,t) &= T^0 + T^*(x_i,t) \qquad & p(x_i,t) &= p^0 + p^*(x_i,t) \\ \tau'_{kl}(x_i,t) &= \tau'^0_{kl} + \tau'^*_{kl}(x_i,t) \qquad & u_k(x_i,t) &= u_k^0(x_i) + u_k^*(x_i,t) \\ & & \omega_k^c(x_i,t) &= \omega_k^{c0} + \omega_k^{c*}(x_i,t) \end{aligned} \tag{2.53}$$

where the superscript * denotes a perturbation from the reference homogeneous state.

The constitutive equations 2.37 can be linearized around the reference state to obtain the following relationships between the perturbations of stresses, couple stresses, strains and curvatures:

$$\begin{aligned} \tau'^*_{kl} &= C^{ep}_{klmn}\ \gamma^*_{mn} + D^{ep}_{klmn}\ \kappa^*_{mn} + E^{ep}_{klmn}\ T^*\ \delta_{mn} \\ \mu^*_{kl} &= M^{ep}_{klmn}\ \kappa^*_{mn} + L^{ep}_{klmn}\ \gamma^*_{mn} + N^{ep}_{klmn}\ T^*\ \delta_{mn} \end{aligned} \tag{2.54}$$

Eqs. 2.4, 2.5, 2.8 and 2.17 become then:

$$C^{ep}_{klmn}(u^*_{m,nl} + e_{mnq}\ \omega^{c*}_{q,l}) + E^{ep}_{klmn}\ T^*_{,l}\delta_{mn} + D^{ep}_{klmn}\ \omega^{c*}_{m,nl} - p^*_{,l}\ \delta_{kl} - \rho\frac{\partial^2 u^*_k}{\partial t^2} = 0 \quad (2.55)$$

$$M^{ep}_{klmn}\ \omega^{c*}_{m,nl} + L^{ep}_{klmn}\ (u^*_{m,nl} + e_{mnq}\ \omega^{c*}_{q,l}) + N^{ep}_{klmn}\ T^*_{,l}\delta_{mn}$$

$$-e_{klm}(C^{ep}_{lmnq}(u^*_{n,q} + e_{nqr}\ \omega^{c*}_r) + E^{ep}_{lmnq}\ T^*\delta_{nq} + D^{ep}_{lmnq}\ \omega^{c*}_{n,q}) - \rho I\frac{\partial^2 \omega^{c*}_i}{\partial t^2} = 0 \quad (2.56)$$

$$\rho \mathrm{C}(\frac{\partial T^*}{\partial t} - c_{th}T^*_{,kk}) = \tau'^0_{kl}(\dot{u}^*_{k,l} + e_{klm}\ \dot{\omega}^{c*}_{m,l}) + \mu^0_{kl}\dot{\omega}^{c*}_{k,l} \quad (2.57)$$

$$\frac{\partial p^*}{\partial t} = c_{hy}\ p^*_{,kk} + \Lambda\frac{\partial T^*}{\partial t} - \frac{1}{\beta^*}\frac{\partial u^*_{k,k}}{\partial t} \quad (2.58)$$

To obtain Eq. 2.57, we neglect the perturbations of the elastic deformation and curvature tensors as compared to the plastic ones.

The system of Eqs. 2.55 - 2.58 is a linear system of eight equations with eight unknowns (the perturbed fields). It is convenient to apply a space Fourier transform to study it. The system admits solutions of the form:

$$X^*_k(x_l, t) = \overline{X}_k(t).exp(i\ \xi\ x_l\ n_l) \quad (2.59)$$

where ξ is a wave number, n_j is a polarization direction, $i^2 = -1$ and $X^*_i(x_j, t)$ a vector containing the eight perturbation unknowns as follows:

$$X^*_k(x_l, t) = [u^*_k(x_l, t) \quad \omega^{c*}_k(x_l, t) \quad T^*(x_l, t) \quad p^*(x_l, t)]^t \quad (2.60)$$

Inserting Eq. 2.59 in Eqs. 2.55 - 2.58, we obtain a system of ordinary differential equations, which admits solutions of the form:

$$\overline{X}_k(t) = \overline{X}_k.exp(s\ t) \quad (2.61)$$

where s is the rate of growth of the perturbation and $\overline{X}_k$ a vector of algebraic quantities. This leads to the following linear system of equations, written in matrix form:

$$\begin{bmatrix} \Gamma_{km} - \rho s^2\delta_{km} & \Delta_{km} & E^{ep}_{klmn}i\xi n_l\delta_{mn} & -i\xi n_k \\ \Xi_{km} & \Pi_{km} - \rho I s^2\delta_{km} & -e_{klm}E^{ep}_{lmnq}\delta_{nq} + N^{ep}_{klmn}\delta_{mn} & 0 \\ -\tau'^0_{kl}si\xi n_l\delta_{km} & -\tau'^0_{kl}sie_{klm} - \mu^0_{kl}si\xi n_l\delta_{km} & \rho C(s + c_{th}\xi^2) & 0 \\ \frac{1}{\beta^*}si\xi n_k & 0 & -\Lambda s & s + c_{hy}\xi^2 \end{bmatrix} \begin{bmatrix} \overline{u}_m \\ \overline{\omega}^c_m \\ \overline{T} \\ \overline{p} \end{bmatrix} = 0 \quad (2.62)$$

where

$$\begin{aligned}
\Gamma_{km} &= -C^{ep}_{klmn}\xi^2 n_n n_l \\
\Delta_{km} &= C^{ep}_{klqn}e_{qnm}i\xi n_l - D^{ep}_{klmn}\xi^2 n_n n_l \\
\Xi_{km} &= -L^{ep}_{klmn}\xi^2 n_n n_l - e_{klr}C^{ep}_{lrmq}i\xi n_q \\
\Pi_{km} &= -M^{ep}_{klmn}\xi^2 n_n n_l + L^{ep}_{klrn}e_{rnm}i\xi n_l - e_{klr}C^{ep}_{lrnq}e_{nqm} - e_{klr}D^{ep}_{lrmq}i\xi n_q
\end{aligned} \tag{2.63}$$

For non-trivial solutions, the determinant of the matrix in Eq. 2.62 must be zero. This condition yields a polynomial equation in terms of s. The roots of this equation provide us information about the stability of the system. If one of the roots has a real part strictly positive the considered homogeneous state is unstable. If all the roots have a real part that is strictly negative, the homogeneous state is stable. We cannot conclude anything in the case where at least one of the roots has a real part equal to 0 and all the others have a real part strictly negative.

Note that the classical condition of localization for rate-independent plastic materials with a Cauchy continuum is retrieved (Rudnicki and Rice, 1975b), i.e. $det(\Gamma_{km}) = 0$, where Γ_{km} is the acoustic tensor. The localization condition for a purely mechanical system in the framework of Cosserat continuum is:

$$det\begin{bmatrix} \Gamma_{km} - \rho s^2\delta_{km} & \Delta_{km} \\ \Xi_{km} & \Pi_{km} - \rho I s^2\delta_{km} \end{bmatrix} = 0 \tag{2.64}$$

The singularity of the above tensor is similar to the condition found in Iordache and William (1998), Steinmann and Willam (1991) for the onset of localization ($s = 0$). In these papers, the authors derive the localization condition from the kinematic and static compatibility conditions across the shear band as done classically for strain localization analysis (Vardoulakis and Sulem, 1995).

2.5 Application to rapid shearing in fault zones

Field observations of faults show that shear deformation is extremely localized in so-called slip-zones of finite but small thickness, composed of cataclastic material due to excessive shearing (Engelder, 1974, Myers and Aydin, 2004). Outcrops indicate that an even thinner zone of ultracataclastic material is often identified inside the fault core called the principal slip zone (PSZ) (Rice, 2006b). The thickness of the PSZ appears to be a key parameter for understanding fault behavior (Kanamori and Brodsky, 2004) as it is related to the triggering and evolution of various multi-physical couplings and energy dissipation during seismic slip. From the mechanics point of view, the deformations are localized in a shear band whose thickness can be measured from field observations and laboratory tests.

Strain localization in narrow bands can be seen as a bifurcation from the homogeneous deformation solution of the underlying mathematical problem. In this section, we determine the conditions for shear band formation by taking into account the THM couplings developed in the previous sections. The results are then compared to field and experimental data.

2.5.1 Fault core model under THM couplings

A simple configuration of a fault core is represented in Fig. 2.2 as a homogeneous infinite layer of fluid saturated granular material with a thickness h. The material inside this layer is modeled as a Cosserat continuum in order to take into account its granular microstructure.

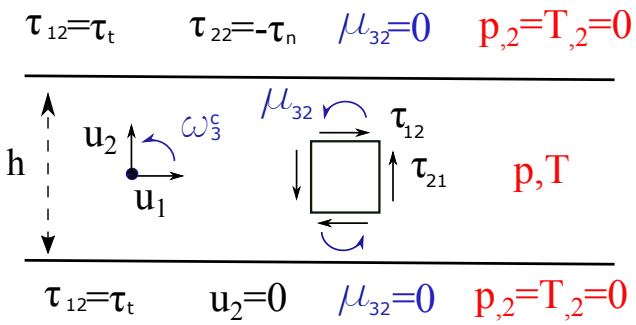

Figure 2.2: Boundary conditions for the infinite sheared layer modeling a saturated gouge

Prior to localization, the state of stress, strain, pore pressure and temperature is assumed to be homogeneous in the layer. As a condition of zero couple stress is applied at the boundaries, the couple stresses are identically zero in the medium. Thus, the medium behaves like a Cauchy continuum.

$$\tau_{12} = \tau_{21} \quad \mu_{ij} = 0 \tag{2.65}$$

Moreover, the different fields depend only on the component x_2 due to the invariance in the x_1 and x_3 directions. Eqs. 2.48 to 2.52 can be simplified at the homogeneous state:

$$\frac{\partial F}{\partial \sigma_{ij}} C_{ijkl} \frac{\partial Q}{\partial \sigma_{kl}} = \mu\beta K + G \tag{2.66}$$

$$\frac{\partial F}{\partial m_{ij}} M_{ijkl} \frac{\partial Q}{\partial m_{kl}} = 0 \tag{2.67}$$

so,

$$H_p = \mu\beta K + G + H_s \tag{2.68}$$

Moreover,

$$b_{ij}^{QM} = b_{kl}^{FM} = 0 \tag{2.69}$$

$$b_{ij}^{Q} b_{kl}^{F} = K^2\mu\beta\delta_{ij}\delta_{kl} + \frac{K\mu G}{\tau}s_{ij}\delta_{kl} + \frac{K\beta G}{\tau}\delta_{ij}s_{kl} + \frac{G^2}{\tau^2}s_{ij}s_{kl} \tag{2.70}$$

We introduce the following dimensionless quantities:

$$\begin{aligned} x = \frac{x_1}{R}; \qquad z = \frac{x_2}{R}; \qquad \overline{\overline{u}}_i = \frac{\overline{u}_i}{R}; \qquad \overline{\overline{p}} = \frac{\overline{p}}{\tau_n}; \\ \overline{\overline{\tau}}_{ij} = \frac{\overline{\tau}_{ij}}{\tau_n}; \qquad \bar{t} = \frac{c_{th}}{R^2}t; \qquad \overline{\overline{T}} = \frac{\Lambda}{\tau_n}\overline{T}; \qquad \bar{\xi} = \frac{\xi}{R} \end{aligned} \tag{2.71}$$

Considering Eq. 2.71 , the dimensionless form of the matrix in 2.62 is:

$$\begin{bmatrix} \frac{1}{\sigma_n}\Gamma_{km} - Is^2 & \tilde{\Delta}_{km} & \frac{1}{\Lambda}E^{ep}_{klmn}i\bar{\xi}n_l\delta_{mn} & -i\bar{\xi}n_i \\ \tilde{\Xi}_{km} & \tilde{\Pi}_{km} - \frac{I}{2}s^2 & \frac{1}{\Lambda R}(-Re_{klm}E^{ep}_{lmnq}\delta_{nq} + N^{ep}_{klmn}\delta_{mn}) & 0 \\ -\alpha_{kl}si\bar{\xi}n_l\delta_{km} & -\frac{1}{R}\alpha_{kl}sie_{klm} - \zeta_{kl}si\bar{\xi}n_l\delta_{km} & s + \bar{\xi}^2 & 0 \\ \frac{1}{\beta^*\sigma_n}si\bar{\xi}n_k & 0 & -s & s + \frac{1}{Le}\bar{\xi}^2 \end{bmatrix} \tag{2.72}$$

where,

$$\begin{aligned} \tilde{\Delta}_{ik} &= \frac{1}{\tau_n}(C^{ep}_{ijql}e_{qlk}i\xi n_j - \frac{1}{R}D^{ep}_{ijkl}\xi^2 n_l n_j) \\ \tilde{\Xi}_{ik} &= \frac{1}{\tau_n}(-\frac{1}{R}L^{ep}_{ijkl}\xi^2 n_l n_j - e_{ijq}C^{ep}_{jqkm}i\xi n_m) \\ \tilde{\Pi}_{ik} &= \frac{1}{\tau_n}(-\frac{1}{R^2}M^{ep}_{ijkl}\xi^2 n_l n_j + \frac{1}{R}L^{ep}_{ijql}e_{qlk}i\xi n_j - e_{ijq}C^{ep}_{jqlm}e_{lmk} - \frac{1}{R}e_{ijq}D^{ep}_{jqkm}i\xi n_m) \\ \alpha_{ij} &= \frac{\tau'^0_{ij}\Lambda}{\rho C\tau_n}; \qquad \zeta_{ij} = \frac{\mu^0_{ij}\Lambda}{\rho C\tau_n R}; \qquad Le = \frac{c_{th}}{c_{hy}} \end{aligned} \tag{2.73}$$

parameters	values	units	parameters	values	units
K	16.67×10^3	MPa	μ	0.5	
G	10×10^3	MPa	β	0	
Gc	5×10^3	MPa	λ^*	7.4×10^{-5}	$/^o$C
R	0.01	mm	ρC	2.8	MPa/^{o}C
ρ	2500	kg/m^3	c_{th}	1	mm^2/s
σ_n	200	MPa	c_{hy}	12	mm^2/s
τ'^0	67	MPa	α_s	2.5×10^{-5}	$/^o$C
β^*	8.2×10^{-5}	MPa^{-1}	n	0.04	

Table 2.2: Numerical values for the parameters of a deep rock gouge from Sulem et al. (2011), Rice (2006b)

2.5.2 Linear stability and wavelength selection

We consider a fault at 7km depth to study its stability and the shear band thickness predicted by our model. The values of the different parameters are retrieved from Sulem et al. (2011) and Rice (2006b). They correspond to fault gouge and were obtained from experiments on samples from the Median Tectonic Line, Japan, and the Aegion fault in Greece. They are summarized in Table 2.2. In this example, we obtain a a critical value for the hardening parameter at bifurcation state $H_{cr} = 2$MPa (corresponding to $h_s = 0.015$). For $H_s > H_{cr}$, all the real roots of the polynomial are negative (Figure 2.3) and some complex roots feature a positive real part. For $H_s < H_{cr}$, some real roots are positive (Figure 2.3).

In Figures 2.3 and 2.4, the dashed lines represent the real parts of the roots that have a nonzero imaginary part. For these values the system diverges by oscillating, it corresponds to a so-called "flutter instability". As mentioned in Benallal and Comi (2003), our system is not differentiable due to the Kuhn-Tucker condition (Eq. 2.54), therefore to develop the above equations, we have assumed monotonous loading conditions to stay in the plastic regime. Therefore, one cannot assess that the flutter type instabilities obtained in this analysis are meaningful. Moreover, in Simões and Martins (2005), the authors performed linear stability and finite element analyses for a non-associative elastic-plastic layer and observed that the complex eigenvalues with a positive real part, do not always correspond to an unstable behavior in the numerical results.

The value for the critical hardening modulus given in Sulem et al. (2011) is retrieved. The results are very sensitive to the ratio λ^*/β^* because shear heating destabilizes the system and instability can occur even in the hardening regime. When plastic shear deformations occur, the energy is dissipated by heat and the temperature in the gouge increases. The presence of the thermal pressurization term $\frac{\lambda^*}{\beta^*}\frac{\partial \mathrm{T}}{\partial t}$ in the mass balance equation, entails an increase of the pore pressure and thus a decrease of the effective normal stresses if the total stress is kept constant. This decrease of the normal stress induces a decrease of the

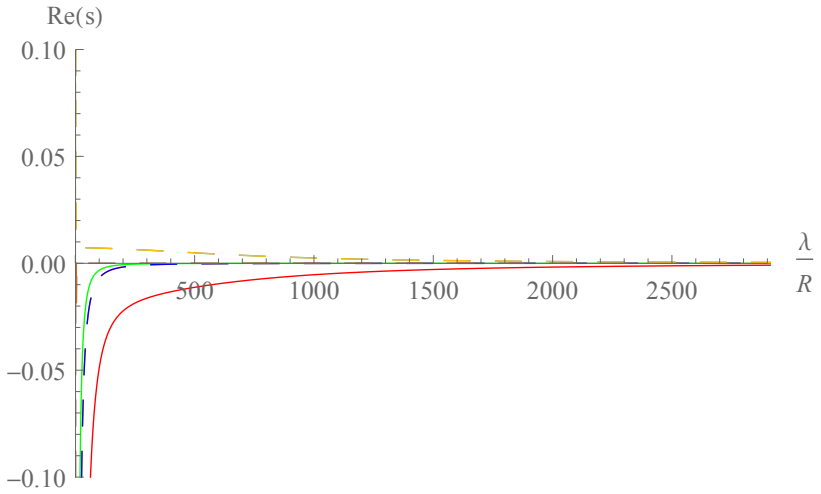

Figure 2.3: Real parts of the growth coefficient as a function of the wavelength of the perturbation for $H_s = 2.1$ MPa $> H_{cr}$. The different colors represent different roots. The dashed lines represent the real part of the roots with non zero imaginary parts whereas the continuous lines correspond to real roots.

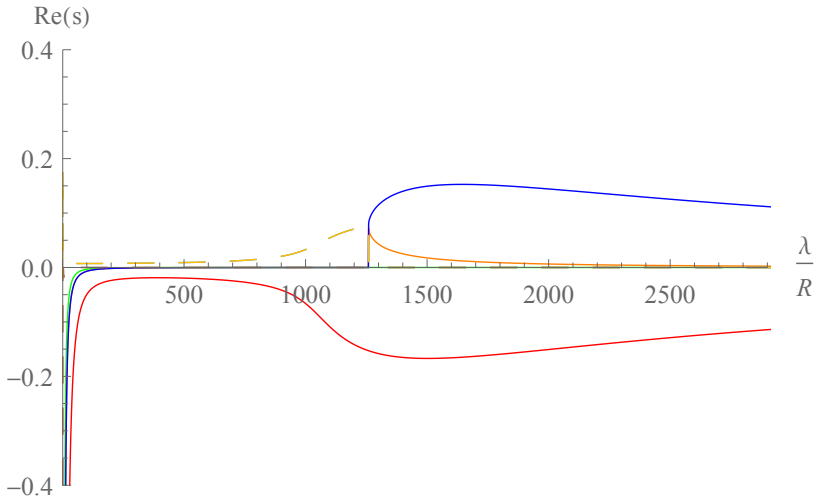

Figure 2.4: Real parts of the growth coefficient as a function of the wavelength of the perturbation for $H_s = 1.9$ MPa $< H_{cr}$. The different colors represent different roots. The dashed lines represent the real part of the roots with non zero imaginary parts whereas the continuous lines correspond to real roots.

fault strength and destabilizes the system.

For a given hardening modulus below the critical value $H_s < H_{cr}$, we can see in Figure 2.4 that the real roots of the polynomial equation present a maximum. This finite maximal growth coefficient of the instability is obtained thanks to the introduction of the inertia terms (Sulem et al., 2011). For a Cauchy continuum, we would obtain infinite growth for a zero wavelength of the perturbation and for a Cosserat continuum without the inertia terms infinite growth for a finite wavelength of the perturbation (Sulem et al., 2011). This maximum corresponds to the instability mode with fastest growth (see Eq. 2.61). If we consider that the width of the localized zone corresponds to the wavelength of fastest growth, we can plot in Fig. 2.5 the evolution of the selected wavelength λ_{max} (normalized by the Cosserat material length R) as a function of the hardening modulus.

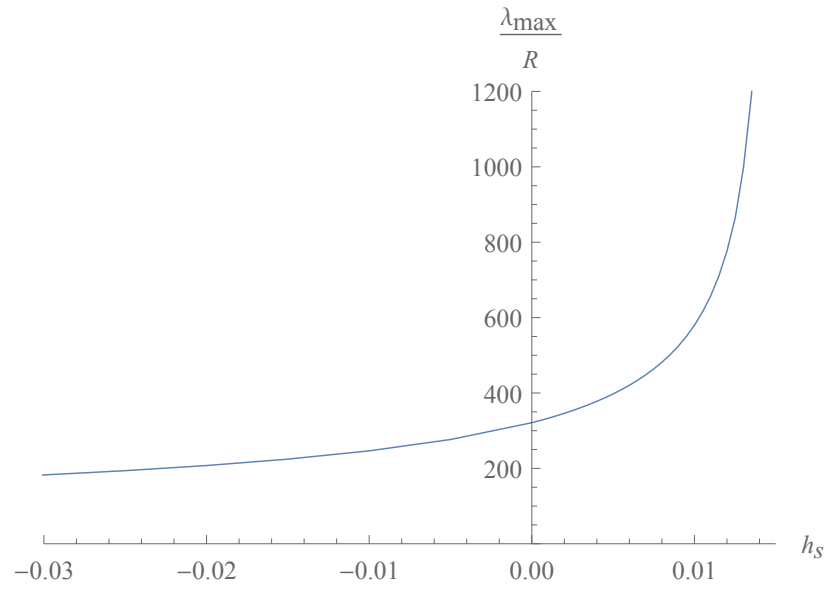

Figure 2.5: wavelength of the perturbation with fastest growth λ_{max} as a function of the hardening coefficient h_s

The selected wavelength tends to infinity for $H_s \to H_{cr}^-$ and decreases with decreasing hardening modulus. This general trend is similar to (Mühlhaus and Vardoulakis, 1987). The authors observed that for dry granular materials the shear band thickness is infinite at the bifurcation state and then decreases in the post-bifurcation regime as the strain localization evolves.

When a layer of granular material is sheared, experiments show that the shear stress evolves towards a residual value and, thus, the hardening modulus tends to 0 after sufficient slip (see Fig. 2.12 and Chambon et al. (2006), Di Toro et al. (2011)). In this example, the width of localization for $H_s \to 0$ is $320 \times R = 3.2mm$. Indeed, Rice (2006b) stated that most of the models that calculate the width of localization for dry granular materials predict a thickness between 7 to 30 times d_{50} (the mean particle diameter)(Oda and Kazama, 1998,

Muir Wood, 2002, Tordesillas et al., 2004) and this is much smaller that what is observed here. However, it should be noted that most of these analyses were performed considering sand and calibrated on data from triaxial experiments performed at much lower confining pressure than the ones acting at a depth of a few kilometers.

2.5.3 Effect of friction and dilatancy on localization

The yield surface for a Drucker-Prager model is defined with two parameters: the friction and the dilatancy coefficients. In this section, we look at their influence on the triggering of localization. The critical hardening parameter, under which the homogeneous state of deformation is unstable for some wavelengths of the perturbation, is plotted as a function of β and μ.

In granular materials, inelastic deformations can induce volume changes. In low porosity rocks dilatancy can be the result from rearrangement of close packed particles due to shearing or from uplift sliding over asperity contacts. But the opposite effect, compaction, can also be observed as a result of pore collapse or grain crushing (Rudnicki, 2000). To illustrate the influence of these effects on the stability of our system, we plot on Fig. 2.6 the value of the bifurcation parameter H_{cr} as a function of the dilatancy coefficient β ranging from -0.004 to 0.004 for Mechanical, Hydro-Mechanical and Thermo-Hydro-Mechanical couplings.

The mechanical system presents a linear evolution of the critical hardening modulus with β. For a dilatant material ($\beta > 0$), bifurcation occurs in the softening regime, whereas for a compacting material ($\beta < 0$), bifurcation occurs in the hardening regime for a value much greater than the one obtained for $\beta = 0$.

For HM couplings, the evolution is bilinear and the two lines intersect at $\beta = 0$. The bifurcation is the same as for the mechanical system in the dilatant regime, whereas it is obtained for higher values of H_s in the contractant regime. The appearance of this second line in the contractant regime is due to the undrained behavior that becomes unstable before the underlying drained one (Rice, 1975). Indeed, the dilatancy coefficient affects the evolution of pore pressure. If the material is compacting the pore volume decrease induces pore fluid pressurization, which triggers instability.

The introduction of thermal pressurization in the THM model has the effect of shifting the line in the contractant regime to even higher values of H_{cr}, but the slope remains the same. Thus, the undrained behavior is affected by thermal pressurization but the drained behavior is not.

The initial friction coefficient μ also plays a role in the value of the bifurcation parameter. In Fig. 2.7, we plot the value of the critical hardening parameter against the initial friction coefficient ranging from 0.3 to 0.8 (typical values obtained experimentally for a gouge

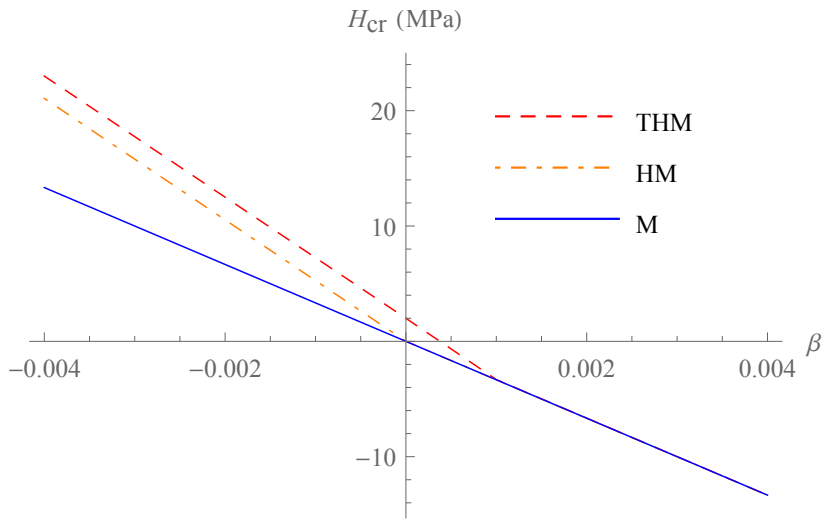

Figure 2.6: Critical hardening modulus at bifurcation H_{cr} plotted as a function of the dilatancy coefficient β considering Mechanical (M), Hydro-Mechanical (HM) and Thermo-Hydro-Mechanical (THM) couplings ($\mu = 0.5$).

(Scott et al., 1994, Scuderi et al., 2013)). For a higher value of μ, the shear stress applied to the sheared layer is greater and thus the mechanical energy dissipated is greater which makes the system more unstable.

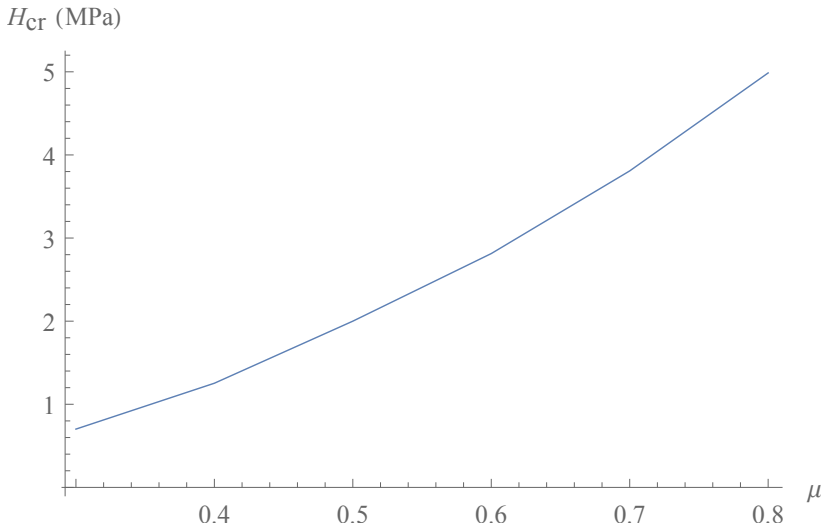

Figure 2.7: Critical hardening modulus at bifurcation H_{cr} for different values of friction coefficient considering THM couplings ($\beta = 0$).

2.5.4 Sensitivity analysis to hydraulic parameters and normal stress

The hydraulic parameters of the problem are not well constrained, they depend on the material, the pore pressure, the temperature, the porosity, etc... To have a better insight

into the effects of some parameters on the behavior of the system, we plot the evolution of the wavelength selection λ_{max} with the hardening coefficient for different values of them.

Several studies were conducted in order to investigate the value of permeability and diffusivity inside the fault core (Wibberley and Shimamoto, 2003, Sulem et al., 2004, Rafini, 2008). They show that the gouge has a much lower permeability than the surrounding fractured rock mass. It can be three orders of magnitude less ($10^{-19}m^2$ for the gouge compared to $10^{-16}m^2$ for surrounding rock). In Figure 2.8, the selected wavelength is plotted as a function of the hardening modulus for three values of χ. For a very low permeability $\chi = 10^{-21}m^2$ the results are similar to $\chi = 10^{-19}m^2$. For $\chi = 10^{-17}m^2$, the bifurcation parameter is the same but the significant effect is on the wavelength selection. For $H_s \to 0$, λ_{max}/R tends towards 373 for $\chi = 10^{-17}m^2$.

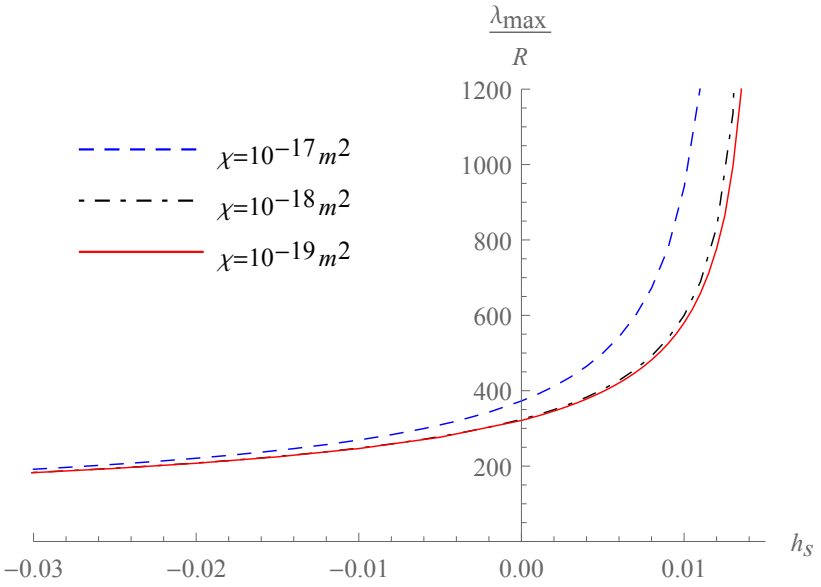

Figure 2.8: wavelength selection λ_{max} as a function of the hardening coefficient h_s for different values of the permeability χ.

Several parameters of the model also depend on the porosity (e.g. the permeability, the thermal pressurization term, the mixture compressibility...). In addition, they evolve during the shear process because of deformations and possible thermally activated chemical reactions (Sulem and Famin, 2009b). To take into account the effect of porosity on the permeability, we use a cubic Kozeny-Carman permeability law.

$$\chi = \chi_0 \left(\frac{1-n_0}{1-n}\right)^2 \left(\frac{n}{n_0}\right)^3 \tag{2.74}$$

where χ_0 and n_0 are the reference permeability and porosity respectively and their values are the ones considered in Table 2.2. The other parameters of the model modified by the change of porosity in this study are the ratio λ^*/β^* and the mixture compressibility. The effect of porosity on the wavelength selection is shown in Figure 2.9. It has a major effect

on the bifurcation parameter and on the shear band width. The greater the porosity, the more unstable the system is. Indeed, when the porosity increases the pore pressure increase due to thermal pressurization is more pronounced and further destabilizes the system.

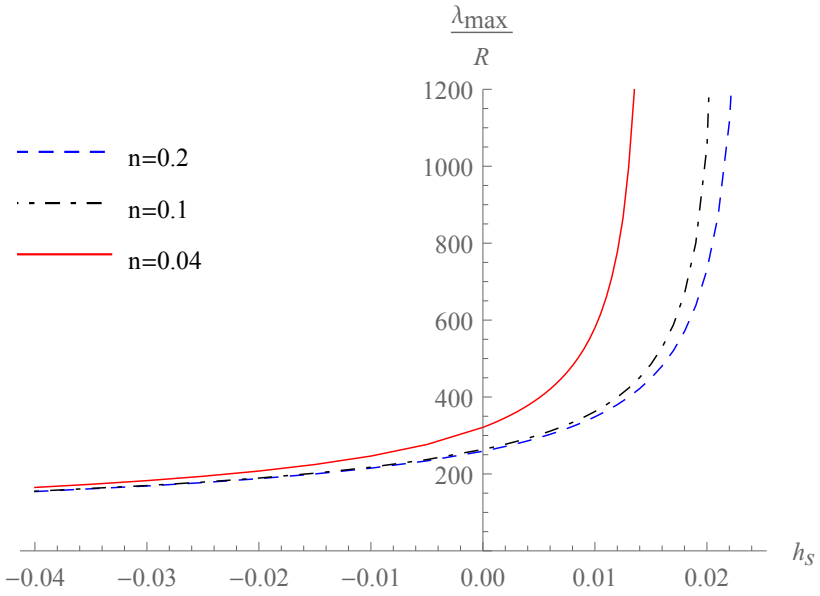

Figure 2.9: wavelength selection λ_{max} as a function of the hardening coefficient h_s for different values of the porosity n.

However, the parameter that has the biggest impact on the stability is the ratio λ^*/β^* as shown in Figure 2.10. Considering the different values of the thermal expansion coefficient and of the compressibility for the fluid and the solid given in Rice (2006b), it varies between 0.59 and 1.62 MPa/^{o}C(its value is 0.9 MPa/^{o}C in Table 2.2) . We can see that for a value of 0.59 MPa/^{o}C, the bifurcation is obtained for a value of the hardening coefficient close to zero ($h_{crit} = 0.002$). However, for λ^*/β^*=1.62 MPa/^{o}C, the critical value of the hardening coefficient lies clearly in the hardening regime ($h_{crit} = 0.045$).

Another effect studied here is the change of the normal stress applied to the sheared layer and its effect on the wavelength selection. We have taken values of 100 and 300 MPa corresponding to 3.5 and 10 kilometers depth in the crust respectively. The highest value corresponds to a typical depth of transition between brittle and ductile behavior in the Earth crust. As for the permeability, the bifurcation state is not strongly affected whereas the wavelength selection is. The greater the normal stress is, the smaller the selected wavelength is and thus the thinner the shear band is.

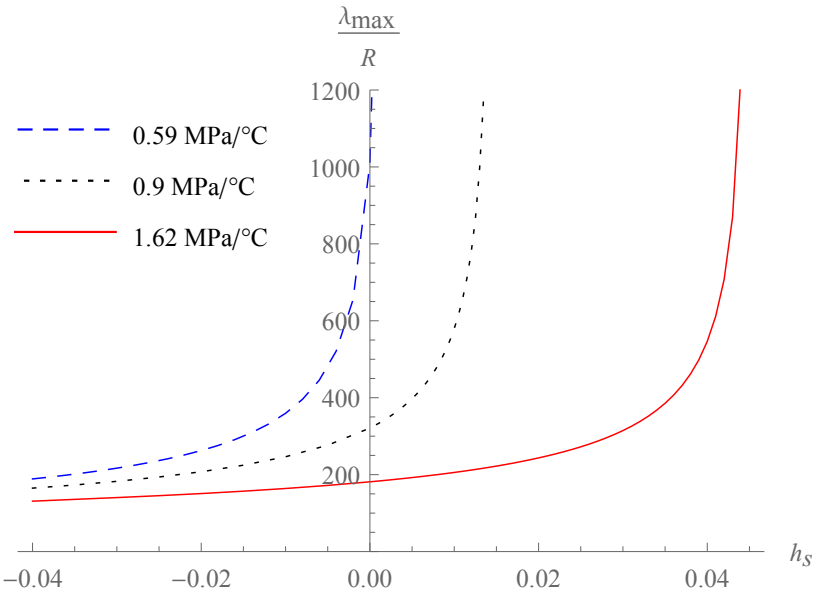

Figure 2.10: wavelength selection λ_{max} as a function of the hardening coefficient h_s for different values of the ratio λ^*/β^* that governs the thermal pressurization effect.

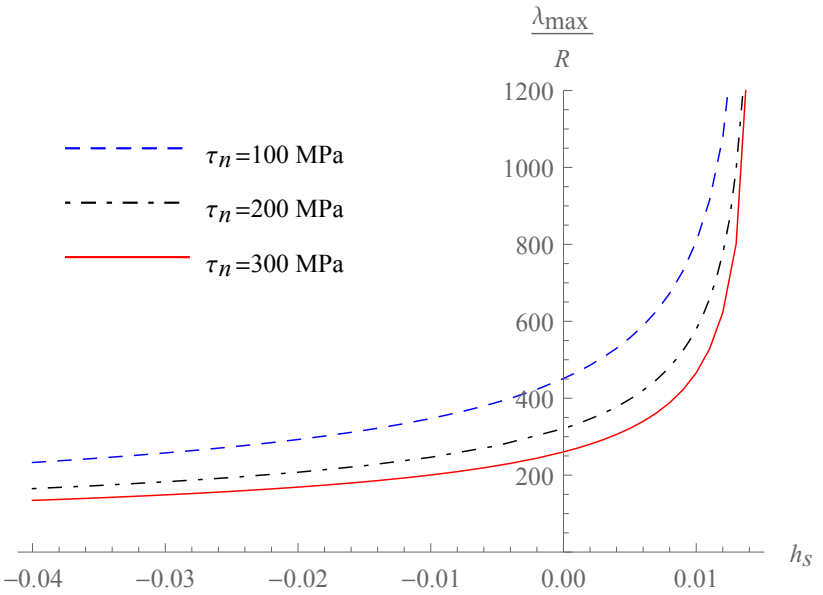

Figure 2.11: wavelength selection as a function of the hardening coefficient h_s for different values of normal stress τ_n

2.5.5 Evolution of the shear band thickness with the hardening state

In the previous section, we have studied how the selected wavelength evolves with the hardening modulus for various values of the material parameters. We recall that the above linear stability analysis (LSA) is performed from a reference state which is assumed homogeneous in the system. In the following, we consider a typical stress-strain curve for a fault gouge material under shear and explore the evolution of shear band thickness in due course of the shearing process. This is done by evaluating the selected wavelength from the LSA assuming homogeneous deformation at each state which is not strictly speaking the case because of progressive strain localization. However, it can give an interesting insight which will be confirmed in Chapter 4 by performing a fully coupled numerical analysis of the post-localization regime.

Ikari et al. (2009) performed double direct shear experiments on a series of saturated fault gouges containing Montmorillonite, Illite, Chlorite and Quartz at effective normal stresses from 12-59 MPa and at subseismic velocities (1 to 300 $\mu m/s$). In Fig. 2.12, results for a Montmorillonite-Quartz mixture are presented. From the curve τ (the tangential stress applied) versus γ (the total shear deformation), the plastic hardening modulus is related to tangent modulus H_{tan} through the relationship $H_{tan} = \frac{H_s}{1+\frac{H_s}{G}}$. The hardening coefficient is related to the plastic hardening modulus by $h_s = \frac{H_s}{\tau_n}$.

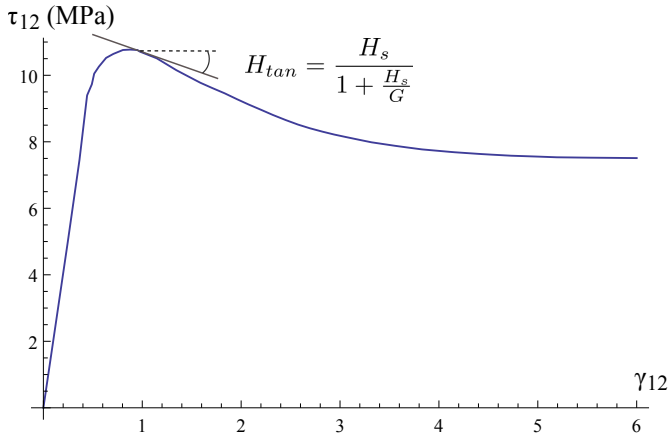

Figure 2.12: Stress-strain curve for a clay-rich gouge from Ikari et al. (2009).

In Fig. 2.13, the evolution of the hardening coefficient with the shear deformations obtained from Fig. 2.12 is shown. It is positive until the maximum shear stress is reached and then negative. Its evolution presents a minimum value of -0.055, which corresponds to the minimum value of the shear band thickness and then it increases towards zero.

From the evolution of the plastic hardening coefficient in Fig. 2.13, we can calculate the evolution of the selected wavelength as shown in Fig. 2.14 for the material parameters considered in Table 2.2. In Fig.2.14, we observe that the evolution of the selected wave-

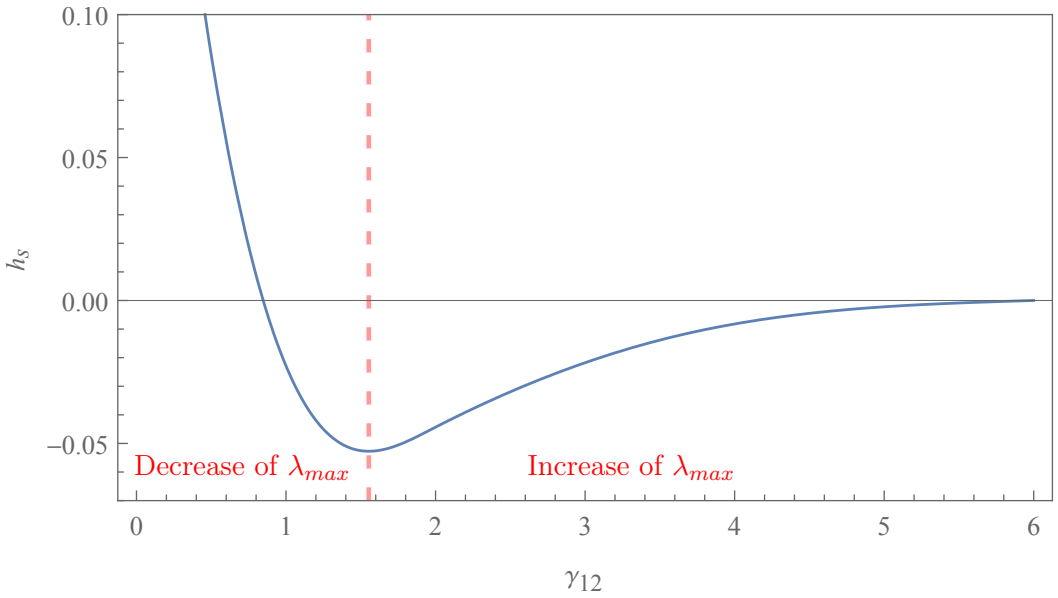

Figure 2.13: Evolution of the plastic hardening coefficient for the stress-strain response given in Fig. 2.12.

length follows the evolution of the plastic hardening coefficient h_s: Consequently, the shear band thickness first decreases to a minimum value of 1.5 mm and then increases to reach a residual value of 3.2 mm.

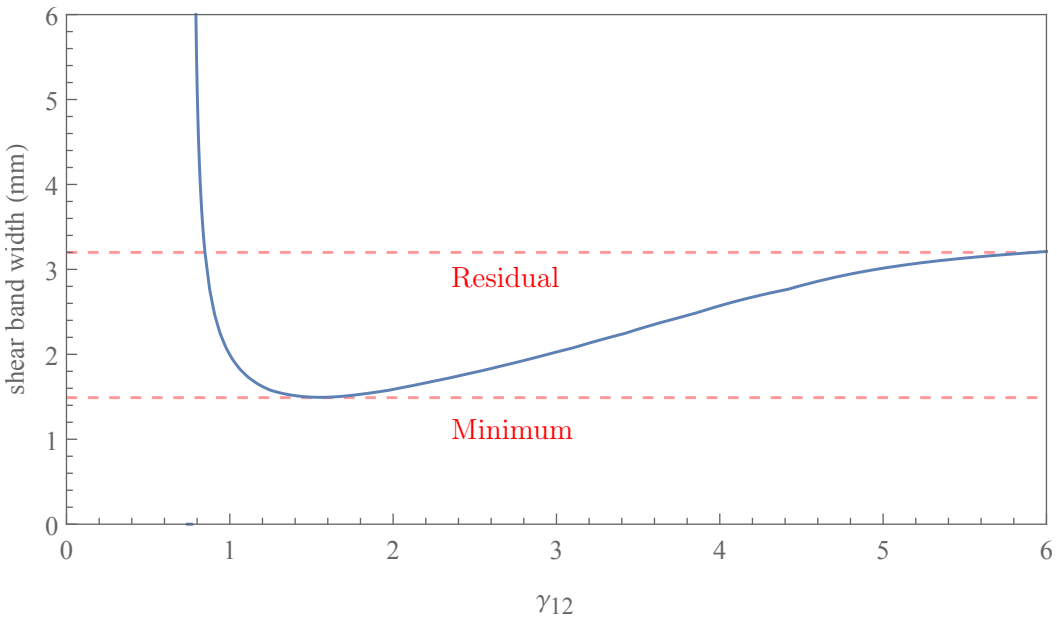

Figure 2.14: Evolution of the wavelength selection along with deformations considering the evolution of the hardening coefficient depicted in Fig. 2.13.

2.5.6 Effect of microstructure evolution

At high mean stresses, like for faults at great depth, grain crushing is observed from exhumed samples and also in experiments (Verberne et al., 2013, Brantut et al., 2008, Marone and Scholz, 1989). Structural fabrics occurring within fault zones are commonly characterized by distinct grain size and shape distributions that are generally interpreted as strain localization indicators.

Sammis et al. (1987) measured the particle distribution of intact gouge samples, retrieved from the Lopez Fault in the San Gabriel Mountains of Southern California and observed a fractal dimension of approximately 2.6. On the basis of the observations, they proposed the so-called comminution model, for the mechanical processes that generate fault gouges. Several experiments were conducted on natural and simulated fault gouges supporting Sammis' theory (Steacy and Sammis, 1991, An and Sammis, 1994) with some exceptions (Marone and Scholz, 1989, Storti et al., 2003).

The introduction of a characteristic length in the Cosserat continuum enables us to take into account the microstructure evolution of the medium (Bauer, 2016). In our model this characteristic length is related to the mean grain diameter (see Appendix A.2). Thus, to model a grain size evolution, we assume an exponential decrease with increasing total shear strain γ_{12} (Montési and Hirth, 2003).

$$D(\gamma_{12}) = (D_0 - D_{fin})e^{-\frac{\gamma_{12}}{\gamma_c}} + D_{fin} \tag{2.75}$$

where D_0 is the initial grain diameter, D_{fin} is the final grain diameter and γ_c is a characteristic deformation that accounts for the rate of evolution (here taken as 1). In Gu and fong Wong (1994), the authors conducted saw-cut experiments on simulated quartz gouges. The particle size distributions of gouge samples before and after frictional sliding were characterized using a laser diffraction particle size analyzer. They obtained a decrease of 30 % of the mean grain diameter after a total shear strain γ_{12} of 6 . To see the effect of a more intense grain crushing, we study also the case of a decrease of 50 % of the mean grain diameter.

In Fig. 2.15, we have taken into account the evolution of both the grain size and the hardening modulus with the total shear strain. The decrease of shear band width is almost proportional to the decrease of grain size: for a decrease of 50 % of D we have a decrease of 50 % of the shear band width.

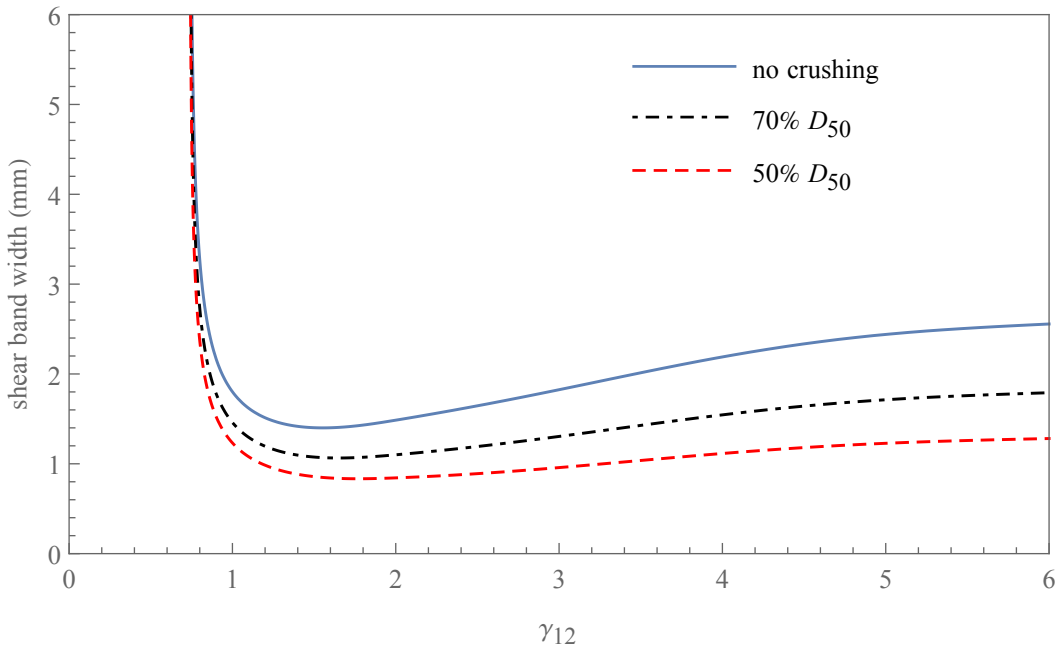

Figure 2.15: Evolution of the shear band thickness along with deformations considering the evolution of the hardening coefficient as plotted in Fig. 2.13 and a final mean grain diameter that is 70 % and 50 % of the initial one.

2.6 Conclusion

In this chapter, a THM model for three dimensional Cosserat continua is developed. It is based on the generalization in 2D for Cosserat continua of the Drucker-Prager yield criterion (Mühlhaus and Vardoulakis, 1987). The application of bifurcation theory to this set of equations is presented and appears to be a generalization of the study of the classical acoustic tensor for Cauchy continua.

This framework is applied to analyze the formation of shear bands inside fault gouges. The destabilizing effect of thermal pressurization is highlighted. Indeed, the gouge layer becomes unstable even in the hardening regime. Moreover, taking into account the inertia terms in the momentum balance equations enable us to obtain a finite Lyapunov exponent for all unstable wavelengths of the perturbation. Therefore, the shear band thickness is evaluated as the wavelength of maximum growth and is plotted as a function of the hardening modulus. The sensitivity of the shear band size to the initial porosity, permeability, pressurization coefficient and normal stress is investigated. The calculation of a hardening modulus evolution from experimental results enable us to follow the localization process during the shearing of a gouge. We observe a decrease of the shear band thickness at the beginning of the process, followed by a progressive increase towards a steady state value. The modification of the microstructure with deformations can also be taken into account with our model by modifying the internal length in the constitutive laws. A grain comminution causes a decrease of the shear band width.

This model is a promising step in studying the stability fault gouges and enables us to take into account the microstructure within the constitutive equations as several studies have shown its importance on the behavior of faults (Anthony and Marone, 2005, Cashman et al., 2007). However, this analysis determines only the stability and shear band thickness considering infinitesimally small perturbations away from uniform shear. Nonlinear effects become important when the perturbation grows and numerical analyses are required to follow the evolution of the considered system in the post-bifurcation regime. In Chapter 4, the full system of equations is integrated using finite elements, allowing also a determination of the material response.

Chapter 3

Implementation and validation of a Finite Element code for Thermo-Hydro-Mechanical couplings in a Cosserat continuum

Dans cette partie, nous présentons l'implémentation et la validation numérique du modèle défini dans le chapitre précédent. Le système d'équations non linéaires est intégré en utilisant la méthode des éléments finis. Ce développement a été réalisé au sein de l'école d'ingénierie pétrolière de l'Université de Nouvelle Galles du Sud (UNSW, Sydney) en utilisant le code intitulé REDBACK créé dans ce laboratoire. Ce code a pour objectif de résoudre des problèmes multi-physiques pour les géomatériaux. Il est basé sur le logiciel MOOSE qui offre un cadre structurel de résolution d'équations par éléments finis avec couplages forts.

Dans un premier temps, les différents logiciels sont présenté ainsi que la façon dont les milieux de Cosserat et les couplages THM sont intégrés. Nous exposons l'algorithme de retour radial utilisé pour les équations incrémentales de plasticité locale, ainsi que l'algorithme de résolution global du sytème.

Dans un second temps, la démarche suivie afin de vérifier que les équations sont correctement définies est présentée en détails. Tous les termes sont vérifiés un par un en comparant les résultats obtenus lors de simulations avec solutions analytiques ou des résultats d'autres simulations présentes dans la littérature.

Contents

3.1 Introduction

In order to integrate numerically the full system of equations presented in Chapter 2, the finite element method has been chosen as it enables us to model complex geometries and more importantly to efficiently solve highly nonlinear coupled problems. The model of a fault core developed in Chapter 2 is an infinite sheared layer, a 1D problem, for which the pseudo-spectral method is a suitable candidate, however the aim was to develop a code that can be used also for various geomechanical applications. Moreover, the FEM offers a more flexible and efficient way to treat highly nonlinear incremental problems including plasticity which is used here. For this reason, we chose to use the FEM and in particular the software MOOSE, which allows us to easily perform computations on parallel architectures.

3.2 Implementation of the model

3.2.1 MOOSE Framework and REDBACK

The Multiphysics Object-Oriented Simulation Environment (MOOSE) is a finite element framework developed at the Idaho National Laboratory since 2008. It is an open-source software written in C++ that uses advanced nonlinear solvers and offers a general environment for solving systems of tightly coupled multi-physical systems of partial differential equations (Gaston et al., 2009). Underneath MOOSE is libMesh, another finite element framework developed by the CFDLab at the University of Texas at Austin that provides general finite element functions (Kirk et al., 2006). LibMesh furnishes a set of utilities for massively parallel finite element based computations, including mesh generation, a finite element library, and interfaces to solver packages such as the Portable, Extensible Toolkit for Scientific Computation (PETSc) for both serial and parallel platforms (Balay et al., 2017) and LASPack on serial machines (Skalicky, 1995). To profit from the fact that the code can be run on state-of-the-art high-performance computational resources, we mainly use the PETSc solvers, which are based on the Message Passing Interface (MPI) standard. Note that Moose is a layered program and its structure is summarized in Fig. 3.1.

MOOSE is appealing as it is not only a user-friendly framework for modelers, but also acts as a code development tool. Indeed, users are encouraged to contribute to the development of the code by adding new physics and capabilities within the framework through the Github development environment (Gaston et al., 2014). These changes, which must be approved by the main development team, help to rapidly improve this multi-physics tool. Each module, or application, within MOOSE is usually named after an animal and is devoted to the study of a particular multi-physical system of equations. BISON is the

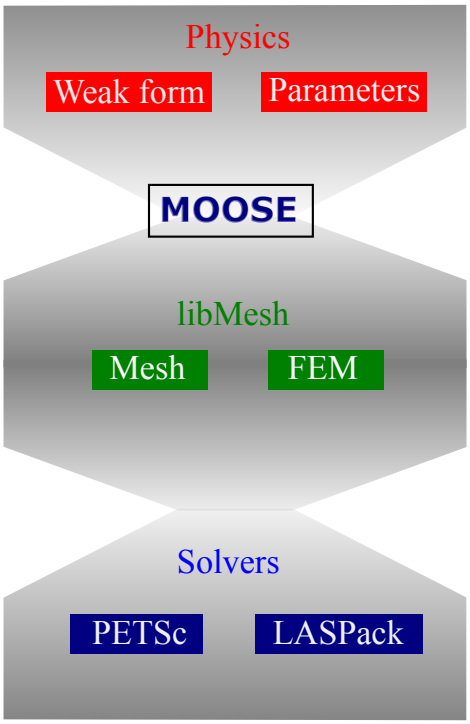

Figure 3.1: MOOSE Structure

first MOOSE application and solves the fully coupled equations of thermomechanics and species diffusion for fuel performance. Table 3.1 clusters some applications of MOOSE and a short description for each one of them.

Name	Desciption
Bison	Thermo-mechanics, Chemical, diffusion, coupled mesoscale
Marmot	4th order phasefield mesoscale
Falcon	Geomechanics, coupled mesoscale
Rat	Porous ReActive Transport
Pronghorn	Neutronics, Porous flow
Redback	Thermo-hydro-chemo-mechanical couplings in Geomechanics

Table 3.1: Examples of MOOSE Applications and their description.

Among the over twenty MOOSE-based applications now in development, REDBACK is derived to tackle the problem of Rock mEchanics with Dissipative feedBACKs (Poulet and Veveakis, 2016) at the University of New South Wales in Sydney, Australia. It is named after a notorious Australian spider. REDBACK is built on MOOSE's tensor mechanics module and extends this module with additional constitutive models for the overstress plasticity formulation following the generic approach from (Wang et al., 1997) and using a

fully implicit integration scheme for the stress update algorithm. The aim is to solve tightly coupled Thermo-Hydro-Mechanical-Chemical (THMC) systems of equations in geomaterials targeting applications involving material instabilities. For instance, REDBACK was used to study fault mechanics (Poulet et al., 2016, Tung et al., 2017), fluid-microstructure interaction (Lesueur et al., 2017), borehole stability (Hu et al., 2017), boudinage and folding (Peters, 2016), or the phenomenon of pore collapse in sandstone and mudstone (Poulet and Veveakis, 2016). The model presented in Chapter 2 is implemented in this module as most of the physics is already present and the field of study is similar. Nevertheless, we use a consistent plasticity algorithm different from the overstress plasticity already applied but it will enable comparisons and combinations of the different methods in the future.

3.2.2 Weak form of the equations

A displacement-rotation-temperature-pore pressure incremental finite element formulation is used to numerically integrate our model. The integration in time is implicit using the backward Euler method, which is implemented in REDBACK (Poulet et al., 2016).

The weak form of the linear and angular momentum balance equations Eqs.2.4-2.5 is written (Godio et al., 2015) using Green's identity:

$$-\int_{\Omega} \tau_{ij}\psi_{i,j}d\Omega + \int_{\partial\Omega_{\Sigma}} \tau_{ij}n_j\psi_i dS = 0 \tag{3.1}$$

$$-\int_{\Omega} \mu_{ij}\psi_{i,j}d\Omega + \int_{\partial\Omega_{\Sigma}} \mu_{ij}n_j\psi_i dS - \int_{\Omega} \varepsilon_{ijk}\tau_{jk}\psi_i d\Omega = 0 \tag{3.2}$$

The energy and fluid mass balance equations are also written in their weak forms:

$$\int_{\Omega} \dot{p}\psi d\Omega + c_{hy}\left(\int_{\Omega} p_{,i}\psi_{,i}d\Omega - \int_{\partial\Omega} p_{,i}n_i\psi dS\right) - \Lambda\int_{\Omega}\dot{T}\psi d\Omega + \frac{1}{\beta^*}\int_{\Omega}\dot{\varepsilon_v}\psi d\Omega = 0 \tag{3.3}$$

$$\int_{\Omega} \dot{T}\psi d\Omega + c_{th}\left(\int_{\Omega} T_{,i}\psi_{,i}d\Omega - \int_{\partial\Omega} T_{,i}n_i\psi dS\right) - \frac{1}{\rho C}\int_{\Omega}(\tau_{ij}\dot{\gamma}^p_{ij} + \mu_{ij}\dot{\kappa}^p_{ij})\psi_{,i}d\Omega = 0 \tag{3.4}$$

where ψ and ψ_i are tests functions. c_{hy}, c_{th}, ρC, β^* and Λ are considered constant herein.

Linear Lagrange test functions are chosen for all the fields and full integration is performed. An alternative choice would be to use quadratic functions with reduced integration to improve the rate of mesh convergence (Godio et al., 2015), but they are not used here for simplicity.

The different terms of the system of Eqs.3.1,3.2, 3.3 and 3.4 are implemented one by one, called Kernels and boundary conditions in MOOSE, in order to include/exclude these terms in/from a simulation as desired. MOOSE provides by default some common Kernels and

Boundary Conditions, which were used to account for the time derivative and diffusion terms. The other kernels were implemented in REDBACK specifically.

Some Kernels were added for the use of Cosserat continuum and most of the others had to be modified as their expressions changed or the number of coupled variables increased, due to the rotations.

The break down of the equations in Kernels (in red) and Boundary Conditions (in blue) is shown below:

$$\overbrace{-\int_\Omega \tau_{ij}\psi_{i,j}d\Omega}^{CosseratStressDivergenceTensors} + \overbrace{\int_{\partial\Omega_\Sigma} \tau_{ij}n_j\psi_i dS}^{BCs} = 0 \tag{3.5}$$

$$\overbrace{-\int_\Omega \mu_{ij}\psi_{i,j}d\Omega}^{CosseratStressDivergenceTensors} + \overbrace{\int_{\partial\Omega_\Sigma} \mu_{ij}n_j\psi_i dS}^{BCs} - \overbrace{\int_\Omega \varepsilon_{ijk}\tau_{jk}\psi_i d\Omega}^{MomentBalancing} = 0 \tag{3.6}$$

$$\overbrace{\int_\Omega \dot{p}\psi d\Omega}^{TimeDerivative} + \overbrace{c_{hy}\int_\Omega p_{,i}\psi_{,i}d\Omega}^{MassDiffusion} - \overbrace{c_{hy}\int_{\partial\Omega} p_{,i}n_i\psi dS}^{BCs} - \overbrace{\Lambda\int_\Omega \dot{T}\psi d\Omega}^{ThermalPressurization} + \overbrace{\frac{1}{\beta^*}\int_\Omega \dot{\varepsilon_v}\psi d\Omega}^{Poromechanics} = 0 \tag{3.7}$$

$$\overbrace{\int_\Omega \dot{T}\psi d\Omega}^{TimeDerivative} + \overbrace{c_{th}\int_\Omega T_{,i}\psi_{,i}d\Omega}^{ThermalDiffusion} - \overbrace{c_{th}\int_{\partial\Omega} T_{,i}n_i\psi dS}^{BCs} - \overbrace{\frac{1}{\rho C}\int_\Omega (\tau_{ij}\dot{\gamma}^p_{ij} + \mu_{ij}\dot{\kappa}^p_{ij})\psi_{,i}d\Omega}^{MechDissipHO} = 0 \tag{3.8}$$

Note that the first terms of the momentum and angular balance equations are implemented in the *CosseratStressDivergenceTensors* as their expressions are very similar, but they are applied to different variables. The use of flags enable us to modify the terms in the Jacobian matrix.

3.2.3 Return map algorithm for plasticity

Based on the above finite element formulation, the software solves the system for the unknown variables, which are displacements, rotations, pressure and temperature. The parameters of the model as well as the stresses and couple-stresses are updated through a procedure called Materials, in which the constitutive law is implemented. However, as an elasto-plastic constitutive law is considered here, an iterative solution scheme must be introduced to determine at each Gauss point and each increment, the values of stresses and couple-stresses. Herein, an implicit backward-Euler Closest-Point-Projection (CPP)

solution algorithm is adopted (Godio et al., 2016).

Non-associated plasticity requires the definition of a plastic potential (see Eq. 2.39). The flow rule (Eqs. 2.25) states that in the plastic regime, the changes of plastic strains and curvatures and the normal to the potential surface have the same direction. The magnitude of the plastic strain increment is determined by the plastic multiplier $\dot{\lambda}$ and together with the yield surface, they must respect the Karush-Kuhn-Tucker conditions (Kuhn and Tucker, 1951, Lemaitre et al., 2009):

$$F \leqslant 0 \qquad \dot{\lambda} \geqslant 0 \qquad \dot{\lambda} F = 0 \tag{3.9}$$

The class of return map algorithms intially introduced by Wilkins (1964) enables us to integrate the incremental constitutive equations of plasticity that respect the conditions 3.9. Among these algorithms, the CPP algorithm is probably the most employed (Simo and Taylor, 1985) as it provides an effective and robust integration scheme. It was generalized and enhanced by Godio et al. (2016) for Cosserat continua with multi-surface plasticity. The simplified procedure for a single surface Cosserat continuum consists of the following steps:

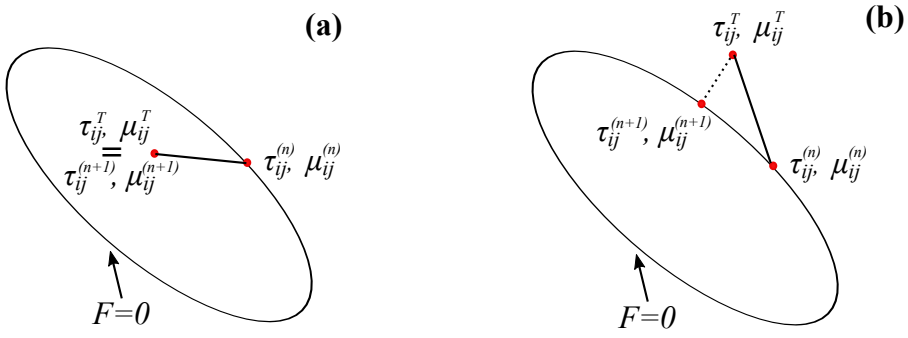

Figure 3.2: Geometrical interpretation of the CPP algorithm adopted for Cosserat materials: (a) Elastic unloading (b) Closest point projection.

(1) Increments of the displacement du_i^{n+1} and Cosserat rotation fields $d\omega_i^{c,n+1}$ are given for the generic load step (n + 1).

(2) Total strain and curvature increments $d\gamma_{ij}$ and $d\kappa_{ij}$ are computed through Eqs. 2.3.

(3) An elastic solution is predicted as trial $[\,]^T$ solution:

$$\begin{cases} \gamma_{ij}^{e,T} = \gamma_{ij}^{e,n} + d\gamma_{ij}^{e,n+1} \\ \kappa_{ij}^{e,T} = \kappa_{ij}^{e,n} + d\kappa_{ij}^{e,n+1} \\ \gamma_{ij}^{p,T} = \gamma_{ij}^{p,n} \\ \kappa_{ij}^{p,T} = \kappa_{ij}^{p,n} \\ q^T = q^n \\ \tau_{ij}^T = C_{ijkl}^e \ \gamma_{kl}^{e,T} \\ \mu_{ij}^T = M_{ijkl}^e \ \kappa_{kl}^{e,T} \end{cases} \tag{3.10}$$

We denote by q the hardening variable that allows the yield surface to evolve.

(4) The yield criterion is checked $F(\tau_{ij}^T, \mu_{ij}^T, q^T)$.

(5) If the trial state falls inside the elastic domain i.e.:

$$F(\tau_{ij}^T, \mu_{ij}^T, q^T) \leqslant 0 \tag{3.11}$$

then the trial solution is retained as the solution for the step (elastic increment illustrated in Fig.3.2(a)).

(6) If the plastic surface is activated, i.e.:

$$F(\tau_{ij}^T, \mu_{ij}^T, q^T) > 0 \tag{3.12}$$

then an elastoplastic increment occurs, and the trial state needs to be corrected (see Fig. 3.2(b)). Procedure 1 consists of solving the incremental elastoplastic problem, here reported as:

$$\begin{cases} \tau_{ij}^{n+1} = C_{ijkl}^e(\gamma_{ij}^{n+1} - \gamma_{ij}^{p,n+1}) \\ \mu_{ij}^{n+1} = M_{ijkl}^e(\kappa_{ij}^{n+1} - \kappa_{ij}^{p,n+1}) \\ dq = d\lambda \\ q^{n+1} = q^n + dq \\ \gamma_{ij}^{p,n+1} = \gamma_{ij}^{p,n} + d\lambda \frac{\partial Q}{\partial \tau_{ij}} \\ \kappa_{ij}^{p,n+1} = \kappa_{ij}^{p,n} + d\lambda \frac{\partial Q}{\partial \mu_{ij}} \\ F(\tau_{ij}^{n+1}, \mu_{ij}^{n+1}, q^{n+1}) = 0 \end{cases} \tag{3.13}$$

This problem is solved at every increment (n) by employing a classical Newton-Raphson iterative method as described in (Godio et al., 2016).

(8) If the condition $d\lambda \geqslant 0$ is satisfied, the algorithm has converged to the elasto-plastic

solution.

This procedure is schematized in Fig. 3.3. All the symbolic calculations for the return map algorithm are performed with the software Mathematica. The results are then exported in a Fortran file that is compiled independently as a library. This library is called inside the Materials module in REDBACK. This procedure enables us to easily change the yield criterion without having to write another algorithm for studying a different plastic surface.

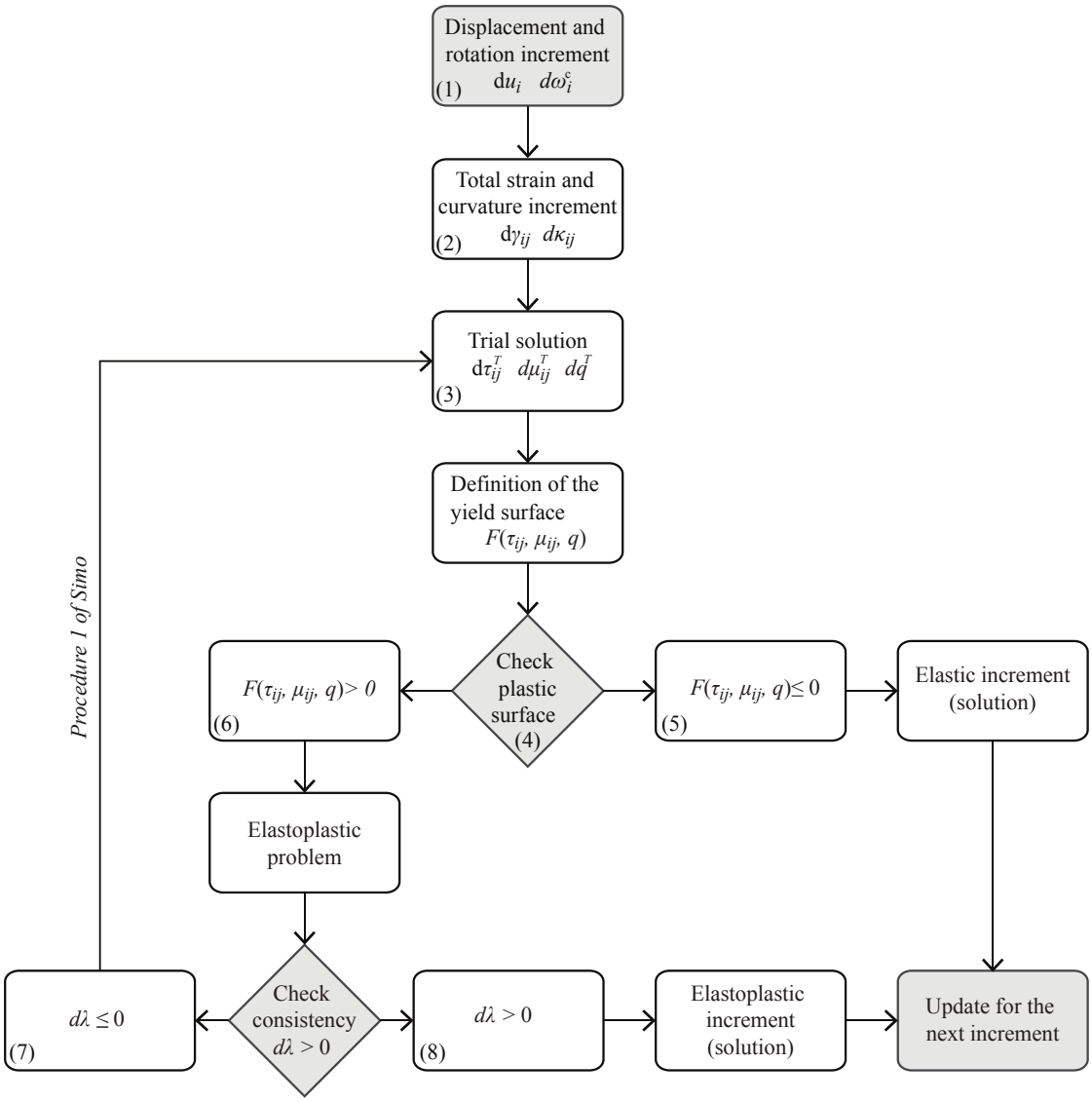

Figure 3.3: Illustration of the return map algorithm adopted for Cosserat materials (Godio et al., 2016).

3.2.4 Global integration of the nonlinear set of equations

The weak form of the equations is then expressed in the form of a residual function as follows:

$$R_j(u_i, \omega_i^c, p, T) = 0 \qquad j = 1, ..., N \tag{3.14}$$

where $R_j : \mathbb{R}^N \to \mathbb{R}^N$, where N is the number of unknowns (here eight). We name z_k the vector containing all the unknowns $z_k = [u_i, \omega_i^c, p, T]^t$. This leads to the following form of Newton's Method:

$$J_{ij}(z_k)\ \delta z_j^{(n+1)} = -R_j(z_k^{(n)}) \tag{3.15}$$

$$z_j^{(n+1)} = z_j^{(n)} + \delta z_j^{(n+1)} \tag{3.16}$$

where the superscript (n) denotes the iteration count of the Newton iteration and $J_{ij}(z_k)$ is the Jacobian matrix evaluated at the current iterate. $J_{ij} : \mathbb{R}^N \to \mathbb{R}^{N \times N}$ is defined by:

$$J_{ij}(z_k) = \frac{\partial R_i(z_k)}{\partial z_j} \tag{3.17}$$

To solve the linear system at each iteration, the expression for the Jacobian matrix is needed. Alternatively, the GMRES (Generalized Minimal RESidual) method can be used (a Krylov iterative method) as it is already implemented in MOOSE. In GMRES, the expression $J_{ij}(z_k)$ is never explicitly needed, only its action on a vector. Thus, it can be approximated using finite differences. Using this Jacobian-free approach, the dominant cost of the algorithm shifts from evaluating the Jacobian to the solution of the linear system. Nevertheless, this method is efficient only if a good preconditioning is applied to the system and the preconditioner depends on the problem studied. In our case, the rate of convergence was better with the use of the expression for the Jacobian matrix (probably due to the many nonlinearities of the problem). Thus, all the the terms in $J_{ij}(z_k)$ had to be calculated and implemented. To help with this task, MOOSE comes with a Jacobian Debugger script to assist the developers. It compares the Jacobian approximated with finite differences and the one defined analytically.

3.3 Validation of the code

The implementation is tested through a series of tests based on various benchmarks for all physical couplings. The tests are summarized in this section. All the input files and results for these tests are stored in REDBACK. When a modification of the code is carried out,

the tests are executed and the results are compared to the existing ones in order to verify that the modifications did not cause unwanted side-effects.

3.3.1 Mechanical tests

As a first step, the implementation of the equations for a Cosserat continuum and of the constitutive laws are checked. For elasticity, the numerical results are compared to the analytical solution of shearing of an elastic layer and for plasticity with results found in the literature.

3.3.1.1 Elasticity tests

The numerical results are compared with an analytical solution called the boundary layer effect in Cosserat continua described in Vardoulakis and Sulem (1995). We consider the shearing of an elastic infinite layer of thickness h in plane strain conditions. The geometry is described in Fig. 3.4.

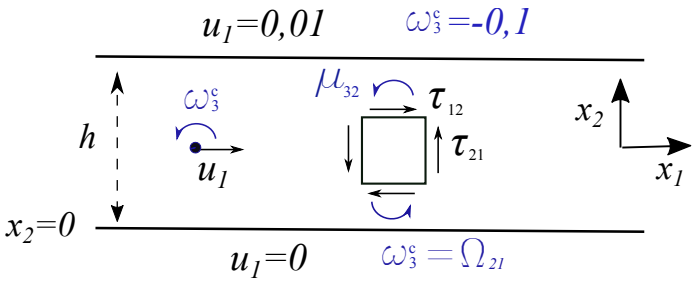

Figure 3.4: Simple shear of a strip consisting of linear elastic Cosserat material

We use the stress-strain relationships of a 2D-linear isotropic elastic Cosserat medium in plane strain conditions.

$$\tau_{11} = (k+G)\gamma_{11} + (k-G)\gamma_{22} \tag{3.18}$$

$$\tau_{22} = (k+G)\gamma_{22} + (k-G)\gamma_{11} \tag{3.19}$$

$$\sigma_{12} = \sigma_{21} = 2G\ \varepsilon_{12} \tag{3.20}$$

$$\tau_{[12]} = -\tau_{[21]} = 2G_c\ \gamma_{[12]} \tag{3.21}$$

$$\mu_{(ij)} = 2M\ \kappa_{(ij)} \tag{3.22}$$

$$\mu_{[ij]} = 2M\ \kappa_{[ij]} \tag{3.23}$$

where k is the 2D-bulk modulus, $\mu_{(ij)}$ and $\mu_{[ij]}$ are the symmetric and antisymmetric parts of the couple-stress tensor respectively, $\kappa_{(ij)}$ and $\kappa_{[ij]}$ are the symmetric and antisymmetric parts of the curvature tensor respectively. All the other symbols are defined in Section 2.2.1. The torsion modulus L is taken 0 and the two other moduli from the flexural bending rigidity tensor M and M_c are equal (see Eq. 2.22). All mechanical properties are assumed to be independent from the x_1 coordinates, which results in $\gamma_{11} = 0$ and $\kappa_{31} = 0$. We also assume that $\tau_{22} = 0$ at the top and $u_2 = 0$ at the bottom, which results in $\tau_{11} = \tau_{22} = \gamma_{22} = 0$ everywhere in the layer.

In that case, the equilibrium equations can be reduced to only two equations:

$$\frac{\partial \tau_{12}}{\partial x_2} = 0 \quad \text{or} \quad \tau_{12} = \text{constant} = \tau_c \tag{3.24}$$

$$\frac{\partial \mu_{32}}{\partial x_2} + \tau_{21} - \tau_{12} = 0 \tag{3.25}$$

Then, we insert the constitutive equations to obtain a coupled system of partial differential equations in u_1 and ω_3^c :

$$(G + G_c)\frac{\partial^2 u_1}{\partial x_2^2} + 2G_c\frac{\partial \omega_3^c}{\partial x_2} = 0 \tag{3.26}$$

$$M\frac{\partial^2 \omega_3^c}{\partial x_2^2} - 4G_c\omega_3^c = 2G_c\frac{\partial u_1}{\partial x_2} \tag{3.27}$$

The general solution of this system is:

$$\omega_3^c = K_1\, e^{\delta.x_2} + K_2\, e^{-\delta.x_2} - \frac{\tau_c}{2G} \tag{3.28}$$

$$u_1 = -\frac{2G_c}{G + G_c}\left(\frac{K_1}{\delta}\, e^{\delta.x_2} - \frac{K_2}{\delta}\, e^{-\delta.x_2}\right) + \frac{\tau_c}{G}x_2 + K_3 \tag{3.29}$$

where $\delta = 2\sqrt{\frac{G\ G_c}{(G+G_c)M}}$

The four constants (K_1, K_2, K_3 and τ_c) are determined from the boundary conditions in u_1 and ω_3^c.

At the bottom of the layer ($x_2 = 0$), the displacement is equal to 0 and the Cosserat rotation is constrained to be equal to the rigid body rotation.

$$u_1(x_2 = 0) = 0 \quad \text{and} \quad \omega_3^c(x_2 = 0) = \Omega_{21}(x_2 = 0) = -\frac{1}{2}\frac{\partial u_1}{\partial x_2}(x_2 = 0) \tag{3.30}$$

At the top of the layer ($x_2 = h$), the displacement is imposed equal to 0.01mm and the Cosserat rotation is equal to -0.1.

$$u_1(x_2 = h) = 0.01\text{mm} \quad \text{and} \quad \omega_3^c(x_2 = 0) = -0.1 \tag{3.31}$$

We plot the solutions in Fig.3.5 for the set of parameters defined in Table 3.2.

Parameters	values	units
G	10	GPa
G_c	20	GPa
h	10^{-3}	m
R	10^{-4}	m
M	$G\ R^2$	kN

Table 3.2: Values of the parameters used for the boundary layer elastic test

We choose a characteristic length R (or bending length) one order of magnitude less than the thickness of the band and we observe that the Cosserat effects are confined in a layer of size about three times R adjacent to the upper boundary, where the rotation and displacement are imposed.

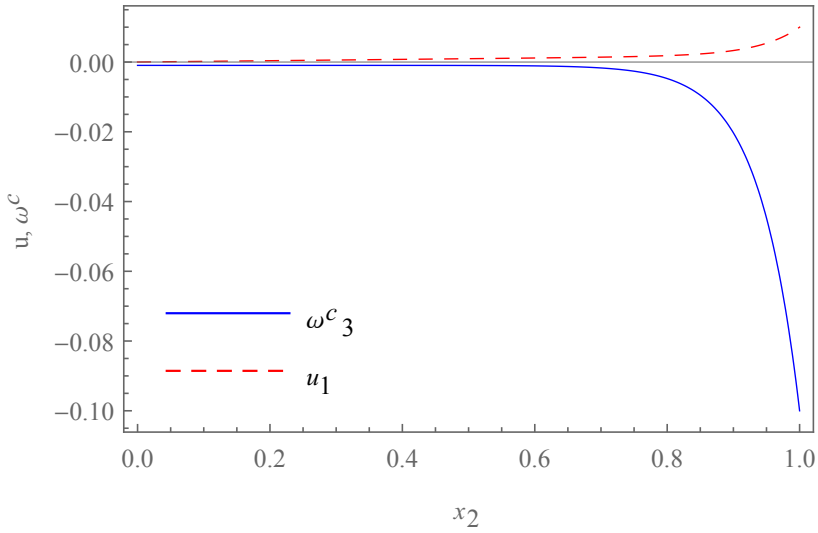

Figure 3.5: Analytical solutions for the displacement and the rotation for the example of the boundary layer in elastic Cosserat continua

For the geometry of the numerical simulation, we consider a cube of dimensions 1*1*1mm^3 with 50 elements along x_2-direction, 10 along x_1-direction and 1 along x_3-direction. The elements chosen are hexaedric with eight nodes (linear shape functions).

We prescribe periodic boundaries in the x_1- and x_3-directions. We have 6 variables in our model (u_1, u_2, u_3, ω_1^c, ω_2^c, ω_3^c), thus their values or the values of their derivatives have to be imposed at the top and bottom edges.

Bottom edge (x_2=0) :

$$u_1 = 0; \quad u_2 = 0; \quad u_3 = 0; \quad \omega_1^c = 0; \quad \omega_2^c = 0; \quad \omega_3^c = \Omega_{21} \tag{3.32}$$

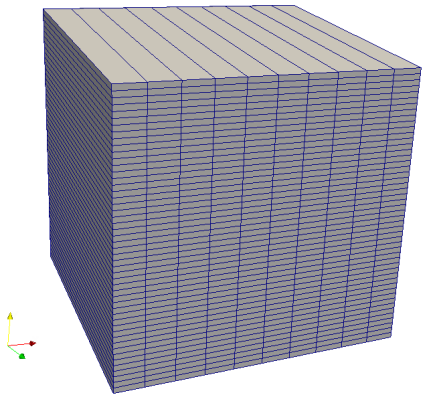

Figure 3.6: Geometry and mesh considered for the Finite Element model in Redback

Top edge (x_2=h) :

$$\frac{u_1}{h} = 0.01; \quad \frac{\partial u_2}{\partial x_2} = 0; \quad u_3 = 0; \quad \omega_1^c = 0; \quad \omega_2^c = 0; \quad \omega_3^c = -0.1 \tag{3.33}$$

Applying the condition $\omega_3^c = \Omega_{21}$ at the bottom of the layer poses certain difficulties. In order to solve them, we use a boundary condition module called *Postprocessor Dirichlet Boundary condition*, which prescribes the value obtained through a postprocessor to the variable. Thus, the antisymmetric part of the strain (or macro-rotation) Ω_{21} is calculated at the end of an iteration of the global Newton's algorithm and this numerical value is prescribed to the Cosserat rotation around x_3 for the next iteration.

In Fig. 3.7, the results for the displacements are plotted on the deformed mesh. In Figs. 3.8-3.9, we compare the values obtained for u_1 and ω_3^c with the analytical solution presented above. The difference between the numerical and analytical solutions is negligible. Moreover, a mesh convergence analysis is conducted for the value of the Cosserat rotation at $x_2 = 0.9$ (see Fig.3.10), which shows that the relative error is less than 1.2 % for 40 elements and decreases to 0.01 % for 400 elements (see also Godio et al. (2015) for a mesh convergence in terms of modal frequencies with Cosserat continuum).

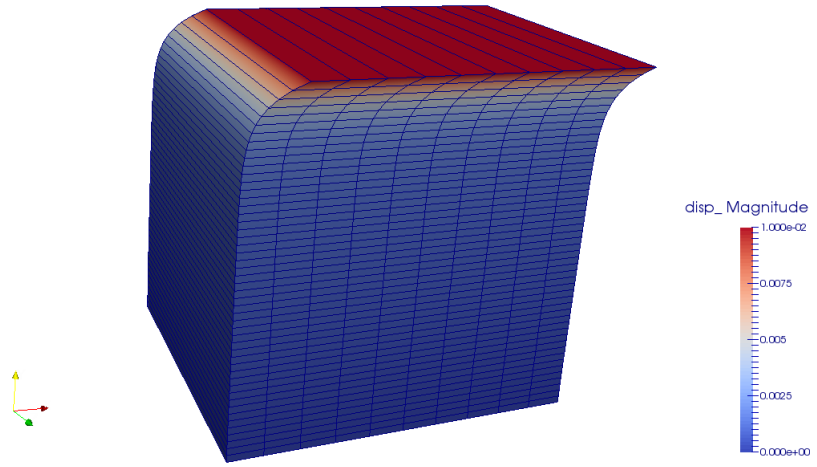

Figure 3.7: Results of the FEM simulation for the elasticity test with 50 elements in the vertical direction (Deformation Scale Factor: 20)

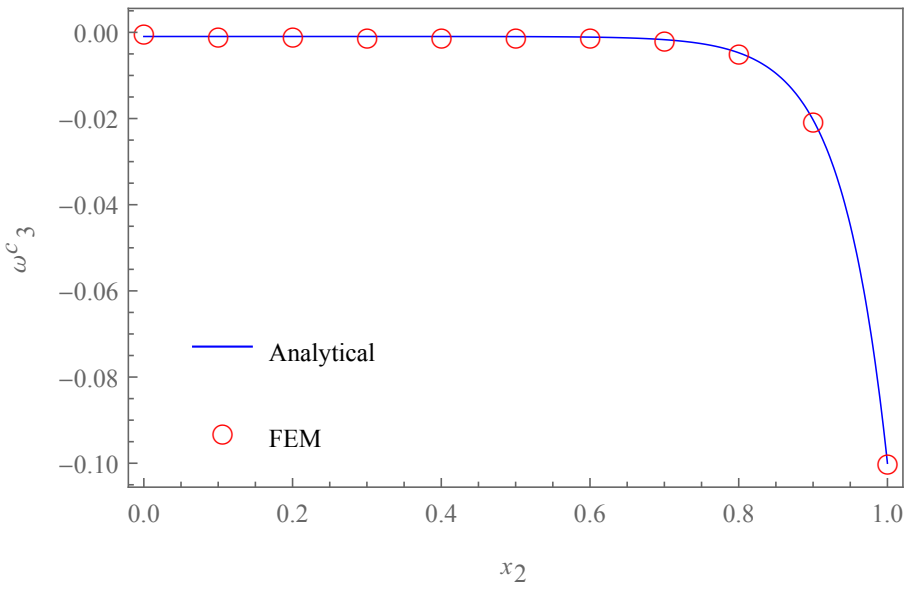

Figure 3.8: Comparison of the profiles of the Cosserat rotation ω_3^c obtained from the analytical solution and the FEM simulation with 50 points in the x_2-direction

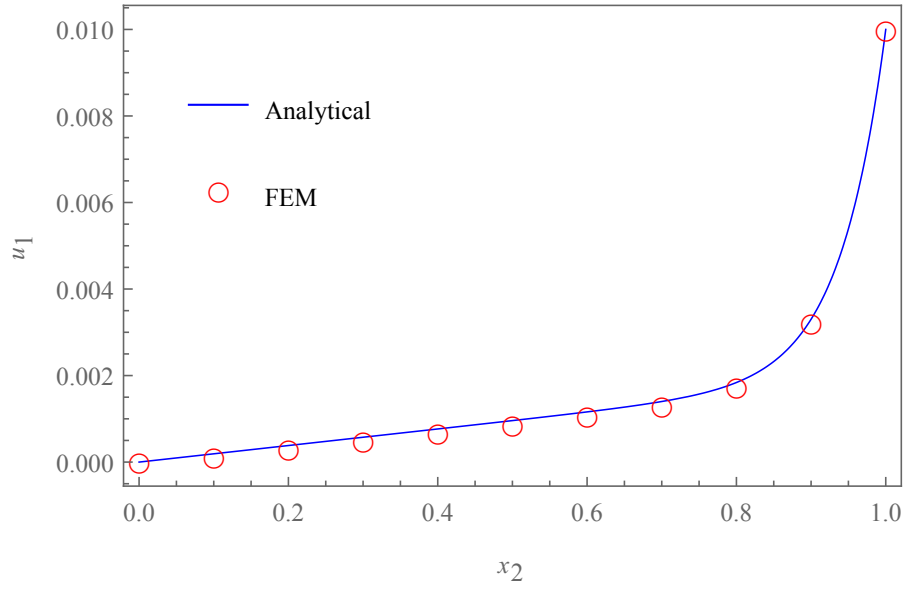

Figure 3.9: Comparison of the profiles of the displacement u_1 obtained from the analytical solution and the FEM simulation with 50 points in the x_2-direction

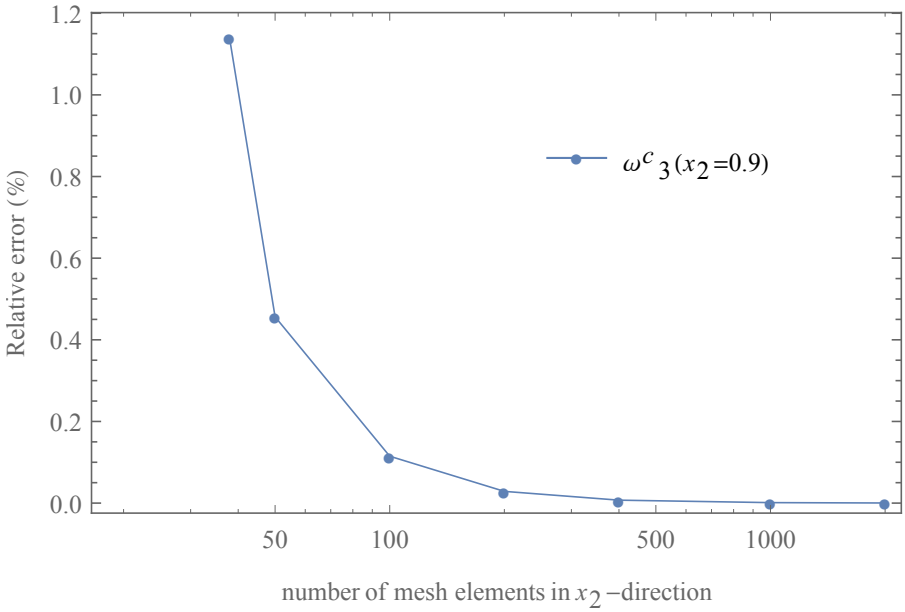

Figure 3.10: Relative error of the results obtained by FEM for the Cosserat rotation $\omega_3^c(x_2 = 0,9)$ as a function of the number of elements in the x_2-axis direction

3.3.1.2 Plasticity tests

The Drucker-Prager plastic model for three dimensional Cosserat continua is developed in Chapter 2 assuming a hardening law arising from the evolution of the friction coefficient (see Eq.2.43). In order to compare with results in the literature that consider a von Mises yield criterion, we assume the following expression for the yield criterion:

$$F = \tau + \mu\sigma(1 + h_s q\xi) - c(1 + h_s q(1 - \xi)) \tag{3.34}$$

$$Q = \tau + \beta\sigma(1 + h_s q\xi) - c(1 + h_s q(1 - \xi)) \tag{3.35}$$

where $\sigma = \frac{\tau_{kk}}{3}$ and τ is the generalized second invariant of the deviatoric stresses. ξ is a parameter that allows us either to have a hardening on the friction coefficient ($\xi = 1$) as for the Drucker-Prager model derived in Chapter 2, or on the cohesion ($\xi = 0$) as for the von Mises yield criterion. h_s is a parameter controlling the magnitude of the hardening/softening rate and q is the hardening variable.

As an example, we consider an infinite layer of height $h = 60$mm subjected to pure shear at constant velocity V(see Fig.4.1). The same material parameters with Godio et al. (2016) are chosen in order to have a comparison.

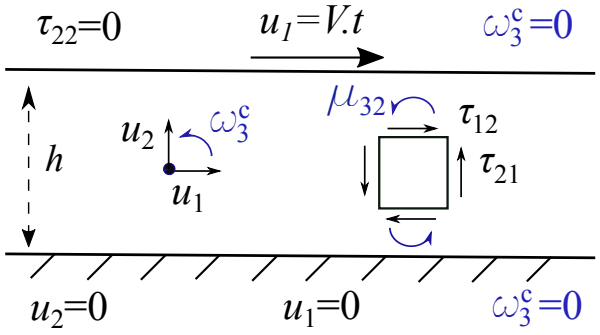

Figure 3.11: Pure shear of an infinite layer with Cosserat microstructure. Notations and boundary conditions.

The yield criterion is based on a von Mises model adapted for Cosserat continua, as in de Borst et al. (2012). In the equation 3.34, we consider $\xi = 0$, $\mu = 0$ in order to obtain the same expression.

$$F = \tau - c(\gamma^p) \tag{3.36}$$

where c is the equivalent plastic stress (or cohesion) that depends linearly on γ^p the equivalent plastic strain and τ is the generalized invariant of the deviatoric stress tensor, defined

in Eq.2.3.3. The coefficients in the stress invariant are $h_1 = h_2 = \frac{3}{4}$, $h_3 = \frac{3}{2}$ and $h_4 = 0$. In the plastic strain invariant they are $g_1 = g_2 = \frac{1}{3}$, $g_3 = \frac{2}{3}$ and $g_4 = 0$. These values for the coefficients differ from Mühlhaus and Vardoulakis (1987), Mühlhaus (1986), Vardoulakis and Sulem (1995) (see Table 2.1), because of the use of a von Mises criterion for which yielding occurs when τ reaches the yield strength of the material in simple tension, leading to the conditions $h_1 + h_2 = \frac{3}{2}$ and $g_1 + g_2 = \frac{2}{3}$. In the other papers, yielding is chosen to occur when τ reaches the yield strength of the material in pure shear, leading to the conditions $h_1 + h_2 = \frac{1}{2}$ and $g_1 + g_2 = 2$. The influence of the invariants' expression on the stress-strain graph is shown in Fig. 3.15.

In this purely mechanical example, a linear softening rule is chosen to exhibit a localization of the deformations. The equivalent plastic stress is $c = 100$ MPa and the hardening modulus is $h_s = -4$ MPa.

The elastic properties of the material are $K = 4000$ MPa, $G = 4000$ MPa and $G_c = 2000$ MPa. The internal length of the microstructured continuum is chosen to be $R = 2.5$ mm.

We investigate, first, the mesh-convergence of the model, which is the one of the most interesting features of the Cosserat continua. A three-dimensional geometry is considered with periodic boundary conditions for the right, left, front and back side of the cube. A regular mesh is chosen with one element in directions x_1 and x_3, and a range of 32 to 300 in the direction x_2. In Fig. 3.12, the shear stress τ_{12} at the top of the layer is plotted versus the normalized horizontal displacement at the top. The plastic regime is reached for $\tau_{12} = \frac{c}{\sqrt{3}}$ as expected and shows a softening behavior, exactly like Godio et al. (2016) and de Borst (1991). The results for 200 and 300 elements in the vertical direction exhibit no clear difference, showing a mesh-convergence.

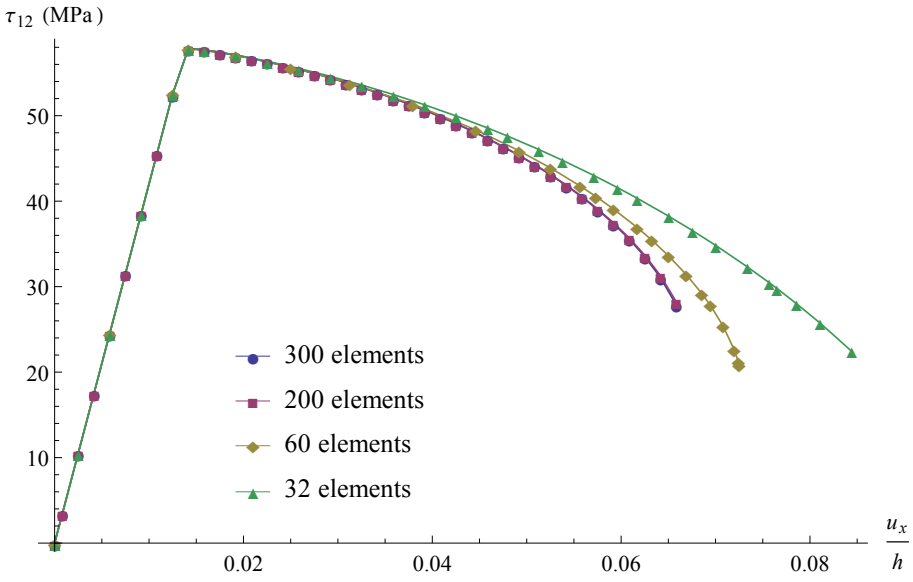

Figure 3.12: Mesh convergence with Cosserat continua

In Fig. 3.13, the Cosserat rotation around direction x_3 is plotted on the deformed mesh for $\tau_{12} = 26$MPa. The magnitude of the rotations is higher inside the zone of localized deformations as observed experimentally (Hall et al., 2010).

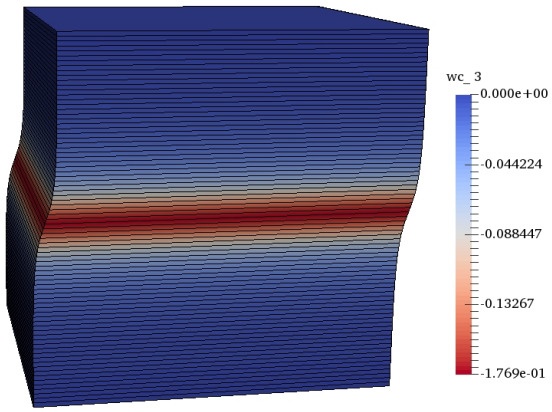

Figure 3.13: Cosserat rotation with 80 elements for the last timestep

In Fig. 3.14, the shear strain γ_{12} is plotted along the height of the layer for different discretizations and for $\tau_{12} = 26$MPa. The deformation profile is practically identical for 80 and 200 elements showing also a mesh convergence.

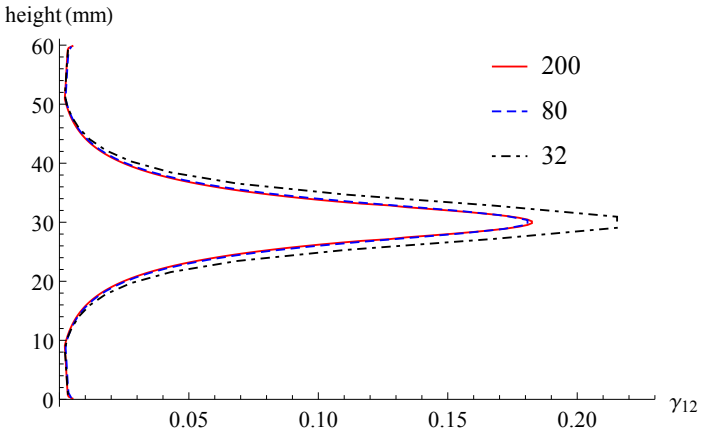

Figure 3.14: Mesh convergence of the strain profile

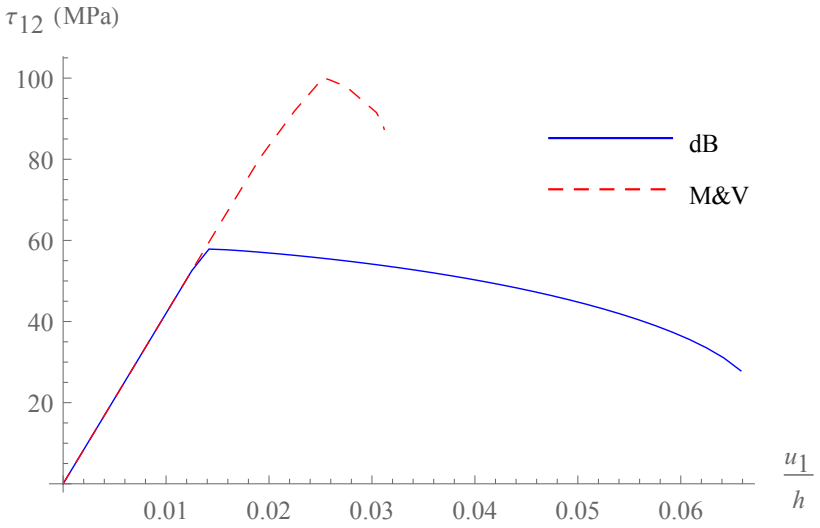

Figure 3.15: Stress-strain graph for converged meshes with coefficients of Mühlhaus and Vardoulakis (1987) ("M&V") and de Borst (1991) ("dB") for the stress and strain invariants

To test the hardening implementation more quantitatively for the friction coefficient and for the cohesion as well, we perform two tests using the coefficients of De Borst for a positive and a negative hardening modulus (-400 MPa and 400 MPa), and two others are performed using the static Mühlhaus-Vardoulakis coefficients for a positive and a negative hardening modulus (-400 MPa and 400 MPa). The stress-strain graph for these simulations executed with only one element for the mesh are shown. In Fig. 3.16, we present the stress-strain evolution of the shear layer discretized with only one element. This allows us to test the implementation of the hardening/softening constitutive behavior. Both the static Mühlhaus-Vardoulakis and De Borst coefficients for the shear stress and shear strain generalized invariants are used and a hardening/softening coefficient of 4/-4 MPa is used. We observe that the yield criterion is reached for $\tau_{12} = \frac{c}{\sqrt{3}}$ considering De Borst coefficients and $\tau_{12} = c$ considering Mühlhaus-Vardoulakis choice of coefficients.

In Fig. 3.17, we plot the generalized stress invariant τ as a function of the generalized plastic strain invariant γ_p. The slopes in this diagram enable us to verify that the value of the hardening modulus is the one expected.

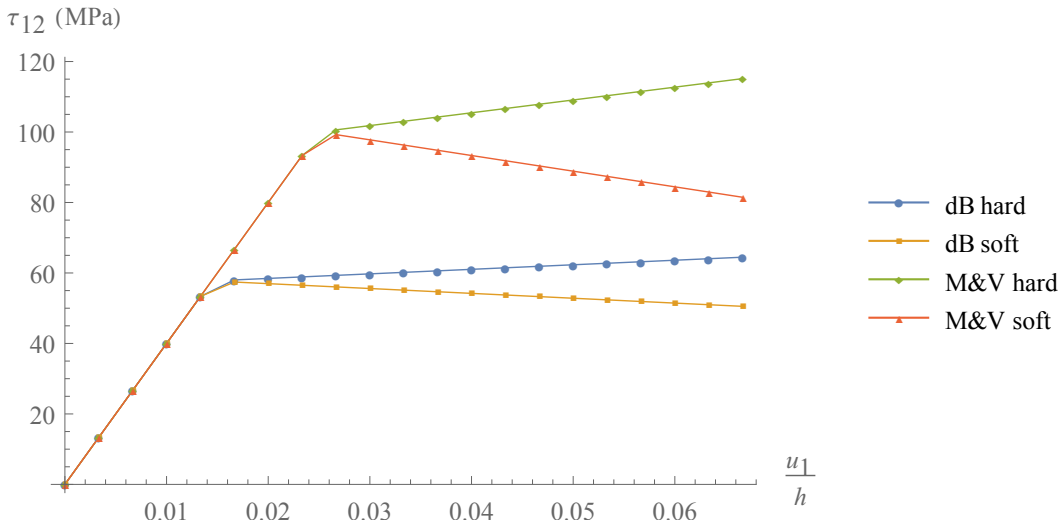

Figure 3.16: Stress-strain graph with coefficients of Mühlhaus and Vardoulakis (1987) ("M&V") and de Borst (1991) ("dB")

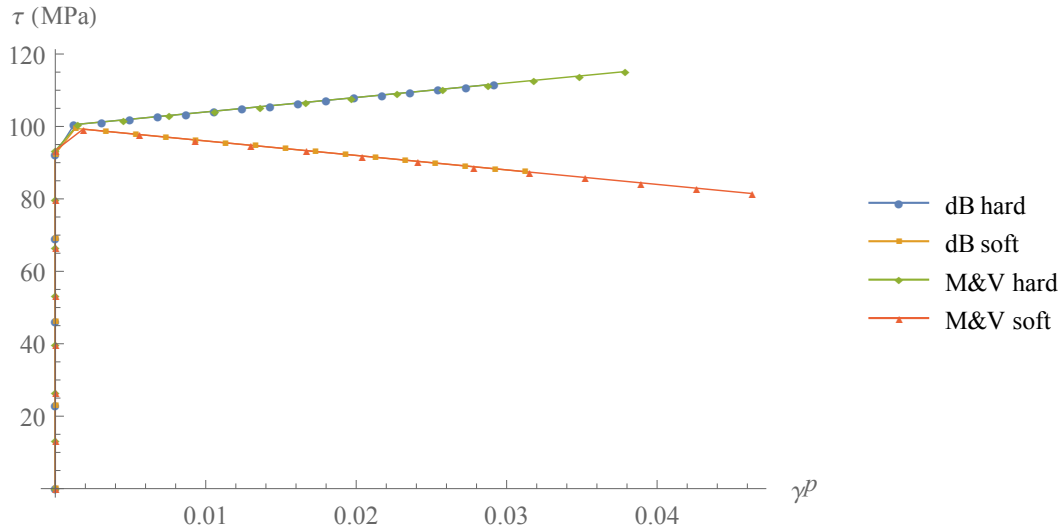

Figure 3.17: Shear stress invariant as a function of the plastic shear strain invariant with coefficients of Mühlhaus and Vardoulakis (1987) ("M&V") and de Borst (1991) ("dB")

3.3.2 Thermo-Mechanical tests

These tests concern the verification of the coupling between the energy balance equation and the mechanical equations (Eqs. 3.1, 3.2 and 3.4).

First, we look at the heating of a rod of length 10mm with a section of $1 \times 1\text{mm}^2$ (Fig. 3.18).

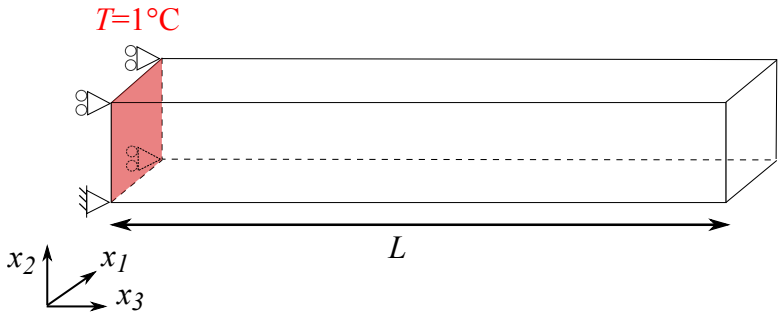

Figure 3.18: Geometry and boundary conditions for the rod used in the first test for Thermo-Mechanical couplings

For the first test, two different thermal diffusivities are used $c_{th} = 1-2$ mm^2/s. In Fig. 3.19, the evolution of temperature at the middle of the rod is compared to the solution obtained analytically using series. In both cases we observe a good agreement. In Fig. 3.20, the evolution of the displacement at the free end of the rod is plotted for $c_{th} = 1$ mm^2/s. It tends to a value of 2.5×10^{-2}mm as expected (thermal dilation coefficient : 2.5×10^{-2}/°C).

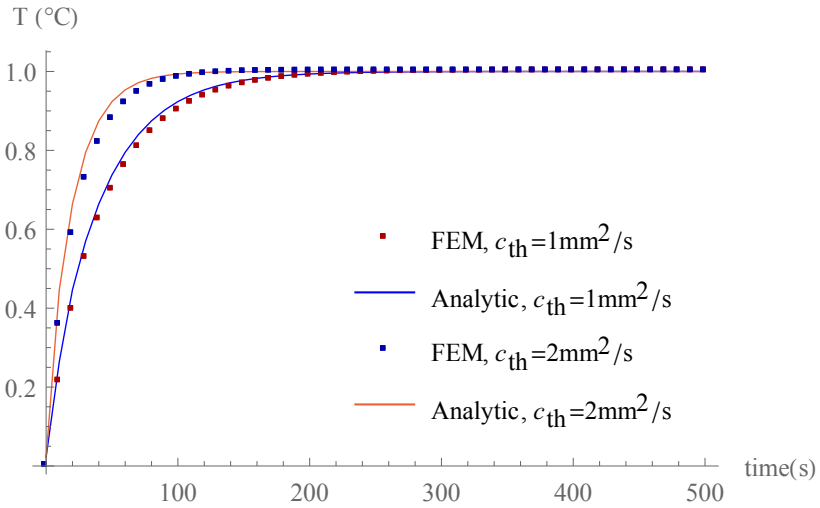

Figure 3.19: Comparison of the FEM and analytical results for temperature. Results show the temperature evolution in time for a point in the middle of the rod with two different thermal diffusivities $c_{th} = 1 - 2$ mm^2/s.

Additional tests are performed, for the same geometry of the rod, but with different boundary conditions. In these tests the normal displacements of all faces are fixed except on one

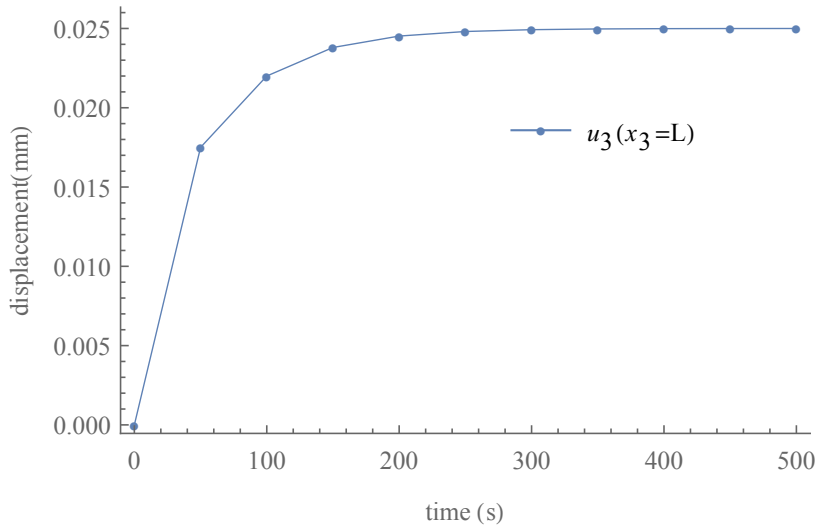

Figure 3.20: Normal displacement at the end of the rod $u_3(x_3 = L)$ due to thermal dilation for $c_{th} = 1$ mm^2/s

side as shown in Fig. 3.21. The rod is no longer free to expand in all directions and the precluded deformations cause the development of stresses that can be calculated analytically in elasticity.

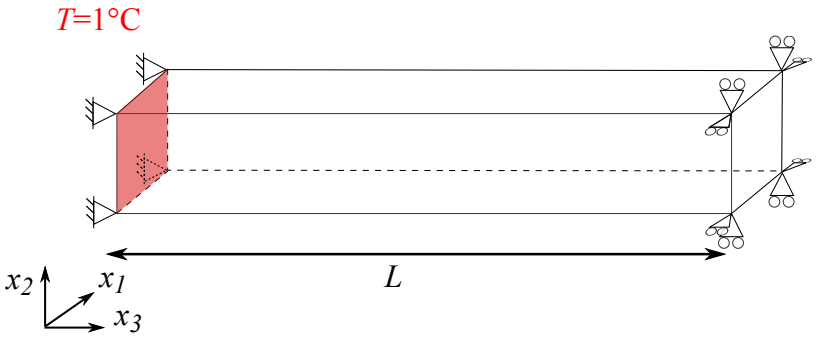

Figure 3.21: Geometry and boundary conditions for the second rod used in the tests for Thermo-Mechanical couplings

The deformation along the x_3-axis of the rod is given by:

$$\gamma_{33} = \frac{3K}{K + \frac{4}{3}G}\alpha\Delta T \tag{3.37}$$

and the stresses perpendicular to the axis of the rod are:

$$\tau_{11} = \tau_{22} = (K - \frac{2}{3}G)\gamma_{33} - 3K\alpha\Delta T \tag{3.38}$$

Therefore, when the temperature reaches a steady state $\Delta T = 1°$C, we obtain $\gamma_{33} =$

3.75×10^{-2} and $\tau_{11} = \tau_{22} = -1.125 \times 10^{-2}$MPa (with $K = 3$MPa and $G = 1.5$MPa). These values are in agreement with the results of the numerical simulation shown in Fig. 3.22.

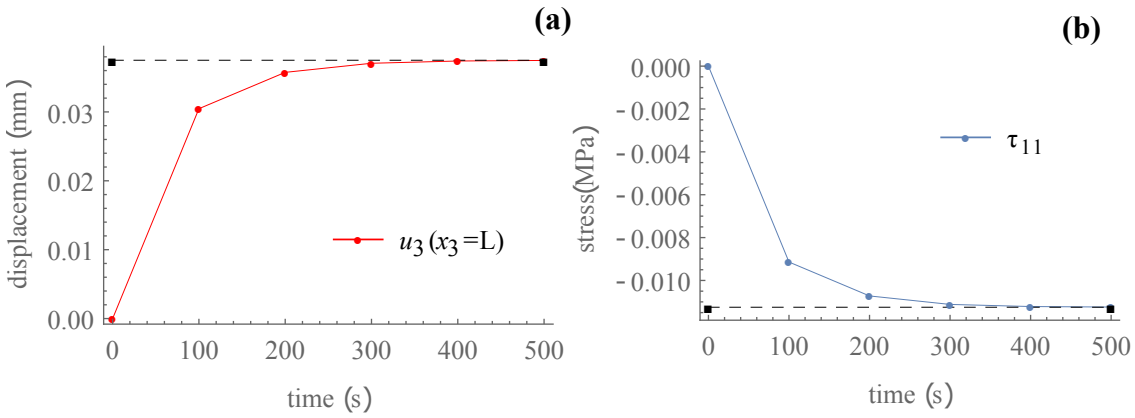

Figure 3.22: Results for the heated elastic confined rod: (a) stress τ_{11} as a function of time, (b) displacement u_3 at the end of the rod as a function of time.

The two last tests are dedicated to Thermo-Mechanical couplings considering an elasto-plastic behavior in order to observe the influence of a temperature rise on the plastic behavior of the material. The configuration for the first test is the one shown in Fig. 3.21, but this time a yield stress (cohesion) is set to 0.01MPa. Perfect plasticity is considered in this example but with no plastic dissipation in the energy balance equation. In Fig. 3.23, the results for the stress and displacement are compared. We observe that τ_{11} remains constant after reaching the value of 0.01MPa. The development of plastic deformations also has a consequence on the displacement in the rod axis direction (x_3), which is higher than that for the elastic rod. Nevertheless, no difference is observed for the evolution of the temperature as the mechanical dissipation term is neglected in this example. Thus, no feedback between the mechanical behavior and the energy balance is possible.

In order to have an insight into the feedback of the mechanics on the energy balance equation (due to the plastic dissipation term), a shear test is modeled. The same parameters as the plastic tests with a height of 60mm and only one element is considered for the mesh in the vertical direction. For simplicity, we neglect heat diffusion and only consider the effect of plastic dissipation on the temperature change:

$$\rho \mathrm{C} \frac{\partial \mathrm{T}}{\partial t} = \sigma_{ij} \dot{\varepsilon}^p_{ij} + \tau_{[ij]} \dot{\gamma}^p_{[ij]} + \mu_{ij} \dot{\kappa}^p_{ij} \tag{3.39}$$

From this test, we verify the value of the mechanical dissipation$\tau_{12} \frac{\Delta \gamma^p_{12}}{\Delta t}$ at each time step. Moreover, from the energy balance equation (Eq. 3.39), the temperature increase between

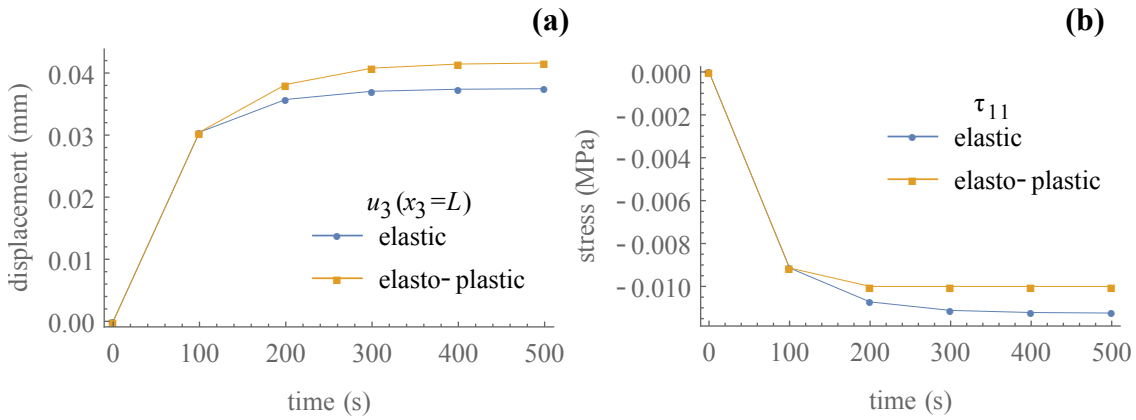

Figure 3.23: Comparison of results for (a) the displacement $u_3(x_3 = L)$ and (b) the stress τ_{11}, for the heated confined rod in elasticity and plasticity

two time steps in the plastic regime is equal to $\frac{\tau_{12}\Delta\gamma^p_{12}\Delta t}{\rho C}$ (with ρC taken equal to 1 MPa/°C here). The comparison of this expression and of the actual temperature increase is plotted in Fig. 3.24 showing no difference.

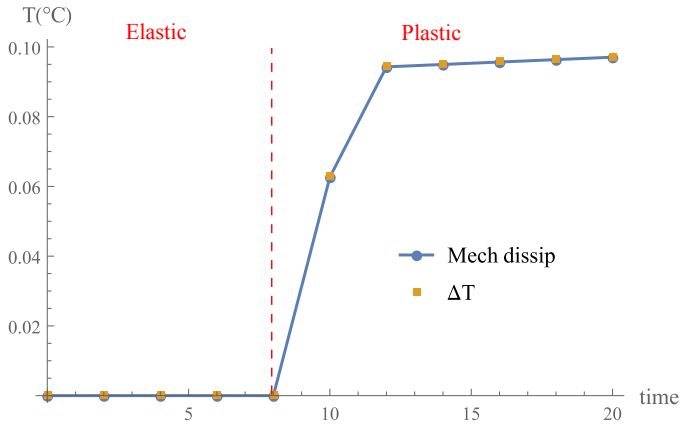

Figure 3.24: Comparison of the temperature increment as a function of time for the shearing test with the mechanical dissipation term considered in the energy balance equation.

3.3.3 Hydro-Mechanical tests

Four tests have been designed in order to check the hydro-mechanical couplings (Eqs. 3.3, 3.1 and 3.2).

The first test is the same as the diffusion test for the temperature, but this time it is applied to the mass balance equation to examine the pore pressure increase. The exact same results are found as in Fig. 3.19 considering this time different hydraulic diffusivities instead of the thermal diffusivities.

For the three other tests, an undrained oedometer configuration is considered. The geometry and boundary conditions are shown in Fig. 3.25.

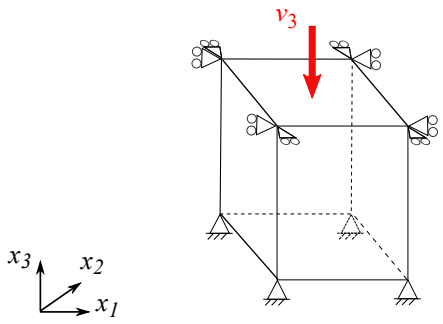

Figure 3.25: Geometry and boundary conditions used for hydro-mechanical oedometer tests.

No mass diffusion is considered in these tests and, therefore, the mass conservation equation becomes:

$$\frac{\partial p}{\partial t} = -\frac{1}{\beta^*}\frac{\partial \varepsilon_v}{\partial t} \tag{3.40}$$

A cubic single element of dimensions $1 \times 1 \times 1$ mm^3 representing a fully saturated sample with its lateral displacements prevented is considered. Moreover, all boundaries are impervious. A constant downward velocity v_3 is applied on the top boundary.

The deformation of the cube in the direction of the applied velocity is:

$$\gamma_{33} = -\frac{v_3 t}{L} \tag{3.41}$$

The effective normal stresses are linked to the elastic deformation by:

$$\tau'_{11} = \tau'_{22} = (K - \frac{2G}{3})\gamma_{33} \tag{3.42}$$

$$\tau'_{33} = (K + \frac{4G}{3})\gamma_{33} \tag{3.43}$$

No shear stresses are developed and the rise in pore pressure is obtained by:

$$p = -\frac{\gamma_{33}}{\beta^*} \tag{3.44}$$

We consider first two tests with an elastic behavior for the material and two different values of β^*. The comparison of the pore pressure rise compared to the analytical solution is plotted in Fig. 3.26 and the two evolution match perfectly ($v_3 = 10^{-2}$mm.s^{-1}).

The solution in terms of total stresses validated against analytical results is shown in Fig. 3.27.

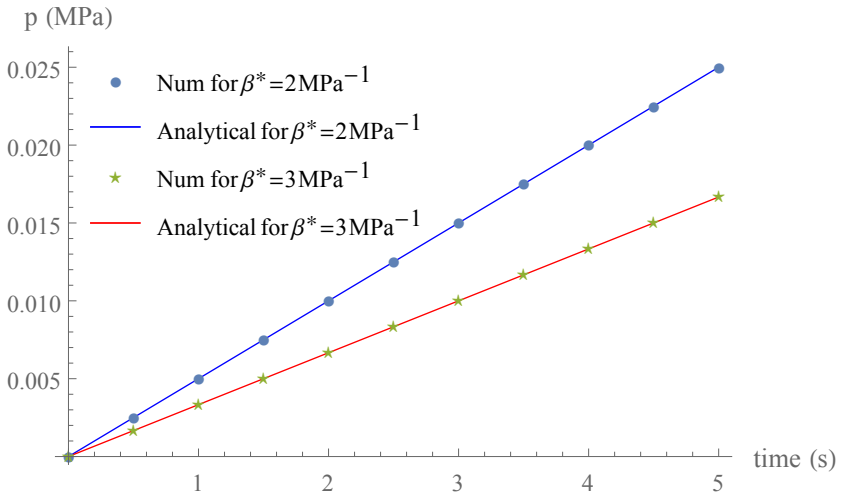

Figure 3.26: Comparison of numerical and analytical results for the pore pressure in a undrained oedometric test for different mixture compressibility β^*

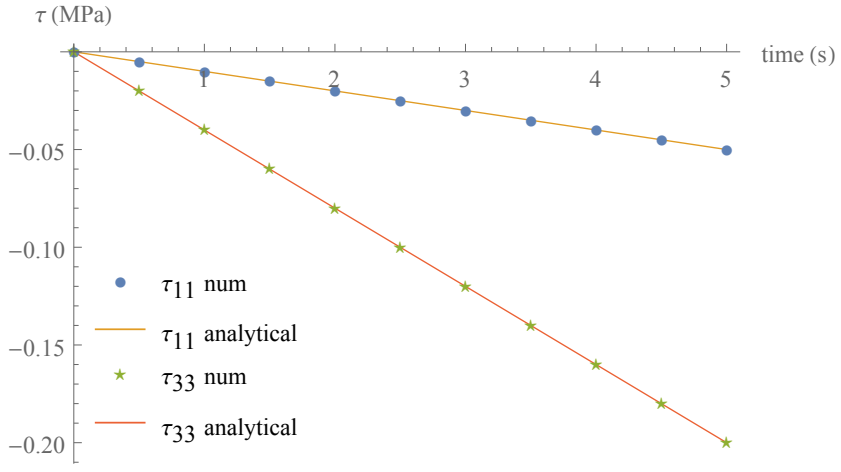

Figure 3.27: Comparison of numerical and analytical results for the stresses in a undrained oedometric test

A last test is designed for HM couplings considering an elasto-plastic behavior and allows us to test the numerical implementation of the plastic constitutive behavior and its coupling with the pore pressure. In this test a cohesion of 0.1 MPa is considered with zero friction.

In oedometric conditions, the generalized shear stress invariant is equal to:

$$\tau = \sqrt{\frac{2}{3}(h_1 + h_2)(\tau'_{11} - \tau'_{33})^2} \tag{3.45}$$

Combining Eqs. 3.45, 3.42 and 3.3.3 the yield criterion is reached at a time:

$$t = \frac{\sqrt{3}cL}{2Gv_3\sqrt{2(h_1 + h_2)}} \tag{3.46}$$

which is equal to 3.33s for the parameters considered here ($G = 1.5$MPa, $v_3 = 10^{-2}$mm.s^{-1} and De Borst coefficients in the invariant). This value is compatible with the numerical results presented in Fig. 3.28.

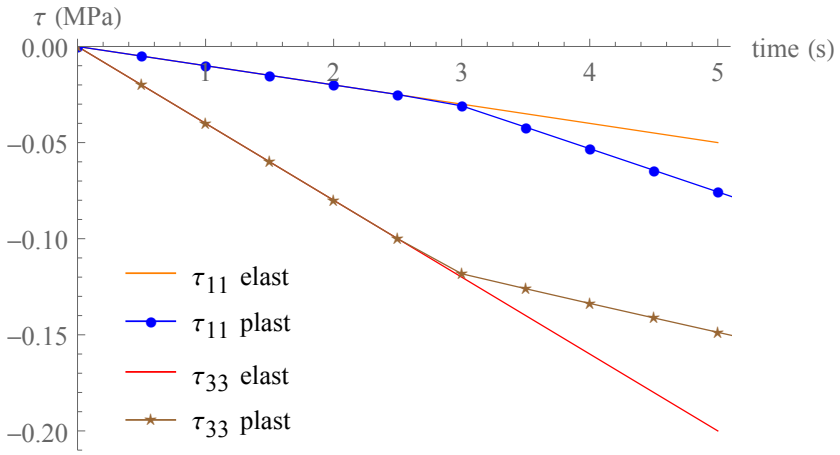

Figure 3.28: Stresses evolution with time in a undrained oedometric test in the elastic and elasto-plastic regimes

3.3.4 Thermo-Hydro-Mechanical tests

In order to test the implementation of THM couplings, we consider a shear test taking into account the full set of equations of our model (Eqs. 3.3, 3.4, 3.1 and 3.2). Similar to the shearing test for Thermo-Mechanical couplings, a height of 60mm with only one element in the vertical direction is considered. Assuming no heat and fluid flux (undrained adiabatic case), the mass balance equation is:

$$\frac{\partial p}{\partial t} = \frac{\lambda^*}{\beta^*}\frac{\partial T}{\partial t} \tag{3.47}$$

In this test, we focus on the thermal pressurization term in the mass balance equation. The coefficient $\frac{\lambda^*}{\beta^*}$ is taken equal to 0.5 MPa/°C. The results for the pressure and temperature are plotted in Fig. 3.29.

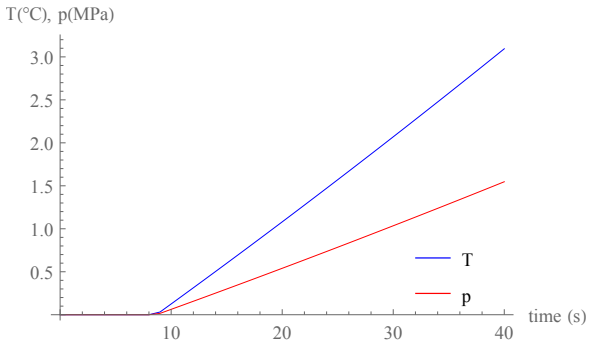

Figure 3.29: Evolution of the pore pressure and temperature for the sheared layer of 60mm with a mesh of only one element considering simplified THM couplings (no diffusion)

We can see that there is a ratio of 0.5 MPa/°C between the two graphs, which corresponds to the value of the thermal pressurization coefficient. We observe here that the plastic dissipation induces an increase of temperature, which leads to a pore pressure increase (thermal pressurization).

3.4 Conclusion

In this chapter, the numerical implementation of a three dimensional Cosserat continuum with THM couplings is presented and thoroughly tested. The model defined in Chapter 2 is introduced in the Finite Element solver REDBACK, part of the MOOSE software, in order to create a general code that can be used not only for the problem of the infinite sheared layer, but also for other geomechanical problems. The return map and the global integration algorithms are also presented in details. All the tests developed to verify and validate the implementation are successfully passed. The proposed tests can be used also as guidelines for implementations of a THM code.

Chapter 4

Post-bifurcation analysis in a 3D continuum with microstructure and multi-physical couplings

Un modèle élasto-plastique prenant les couplages THM pour les milieux de Cosserat a été développé au Chapitre 2. Son implémentation numérique ainsi que sa validation ont été présentées au Chapitre 3. Dans le présent Chapitre, des simulations numériques sont réalisées afin d'étudier le problème de localisation dans les noyaux de faille et compléter les résultats obtenus par l'analyse de stabilité linéaire. La présence d'une longueur interne dans la loi constitutive des milieux de Cosserat permet de régulariser le problème de localisation et ainsi de résoudre le problème de dépendance au maillage rencontré dans les milieux de Cauchy.

D'autre part, les influences de la microstructure et la loi d'écrouissage choisie sont mises en relief pour un système purement mécanique. Cette étude permet d'étudier quantitativement l'évolution de l'épaisseur de localisation qui est ensuite confrontÃľe à celle obtenue en ajoutant les couplages THM.

Ces développements de la taille de la bande de cisaillement sont ensuite comparés avec ceux obtenus via l'analyse de stabilité linéaire. Quand le champ de déformation inhomogène domine, les estimations de la taille de bande obtenues par analyse de stabilité linéaire diffèrent des résultats numériques. Par ailleurs, l'analyse par éléments finis nous permet d'observer l'influence de tous les paramètres sur la réponse contrainte-déformation de la faille. Cette réponse est primordiale pour la transition d'un glissement asismique à sismique. Elle nous donne aussi des informations sur le budget énergétique du glissement.

Contents

4.1 Introduction

The thickness of the localization zone was investigated using Linear Stability Analysis (LSA) in Chapter 2. This analytical approach allowed us to explore qualitatively the influence of various (bifurcation) parameters of the gouge layer, such as the grain size, the hardening modulus, the friction and dilatancy angles, the thermal pressurization coefficient, the normal stress, the porosity and the permeability.

However, the aforementioned investigation is based on a Linear Stability Analysis that has two drawbacks (see also (Chambon et al., 2004)). The first one is the linearization of the system of equations, which regarding mechanics does not distinguish between loading and unloading conditions. The second one is that the linearization is performed on a reference state that does not evolve with deformation. These are strong assumptions for studying the post-bifurcation behavior of a non-linear system. This is why, in the present Chapter, the full system of non-linear equations (see Chapter 2) is integrated numerically, using a novel three-dimensional (3D) Finite Element (FE) code, which accounts for a general, 3D Cosserat continuum formulation with Thermo-Hydro-Mechanical (THM) couplings. An elasto-plastic constitutive model that accounts for the progressive softening of the material and the grain size is implemented in the numerical code as explained in Chapter 3.

This numerical tool allows us to point out the limitations of the LSA presented in Chapter 2 and offers a more accurate description of the evolution of the thickness of the localization zone. Moreover, it enables us to investigate the full stress-strain response of a fault gouge, and explore its dependency on various parameters such the grain size and the applied shear rate. The precise evaluation of the stress-strain response of the fault zone under THM couplings is of key importance for studying earthquake nucleation as the softening rate controls the transition from aseismic to seismic slip (Scholz, 2002, Tse and Rice, 1986).

It is worth emphasizing that computing the evolution of strain localization is a challenging task due to the difficulties that arise when dealing with softening behavior. It entails a loss of ellipticity of the governing equations in the classical continuum theory framework (Vardoulakis and Sulem, 1995, de Borst et al., 1993). The boundary value problem becomes mathematically ill-posed (Vardoulakis, 1986) and the results of classical finite element computations exhibit a mesh dependency (as deformations localize in a band of thickness equal to the finite element size). Moreover, mesh refinement leads towards zero energy dissipation, which is nonphysical. However, the Cosserat FE formulation followed herein does not suffer from the above issues as it possesses a material parameter with dimension of length which regularizes the numerical problem (see also de Borst (1991), Godio et al. (2016), Stefanou et al. (2017)).

Besides Cosserat, different methods have been developed to address the problem of mesh

dependency: viscoplastcity (but only under dynamic loading conditions) (Needleman, 1988), non-local continua (Pijaudier and Bazant, 1987), gradient plasticity (Vardoulakis and Aifantis, 1991) and continua with microstructure (Papanastasiou and Vardoulakis, 1992, Collin et al., 2006), among others. As these methods are not based on the same assumptions, the choice of one or another depends on the physical mechanisms that the modeler wants to describe (Papanastasiou and Zervos, 2016) (see (de Borst et al., 1993) for a detailed comparison). For instance, if non-negligible rate dependency is experimentally observed for a given material, visco-plasticity is the natural framework. In the case of microstructure with non-negligible size (e.g. granular materials, faults), Cosserat continuum (a special case of continua with microstructure (Germain, 1973b)) appears to be the most appropriate framework (Papanastasiou and Zervos, 2016) (see also the second Chapter (Rattez et al., 2017)).

This Chapter is organized as follows. In Section 4.2, the particular problem of an infinite sheared layer without THM couplings is presented. The limitations of the classical Cauchy continuum are discussed and the advantages of the Cosserat continuum are emphasized for modeling the behavior of a fault gouge. The influence of the main constitutive parameters and of the size of the microstructure on the stress-strain diagram and on strain localization evolution is examined. In Section 4.3, the THM couplings are introduced and their impact on the overall behavior of a fault gouge is investigated. The role of thermal pressurization is highlighted. Finally, in Section 4.4, the numerically obtained shear band thickness is compared to the results of the LSA presented in Chapter 2 (Rattez et al., 2017).

4.2 Simple shear of a layer without THM couplings

In this section, we present the problem of localization of deformation in a sheared layer by considering a geometry and parameters that are consistent with a gouge in a fault core. Only the mechanical equations for an elasto-plastic Cosserat continuum are considered (without couplings). The results are compared to the ones already published (de Borst, 1991, Tejchman, 2008, Godio et al., 2016). The methodology for the evaluation of the shear band thickness is presented. Emphasis is given to describing the influence of the internal length and different softening laws on the localization and the response of the material. These results and investigations are then used as a reference to study the influence of the THM couplings (Section 4.3).

4.2.1 Problem statement and mesh convergence

The fault core is modeled as an infinite layer of height h subjected to pure shear under constant velocity V and normal stress τ_n, as shown in Fig. 4.1. The values of the different parameters are chosen to represent a fault gouge at a seismogenic depth of 7km, which is

a typical centroidal depth for crustal faults. Furthermore, as this set of parameters was used in previous studies, we can compare our results to foregoing works on the subject and complement them (Rice, 2006b, Sulem et al., 2011, Platt et al., 2014). The rotations are imposed at the upper and lower boundaries ($\omega_3^c = 0$) as it entails the development of a single band in the middle of the layer and facilitates the comparisons of stress-strain diagrams as explained in Appendix A.4.

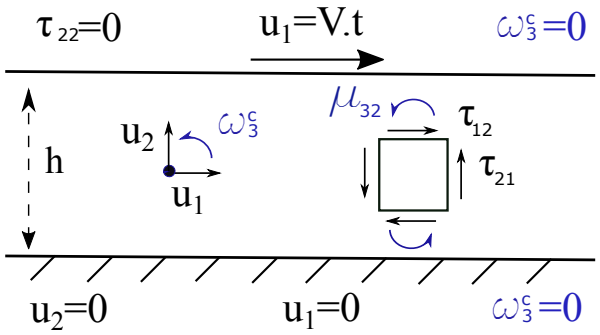

Figure 4.1: Infinite layer of a fault material under shear. Notations and boundary conditions.

The Drucker-Prager yield criterion is generalized for Cosserat continua, as in (Rattez et al., 2017) with a friction coefficient which evolves with plastic shear deformation:

$$F = \tau + \mu.\sigma' - c \tag{4.1}$$

where c is the cohesion and τ is the generalized second invariant of the deviatoric stress tensor, defined by:

$$\tau = \sqrt{h_1\, s_{ij}\, s_{ij} + h_2\, s_{ij}\, s_{ji} + \frac{1}{R^2}(h_3\, m_{ij}\, m_{ij} + h_4\, m_{ij}\, m_{ji})} \tag{4.2}$$

The hardening coefficient h_s defines the evolution of the friction coefficient with the accumulated plastic shear strain:

$$h_s = \frac{d\mu}{d\gamma^p} \tag{4.3}$$

and is linked to the hardening modulus H_s by the equation $H_s = h_s\sigma'$.

The coefficients in the stress invariant are $h_1 = h_3 = \frac{2}{3}$ and $h_2 = h_4 = \frac{-1}{6}$ and R is the internal length of the Cosserat continuum as in (Sulem and Vardoulakis, 1990). The generalized plastic strain rate invariant is defined as:

$$\dot{\gamma_p} = \sqrt{g_1\, \dot{e}^p_{ij}\, \dot{e}^p_{ij} + g_2\, \dot{e}^p_{ij}\, \dot{e}^p_{ji} + R^2(g_3\, \dot{k}^p_{ij}\, \dot{k}^p_{ij} + g_4\, \dot{k}^p_{ij}\, \dot{k}^p_{ji})} \tag{4.4}$$

with $g_1 = g_3 = \frac{8}{5}$, $g_2 = g_4 = \frac{2}{5}$. In (Sulem and Vardoulakis, 1990, Mühlhaus and Vardoulakis, 1987, Mühlhaus, 1986), these coefficients were calculated based on micromechanical considerations. An example of calculation for one set of invariants is presented in Appendix B of the companion paper (Rattez et al., 2017). The influence of the invariants' expression on the stress-strain graph is shown in Fig. 4.5 and the values of the different sets of coefficients are recalled in Table 4.1.

	2D model	3D model
Static model	$\{h_i\} = \{3/4, -1/4, 1, 0\}$ $\{g_i\} = \{3/2, 1/2, 1, 0\}$	$\{h_i\} = \{2/3, -1/6, 2/3, -1/6\}$ $\{g_i\} = \{8/5, 2/5, 8/5, 2/5\}$
Kinematic model	$\{h_i\} = \{3/8, 1/8, 1/4, 0\}$ $\{g_i\} = \{3, -1, 4, 0\}$	$\{h_i\} = \{2/5, 1/10, 2/5, 1/10\}$ $\{g_i\} = \{8/3, -2/3, 8/3, -2/3\}$

Table 4.1: Values for the coefficients of the stress and strain generalized deviatoric second invariants for a Cosserat continuum from (Mühlhaus, 1986, Mühlhaus and Vardoulakis, 1987, Sulem and Vardoulakis, 1990, Unterreiner, 1994)

In this purely mechanical example, a linear softening rule is chosen to illustrate strain localization. In the numerical examples, h=1 mm, the cohesion of the material is chosen equal to $c = 100$ kPa and a linear softening rule with a hardening coefficient equal to $h_s = -0.5$.

The elastic parameters of the material are $K = 20000$ MPa, $G = 10000$ MPa and $G_c = 5000$ MPa. The internal length of the Cosserat continuum is chosen to be $R = 10\mu$m, which is an average grain size for highly finely granulated (ultra-cataclastic) fault core (Chester and Chester, 1998, Rice and Cocco, 2007). An initial isotropic state of stress is applied to the layer, such that $\sigma = -133.33$MPa, which is a typical value at 7km depth. The values of the parameters are summarized in Table 4.2.

Mesh convergence is first investigated for the considered Cosserat model. A 3D geometry is considered with periodic boundary conditions for the lateral sides of the specimen, which results in a 1D problem equivalent to the problem presented in Fig. 4.1. A regular mesh with hexahedric elements is chosen with a single element in directions x_1 and x_3, and a range of 40 to 240 elements in the vertical direction x_2. Given the periodic boundary

parameters	values	units	parameters	values	units
K	20×10^3	MPa	μ	0.5	
G	10×10^3	MPa	β	0	
Gc	5×10^3	MPa	c	100	kPa
R	10	μm	h_s	-0.5	

Table 4.2: Numerical values of the mechanical parameters of a deep rock gouge from (Rice, 2006b, Sulem et al., 2011)

conditions and the choice of the shape functions, the invariance in the x_1 and x_3 directions is guaranteed. In Fig. 4.2, the shear stress τ_{12} at the top of the layer is plotted versus the normalized horizontal displacement at the top. As expected, the plastic regime is reached for $\tau_{12} = \mu\sigma$ and followed by a softening behavior. The results for 160 and 240 elements in the vertical direction exhibit no clear difference, indicating a mesh-convergence.

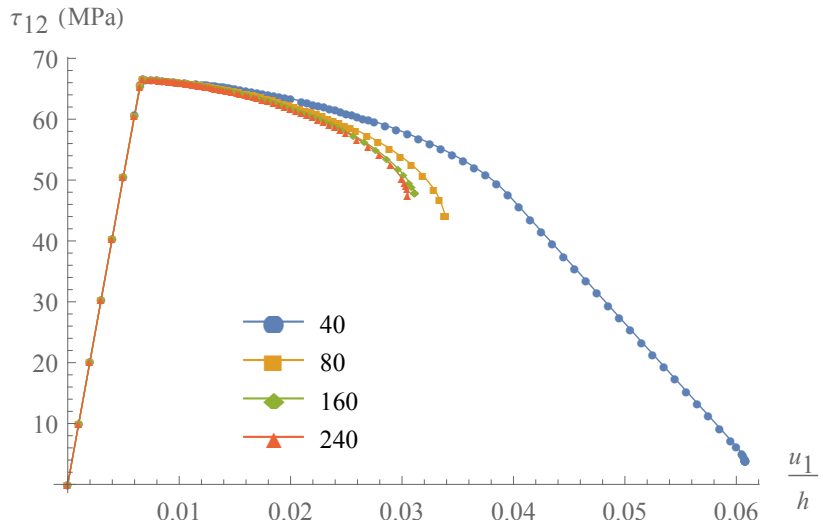

Figure 4.2: Stress-strain diagram obtained for an elasto-plastic infinite sheared layer modeled as a Cosserat continuum for different numbers of elements in the vertical direction

In Fig. 4.3, the Cosserat rotation ω_3^c is plotted on the deformed mesh with 80 elements in the vertical direction (not finer, for a clearer visualization) at the last timestep. The magnitude of the rotations is higher inside the zone of localized deformations as observed experimentally for granular materials (Hall et al., 2010).

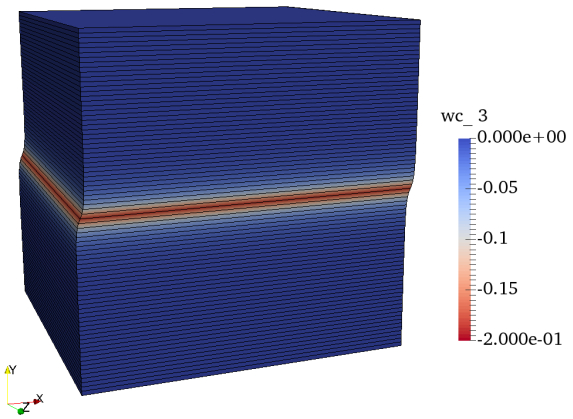

Figure 4.3: Cosserat rotation with 80 elements in the vertical direction for $\tau_{12} = 48$MPa

In Fig. 4.4, the total shear strain γ_{12} is plotted along the height of the layer for different

space discretizations and a shear stress $\tau_{12} = 48$MPa. This graph shows that when the mesh is fine enough, the shear band thickness is indeed mesh-independent which is a key feature of the Cosserat model. The deformation profile is almost identical for 80 and 160 elements. The profile for 240 elements is not represented in this graph as it coincides with the one obtained with the mesh of 160 elements.

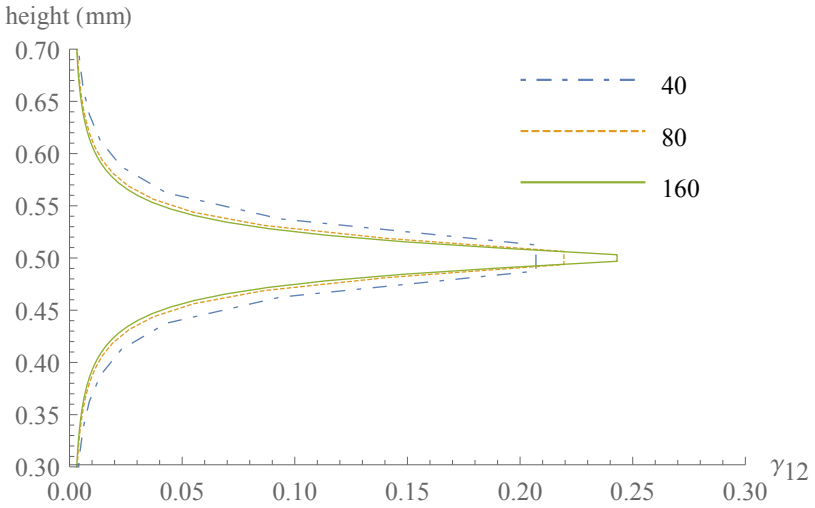

Figure 4.4: Mesh-independency of the shear strain profile for $\tau_{12} = 48$ MPa

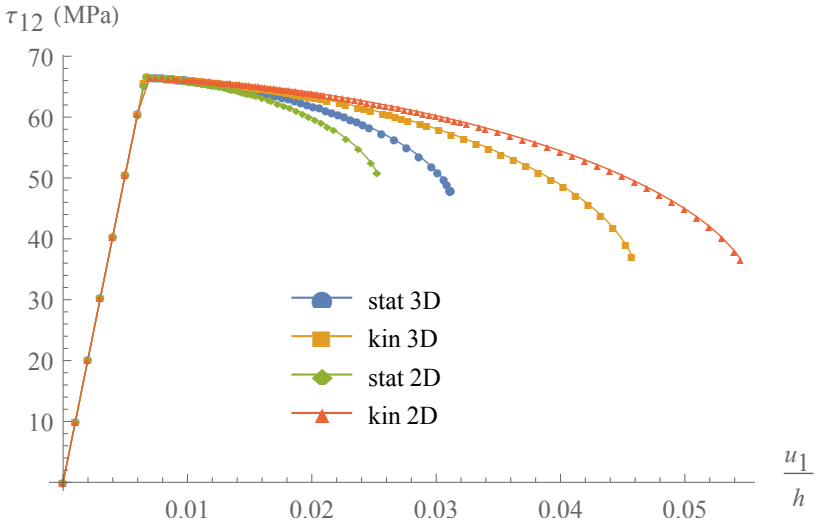

Figure 4.5: Stress-strain graph for converged meshes computed with different values of the coefficients in the stress and strain generalized invariants (see Table 4.1)

4.2.2 Comparison with classical Cauchy continuum

The results obtained using a classical Cauchy continuum are retrieved in the particular case of $G_c \to 0$, and $R \to 0$, as explained in (Iordache and William, 1998). In Fig. 4.6, the

shear stress is plotted as a function of the normalized horizontal displacement at the top.

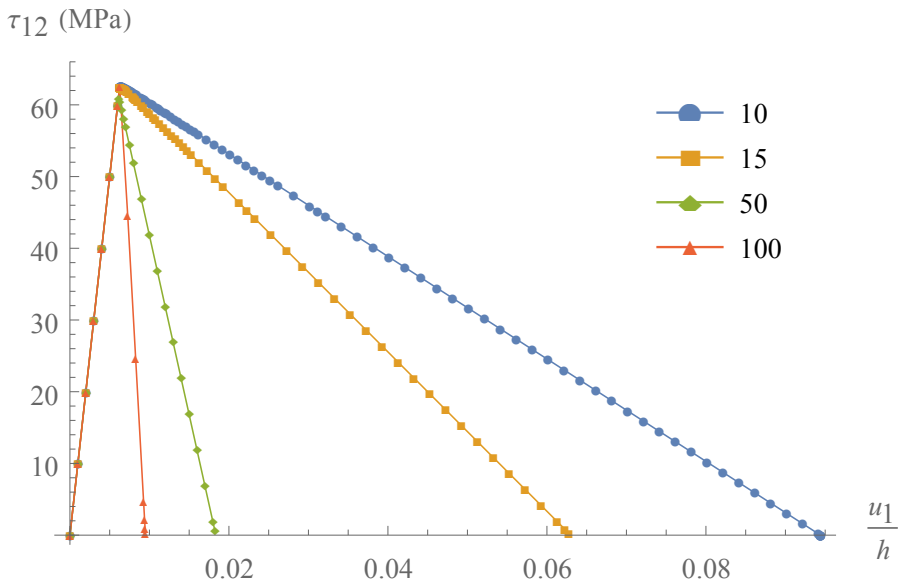

Figure 4.6: Stress-strain diagram obtained for an elasto-plastic infinite sheared layer modeled as a classical Cauchy continuum for different numbers of elements in the vertical direction

This diagram shows the dependency of the softening branch on the mesh size. As expected, the plastic deformations localize in a single hexahedric element (see Fig. 4.7) and the smaller the mesh size is, the steeper the softening branch becomes. Note that the shear band is not located in the middle of the layer. As no imperfection is introduced to restrict its position, it appears "randomly" in the system due to numerical approximations.

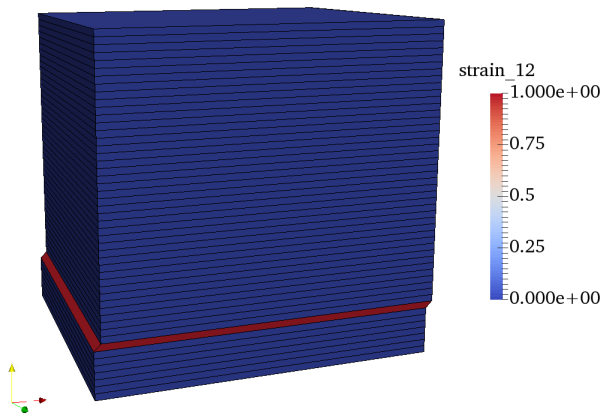

Figure 4.7: Shear strain plotted on the deformed mesh with 50 elements $\tau_{12} = 1$ MPa with a Cauchy continuum

This mesh-dependency of the load-displacement diagram has a consequence on energy dissipation. To investigate this effect, we calculate for different discretizations of the layer

the plastic part of the mechanical energy, E_p, and the elastic part, E_e, both with a Cosserat and a Cauchy continuum. The elastic energy is evaluated by considering an unloading for $\tau_{12} = 48\text{MPa}$. Elastic and plastic parts of the mechanical energy are shown in Fig. 4.8.

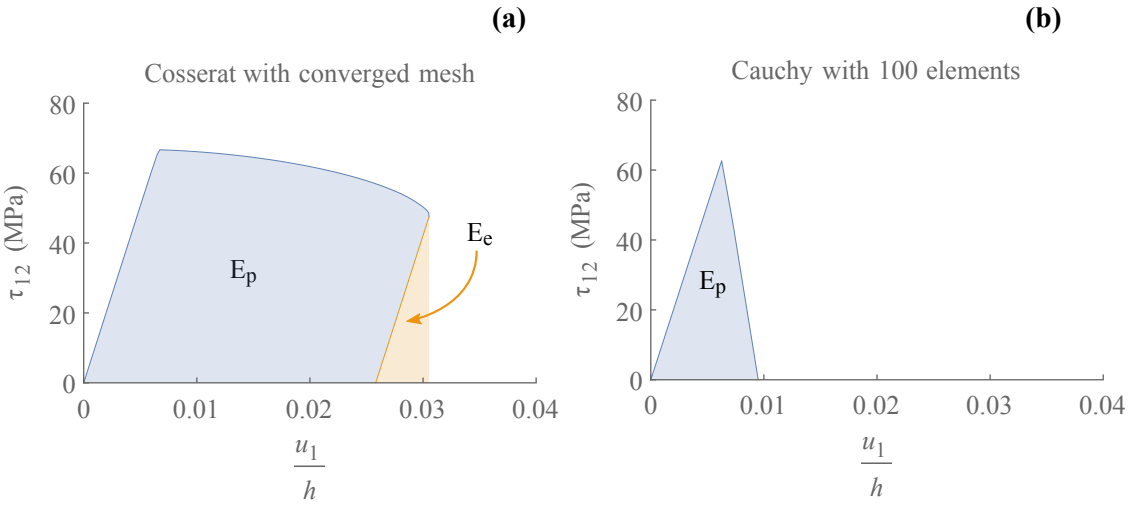

Figure 4.8: Elastic (Ee) and plastic (Ep) parts of the mechanical energy for: (a) a Cosserat continuum with 240 elements in the vertical direction, (b) a Cauchy continuum with 100 elements in the vertical direction.

The energy partition is computed for different numbers of elements (Fig. 4.9). For the Cosserat formulation, the plastic part of the mechanical energy tends to a constant value when the mesh size is small enough, whereas for a Cauchy continuum, the plastic energy tends to the total mechanical energy at peak. This is due to the fact that the softening branch gets steeper while increasing the number of elements. To complete the analysis of the Cauchy continuum with more elements an arc-length algorithm is necessary. It enables us to capture a "snap-back" behavior and the plastic energy will tend to zero (de Borst, 1991).

This mesh-dependency of the energy dissipated by the system leads to unphysical results. It is even more problematic when Thermo-Mechanical couplings are incorporated in the model because the amount of heat produced is calculated from the plastic dissipation (Eq. 2.8).

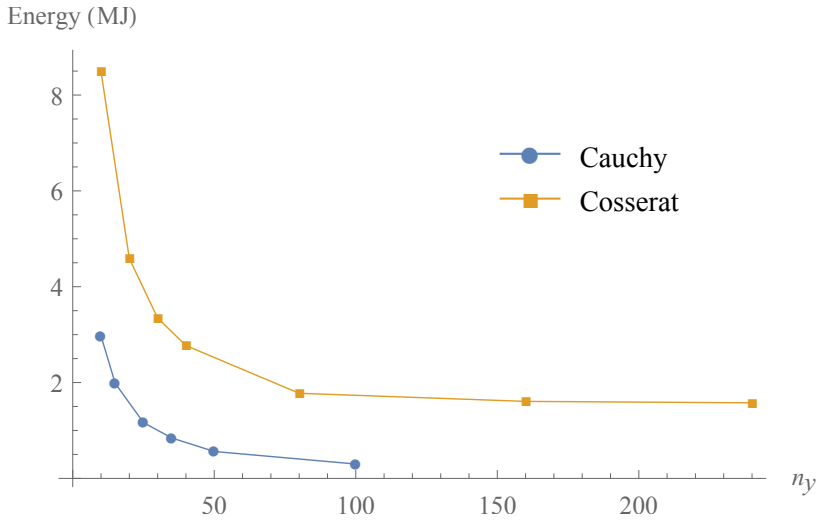

Figure 4.9: Computed dissipation as a function of the number of elements in the vertical direction (n_y) for a Cosserat continuum and a Cauchy continuum

4.2.3 Evaluation of the shear band thickness and sensitivity analysis

As stated in the companion paper (Rattez et al., 2017), the shear band thickness is a key parameter for assessing the energy dissipation when localization occurs. In order to compare the results of the linear stability analysis with the numerical simulations, we need to define a measure of this thickness.

For defining this measure we refer to the profile of the plastic strain rate invariant, $\dot{\gamma}^p(x_2)$ (cf. (Platt et al., 2014)). This a convenient proxy not only for the evaluation of the shear band thickness, as explained below, but also for comparing numerical results with experimental ones that are obtained by Digital Image Correlation (Hall et al., 2010) ($\dot{\gamma}(x_2) \approx \dot{\gamma}^p(x_2)$ inside the shear band). Furthermore, it provides a better representation of the localization process at a given time, unlike the plastic strain invariant, γ^p, or the Cosserat rotation, ω_i^c, whose distributions strongly depend on the stress path and history of the system.

Inside the shear band the computed plastic shear strain increment can be interpolated accurately by a cosine function, whose wavelength is defined here as the thickness of the localization zone:

$$\dot{\gamma}^p(x_2) \approx B.\chi_{[Y-\frac{\lambda}{2};Y+\frac{\lambda}{2}]}(x_2).[\cos(2\pi\frac{(x_2-Y)}{\lambda})+1] \tag{4.5}$$

where B is half of the maximum plastic strain rate, Y is the position of the center, λ is the wavelength of the cosine function and $\chi_{[Y-\frac{\lambda}{2};Y+\frac{\lambda}{2}]}(x_2)$ is a rectangular function defined by:

$$\chi_{[Y-\frac{\lambda}{2};Y+\frac{\lambda}{2}]}(x_2) = \begin{cases} 1 & \text{if } x_2 \in [Y-\frac{\lambda}{2};Y+\frac{\lambda}{2}] \\ 0 & \text{otherwise} \end{cases} \tag{4.6}$$

Notice that this definition of the thickness of the localization zone allows a clear link with the results of the Linear Stability Analysis performed in Chapter 2. More details and arguments on the choice of this definition as well as comparisons with alternative ones found in the literature are given in Appendix A.3.

A key parameter to determine the localization of deformation and used as a bifurcation parameter in linear stability analyses is the softening modulus H_s (Rudnicki and Rice, 1975b, Issen and Rudnicki, 2000). Thus, we investigate numerically its effect in the following. The stress-strain diagram depicted in Fig. 4.10 shows as expected that the higher (in absolute value) the softening modulus is, the steeper the stress-displacement response becomes.

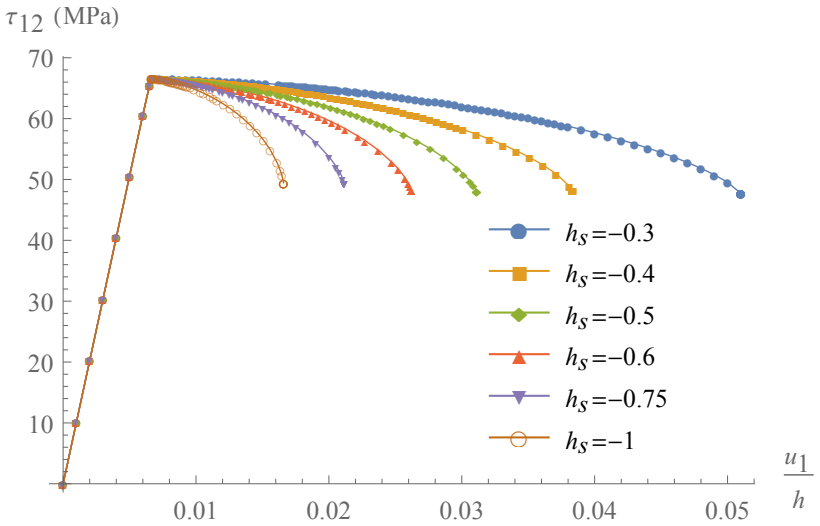

Figure 4.10: Effect of the hardening coefficient on the stress-strain diagram

In Fig. 4.11, the total shear strain profile is plotted for different hardening values but for the same shear stress applied at the boundary of the layer (48 MPa). We observe that the shear strain profiles are mathematically similar and in particular the higher the hardening is, the higher the maximum shear strain gets. Note that, these profiles correspond to the same applied shear stress τ_{12} (48 MPa) and therefore to different displacement at the boundary. Less negative values of the softening coefficient correspond to larger applied displacement and consequently to a larger maximum shear strain γ_{12} inside the localized zone. In other words, the hardening plays a direct role in the evolution rate of localization and determines the maximum total shear strain. However, the thickness of the shear band, described in Eqs. 4.5 and 4.6, is unchanged.

The evolution of the shear band thickness in the post-localization regime is shown in

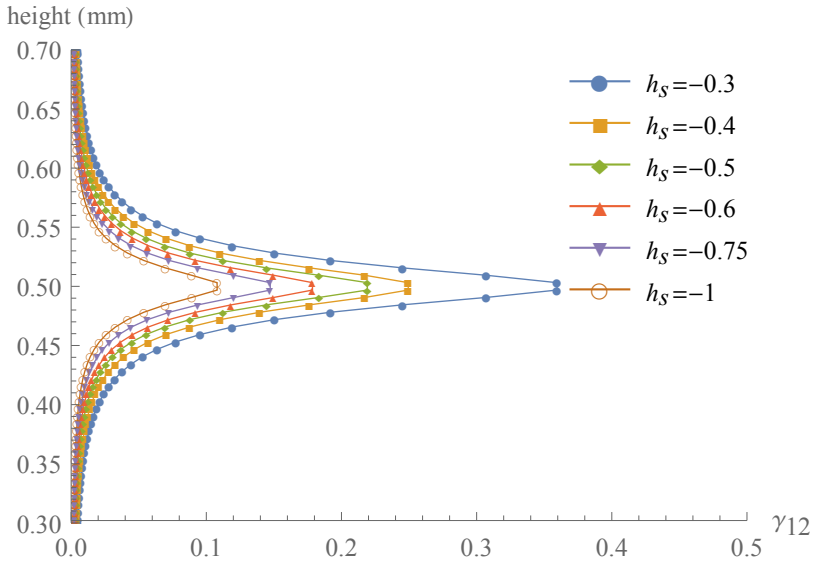

Figure 4.11: Effect of the hardening coefficient on the shear strain γ_{12} profile for τ_{12} = 48MPa

Fig. 4.12. In all cases, the thickness decreases faster at the beginning of the post-peak regime. For a more negative softening coefficient, and for the same value of the shear displacement at the boundary $\frac{u_1}{h}$, the shear stress drop is stronger which results in a narrower shear band. Thus, the hardening modulus has an effect on the shear stress evolution, but directly not on the shear band thickness. The different shear band thickness evolutions with increasing deformation are due to the different evolutions of the shear stress (Fig.4.12).

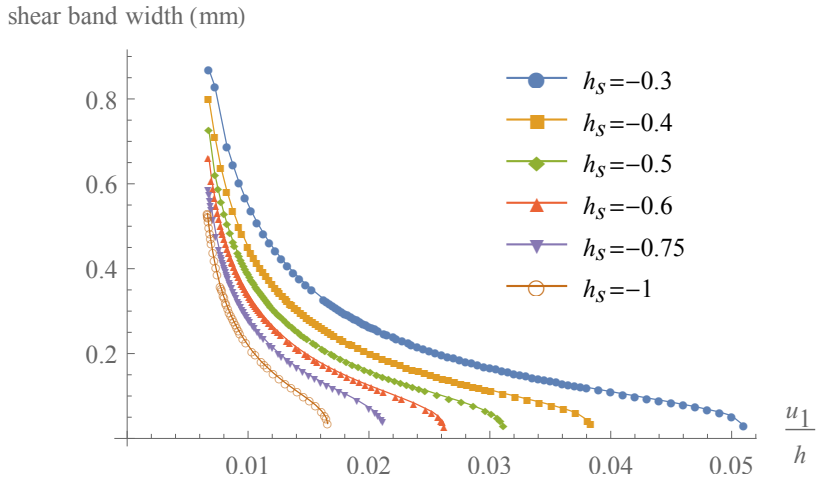

Figure 4.12: Effect of the hardening modulus on the shear band thickness evolution

It is also interesting to explore how the internal length of the Cosserat model affects the response of the system in terms of the stress-strain diagram, the shear band thickness

evolution and the shear strain profile (Khoei et al., 2010, Ebrahimian et al., 2012). In Fig. 4.13, the stress-strain diagrams for different values of Cosserat internal length are plotted for a hardening coefficient $h_s = -0.5$. For lower values of the internal length, the softening branch of the stress-displacement curve is steeper.

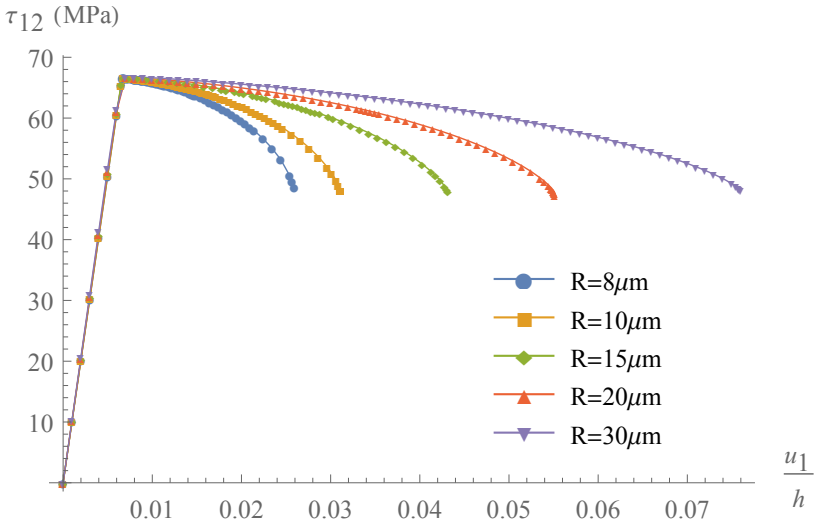

Figure 4.13: Effect of the internal length on the stress-strain graph

In Fig. 4.14, the effect of the internal length on the shear band thickness evolution is shown. For smaller internal length, shear band thickness decreases faster with increasing strain.

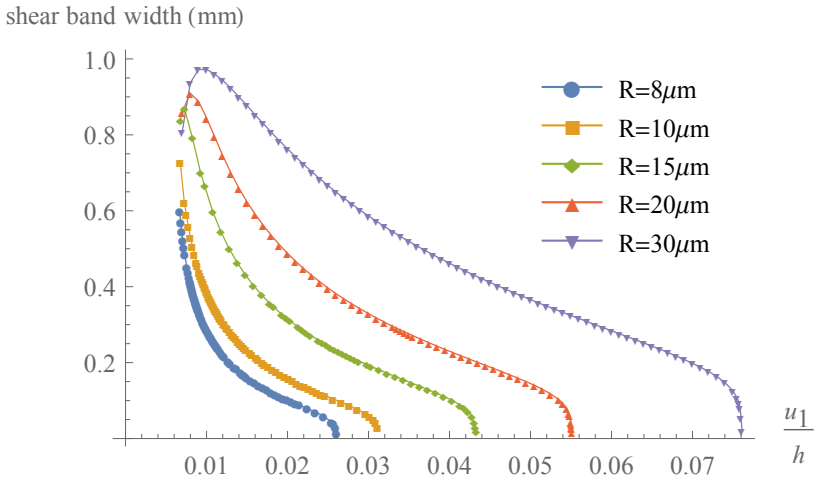

Figure 4.14: Effect of the internal length on the shear band thickness evolution

As shown in Fig. 4.15, the distribution of the shear strain γ_{12} differs for different values of the internal length R. The value of the maximum is the same, but the profiles are different (unlike Fig. 4.12). For larger internal lengths, the shear band thickness is larger, in agreement with previous studies (Mühlhaus and Vardoulakis, 1987, Sharbati and Naghdabadi, 2006, Sulem et al., 2011). Thus, the difference of the stress-strain curves in the

post-bifurcation regime for different internal lengths is mainly due to different values of shear band thickness.

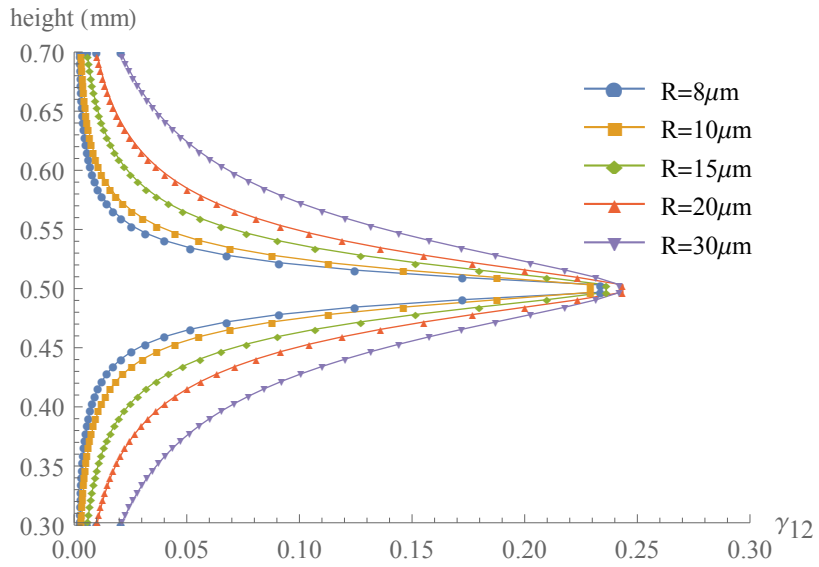

Figure 4.15: Effect of the internal length on the total shear strain profile for $\tau_{12} = 48$MPa

4.2.4 Exponential softening law to model granular flow

Experimental works on granular materials have shown that a granular medium under shear evolves towards a steady state characterized by a constant friction coefficient and zero dilatancy. In the frame of classical soil mechanics, this state is called the critical state (Schofield and Wroth, 1968). Faults exhibit a similar behavior when sheared over sufficiently large distances (see (Chambon et al., 2002)). This behavior has to be integrated into the constitutive description of the material in order to approximate the overall mechanical response of the system. An exponential evolution of the friction coefficient is thus assumed, which can be easily calibrated from experimental data (Mizoguchi et al., 2007, Di Toro et al., 2011). In Mizoguchi et al. (2007), Di Toro et al. (2011), the authors have conducted shear experiments on simulated fault gouges at seismic slip rate and they observed an exponential decay of the friction coefficient due to various multi-physical mechanisms. For experiments performed on dry materials, these authors suggest that friction softening can be attributed to gel lubrication or nano-particles lubrication.

$$\mu = \mu_{res}(1 + \frac{\Delta\mu}{\mu_{res}}.e^{-q/\gamma_e}) \tag{4.7}$$

$$\dot{q} = \dot{\gamma}^p \tag{4.8}$$

where μ_{res} is the residual friction coefficient, $\Delta\mu = \mu_{ini} - \mu_{res}$ the variation of the friction coefficient (μ_{ini} is the initial friction coefficient), γ_e is a characteristic slip weakening

deformation and q is the hardening variable. An example of evolution of the friction coefficient from μ_{ini}=0.5 to μ_{res}=0.3 is shown in Fig. 4.16. Alternatively to the flow theory of plasticity that is used in the present paper, a Cosserat continuum within the framework of hypoplasticity can be used to model granular materials (Huang and Bauer, 2003, Tejchman, 2008).

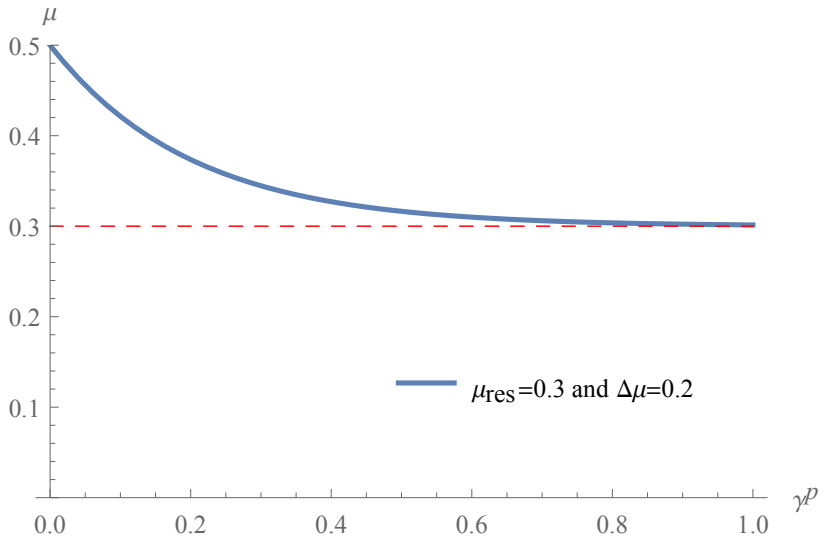

Figure 4.16: Example of evolution of the friction coefficient in terms of the plastic deformation for an exponential hardening law ($\gamma_e = 0.2$).

In Fig. 4.17(a), the influence of the characteristic deformation γ_e is investigated. The initial friction coefficient is 0.5 and the residual one is 0.3. As expected, the bigger the factor is, the steeper the softening branch becomes. However, all the curves tend to the same asymptote around 43.73 MPa, a value higher than $\mu_{res}.\sigma = 40$MPa. The reason is that the yield surface is written in terms of the generalized stress invariant τ (see Eq. 4.1) and not of τ_{12}. This formulation is more general and efficient for geomaterials as it allows us to take into account the evolution of all the components of the stress and couple stress tensors that are especially important under multi-physical couplings. An example of the distribution of shear stresses τ_{12} and τ_{21} as well as the couple stress μ_{32} is shown in Fig. 4.18 for a global deformation of the layer $\frac{u_1}{h}$ of 1.2 for the case $\gamma_e = 0.2$ and $\mu_{res} = 0.3$.

In Fig. 4.17(b), the evolution of shear band thickness is plotted for different values of the parameter γ_e. We observe that, at the beginning of the localization, the shear band size decreases until a minimum that corresponds to the inflection point of the softening branch. Then, it progressively increases towards a finite value, which is independent of the γ_e value. Thus, this parameter only affects the evolution of the softening behavior and the evolution of the shear band thickness but not their final values.

The stress-strain diagram for various values of the residual friction coefficient is depicted in Fig. 4.19 for a given value of the characteristic weakening deformation ($\gamma_e = 1$). In

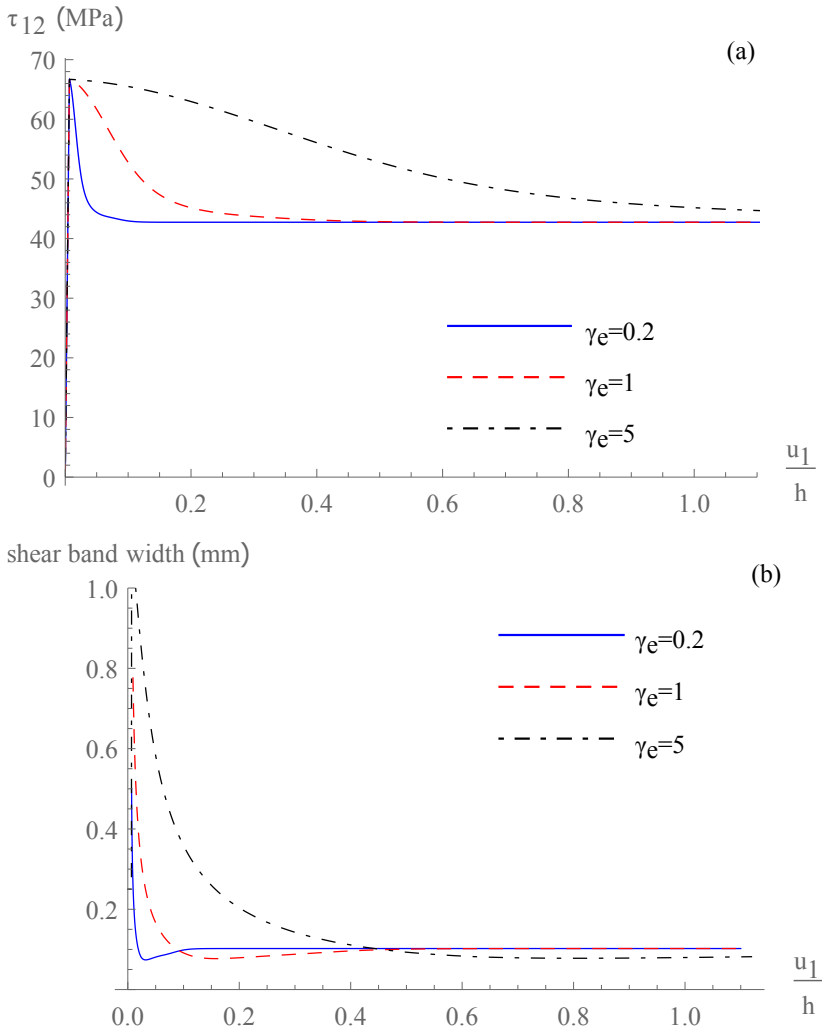

Figure 4.17: Effect of characteristic weakening deformation, γ_e, on: (a) the stress-strain diagram, (b) the shear band thickness evolution ($\mu_{res} = 0.3$).

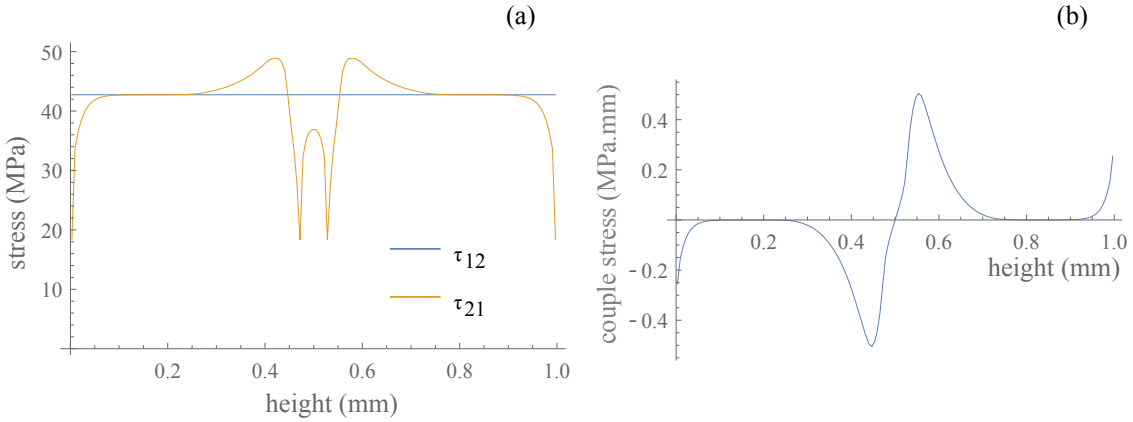

Figure 4.18: In the case of $\gamma_e = 0.2$ and $\mu_{res} = 0.3$.(a) Profile of the stresses τ_{12} and τ_{21} (b) Profile of the couple stresses μ_{32}

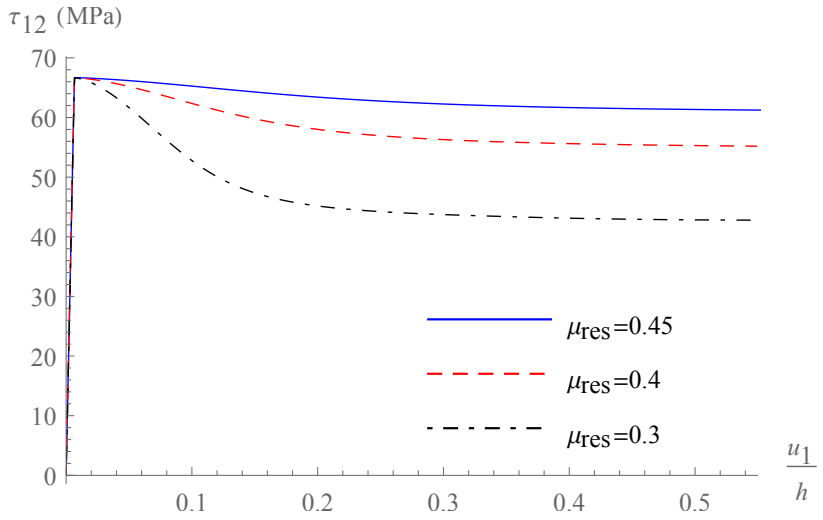

Figure 4.19: Effect of the residual friction, μ_{res}, on the stress-strain diagram($\gamma_e = 1$).

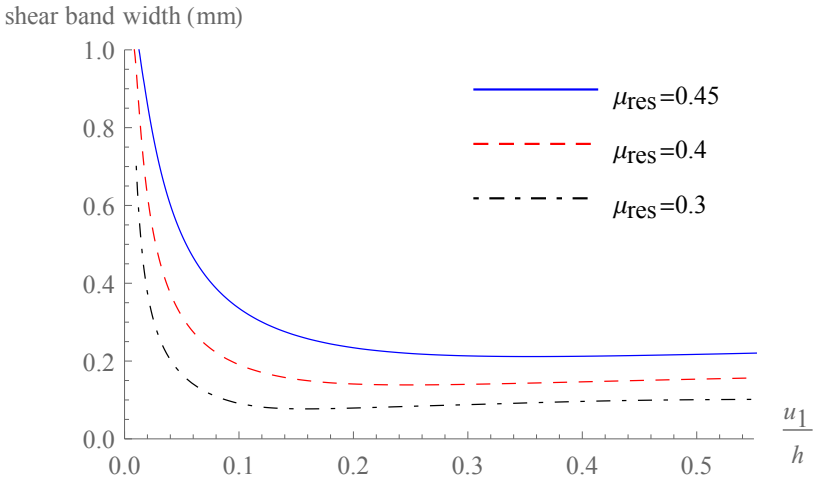

Figure 4.20: Effect of the residual friction, μ_{res}, on the shear band thickness evolution ($\gamma_e = 1$).

Fig. 4.20, the evolution of the shear band thickness with the deformation shows that the final value and also the minimum of the shear band size are influenced by the residual friction and consequently by the total shear stress drop. A larger stress drop is associated with a thinner localized zone.

A single material length R is used in the present model to represent the size of the microstructure. Previous studies on sands with a narrow grain size distribution showed a good agreement between the shear band size observed experimentally and the results obtained with a Cosserat continuum taking R equal to the mean grain size (Mühlhaus and Vardoulakis, 1987, Alsaleh, 2004). However, as noted by Rice (2006b), the distribution in gouge materials follows a fractal law and is much broader. Based on these observations, Sammis et al. (1987) developed a communition model to explain the generation of fault gouges. This theory is supported by experiments conducted in the laboratory (Steacy and Sammis, 1991, An and Sammis, 1994). Therefore, the use of a single material length (i.e. the mean grain size D_{50}) to describe gouge materials is an open question. However, Rice (2006b) argues that the cohesion between small particles in an ultracataclasite layer would be much more important and could lead to the clustering of small particles into aggregates. This effect would raise the effective size of the microstructure to consider in the analysis (greater than D_{50}). Moreover, the formation of vortex patterns linked to force chain bucklings in shear bands (Rognon et al., 2015, Tordesillas et al., 2016) imply the rotation of a set of particles and would also lead to a larger effective internal length. Therefore, a sensivity analysis on the parameter R is carried out to explore its effect on the global softening response.

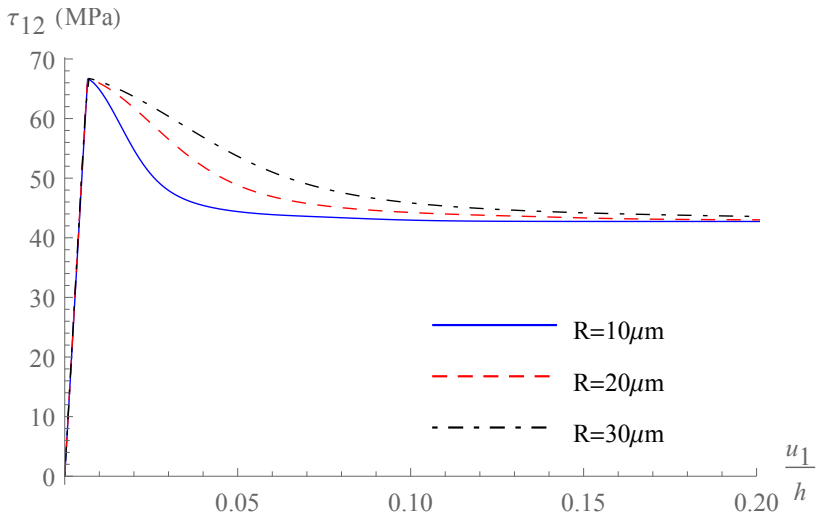

Figure 4.21: Effect of the internal length, R, on the stress-strain diagram ($\mu_{res} = 0.3$ and $\gamma_e = 0.2$).

We observe the influence of the internal length on the stress-strain diagram (Fig. 4.21) and the shear band thickness (Fig. 4.22). The shear stresses tend to the same values

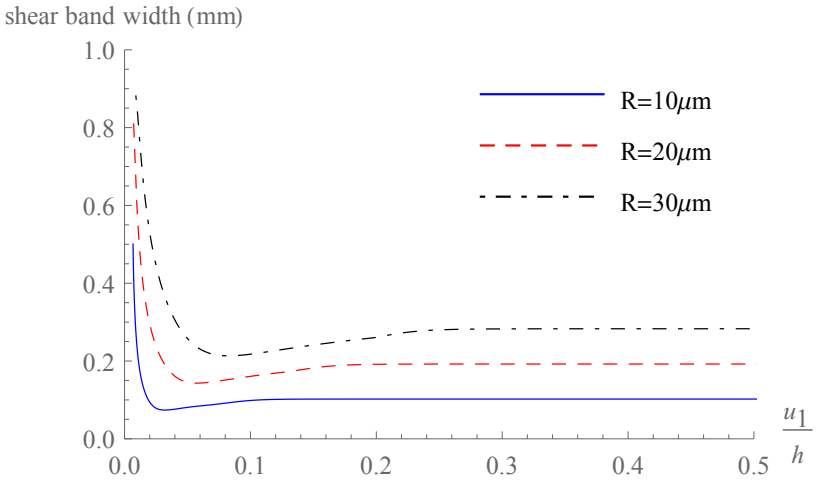

Figure 4.22: Effect of the internal length, R, on the shear band thickness evolution ($\mu_{res} = 0.3$ and $\gamma_e = 0.2$).

asymptotically. However, the final values of the shear band thicknesses are different. The minimum and the residual values are plotted in Fig. 4.23 and we observe a linear evolution for the two estimations. A similar trend is found using hypoplastic model in the frame of Cosserat continua (Huang and Bauer, 2003).

In Rice (2006b), the case of a principal slip zone observed in an exposure of the Punchbowl fault (Chester et al., 2005) is presented. Inside the ultacataclasite layer, a shear band with an apparent thickness of 100-300 μm seems to have accommodated most of the slip. The mean grain size is estimated to be D_{50}=1μm. Therefore, with the set of parameters chosen here, the internal length appropriate to reproduce this pattern is one order of magnitude larger than the mean grain size (Fig. 4.23).

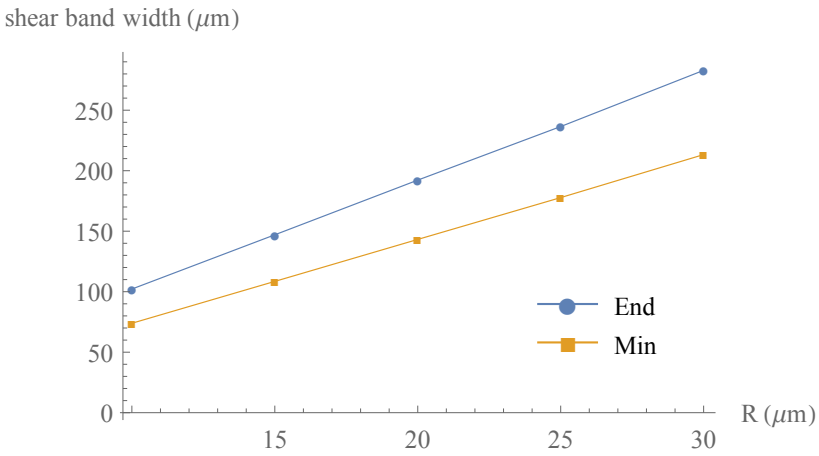

Figure 4.23: Evolution of the minimum and residual shear band thickness with the internal length R.

parameters	values	units	parameters	values	units
K	20×10^3	MPa	μ	0.5	
G	10×10^3	MPa	β	0	
Gc	5×10^3	MPa	λ^*	7.4×10^{-5}	$/^o$C
R	10	μm	ρC	2.8	MPa/^{o}C
ρ	2500	kg/m^3	c_{th}	1	mm^2/s
β^*	8.2×10^{-5}	MPa^{-1}	c_{hy}	12	mm^2/s
n	0.04		α_s	2.5×10^{-5}	$/^o$C

Table 4.3: Numerical values for the parameters of a deep rock gouge from (Sulem et al., 2011, Rice, 2006b).

4.3 Effect of Thermo-Hydro-Mechanical couplings

In the section above, the results of a dry sheared layer modeled as a Cosserat continuum have been shown in terms of stress-strain response and evolution of the shear band thickness. In this section, we consider a saturated layer and explore the effect of pore pressure and temperature changes on the strain localization process.

The numerical values for the parameters of the model refer to a saturated fault gouge at 7km depth, a centroidal depth for crustal faults (Rice, 2006b, Sulem et al., 2011). The mechanical conditions are the same as in Section 4.2 and the values for all parameters are summarized in Table 4.3.

An homogeneous and isotropic initial state of total stress of -200 MPa and an initial homogeneous pore pressure of 66.66 MPa is assumed. In terms of initial effective stresses, it corresponds to $\tau'_{11} = \tau'_{22} = \tau'_{33} = -133.33$MPa. A constant velocity of 1m/s, in the range of values estimated for seismic slip (Sibson, 1973), is applied at the top of the layer.

4.3.1 Influence of the various couplings

In this section, we highlight the effects and the importance of Thermo-Mechanical (TM), Hydro-Mechanical (HM) and Thermo-Hydro-Mechanical (THM) couplings on the overall behavior of the system. The geometry and boundary conditions are kept the same as in the previous section. In Figs. 4.24 and 4.25, we present the shear stress-strain response, for $h_s = -0.5$ and $h_s = 0$ respectively, of the fault gouge by activating the various couplings. The response is juxtaposed with the response of the gouge without any couplings. We observe that a clear difference is observed only when the thermal pressurization term (Eq. 2.8) is activated, i.e. for the THM model. The system under HM couplings does not show any difference compared to the purely mechanical one as no dilatancy is considered. This assumption is common for fault gouges (Sulem et al., 2011), which have already experienced significant sliding. For more details on the effect of dilatancy, we refer to

Chapter 2 and to Rice (1975), Vardoulakis (1985, 1996), Garagash and Rudnicki (2003), Benallal and Comi (2003).

Regarding the TM response, it barely differs from the mechanical one. The reason is that thermal expansion is restrained by the boundary conditions and therefore it entails only a slight increase of the isotropic part of the stress tensor, which in turn leads to a slight strengthening of the system.

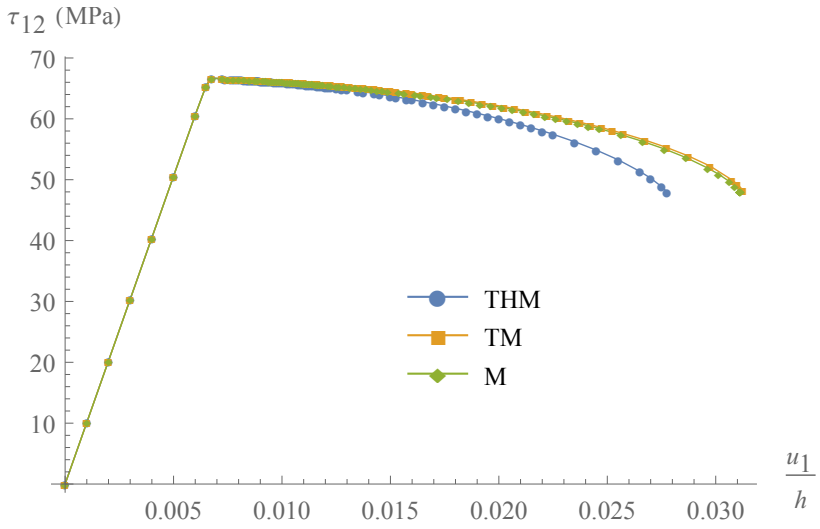

Figure 4.24: Effect of Thermo-Mechanical (TM) and Thermo-Hydro-Mechanical (THM) couplings on the stress-strain diagram with a linear softening law $h_s = -0.5$ (R=10 μm).

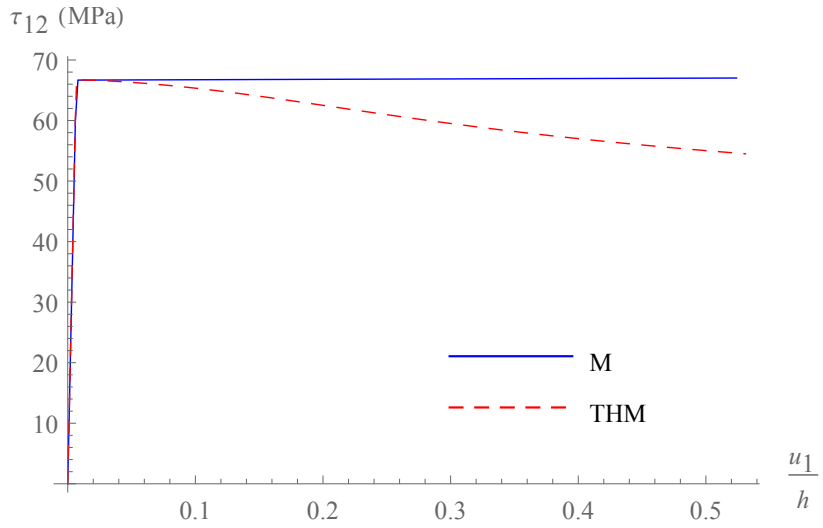

Figure 4.25: Effect of Thermo-Hydro-Mechanical (THM) couplings on the stress-strain diagram assuming perfect plasticity (R=10 μm).

4.3.2 Effect of the thermal pressurization coefficient

Thermal pressurization is a weakening mechanism that has been largely studied in the context of earthquakes in order to explain the reduction of fault strength with slip (Sibson, 1973, Lachenbruch, 1980, Rempel and Rice, 2006). This phenomenon is due to the discrepancy between thermal expansion coefficients of the solid matrix and pore fluids. Frictional heat induces a pore fluid pressure increase that results in a decrease of the effective mean stress. This weakening mechanism is controlled by the thermal pressurization coefficient Λ.

In Fig. 4.26, we investigate the influence of the thermal pressurization coefficient, Λ, on the mechanical behavior of the system. This coefficient depends on many parameters, such as the nature of the material and of the pore fluid, the stress state and the temperature among others. Previous studies have proposed a wide range of values for Λ. For instance in Palciauskas and Domenico (1982), the authors take a value of 0.59 MPa/^{o}C for Kayenta sandstone, while in Lachenbruch (1980), the value taken for an intact rock at great depth is 1.5 MPa/^{o}C. For the analysis, presented in the companion paper, the thermal pressurization coefficient was considered equal to 0.9 MPa/^{o}C for a fault at 7km depth. Of course, if Λ= 0 MPa/^{o}C, the response coincides with that of the purely mechanical system, and the higher the thermal pressurization coefficient is, the stronger the weakening becomes.

In Fig. 4.27, we focus on the evolution of pore pressure and temperature in the middle of the shear band. The temperature evolution shows an exponential development and is slightly influenced by the value of the thermal pressurization coefficient. For Λ=2 MPa/^{o}C, the increase of temperature is faster than for lower thermal pressurization coefficients, but the final value attained is lower as the shear band width is decreasing faster and thus the

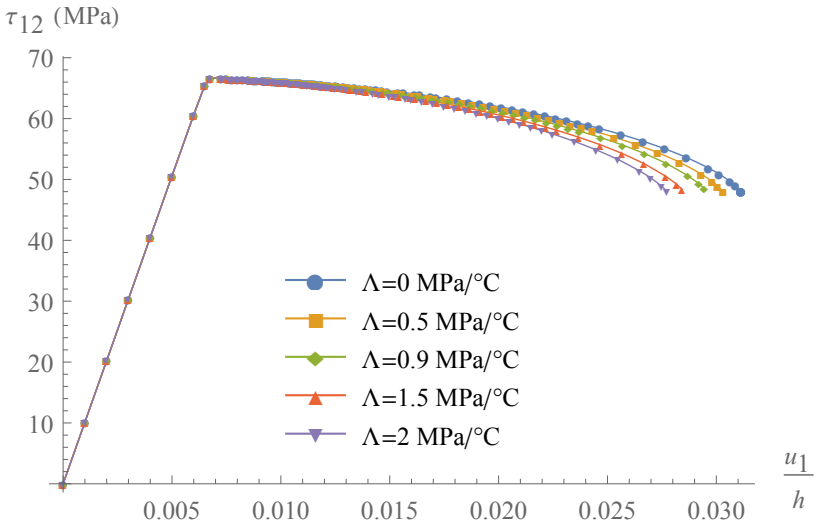

Figure 4.26: Effect of thermal pressurization coefficient on the stress-strain diagram for h_s=-0.5 and an internal length R=10 μm.

maximum shear strain reached is smaller. The pore pressure evolution is more affected than the temperature by the thermal pressurization, as it is acting as a source term in the fluid mass balance equation. When the pore pressure increases, τ'_{11} and τ'_{33} and τ'_{22} decrease in the same way. It results in a decrease of the mean effective normal stress and causes a weakening of the shear stress.

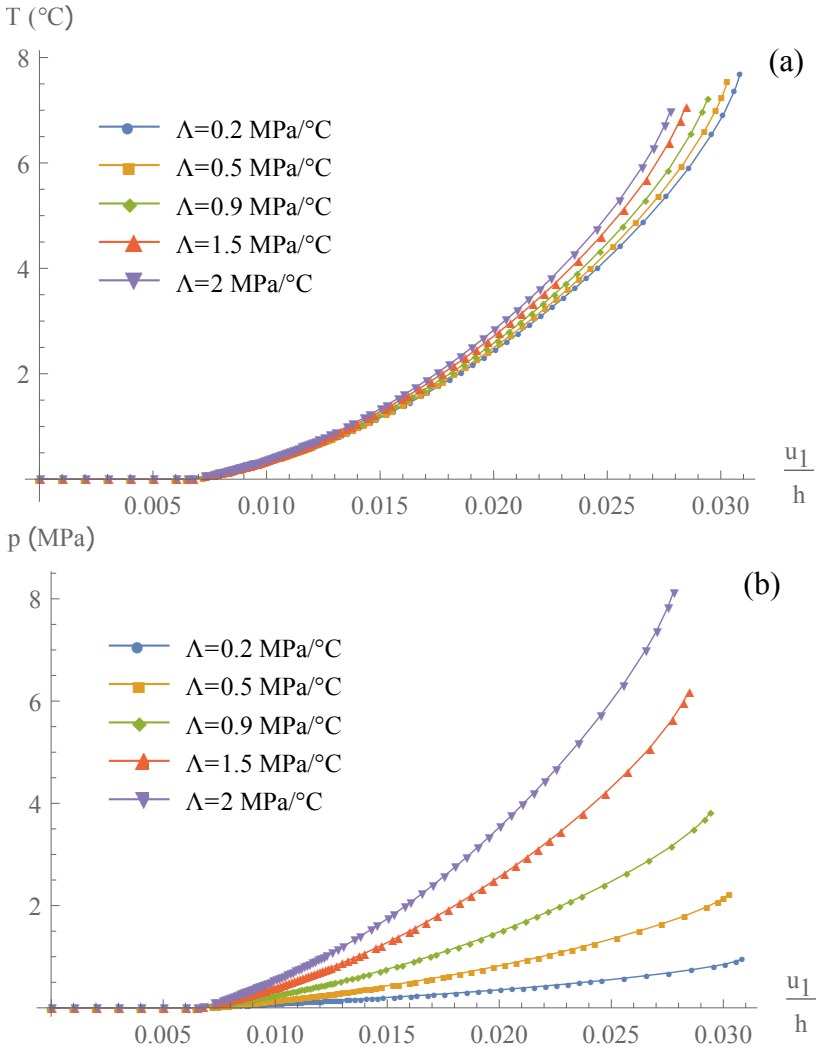

Figure 4.27: Effect of the thermal pressurization coefficient for h_s=-0.5 and an internal length R=10 μm : Evolution of (a) the increase of pore pressure and (b) the increase of temperature, in the middle of the layer.

4.3.3 Rate dependency induced by THM couplings

As shown in Section 4.2, the mechanical constitutive law that is used in the present paper is rate independent. This means that the constitutive behavior of the fault gouge is considered independent of the applied shear velocity at the boundary of the system. However, this does not mean that the overall behavior of the system remains rate-independent when THM couplings are activated due to thermal pressurization and diffusion. It is worth emphasizing that due to the Cosserat formulation, which leads to a finite dissipation and thickness of the localization zone (see Section 4.2), that the effect of rate dependency due to THM couplings is possible to study.

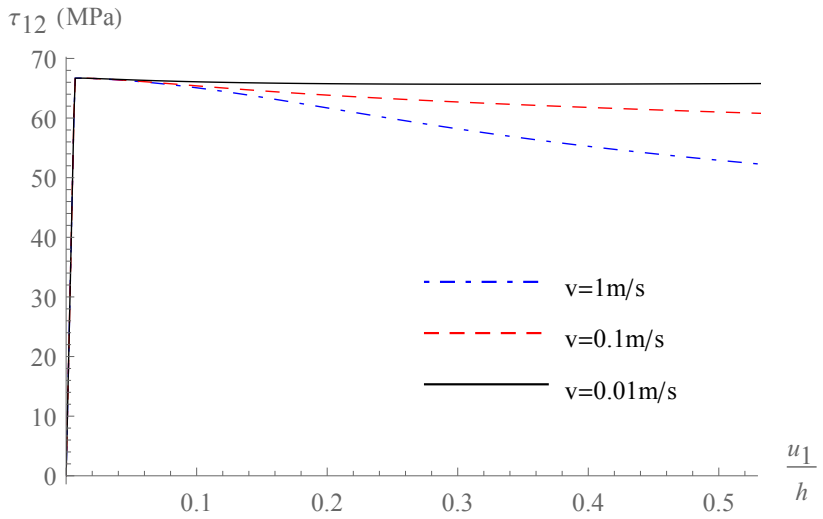

Figure 4.28: Effect of slip rate on the stress-strain diagram for perfect plasticity ($h_s = 0$), and an internal length R=10 μm

In Fig. 4.28, we present the stress-strain diagram for different slip rates that vary from 100 μm/s to 1m/s. Constant temperature and pore pressure are imposed at the top and bottom boundaries. The hardening modulus is taken equal to zero (perfect plasticity) in order to illustrate the effect of softening due to thermal pressurization. Notice that for low velocities, no softening is observed as the effect of thermal pressurization is negligible. On the contrary, for higher velocities that reach the co-seismic slip velocities the softening is significant. In Fig. 4.29, the evolution of the shear band thickness is plotted. For high velocities, a more intense localization is observed. In particular, for slip velocity lower than 0.01 m/s, no localization occurs. The reason is that due to the low shear velocity, temperature and pore pressure increase rates are low, allowing diffusion to dominate, which inhibits localization. In other words the source term is counterbalanced by diffusion, which leads eventually to a steady state (constant pressure and temperature profiles).

During the nucleation of an earthquake, the slip accelerates to reach a maximum velocity of about 1m/s. The total slip required to reach that speed is in the order of a few millimeters

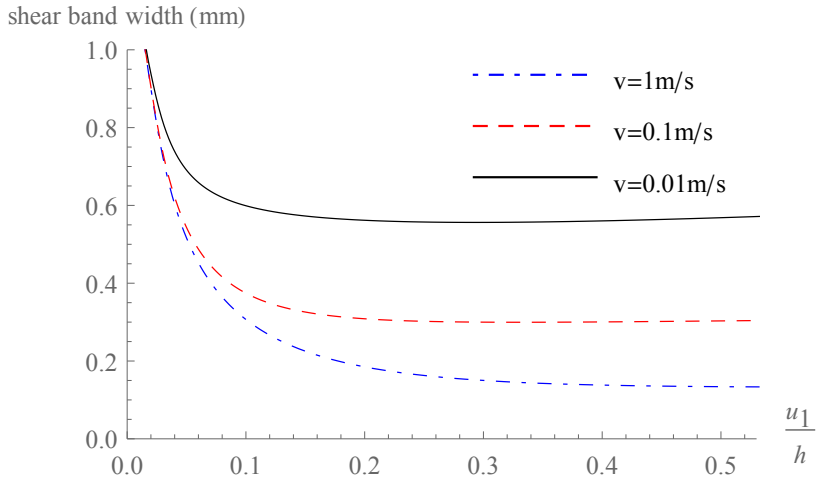

Figure 4.29: Effect of slip rate on the shear band thickness for perfect plasticity ($h_s = 0$), and an internal length R=10 μm

(Segall and Rice, 2006). Therefore, Fig. 4.28 shows that THM couplings can greatly affect the fault behavior during this phase (after a sufficient slip necessary for thermal pressurization to become significant). Moreover, the slip along the fault is not homogeneous (Wald and Heaton, 1994) and at the border of the slip patch, the displacements are much smaller than in the middle. The large difference of shear band thickness obtained in Fig. 4.29 can explain the heterogeneity of localization thickness observed along the same fault as the slip is highly heterogeneous. For example, two drilling projects at different locations in the Chelungpu fault found very different sizes of the localization zone. Boullier et al. (2009) found a principal slip zone of 3-20mm thick, whereas Heermance et al. (2003) observed a PSZ 50-300 μm in the same range as for the exhumed part of the Punchbowl fault.

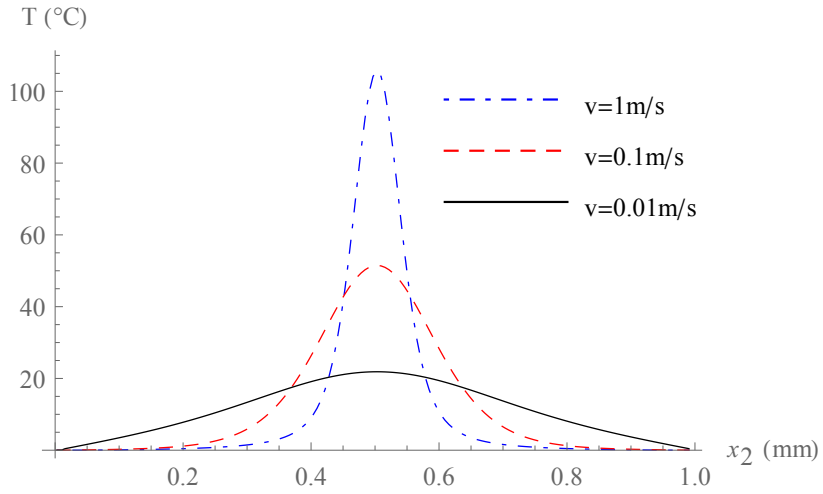

Figure 4.30: Effect of slip rate for perfect plasticity ($h_s = 0$), and an internal length R=10 μm on the temperature profile, at $\frac{u_1}{h} = 0.5$.

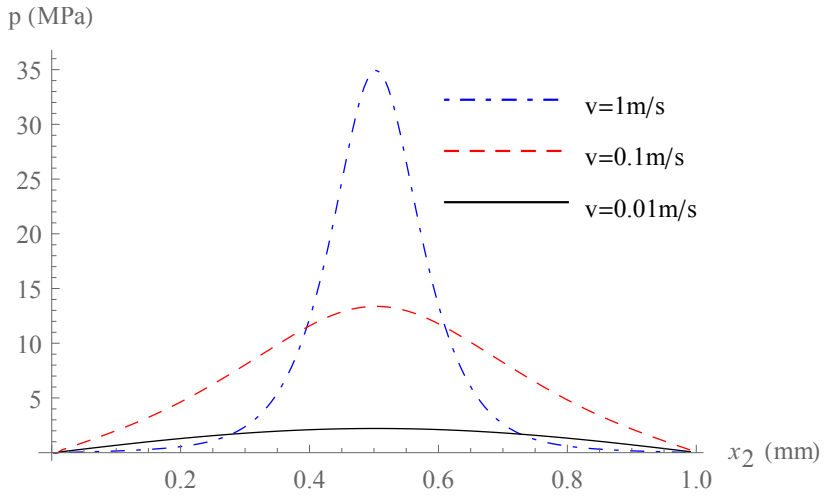

Figure 4.31: Effect of slip rate for perfect plasticity ($h_s = 0$), and an internal length R=10 μm on the pore pressure profile, at $\frac{u_1}{h} = 0.5$.

4.3.4 Exponential softening law

The computations presented in Section 4.2.4 with an exponential softening are performed again with the addition of the THM couplings. We present here the results for different values of the internal length. In Fig. 4.32, the stress-displacement diagram is plotted. We observe that when THM couplings are considered, the shear stress τ_{12} does not reach a plateau, but keeps decreasing, as the heat produced by plastic dissipation continues to reduce the strength due to thermal pressurization. Nevertheless, the mechanical and THM models follow the same decrease at the beginning of the softening and then diverge with increasing shear deformation. As expected, thermal pressurization does not play a significant role on the nucleation of the instability, but rather on the evolution of the slip and on energy dissipation (Segall and Rice, 2006).

In Fig. 4.33, the evolution of the shear band thickness is investigated for the exponential softening. The THM couplings tend to make the band thinner and have more effect on the residual thickness than on the minimum. We notice that even though the shear stress does not reach a steady state, the width of the band does. The minimum and the residual values for various internal lengths are represented in Fig. 4.34, and we observe also a linear evolution for the two estimations with THM couplings.

For R=10μm, we compare these minima and residual values of the shear band width with the values obtained for perfect plasticity (Fig. 4.29). In both cases, the shear rate applied is 1m/s. The evolution of the thickness is similar as we first observe a decrease followed by an increase. Still, the values of the minimum and residual thickness are different. In the case of perfect plasticity, the minimum value is 124 μm and the residual thickness is 128 μm (Fig. 4.29). They are larger than the values obtained considering an exponential

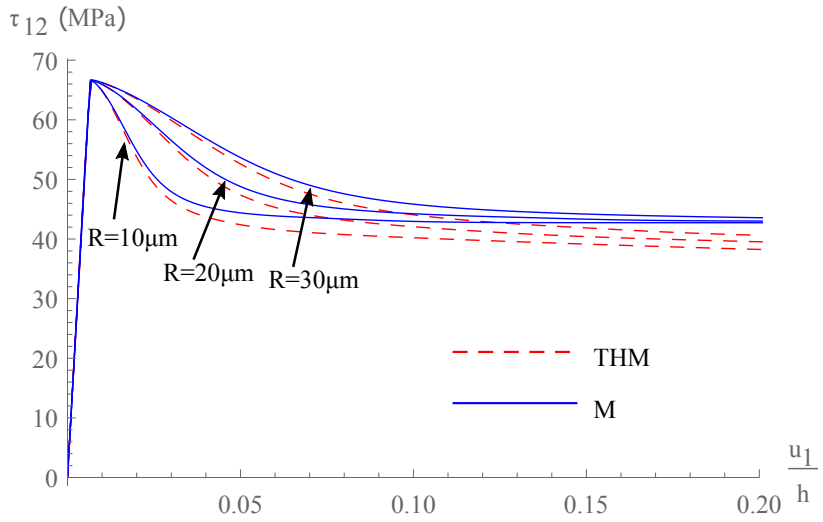

Figure 4.32: Effect of THM couplings on the stress-strain diagram for an exponential hardening ($\mu_{res} = 0.3$ and $\gamma_e = 0.2$) and different internal lengths (R=10, 20 and 30 μm) considering a slip rate of 1m/s.

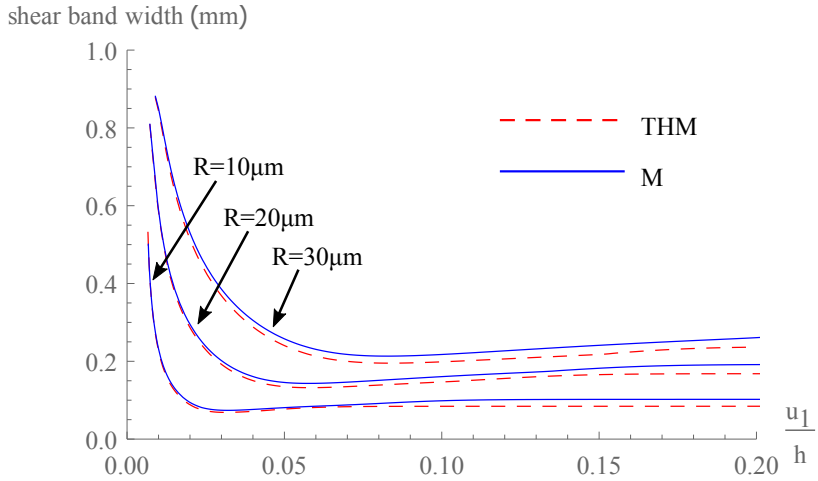

Figure 4.33: Effect of THM couplings on the shear band thickness evolution for an exponential hardening ($\mu_{res} = 0.3$ and $\gamma_e = 0.2$) and different internal lengths (R=10, 20 and 30 μm).

softening: 69 μm and 85 μm (Fig. 4.33). Thus, we can conclude that the localization process also depends on the history of the loading.

Finally, thermal pressurization does not greatly affect the shear band thickness when the material softening alone is significant (Fig. 4.33). However, if the mechanical behavior is perfectly plastic, no localization is observed unless THM couplings are considered and, therefore, the thermal pressurization plays a crucial role in the control of the size of the principal slip zone. In both cases, the internal length required to simulate a shear band thickness with a size in agreement with observations of the Punchbowl fault (see Section 4.2.4) is one order of magnitude larger than the mean grain size and is closer to D_{70} (mesh size corresponding to 70% of passing mass in sieve analysis). Note that most of the existing laboratory experiments and DEM simulations have been performed with a relatively narrow grain size distribution. For this case, taking a Cosserat length of the order of D_{50} is valid (see (Mühlhaus and Vardoulakis, 1987)). We expect in the future to bring new experimental results on the effect of wider grain size distribution on the shear band thickness.

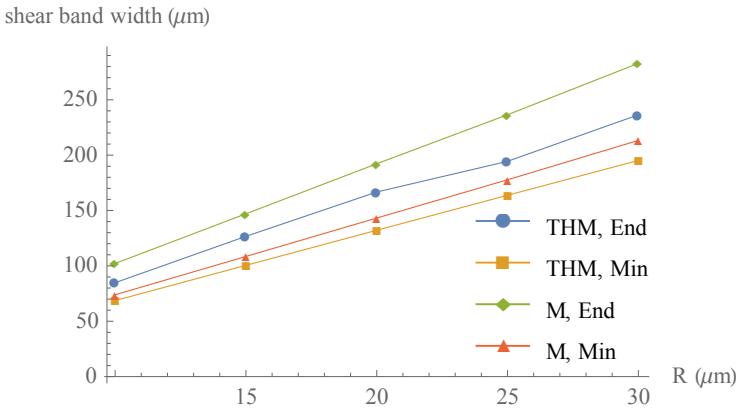

Figure 4.34: Effect of THM couplings on the evolution of the minimum shear band thickness and the residual one with the internal length.

4.4 Comparisons with results of the linear stability analysis

Strain localization is seen as an instability of the inelastic macroscopic constitutive laws. The initial homogeneous state becomes unstable (bifurcation) which triggers the onset of localization (Rudnicki and Rice, 1975b). Moreover, we can assess the size of the localized zone by analyzing the dominant wavelength of the perturbation modes. In (Rice et al., 2014), the system of equations presents a critical wavelength over which all perturbations are unstable. The band width is estimated as half the value of the critical wavelength. In Chapter 2 (see also (Sulem et al., 2011, Veveakis et al., 2013)) the use of a Cosserat continuum with inertia terms enables us to have a stability diagram (Lyapunov exponent

(Lyapunov, 1992) plotted versus the wavelength of the perturbation) that does not present a vertical asymptote. Thus, the shear band thickness is calculated from the value of the wavelength of the perturbation that grows the fastest (the maximum of the Lyapunov exponent).

In this section, we will compare the values of the shear band thickness obtained from the LSA and the one obtained from FEM computations. For that, at each time step of the numerical computation, we define an associated system of a homogeneous state for which LSA is performed. This associated homogeneous system is assumed to be in a softening state obtained from the slope of the numerical stress-strain (τ_{12} in function of u_1/h) curve at the considered time step. Moreover, this methodology which is explained in details in Appendix A.5, permits us to understand how the loss of homogeneity in the system further influences the evolution of the localization process.

4.4.1 Comparisons for mechanical simulations with linear softening

In this section, we compare the evolution of the shear band thickness obtained numerically as described in 4.2.3 with the one predicted by the linear stability analysis for purely mechanical examples and considering a linear evolution of the friction coefficient. The parameters chosen are defined in Section 4.2.1 and we study the effect of the internal length and the height of the layer on the comparison.

In Fig. 4.35, we compare the shear band thickness evolution obtained with LSA considering the minimum wavelength for which the system is unstable λ_{min} and the wavelength with the fastest growth λ_{max}. We observe that the shear band thickness evolution deduced from LSA considering λ_{min} is closer to the one obtained from FEM computations. Therefore, in the following the comparison will be performed on the basis of λ_{min} without specifying it in the graphs.

In Fig. 4.36, we consider internal lengths ranging from 10 μm to 30 μm and heights of the layer of 1 or 2 mm. For a height of 1mm and R=10μm (Fig. 4.36 (a)), the thickness obtained at the initiation of the localization process is identical for the LSA and the finite element simulation as this state of the layer is the closest to a homogeneous state of deformation as considered in the definition of the associated system for which the linear analysis is applied. Nevertheless, for R=20 and 30 μm and the same height (Fig. 4.36 (b) and (c)), we do not observe the same behavior. This apparent discrepancy is due to the height of the layer which is not sufficiently large to have vanishing couple stresses in the profile. The associated problem differs significantly from the original one in that case and leads to different values of the shear band thickness. For a height of 2mm (Fig. 4.36 (e) and (f)), this is no longer an issue and the size of the bands obtained at the nucleation by LSA and FEM match.

After the initiation of localization, the LSA tends to overestimate the thickness of the

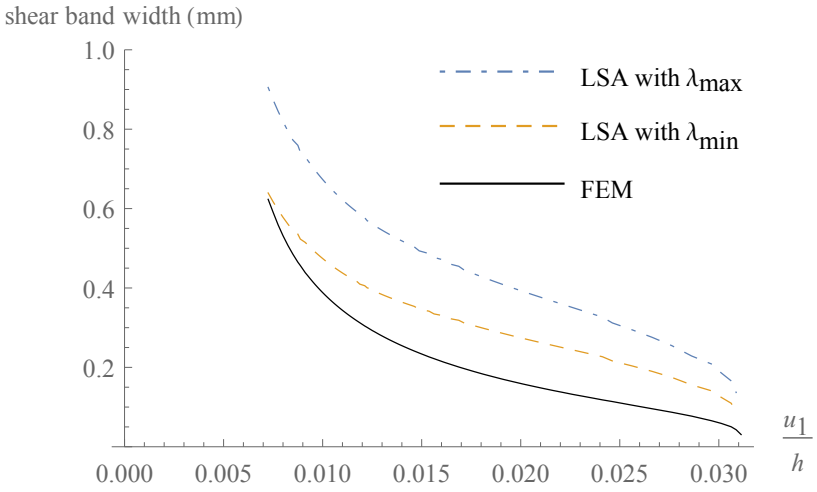

Figure 4.35: Comparisons of the shear band thickness evolution obtained by FEM, LSA with λ_{min} and LSA with λ_{max} for R=10μm, h=1mm using a linear evolution of the friction coefficient.

shear band, as the state of deformation in the original system is no longer homogeneous. Yet, the difference remains small and tends to decrease as the height of the layer increases, but if the height gets too large, we face convergence problems as the softening branch gets too steep. The tendency at the end of the numerical simulations to have a thickness that decreases to the value of the internal length is also captured by the LSA.

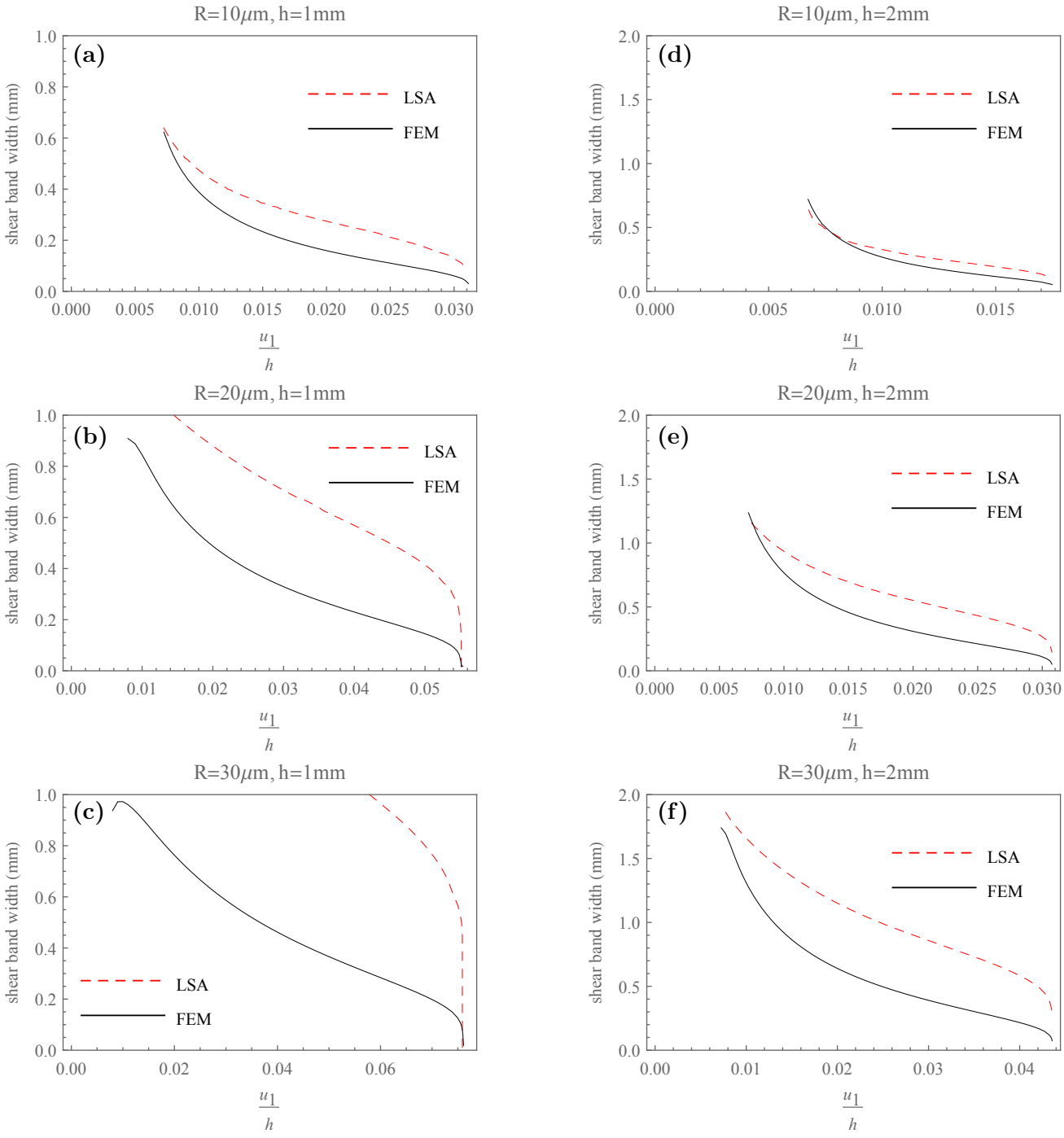

Figure 4.36: Comparisons of the shear band thickness evolution for internal lengths between 10 and 30 μm and two heights of the layer h, 1 and 2 mm using a linear evolution of the friction coefficient.

4.4.2 Comparisons for mechanical simulations with exponential hardening

The comparison between LSA and FEM is also made for the case of an exponential hardening evolution in Fig. 4.37 . The parameters and the results of the simulations are presented in Section 4.2.4. We consider here a residual friction coefficient of 0.3 and a factor in the exponential γ_e of 0.2. As in the preceding section, the analysis focuses on the effect of the internal length and of the height of the layer.

For the initiation of localization, we observe that the thicknesses predicted by the LSA fit well the numerical ones for internal lengths of 10 and 20 μm (Fig. 4.37 (a), (b), (d) and (e)). It is not the case for R=30 μm as the distribution of couple stress μ_{32} over the layer doesn't reach a value close to zero at the boundary, even for a height of 2 mm (Fig. 4.37 (c) and (f)). Note that in Fig. 4.37(d) (R=10μm and h=2mm), the y-axis ranges from 0 to 1mm. Indeed, the numerical results exhibit the formation of two symmetrical shear bands at a quarter and three quarters of the layer thickness. Therefore the comparison with LSA is performed by considering only half of the layer (of thickness 1mm) in order to capture only one band.

After the nucleation, the shear band size decrease is well captured by the LSA. But as the thickness approaches its minimum value, the two curves begin to diverge significantly. The level of deformation is higher than the one corresponding to a linear softening of the friction coefficient, which explains this apparent contradiction with the section above. Moreover, when the shear stress tends to the residual value, the hardening modulus tends to zero. Thus, the shear band thickness obtained by the linear analysis grows indefinitely.

4.4.3 Comparisons for THM simulations

The comparison of LSA and FEM results is then performed for the system of the infinite sheared layer considering Thermo-Hydro-Mechanical couplings with the set of parameters described in Table 4.3. Only one example for a linear evolution of the friction coefficient and one example for the exponential law are presented here.

In Fig. 4.38, the evolution of the shear band size is plotted for an internal length of 10 μm, a height of 1 mm and a hardening coefficient h_s=-0.5 assuming linear softening. The conclusions of section 4.4.1 remain the same.

In Fig. 4.39, the evolution of the shear band thickness is shown for an internal length of 10 μm, a height of 1 mm for an exponential softening with μ_{res}=0.3 and γ_e=0.2. The initiation and the decrease of the shear band size at the beginning of the localization process are well captured by the LSA. When the deformation increases, the two lines diverge as it is observed for the purely mechanical system. However, unlike the mechanical system, when the shear stress converges to a residual value and the hardening modulus tends to zero,

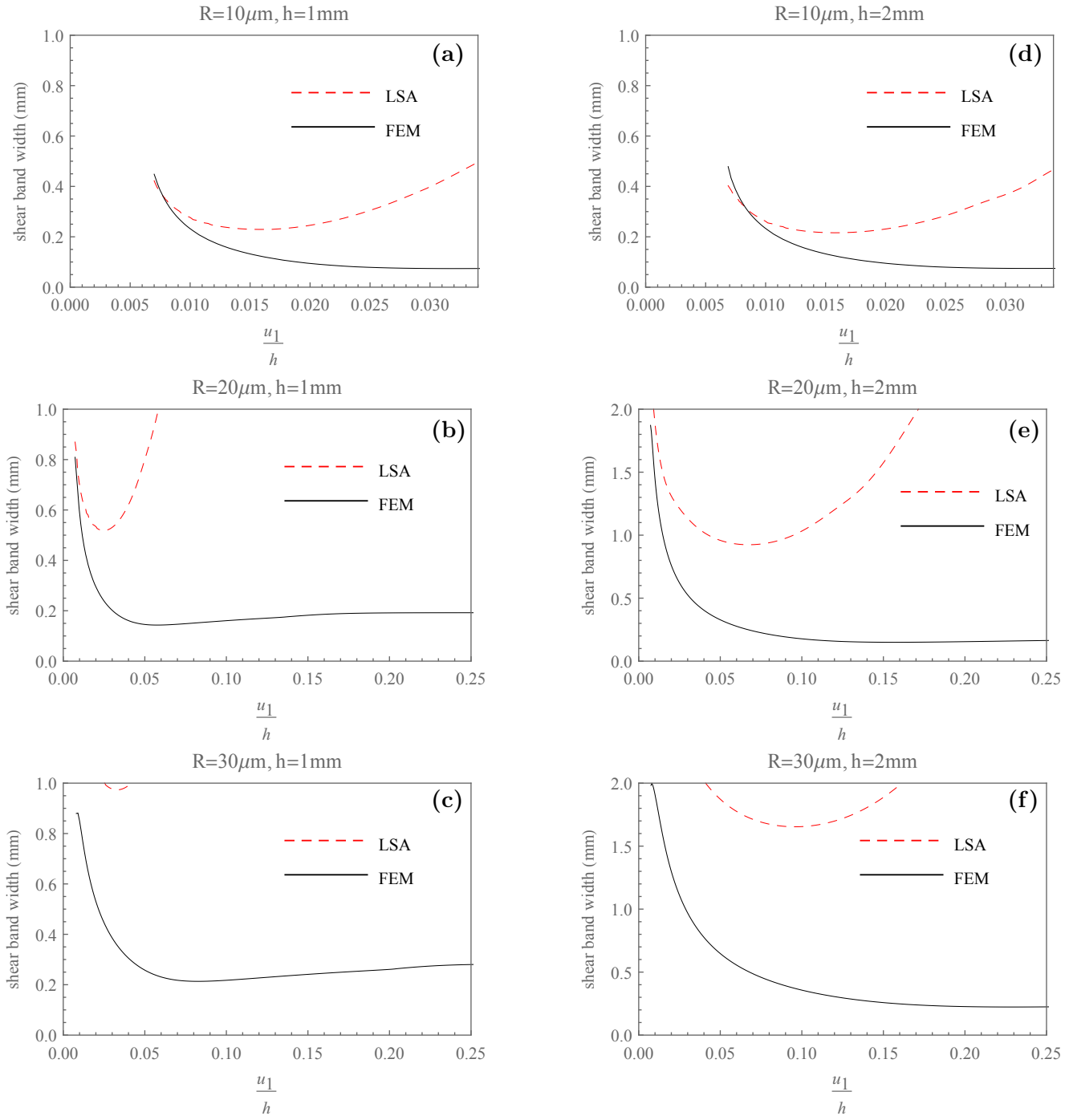

Figure 4.37: Comparisons of the shear band thickness evolution for internal lengths between 10 and 30 μm and two heights of the layer h, 1 and 2 mm using an exponential evolution of the friction coefficient.

the linear analysis tends to a finite value in the THM system because the bifurcation is obtained for a positive hardening modulus (see Chapter 2). This value is larger than the height of the layer and one order of magnitude larger than the residual thickness obtained numerically.

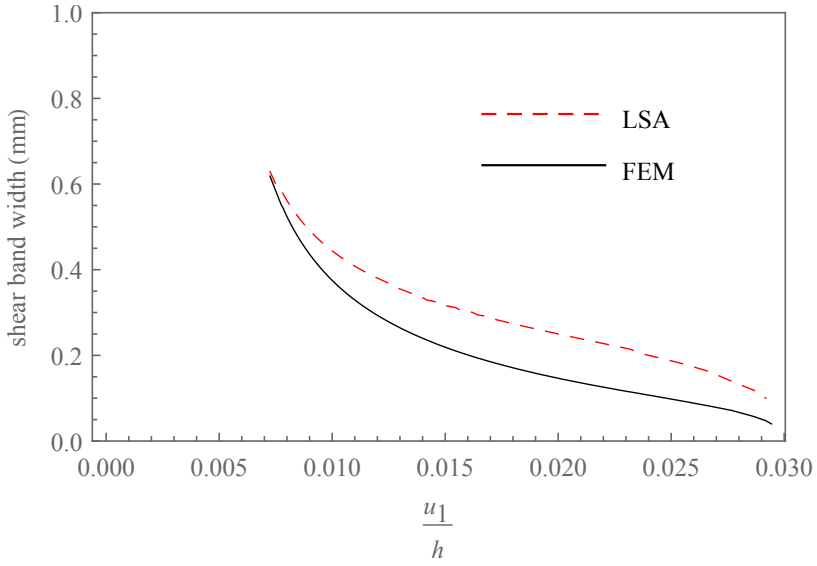

Figure 4.38: Comparisons of LSA and FEM results for the shear band thickness evolution for the THM model assuming an internal length $R = 10\mu$m, a height of 1 mm, a hardening coefficient $h_s = -0.5$ and using a linear evolution of the friction coefficient.

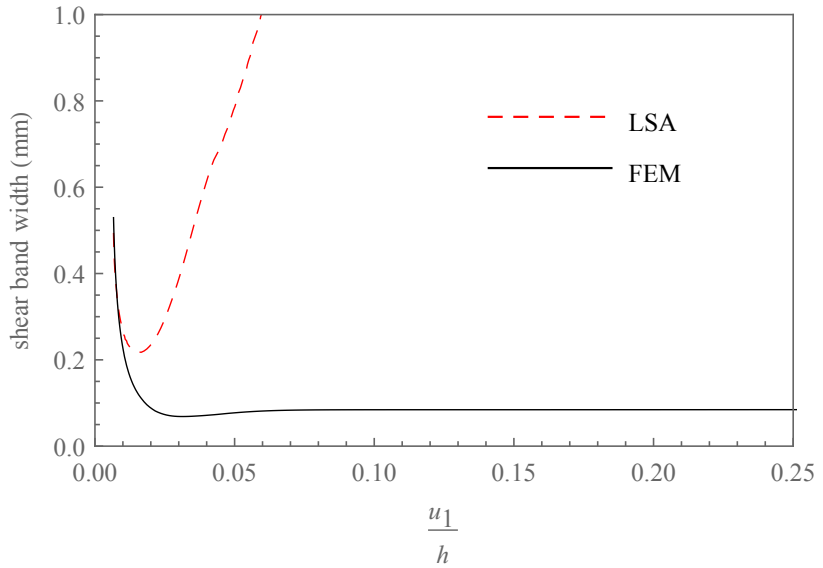

Figure 4.39: Comparisons of LSA and FEM results for the shear band thickness evolution for the THM model assuming an internal length $R = 10\mu m$, a height of 1 mm and using an exponential evolution of the friction coefficient ($\mu_{res} = 0.3$ and $\gamma_e = 0.2$).

4.5 Conclusion

In this chapter, the importance of using a continuum with microstructure to model a fault zone is shown. It enables to study the role of the microstructure on the localization process and on the energy budget. The influence of the constitutive parameters is investigated. For instance, the hardening (softening) modulus encapsulates and upscales various micromechanical phenomena and, together with the intrinsic Cosserat lengths, affects the stress-strain response. However, the roles of the hardening modulus and grain size are distinct. It is shown that the hardening modulus controls only the slope of the softening branch, while the grain size controls the slope and the localization thickness as well. Different softening laws are used and the most appropriate to model the granular nature of a fault gouge is an exponential decrease of the friction coefficient. This law can also be easily calibrated based on experimental data.

The thermal pressurization appears to be a mechanism that gradually destabilizes the system but is not active at the nucleation of the slip. It is shown that both the softening behavior and the shear band thickness depend on the applied velocity, despite the fact that the constitutive description of the material was considered rate-independent. Rate dependency observed for natural faults can be explained by a thermal and pore-pressure diffusions mechanism.

The comparison of the shear band thicknesses obtained from the linear stability analysis and the finite element simulations are compatible as long as the effects of the induced

perturbation of the initial homogeneous state are small enough. It highlights the relevance of using numerical simulations to study localization problems. They also provide an insight into the complete material response of the system, a key feature to determine the stability of a fault and the transition from aseismic to seismic slip.

In this study, we focus on the thermal pressurization phenomenon that has been shown to be prominent for seismic slips (Viesca and Garagash, 2015). Yet, the model can be extended to account for other weakening processes active in fault zones, such as grain cataclasis by varying the internal length of the model (Bauer, 2016) or chemical dissolution (Veveakis et al., 2013).

Conclusions and future work

4.6 Concluding remarks

Seismic slip takes place in a narrow, thin zone (PSZ), whose thickness plays a fundamental role regarding the behavior of ultracataclastic fault cores. In this Thesis we investigate the effects of the microstructure on the evolution of the thickness of the PSZ. The various Thermo-Hydro-Mechanical couplings that are fundamental during pre- and co-seismic slip of faults are also considered.

Our analysis is based on a three-dimensional Thermo-Hydro-Mechanical model for Cosserat continua. The latter allows to take into account in a direct way the size of the microstructure and its evolution. The model is a generalization of the (Mühlhaus and Vardoulakis, 1987, Vardoulakis and Sulem, 1995) model in three-dimensions (3D). Regarding the constitutive description of the fault gouge material, an elasto-plastic constitutive model is adopted. The constitutive description is general and can be calibrated from experimental tests. Our formulation extends the existing ones on Cosserat (Sulem et al., 2011, Iordache and William, 1998, Manzari, 2004, de Borst, 1991) as it is in three-dimensions and accounts for strong couplings between the involved fields, i.e. the temperature, the pore fluid pressure and mechanics. These couplings are derived on one hand by the mass and energy balance equations and on the other hand by the considered constitutive laws.

Bifurcation theory (Linear Stability Analysis) is applied on the coupled, non-linear Cosserat system of equations in order to extract the conditions for the onset of localization. The mathematical treatment of the equations is kept general in order (a) to show the differences with the classical approaches that use the acoustic tensor (Rudnicki and Rice, 1975b) or LSA (Benallal and Comi, 2003) and (b) to allow a variety of applications in geomechanics. However, the derived criteria are used here for studying the onset of localization in fault zones. It is worth mentioning also that the present work extends further the works of (Sulem et al., 2011, Veveakis et al., 2013) by investigating the evolution of the localized zone thickness and its dependency on various parameters such as the grain size, the hardening modulus, the porosity, the permeability, the pressurization coefficient and the normal stress. These parameters have competing effects on the size of the localization thickness, which is assessed from the wavelength of the perturbation with the maximum growth coefficient

(Lyapunov exponent).

The LSA shows that the localization zone thickness is directly scaled with the grain size. This means that the larger the grains are the larger the shear band becomes. This intrinsic, physical length scale is introduced by the material parameters of the Cosserat continuum, which can be experimentally determined. Two additional length scales are intrinsic to the presented model. These lengths emerge from the thermal and hydraulic diffusivities that control equally the shear band thickness. In particular the higher these diffusivites are the larger the localization zone becomes. Consequently, the permeability, which is directly related to the hydraulic diffusivity, influences the size of the shear band, i.e. a more permeable medium leads to a broader localization zone. Nevertheless, this effect is small in the range of typical gouge permeabilities.

The role of porosity is twofold regarding localization. Higher porosity commonly corresponds to higher permeability (e.g. Kozeny-Carman law). It also leads to a lower thermal pressurization coefficient. This latter has a more significant influence on the shear band thickness. Higher permeability and lower thermal pressurization coefficient both result in a broader thickness of the localized zone. On the other hand, higher porosity results in a higher mixture compressibility, which on the contrary leads to thinner localized zone. Of course the dominance of one or another of these competing mechanisms depends on the fault material. However, for the material parameters used here, a more porous material presents a narrower localization zone, because the effect of porosity on mixture compressibility is dominant. Nevertheless, the thermal pressurization is not only affected by the porosity but also by other material parameters and the analysis have shown that this parameter has a very significant influence on the localized zone thickness.

The shear band thickness also depends on the confining stress. Although the condition for localization is independent of the confining stress if we assume a linear yield criterion, it affects the shear band thickness. More specifically, large confining stress (e.g. deeper faults) leads to narrower PSZ.

The evolution of the friction coefficient during shearing has an impact on the shear band thickness development. The friction coefficient evolution is represented by the hardening modulus variation. A typical hardening modulus evolution for gouge material is considered herein and, combined with LSA, allows to follow the evolution of the localization zone during shearing. We observe a decrease of the shear band thickness at the beginning of the localization process, followed by a progressive increase towards a steady value. By assuming an exponential grain size reduction under shearing, which was taken into account by modifying the internal length of the model, a qualitative estimation of the effect grain cataclasis during slip is provided. It is shown that grain communition causes a decrease of the PSZ.

In order to complete the investigation carried out with the LSA, the three-dimensional

model of elasto-plastic Cosserat continuum with THM couplings is implemented numerically in a FEM code. This code allows to perform computations in parallel, which offers an important computational speed up. A detailed description of the implementation and validation is presented and can be used as guidelines for the implementation of a THM code.

The comparison of the shear band thicknesses obtained from the linear stability analysis and the finite element simulations have shown that the obtained values are comparable as long as long as the effects of the induced perturbation of the initial homogeneous state are small enough. It highlights the importance of the induced heterogeneities in the progressive localization process and the importance of using numerical simulations to obtain quantitative results when studying strain localization. Moreover, the numerical simulations provide fundamental information both on the stress-strain response, and also on the temperature and pore pressure evolution inside the PSZ.

As far as it concerns the role of the grain size, the numerical analyses corroborate the analytical findings of the LSA. Indeed, the numerical analyses show that the evolution of the thickness of the localization zone depends on the size of the grains of the fault core. The larger the grains are, the larger the shear band thickness is. Moreover, using an appropriate softening law for fault core materials, it is shown that the final residual thickness of the localization zone is proportional to the grain size.

The numerical analyses allow in addition the investigation of the stress-strain response of the system and its dependence on the size of the microstructure. The smaller the grain size is in our model, the steeper the softening branch becomes. This has a direct effect on earthquake nucleation and on the transition from aseismic to seismic slip (Scholz, 2002).

Given that the Cosserat continuum leads to a localization zone of finite thickness (contrary to the Cauchy continuum, cf. Section 4.2.2) it makes possible the investigation of the influence of the hardening modulus evolution on the shear band thickness. Different softening laws are used, including an exponential softening of the friction coefficient, which is adequate for modeling the mechanical behavior of fault gouges and can be calibrated based on experimental data. Hardening (softening) modulus encapsulates and upscales various micromechanical phenomena and, together with the intrinsic Cosserat lengths, affects the stress-strain response. However, the roles of the hardening modulus and grain size are distinct. It is shown that the hardening modulus controls only the slope of the softening branch, while the grain size controls the slope and the localization thickness as well.

Thermal pressurization is a destabilizing mechanism that is practically negligible at the nucleation phase of seismic slip. Its effect is rather noticed during rapid co-seismic slip, where temperature increases significantly due to friction. The magnitude of this phenomenon is described through the, so-called, thermal pressurization coefficient, which expresses the increase of pore pressure in the gouge due to temperature increase. The numerical anal-

yses confirm the qualitative results of the LSA (Chapter 2), and go further. Under high shearing deformation rates, it is shown that the thermal pressurization coefficient has a direct impact on the post peak evolution of the stress-strain response. In particular, increased softening is observed for higher values of the aforementioned coefficient, which is compatible to the fact that the localization zone is thinner as explained above. The effect of thermal pressurization is pronounced even when no-hardening/softening is considered, showing the significance of the mechanism in modeling the energy budget during seismic slip.

A substantial result exhibited in this Thesis is that both the softening, post-peak behavior and the shear band thickness depend on the applied velocity, showing thus rate dependency. This is despite the fact that the constitutive description of the material is assumed rate-independent. Thermal pressurization is again the central mechanism for this apparent rate-dependent behavior. In particular, the applied velocity controls the local dissipation rate due to friction and, consequently, the pore pressure increase rate. The pore pressure increase rate is controlled in parallel by the thermal and pore-pressure diffusion mechanisms, which introduce a characteristic time scale. Under high velocities the characteristic diffusion rate is small in comparison to the dissipation rate, which has as a result a more localized profile of deformation and a steeper post-peak softening branch. However, under low velocities, the diffusion mechanisms dominate leading to a homogeneous deformation profile and no softening, if perfect plasticity is chosen.

4.7 Perspectives

In this study, we focus on the role of the most prominent THM couplings related to seismic slip and of the microstructure. Yet, the present model can be extended to account for other weakening processes observed in fault zones:

- Grain cataclasis can be modeled by adequately varying the internal length of the Cosserat model (see Chapter 2), but it should be completed by a damage law that takes into account the evolution of mechanical properties with microstructure change.
- Chemical reactions can be taken into account by adding additional terms to the constitutive description of the Cosserat material and the mass and energy balance equations (Veveakis et al., 2013, Sulem and Famin, 2009b, Platt et al., 2015, Brantut and Sulem, 2012b).
- The flash heating phenomenon can also be incorporated into the model considering a thermal weakening into the plastic equations.

The above mentioned processes will provide a finer description of the main weakening mechanisms that take place at finer time and length scales and give valuable results regarding

seismic slip and energy dissipation.

Regarding the constitutive law, the architecture of the numerical implementation is general enough to allow more elaborated constitutive descriptions. For instance, depending on the available experimental data, more sophisticated rate independent or rate dependent elasto-(visco)-plastic laws (Forest et al., 1997) combined with damage can be used. In order to allow a more detailed description of the mechanical behavior of the fault gouge material. Moreover, based on adequate upscaling schemes, detailed micro-mechanical grain-by-grain simulations can be used in order to determine the effective Cosserat constitutive properties and their evolution with seismic slip.

The formulation of this model is limited to small deformations. However, valuable information about earthquake nucleation and seismic slip was obtained. Modeling seismic slip of large magnitude earthquakes which exceeds the centimetric scale is possible by extending our model to large deformations (Sievert et al., 1998). This seems to be straightforward by adopting an updated Lagrange framework.

The present work enabled to assess the influence of the microstructure on the stress-strain response and therefore on the energy dissipation during seismic slip. It is an on-going work to quantify the role of the various weakening mechanisms on the seismic energy budget. This will allow the comparison with field measurements of earthquakes and in this way to obtain more information about the seismic sources.

Finally, despite the fact that we focused in this Thesis on fault mechanics, the developed tools and theory are general and flexible to allow the study of other instability problems in geomechanics.

List of publications

Journal papers

- H. Rattez, I. Stefanou and J. Sulem. Thermo-Hydro-Mechanical couplings and strain localisation in 3D continua with microstructure. Part I: Theory and linear stability analysis. Submitted, 2017.
- H. Rattez, I. Stefanou, J. Sulem, M. Veveakis and T. Poulet. Thermo-Hydro-Mechanical couplings and strain localisation in 3D continua with microstructure. Part II: Numerical implementation and post-bifurcation analysis. Submitted, 2017.
- H. Rattez, I. Stefanou, J. Sulem, M. Veveakis and T. Poulet. Numerical analysis of strain localization in Rocks with THM couplings: Benchmark tests and microstructure. Submitted, 2017.
- H. Rattez, I. Stefanou and J. Sulem. Role of microstructure and Thermo-Hydro-Mechanical couplings in the fracture energy of fault zones. In preparation.
- H. Rattez, F. Disidoro and J. Sulem. Effect of chemical degradation on fault friction and slip stability: application to CO2 storage projects. In preparation.

Book chapter

- I. Stefanou, J. Sulem and H. Rattez. Cosserat approach to localization in geomaterials. In Handbook of Nonlocal Continuum Mechanics for Materials and Structures. Springer, 2017.

Conference papers

- H. Rattez, I. Stefanou, J. Sulem, M. Veveakis and T. Poulet. Effect of Thermo-Poro-Mechanical properties on the stability of faults. Biot Conference (2017).
- H. Rattez, I. Stefanou, J. Sulem, M. Veveakis and T. Poulet. Localization of deformation for shearing of a rock layer with Cosserat microstructure and different couplings. 11th International Workshop on Bifurcation and Degradation in Geomaterials, May 21 - 25, 2017, Limassol, Cyprus.

International Conferences (without proceedings)

- H. Rattez, I. Stefanou, J. Sulem, M. Veveakis and T. Poulet. Numerical analysis of strain localization in a Cosserat continuum with THM couplings. Poster presented in Biot 2017.
- H. Rattez, I. Stefanou, J. Sulem, M. Veveakis and T. Poulet. Localization of deformation in a fault gouge with Cosserat microstructure and THCM couplings. Oral presentation in Geoproc 2017.
- H. Rattez, I. Stefanou, J. Sulem, M. Veveakis and T. Poulet. Couplings involved in the weakening of faults: Comparison of linear stability and finite element analysis with field observations. Oral presentation in 27th ALERT Workshop, Aussois, October 2016.
- H. Rattez, I. Stefanou, J. Sulem, M. Veveakis and T. Poulet. Localization of deformation of a rock layer with multiphysical couplings. Poster presented in 31st Conference on Mathematical Geophysics, Paris, June 2016.
- H. Rattez, I. Stefanou and J. Sulem. Linear stability and post-bifurcation analyzes for localization of deformation of a rock layer with Cosserat microstructure. Oral presentation in ECCOMAS Congress 2016, Crete Island, June 2016.
- H. Rattez, I. Stefanou, J. Sulem, M. Veveakis and T. Poulet. Localization of deformation of a rock layer with multiphysical couplings. Poster presented in 31st Conference on Mathematical Geophysics, Paris, June 2016.
- H. Rattez, I. Stefanou and J. Sulem. Localization of deformation of undrained adiabatic shearing of a rock layer with Cosserat microstructure. Poster presented in the 26th ALERT Workshop, Aussois, October 2015.
- H. Rattez, I. Stefanou and J. Sulem. Effect of CO2 on fault friction and slip stability. Poster presented in 25th ALERT Workshop, Aussois, October 2014. Booklet of abstracts ISBN 978-2-9542517-2-1.

Remerciements and Aknowledgements

Le présent manuscrit est la tentative de regrouper plusieurs année de travail au laboratoire Navier de l'ENPC. Il est le fruit de toutes les interactions que j'ai pu avoir durant cette période. Je ne peux donc le conclure sans essayer de remercier de façon la plus exhaustive possible toutes les personnes qui m'ont entouré, soutenu et conseillé dans cette aventure.

Tout a commencé quand j'ai eu la chance d'assister pendant mon master au cours de mécanique des roches de Jean Sulem, ce qui m'a définitivement convaincu d'orienter mes recherches vers ce domaine. Je le remercie vivement pour avoir accepté de m'encadrer, pour ses nombreux conseils et sa patience. J'ai aussi eu la chance de travailler avec Ioannis Stefanou, qui m'a apportÃľ une aide précieuse. Merci pour tout le temps que tu m'as accordé pour discuter (souvent tard) de problèmes de convergence ou de bien d'autres sujets. Je n'aurais pu, je pense, être mieux encadré pour cette thèse.

Je voudrais ensuite remercier ceux qui ont permis à cette aventure de se terminer: le jury. It was a great honor to have them present for my defense and that they agreed to be associated with this thesis. First of all, I would like to thank the two reviewers, who have accepted the tedious work of reading and commenting my thesis: Dmitry Garagash and Samuel Forest. Thanks a lot for your interest in this work and your numerous comments. Je remercie Renaud Toussaint d'avoir présidé ce jury avec bienveillance. Merci également à Ahmed Benallal, et Frédéric Collin pour leurs précieuses remarques. Finally, I want to thank Manolis Veveakis for having me in Sydney for a few months, his priceless help, and to have made the travel from down under specially for my defense (I'd like to think so). Par la même occasion, je tiens à remercier Thomas Poulet, qui mâĂŹa conseillÃľ comme sâĂŹil faisait partie de mes encadrants. Ta gentillesse et tes suggestions m'ont beaucoup aidé.

Je tiens à remercier aussi sincèrement tous les personnes qui ont partagé mon quotidien au laboratoire dans la bonne humeur, aussi bien dans l'équipe du CERMES : Agustin, Philipp, Marcos, Sara, Hugo, Dong, Tri, Du, Lina, Sadek, Malik, Anaïs, Axelle, Benjamin, Edoardo, Manuel, Youssouf, Radja, Rawaz, Alexandre, Timos, Nick (merci pour toutes les corrections !), Rachida, Armelle, Sabrina, Manu, Hocine, Baptiste, Xavier, Marine, Jean-

Michel et Siavash. But I also had a great time in Sydney in the UGG team, thanks to the minions : Bec, Martin, Alex, Jessie, Lisa, Manman and Mustafa, and the other members: Sotiris and Klaus.

Je terminerai cette "séquence émotion" par remercier tous les amis et la famille pour leur soutien et tous les moments mémorables que j'ai vécu avec eux en dehors du laboratoire : Charles, Adrien, Emilien, Camille, Pierre (les deux), Kenan, Ron, Dimitri, Binault, Laura, Guillaume, Suzanne, Baudouin, Hélène, Pierre, Félix, Charlotte, Julia, Jean-Vivien, Seb, Loïc, Amandine, Lucille, Charles-Edouard, Pauline, Antoine, les butineurs, Lucile, Panagiotis, Maria, Manu, Sophie, Anne-marie, Sylvie, Mamie Monique, Aymeric, Noémie, Bruno, Agnès, Charles, Delphine et enfin Aurèle. Un grand merci à mes deux parents, bien sûr, sans qui je n'en serai pas là. Je concluerai par remercier la personne la plus importante et qui a le plus "subi" cette thèse: Gil.

Appendices

A.1 Link between different formulations of the mass balance equation

After writing the mass conservation for the fluid and the solid phase (see section 2.2.4), we obtain equations 2.12 and 2.13.

$$-\rho^s \frac{\partial n}{\partial t} + (1-n)\frac{\partial \rho^s}{\partial t} + \rho^s \ (1-n)V^s_{i,i} = 0 \tag{A.9}$$

$$\frac{n}{\rho^f}\frac{\partial \rho^f}{\partial t} + \frac{1-n}{\rho^s}\frac{\partial \rho^s}{\partial t} + V^s_{i,i} + \ (n(V^f_i - V^s_i))_{,i} = 0 \tag{A.10}$$

As $V^s_{i,i} = \dot{\varepsilon_v}$, Eqs. A.9 and A.10 can be written:

$$-\frac{1}{1-n}\frac{\partial n}{\partial t} + \frac{1}{\rho^s}\frac{\partial \rho^s}{\partial t} + \dot{\varepsilon_v} = 0 \tag{A.11}$$

$$\frac{n}{\rho^f}\frac{\partial \rho^f}{\partial t} + \frac{1-n}{\rho^s}\frac{\partial \rho^s}{\partial t} + \dot{\varepsilon_v} + \ (n(V^f_i - V^s_i))_{,i} = 0 \tag{A.12}$$

n represents the porosity of the current volume $d\Omega_t$, as it refers the current volume to the current configuration, it is called the Eulerian porosity (Coussy, 2004). In contrast, the Lagrangian porosity, written here ϕ, refers the current porous volume to the initial volume $d\Omega_{t0}$. We have the relationship:

$$n \ d\Omega_t = \phi \ d\Omega_{t0} \tag{A.13}$$

The hypothesis of infinitesimal transformations gives us the approximation:

$$d\Omega_{t0} \approx \frac{d\Omega_t}{1+\varepsilon_v} \approx d\Omega_t(1-\varepsilon_v) \tag{A.14}$$

If we insert Eq. A.14 in Eq. A.13, take the time derivative and neglect the second order

terms, we get the relationship between the variation of Lagrangian porosity and Eulerian porosity.

$$\dot{n} = \dot{\phi} - \phi\ \dot{\varepsilon_v} \tag{A.15}$$

From Eqs. A.11, A.13 and A.15, we have

$$\dot{\varepsilon_v} = \dot{\phi} - \frac{1-\phi}{\rho^s}\frac{\partial \rho^s}{\partial t} \tag{A.16}$$

$$\frac{\phi}{\rho^f}\frac{\partial \rho^f}{\partial t} + \frac{1-\phi}{\rho^s}\frac{\partial \rho^s}{\partial t} + \dot{\varepsilon_v} + \ (\phi(V_i^f - V_i^s))_{,i} = 0 \tag{A.17}$$

We can insert the expression of ε_v in Eq. A.16 into Eq. A.17.

$$\frac{\phi}{\rho^f}\frac{\partial \rho^f}{\partial t} + \dot{\phi} + \ (\phi(V_i^f - V_i^s))_{,i} = 0 \tag{A.18}$$

Following Rice (2006b), the porosity is then decomposed into its elastic and inelastic part $n = n^{el} + n^{ie}$. Thus,

$$\frac{\partial \phi}{\partial t} = \frac{\partial \phi^{el}}{\partial t} + \frac{\partial \phi^{ie}}{\partial t} = \phi\ \beta^n \frac{\partial p}{\partial t} + \phi\ \lambda^n \frac{\partial T}{\partial t} + \frac{\partial \phi^{ie}}{\partial t} \tag{A.19}$$

where β^n and λ^n are the compressibility and the thermal expansivity of the pore volume respectively.

$$\beta^n = \frac{\beta^d - \beta^s}{\phi} - \beta^s$$
$$\lambda^n = \lambda^s \tag{A.20}$$

where $\beta^d = 1/K$ is the drained compressibility. Finally, from Eqs. A.18, A.19, 2.15 and 2.16

$$\frac{\partial \mathrm{p}}{\partial t} = c^*_{hy}\ p_{,ii} + \Lambda \frac{\partial \mathrm{T}}{\partial t} - \frac{1}{\beta^{**}}\frac{\partial \phi^{ie}}{\partial t} \tag{A.21}$$

In Eq. A.21, $c^*_{hy} = \chi/(\eta^f \beta^{**})$ is the hydraulic diffusivity, $\beta^{**} = \phi(\beta^f + \beta^n)$ is the storage capacity, $\Lambda = (\lambda^f - \lambda^n)/(\beta^f + \beta^n)$ is the undrained thermal pressurization coefficient (Rice,

2006b).

A.2 Micro-mechanical considerations

In this section, we will follow the method presented in Mühlhaus and Vardoulakis (1987) to define the stress and plastic strain invariants for a granular medium modeled by a Cosserat continuum. The granular medium is represented by a random assembly of spheres with a radius R. If we consider two spheres in contact embedded in a continuum, which is defined by the fields u_i and ω_i^c, like in Fig. A.40, the relative displacement and rotation of the 2 particles is given by (for small rotations):

$$\begin{aligned} u_i^* - u_i &= 2R\ u_{i,j}\ n_j \\ \omega_{ij}^{c*} - \omega_{ij}^c &= 2R\ \omega_{ij,k}^c\ n_k \end{aligned} \tag{A.22}$$

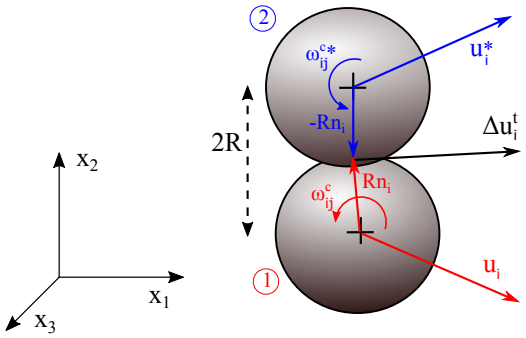

Figure A.40: Relative displacement and rotation for 2 grains in contact

We express the displacement of the different spheres at the contact point:

$$\begin{aligned} u_i^{(1)} &= u_i + R\ \omega_{ij}^c\ n_j \\ u_i^{(2)} &= u_i^* - R\ \omega_{ij}^{c*}\ n_j \end{aligned} \tag{A.23}$$

Thus the relative displacement at the contact point can be written:

$$\Delta u_i = u_i^{(2)} - u_i^{(1)} = 2R(u_{i,j} - \omega_{ij}^c - R\omega_{ij,k}^c\ n_k)\ n_j \tag{A.24}$$

or,

$$\Delta u_i = 2R(\gamma_{ij} + R\ e_{ijk}\ \kappa_{kl}\ n_l)\ n_j \tag{A.25}$$

And the tangential part, of the relative displacement:

$$\Delta u_i^t = 2R(\gamma_{ij} - \gamma_{pq}\ n_p\ n_q\ \delta_{ij} + R\ e_{ijk}\ \kappa_{kl}\ n_l)\ n_j \tag{A.26}$$

We can calculate its quadratic mean around a sphere of radius R, which defines a invariant measure of slip:

$$< \Delta u_i^t >= [\frac{1}{S}\int_s \Delta u_i^t \Delta u_i^t dS]^{1/2} \tag{A.27}$$

where S is the surface of the sphere. By using the following identities:

$$\begin{aligned} \int_s n_i n_j dS &= \frac{4\pi}{3} R^2 \delta_{ij} \\ \int_s n_i n_j n_k dS &= 0 \\ \int_s n_i n_j n_k n_l dS &= \frac{4\pi}{15} R^2 (\delta_{ij}\delta_{kl} + \delta_{ik}\delta_{jl} + \delta_{il}\delta_{jk}) \end{aligned} \tag{A.28}$$

we get,

$$< \Delta u_i^t >= \sqrt{\frac{16}{15}\, e_{ij}\, e_{ij} - \frac{4}{15}\, e_{ij}\, e_{ji} + R^2(\frac{16}{15}\, k_{ij}\, k_{ij} - \frac{4}{15}\, k_{ij}\, k_{ji})} \tag{A.29}$$

In order to retrieve the classical shear strain intensity $\sqrt{2\, e_{ij}\, e_{ij}}$ when the Cosserat effects vanishes ($e_{ij} = e_{ji}$ and $\kappa_{ij} \to 0$), the coefficients in Eq. A.29 are multiplied by a factor 5/2 (Vardoulakis, 2009). It results in the following definition for γ^p:

$$\begin{aligned} \gamma^p &= \sqrt{g_1\, e_{ij}\, e_{ij} + g_2\, e_{ij}\, e_{ji} + R^2(g_3\, k_{ij}\, k_{ij} + g_4\, k_{ij}\, k_{ji})} \\ g_1 = g_3 &= \frac{8}{3} \qquad and \qquad g_2 = g_4 = -\frac{2}{3} \end{aligned} \tag{A.30}$$

The expression of the shearing intensity τ that is dual in energy with γ^p is deduced from Eq. A.30. We set the plastic strain rate to be equal to the Lagrange multiplier and we obtain some conditions. Its final form is:

$$\tau = \sqrt{h_1\, s_{ij}\, s_{ij} + h_2\, s_{ij}\, s_{ji} + \frac{1}{R^2}(h_3\, m_{ij}\, m_{ij} + h_4\, m_{ij}\, m_{ji})}$$
$$h_1 = h_3 = \frac{2}{5} \qquad and \qquad h_2 = h_4 = \frac{1}{10} \tag{A.31}$$

A micro-mechanical model could also be developed by considering that the normal stresses acting on a elementary volume aren't uniform and, thus, introduce moments. This hypothesis is justified knowing that continuum with micro-structure present large gradients of stresses and their variation at the level of micro-structure can't be ignored.

By emphasizing the contact tractions over the periphery of grains, it results on a different definitions of the invariants (Sulem and Vardoulakis, 1990) (Mühlhaus and Vardoulakis, 1987). It is called the "static" Cosserat model.

A.3 Determination of the shear band thickness

In this paper, the plastic strain rate distribution in the layer, $\dot{\gamma}^p(x_2)$, is chosen to evaluate the shear band thickness, like previous numerical as it enables to follow the instantaneous evolution of the system (Platt et al., 2014, Hall et al., 2010). The function used to interpolate this field and determine from its expression the thickness is a Cosine function. However, it is not the only choice and previous authors have used a Gaussian shape approximation of the strain rate profile (Andrews, 2002, Noda et al., 2009, Garagash, 2012, Platt et al., 2014, Rempel and Rice, 2006) at each time step:

$$\dot{\gamma}^p(x_2) \approx \frac{A}{\sqrt{2\pi}D} e^{-\frac{1}{2}(\frac{x_2-Y}{D})^2} \tag{A.32}$$

where A is the amplitude of the maximum plastic strain rate, D is the standard deviation of the Gaussian distribution and Y is the position of the center. From the fitting of $\dot{\gamma}^p(x_2)$ with this Gaussian shape function, we define the shear band thickness as twice the full width at half maximum $2\sqrt{2ln(2)}D$.

The trigonometric interpolating function used in the paper is defined by:

$$\dot{\gamma}^p(x_2) \approx B.\chi_{[Y-\frac{\lambda}{2};Y+\frac{\lambda}{2}]}(x_2).[\cos(2\pi\frac{(x_2-Y)}{\lambda}) + 1] \tag{A.33}$$

where B is twice the maximum plastic strain rate, Y is the position of the center, λ is the wavelength of the cosine function and $\chi_{[Y-\frac{\lambda}{2};Y+\frac{\lambda}{2}]}(x_2)$ is a rectangular function defined by:

$$\chi_{[Y-\frac{\lambda}{2};Y+\frac{\lambda}{2}]}(x_2) = \begin{cases} 1 & \text{if } x_2 \in [Y-\frac{\lambda}{2}; Y+\frac{\lambda}{2}] \\ 0 & \text{otherwise} \end{cases} \tag{A.34}$$

As stated in the paper, the wavelength of the cosine function is interpreted directly as the shear band thickness and allows a clearer link with results of the linear stability analysis (Rattez et al., 2017).

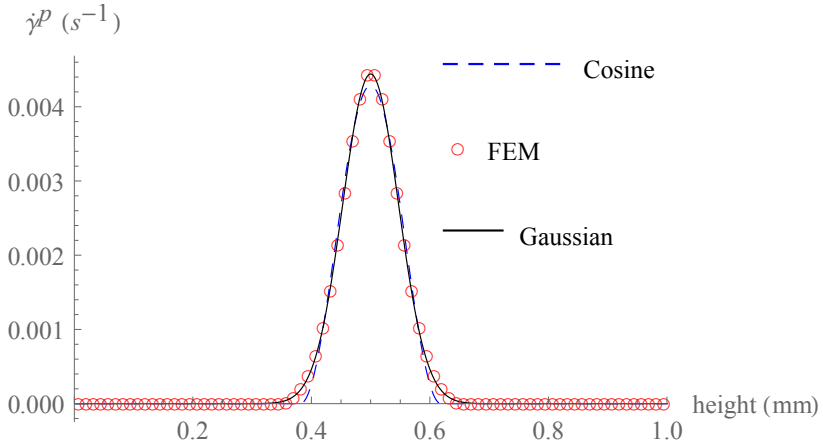

Figure A.41: Interpolation of $\dot{\gamma}^p(x_2)$ with a Gaussian and a cosine functions for $\tau_{12} = 48$ MPa in the example presented in Section 4.2.1

In Fig. A.41, we notice that the interpolation by the two different functions are very similar. To evaluate the goodness of the fit, we determine the adjusted coefficient of determination at each time step in the plastic regime. The mean value over the full localization process of this coefficient for the Gaussian fit is 0.983, whereas the mean value for the cosine fit is 0.995.

In Fig. A.42, the shear band width evaluated by both approximations is shown for the example of Section 4.2.1, with a mesh of 80 elements. Furthermore, we have plotted the size of the plastic zone (the zone defined by $F = 0$ (see Eq. 4.1). All curves exhibit the same tendency: a progressive decrease of the size of the band with accumulated slip. In the paper, the shear band thickness is computed using the Cosine function, as the adjusted coefficient of determination is better.

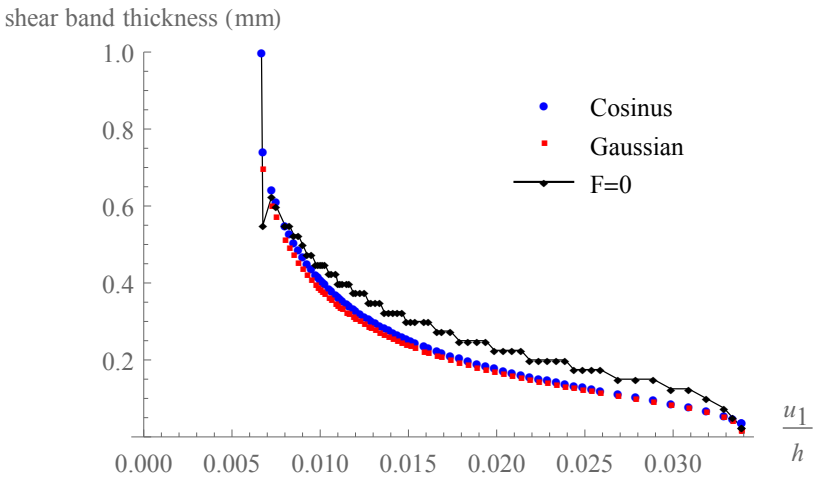

Figure A.42: Interpolation of $\dot{\gamma}^p(x_2)$ with a Gaussian and a Cosine function for the last timestep of the example presented in Section 4.2.1

A.4 Influence of the boundary conditions

The above numerical results are obtained by imposing zero rotations at the upper and lower boundaries of the layer. This type of boundary condition leads to the formation of a boundary layer in the elastic regime at the top and bottom edges. Consequently, no imperfection in the plastic regime is needed to trigger the localization (de Borst, 1991, Ebrahimian et al., 2012). Moreover, it makes the comparison between the different computations easier as the shear band always develops in the middle, where the rotations can freely develop (see Fig.4.3).

In Fig. A.43, we present the results of computations imposing a zero moment boundary condition ($\mu_{32} = 0$) at the top and bottom of the layer. These results are compared with the ones obtained when zero Cosserat rotation is imposed at the boundary $\omega_3^c = 0$. The influence of the position of an imperfection is explored by inserting notches in the geometry. We observe that without any imperfection, numerical errors are sufficient to trigger the localization, which occurs a bit later (in terms of deformation) as compared to the case with zero rotation imposed at the boundary. The position of the shear band is determined by numerical approximations and in general is not located in the middle of the layer (Fig. A.44 (a)). The form of the softening branch in the post localization regime looks the same as only one band develops. To overcome this issue, a notch of 10μm in the middle and at one quarter of the layer is introduced to trigger the localization from the beginning of the softening branch and at the location of the notch (de Borst, 1991).

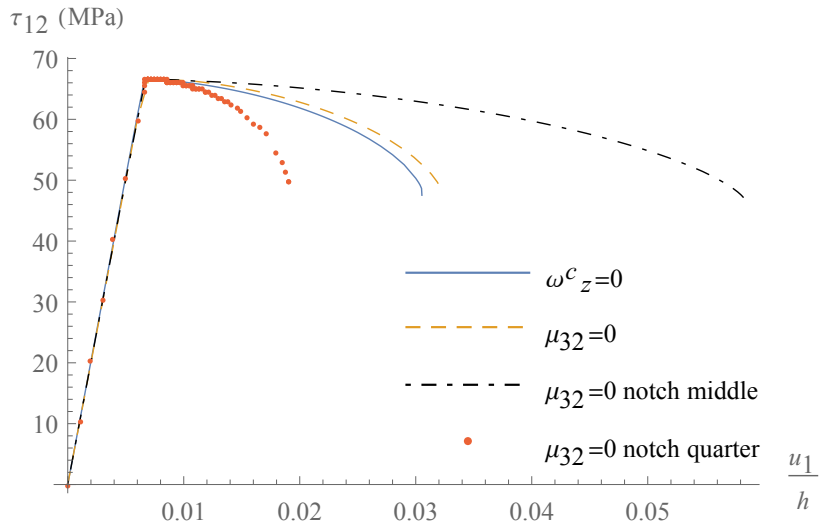

Figure A.43: Effect of the Boundary conditions on the stress-strain diagram

In the example with a notch at one quarter of the layer and zero moment boundary condi-

tions, the shear band develops at the upper boundary (Fig. A.44 (c)). The notch provokes the initiation of the shear band, but the band migrates then to the upper boundary. Thus, only half a band dissipates the energy of the system. This explains why the softening branch gets much steeper.

Nevertheless if we put a notch in the middle, a band appears at the location of the notch and remains there, but we also observe the emergence of two half bands at the top and bottom boundaries (Fig. A.44 (b)). As two full bands in total dissipate the plastic energy in this case, the softening branch is less steep. Appearence of multiple shear bands is acceptable as the solution of the underlying non-linear mathematical problem is not unique, as explained in Chambon et al. (2001). In this paper, the authors have developed a random initialization of the directional searching algorithm to observe different possible solution of a problem in post-localization. As shown in Besuelle et al. (2006) for the case of biaxial loading, different patterns of localized solutions for the same problem are obtained after a random initialization, showing solutions with 1, 2 or 3 bands.

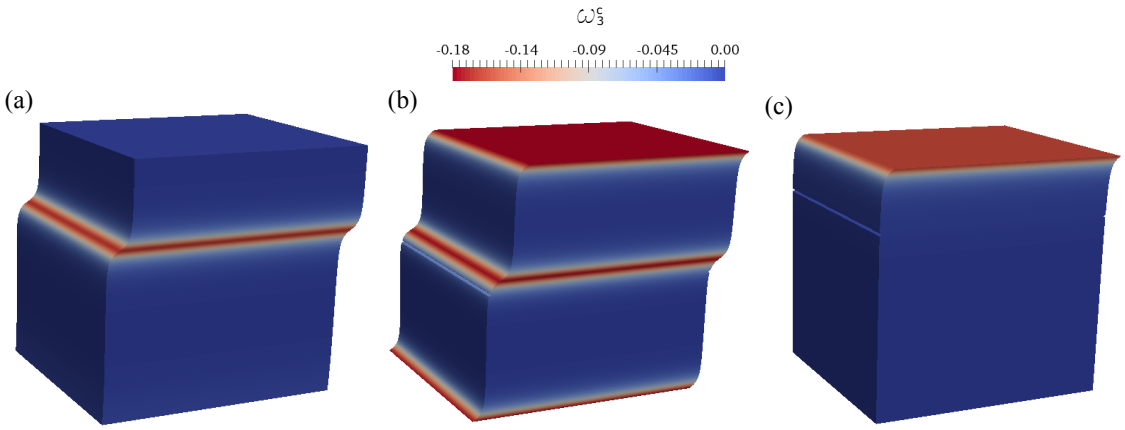

Figure A.44: Cosserat rotations, ω_3^c, plotted on the deformed mesh for $\tau_{12} = 47$MPa of each simulation with $\mu_{32} = 0$ imposed at the top and bottom of the layer and for: (a) no notch (b) a notch in the middle of the layer (c) a notch at the quarter of the layer.

A.5 Methodology to compare LSA and FEM shear band thickness

The methodology to assess the shear band thickness performing a Linear Stability Analysis (LSA) is widely developed in Chapter 2. In this section, we briefly describe the main results and explain how it is applied in order to compare with the numerical results described in Section 4.2.3.

The bifurcation parameter used for the Lyapunov stability analysis in the companion paper is the hardening modulus. For a value of this modulus, the study of the stability diagram enables to obtain an evaluation of the shear band thickness. The way this modulus develops during shearing is calculated from a stress-strain diagram obtained either from an experiment or a numerical simulation. Thus, the first step for the comparison consists in assessing the hardening modulus evolution for each numerical simulations.

In order to determine the hardening modulus evolution to insert in the LSA, some preliminary calculations are performed for compatibility of the homogeneous associated system for which the LSA is applied. The LSA in the companion paper is performed considering boundary conditions for the perturbation to the layer defined as $\mu_{32} = 0$. In other words, the linear stability analysis is valid for a geometry that has no Cosserat effects at its boundary. To fulfil this condition, the evolution of profiles for the shear stresses τ_{12}, τ_{21} and the couple stresses μ_{32} are plotted (see Fig. A.45). From these profiles, we can extract of value of the effective height h^* used to calculate the deformation. h^* is defined as the minimum distance between the points for which μ_{32} is less than 0.1% of the maximum absolute value.

The global deformation for the associated system is then calculated using the formula $\gamma_{12}^* = \frac{u_1(\frac{h-h^*}{2}) - u_1(\frac{h+h^*}{2})}{h^*}$. The elastic part of the deformation is retrieved by $\gamma_{12}^{*e} = \frac{\tau_{12}}{G}$. The plastic part of the shear deformation is calculated by $\gamma_{12}^{*p} = \gamma_{12}^* - \gamma_{12}^{*e}$ and is equal to the generalized plastic shear strain γ^{*p} with the assumptions of small perturbations from the homogeneous state (Cauchy continuum). Furthermore, outside of the shear band, where Cosserat effects are negligible ($\tau_{12} \approx \tau_{21}$ and $\mu_{32} \approx 0$), the generalized shear stress τ is equal to the shear stress τ_{12}. We can therefore plot the $\tau - \gamma^p$ diagram and from the slope of this diagram obtain an effective hardening modulus that can be used for the LSA (see Fig. A.46).

In order to evaluate the shear band thickness in the companion paper from the linear stability analysis, THM couplings and inertia terms are considered. But these assumptions are not fulfilled for all numerical simulations. When only THM couplings are taken into account(but not the inertia), the stability diagram presents a asymptote instead of a

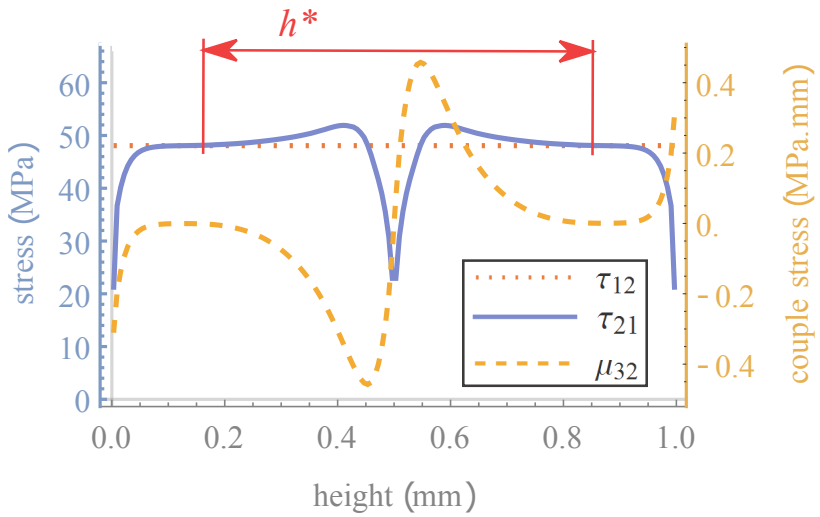

Figure A.45: Profile of shear stresses τ_{12}, τ_{21} and couple stress μ_{32} for h_s=-0.5, $R = 10\mu$m at the last time step to illustrate the effective height for the calculation of the plastic strain.

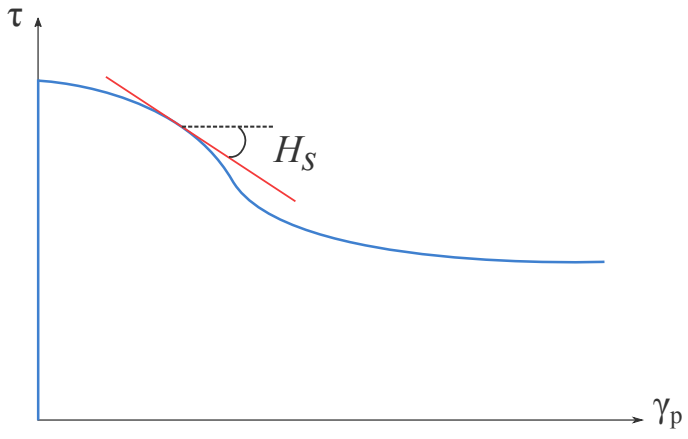

Figure A.46: Schematic diagram of the shear stress invariant versus plastic shear strain invariant showing the geometric interpretation of the hardening modulus H_s

maximum and the shear band thickness is the wavelength associated with the position of this asymptote (see Fig. A.47). If inertia terms are considered for the purely mechanical system, there is a maximum in the stability diagram. Without inertia, it is not possible to perform a LSA for this system as no temporal terms remain in the equations. Therefore, the diagram is plotted with inertia terms, and the values of the minimum unstable wavelength λ_{min} and the wavelength of fastest propagation λ_{max} are extracted (see Figs. A.48 and A.49).

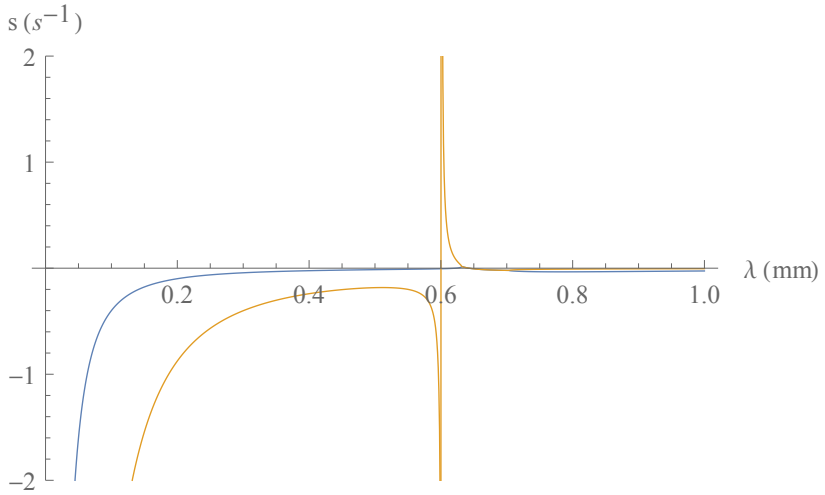

Figure A.47: Example of stability diagram for a THM example neglecting inertia terms showing an asymptote for λ=0.6mm ($H_s = -25$ MPa).

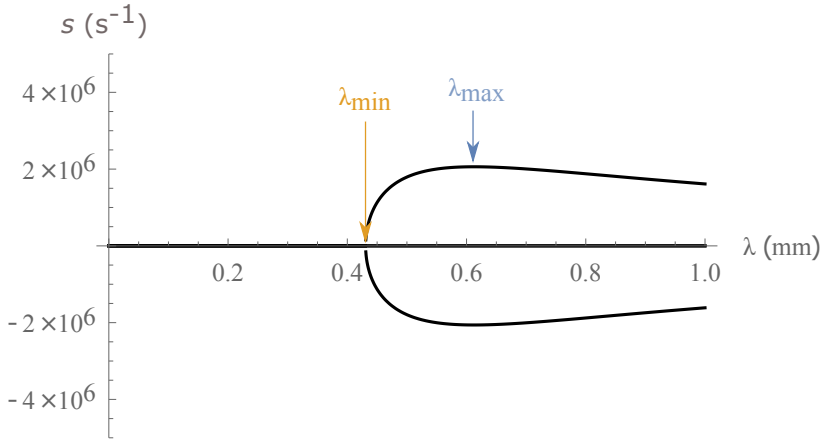

Figure A.48: Example of stability diagram for an isothermal, drained example considering inertia terms showing the wavelength selection ($H_s = -200$ MPa).

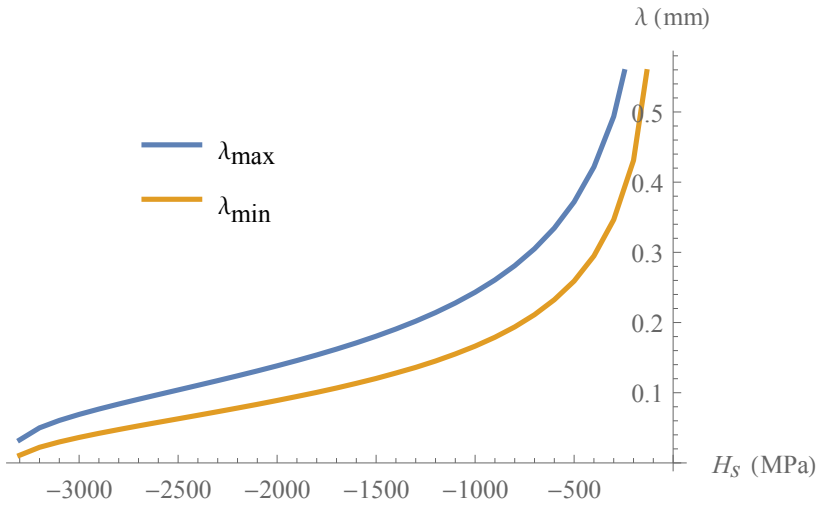

Figure A.49: Example of wavelengths selection evolution with hardening for an isothermal, drained example considering inertia terms.

Bibliography

M. I. Alsaleh. *Numerical Modeling of Strain Localization in Granular Materials Using Cosserat Theory Enhanced With Microfabric Properties*. PhD thesis, Louisiana State University, 2004.

L. J. An and C. G. Sammis. Particle size distribution of cataclastic fault materials from Southern California: A 3-D study. *Pure and Applied Geophysics PAGEOPH*, 143(1-3): 203–227, 1994. ISSN 00334553. doi: 10.1007/BF00874329.

M. Ando. Geological and geophysical studies of the Nojima Fault from drilling: An outline of the Nojima Fault zone probe. *The Island Arc*, 10(3-4):206–214, 2001. ISSN 10384871. doi: 10.1111/j.1440-1738.2001.00349.x.

D. J. Andrews. A fault constitutive relation accounting for thermal pressurization of pore fluid. *Journal of Geophysical Research: Solid Earth*, 107(B12):2363, 2002. ISSN 01480227. doi: 10.1029/2002JB001942. URL http://doi.wiley.com/10.1029/2002JB001942.

J. L. Anthony and C. J. Marone. Influence of particle characteristics on granular friction. *Journal of Geophysical Research B: Solid Earth*, 110(8):1–14, 2005. ISSN 01480227. doi: 10.1029/2004JB003399.

F. Armero and J. Park. An analysis of strain localization in a shear layer under thermally coupled dynamic conditions. Part 1: Continuum thermoplastic models. *International Journal for Numerical Methods in Engineering*, 56(14):2069–2100, 2003. ISSN 00295981. doi: 10.1002/nme.655.

S. Balay, S. Abhyankar, M. F. Adams, J. Brown, P. Brune, K. Buschelman, L. Dalcin, V. Eijkhout, W. D. Gropp, D. Kaushik, M. G. Knepley, L. McInnes, K. Rupp, B. F. Smith, S. Zampini, and H. Zhang. PETSc Users Manual. Technical report, 2017.

J. P. Bardet. A comprehensive review of strain localization in elastoplastic soils. *Computers and Geotechnics*, 10(3):163–188, 1990. ISSN 0266352X. doi: 10.1016/0266-352X(90)90034-S.

E. Bauer. Simulation of the Influence of Grain Damage on the Evolution of Shear Strain Localization. In *Continuous Media with Microstructure 2*, pages 231–244. 2016. ISBN 978-3-319-28239-8. doi: 10.1007/978-3-319-28241-1.

T. Baumberger, P. Berthoud, and C. Caroli. Physical analysis of the state- and rate-dependent friction law. II. Dynamic friction. *Physical Review B*, 60(6):3928–3939, 1999. ISSN 0163-1829. doi: 10.1103/PhysRevB.60.3928. URL https://link.aps.org/doi/10.1103/PhysRevB.60.3928.

Y. Ben-Zion and C. G. Sammis. Characterization of Fault Zones. *Pure and Applied Geophysics*, 160(3):677–715, 2003. ISSN 0033-4553. doi: 10.1007/PL00012554.

A. Benallal. On localization modes in coupled thermo-hydro-mechanical problems. *Comptes Rendus Mécanique*, 333(7):557–564, 2005. ISSN 16310721. doi: 10.1016/j.crme.2005.05.005. URL http://linkinghub.elsevier.com/retrieve/pii/S1631072105000872.

A. Benallal and D. Bigoni. Effects of temperature and thermo-mechanical couplings on material instabilities and strain localization of inelastic materials. *Journal of the Mechanics and Physics of Solids*, 52(3):725–753, 2004. ISSN 00225096. doi: 10.1016/S0022-5096(03)00118-2.

A. Benallal and C. Comi. Perturbation growth and localization in fluid-saturated inelastic porous media under quasi-static loadings. *Journal of the Mechanics and Physics of Solids*, 51(5):851–899, 2003. ISSN 00225096. doi: 10.1016/S0022-5096(02)00143-6.

P. Besuelle, R. Chambon, and F. Collin. Switching deformations modes in post-localization solutions with a quasi-brittle material. *journal of materials and structures*, 1(7):1115–1134, 2006.

D. Bigoni and T. Hueckel. Uniqueness and Localization-I Associative and non associative elastoplasticity. *International Journel of Solid and Structures*, 28(2):197–213, 1991.

M. A. Biot and D. G. Willis. The elastic coefficients of the theory of consolidation. *Journal of Applied Mechanics*, 24:594–601, 1957. ISSN 01651250. doi: 10.1002/9780470172766.ch13. URL http://scholar.google.com/scholar?q=intitle:The+Elastic+Coefficients+of+the+Theory+of+Consolidation{#}0.

A. M. Boullier, E. C. Yeh, S. Boutareaud, S. R. Song, and C. H. Tsai. Microscale anatomy of the 1999 Chi-Chi earthquake fault zone. *Geochemistry, Geophysics, Geosystems*, 10 (3), 2009. ISSN 15252027. doi: 10.1029/2008GC002252.

C. Boulton, L. Yao, D. R. Faulkner, J. Townend, V. G. Toy, R. Sutherland, S. Ma, and T. Shimamoto. High-velocity frictional properties of Alpine Fault rocks: Mechanical

data, microstructural analysis, and implications for rupture propagation. *Journal of Structural Geology*, 97:71–92, 2017. ISSN 01918141. doi: 10.1016/j.jsg.2017.02.003. URL http://dx.doi.org/10.1016/j.jsg.2017.02.003.

J. P. Boyd. *Chebyshev and Fourier Spectral Methods: second edition*. 2000.

W. Brace and J. D. Byerlee. Stick-slip as a mechanism for earthquakes. *Science*, 153(3739):990–2, aug 1966. ISSN 0036-8075. doi: 10.1126/science.153.3739.990. URL http://adsabs.harvard.edu/abs/1966Sci...153..990Bhttp://www.sciencemag.org/content/153/3739/990.short.

N. Brantut. *Couplages thermo-hydro-mécaniques et chimiques lors de la rupture et du glissement sismiques*. PhD thesis, 2010.

N. Brantut and J. Sulem. Strain Localization and Slip Instability in a Strain-Rate Hardening, Chemically Weakening Material. *Journal of Applied Mechanics*, 79(3):031004, 2012a. ISSN 00218936. doi: 10.1115/1.4005880.

N. Brantut and J. Sulem. Strain Localization and Slip Instability in a Strain-Rate Hardening, Chemically Weakening Material. *Journal of Applied Mechanics*, 79(3):031004, 2012b. ISSN 00218936. doi: 10.1115/1.4005880. URL http://link.aip.org/link/JAMCAV/v79/i3/p031004/s1{&}Agg=doi.

N. Brantut and R. C. Viesca. The fracture energy of ruptures driven by flash heating. *Geophysical Research Letters*, 2017. ISSN 00948276. doi: 10.1002/2017GL074110. URL http://doi.wiley.com/10.1002/2017GL074110.

N. Brantut, A. Schubnel, J. N. Rouzaud, F. Brunet, and T. Shimamoto. High-velocity frictional properties of a clay-bearing fault gouge and implications for earthquake mechanics. *Journal of Geophysical Research: Solid Earth*, 113(10), 2008. ISSN 21699356. doi: 10.1029/2007JB005551.

N. Brantut, J. Sulem, and A. Schubnel. Effect of dehydration reactions on earthquake nucleation: Stable sliding, slow transients, and unstable slip. *Journal of Geophysical Research: Solid Earth*, 116(5):1–16, 2011. ISSN 21699356. doi: 10.1029/2010JB007876.

N. Brantut, I. Stefanou, and J. Sulem. Dehydration-induced instabilities at intermediate depths in subduction zones. *Journal of Geophysical Research: Solid Earth*, 122(8):6087–6107, aug 2017. ISSN 21699313. doi: 10.1002/2017JB014357.

J. C. Butcher. A history of Runge-Kutta methods. *Applied Numerical Mathematics*, 20:247–260, 1996. ISSN 01689274. doi: 10.1016/0168-9274(95)00108-5. URL file:///C:/Users/hadrien.rattez/Downloads/00b49533d801c0674a000000.pdf.

F. Cappa. Impact of CO2 geological sequestration on the nucleation of earthquakes. *Geophysical Research Letters, 38, L17313, 2011*, sep 2012. URL http://escholarship.org/uc/item/15f9x6mp{#}page-12.

S. M. Cashman, J. N. Baldwin, K. V. Cashman, K. Swanson, and R. Crawford. Microstructures developed by coseismic and aseismic faulting in near-surface sediments, San Andres fault, California. *Geology*, 35(7):611–614, 2007. ISSN 00917613. doi: 10.1130/G23545A.1.

G. Chambon, J. Schmittbuhl, and A. Corfdir. Laboratory gouge friction: Seismic-like slip weakening and secondary rate- and state-effects. *Geophysical Research Letters*, 29(10): 4, 2002. ISSN 00948276. doi: 10.1029/2001gl014467.

G. Chambon, J. Schmittbuhl, and A. Corfdir. Frictional response of a thick gouge sample: 2. Friction law and implications for faults. *Journal of Geophysical Research: Solid Earth*, 111(9):1–12, 2006. ISSN 21699356. doi: 10.1029/2004JB003339.

R. Chambon, S. Crochepeyre, and R. Charlier. An algorithm and a method to search bifurcation points in non-linear problems. *International Journal for Numerical Methods in Engineering*, 51(3):315–332, 2001. ISSN 00295981. doi: 10.1002/nme.199.

R. Chambon, D. Caillerie, and G. Viggiani. Loss of uniqueness and bifurcation vs instability: some remarks. *Revue Française de Génie Civil*, 8(5-6):517–535, 2004. ISSN 1279-5119. doi: 10.1080/12795119.2004.9692618.

K. Chatzis and M. Brocato. Les frères Cosserat : brève introduction à leur vie et à leurs travaux en mécanique. Introduction., 2009. URL https://halshs.archives-ouvertes.fr/halshs-00543775.

F. M. Chester and J. S. Chester. Ultracataclasite structure and friction processes of the Punchbowl fault, San Andreas system, California. *Tectonophysics*, 295(1-2):199–221, 1998. ISSN 00401951. doi: 10.1016/S0040-1951(98)00121-8.

J. S. Chester, F. M. Chester, and A. K. Kronenberg. Fracture surface energy of the Punchbowl fault, San Andreas system. *Nature*, 437(7055):133–136, 2005. ISSN 14764687. doi: 10.1038/nature03942.

C. Collettini, B. M. Carpenter, C. Viti, F. Cruciani, S. Mollo, T. Tesei, F. Trippetta, L. Valoroso, and L. Chiaraluce. Fault structure and slip localization in carbonate-bearing normal faults: An example from the Northern Apennines of Italy. *Journal of Structural Geology*, 67:154–166, 2014. ISSN 01918141. doi: 10.1016/j.jsg.2014.07.017.

F. Collin, R. Chambon, and R. Charlier. A finite element method for poro mechanical modelling of geotechnical problems using local second gradient models. *International*

Journal for Numerical Methods in Engineering, 65(11):1749–1772, 2006. ISSN 00295981. doi: 10.1002/nme.1515.

N. Coltice, M. Gérault, and M. Ulvrová. A mantle convection perspective on global tectonics. *Earth-Science Reviews*, 165:120–150, 2017. ISSN 00128252. doi: 10.1016/j.earscirev.2016.11.006. URL http://dx.doi.org/10.1016/j.earscirev.2016.11.006.

J. W. Cooley and J. W. Tukey. An Algorithm for the Machine Computation of the Complex Fourier Series. *Mathematics of Computation*, 19:297, 1965.

F. H. Cornet, M. L. Doan, I. Moretti, and G. Borm. Forage au travers de la faille active d'Aigion : L'observatoire constitué par le puits AIG10. *Comptes Rendus - Geoscience*, 336(4-5):395–406, 2004. ISSN 16310713. doi: 10.1016/j.crte.2004.02.002.

E. Cosserat and F. Cosserat. *TheÌĄorie des corps deÌĄformables*. Hermann, 1909.

O. Coussy. *Poromechanics*. Wiley, 2004. ISBN 9780470849200.

S. C. Cowin. Stress Functions for Cosserat Elasticity. *International Journal of Solids and Structures*, 6(4):389–398, 1970.

J. Crank, P. Nicolson, and D. R. Hartree. A practical method for numerical evaluation of solutions of partial differential equations of the heat-conduction type, 1947. ISSN 0305-0041. URL http://acms.arizona.edu/FemtoTheory/MK{_}personal/opti547/literature/CNMethod-original.pdf.

R. de Borst. Simulation of Strain Localization: a Reappraisal of the Cosserat Continuum. *Engineering Computations*, 8(4):317–332, 1991. ISSN 0264-4401. doi: 10.1108/eb023842.

R. de Borst, L. Sluys, H.-B. Mühlhaus, and J. Pamin. Fundamental Issues in Finite Element Analyses of Localization of Deformation. *Engineering Computations*, 10(2):99–121, feb 1993. ISSN 0264-4401. doi: 10.1108/eb023897.

R. de Borst, M. A. Crisfield, J. J. C. Remmers, and C. V. Verhoosel. *Nonlinear Finite Element Analysis of Solids and Structures*. John Wiley & Sons, 2012. ISBN 1118376013.

N. De Paola, C. Collettini, D. R. Faulkner, and F. Trippetta. Fault zone architecture and deformation processes within evaporitic rocks in the upper crust. *Tectonics*, 27(4):1–21, 2008. ISSN 02787407. doi: 10.1029/2007TC002230.

G. Di Toro, G. Pennacchioni, and S. Nielsen. Pseudotachylytes and earthquake source mechanics. In *Fault-Zone Properties and Earthquake Rupture Dynamics, international Geophysics Series*, volume 94, pages 87–133. 2009. ISBN 0074-6142. doi: 10.1016/S0074-6142(08)00005-3.

G. Di Toro, A. Niemeijer, A. Tripoli, S. Nielsen, F. Di Felice, P. Scarlato, G. Spada, R. Alessandroni, G. Romeo, G. Di Stefano, S. Smith, E. Spagnuolo, and S. Mariano. From field geology to earthquake simulation: A new state-of-The-art tool to investigate rock friction during the seismic cycle (SHIVA). *Rendiconti Lincei*, 21(Suppl. 1):95–114, 2010. ISSN 20374631. doi: 10.1007/s12210-010-0097-x.

G. Di Toro, R. Han, T. Hirose, N. De Paola, S. Nielsen, K. Mizoguchi, F. Ferri, M. Cocco, and T. Shimamoto. Fault lubrication during earthquakes. *Nature*, 471(7339):494–498, 2011. ISSN 0028-0836. doi: 10.1038/nature09838. URL http://www.nature.com/doifinder/10.1038/nature09838.

J. H. Dieterich. Modeling of rock friction: 1. Experimental results and constitutive equations. *Journal of Geophysical Research*, 84(B5):2161, 1979. ISSN 0148-0227. doi: 10.1029/JB084iB05p02161. URL http://doi.wiley.com/10.1029/JB084iB05p02161.

J. H. Dieterich. Constitutive properties of faults with simulated gouge. *Geophysical Monograph Series*, 24:103–120, 1981. URL http://www.agu.org/books/gm/v024/GM024p0103/GM024p0103.shtml.

X. Du Bernard, P. Eichhubl, and A. Aydin. Dilation bands: A new form of localized failure in granular media. *Geophysical Research Letters*, 29(24):29–1–29–4, 2002. ISSN 00948276. doi: 10.1029/2002GL015966. URL http://doi.wiley.com/10.1029/2002GL015966.

B. Ebrahimian, A. Noorzad, and M. I. Alsaleh. Modeling shear localization along granular soil-structure interfaces using elasto-plastic Cosserat continuum. *International Journal of Solids and Structures*, 49(2):257–278, 2012. ISSN 00207683. doi: 10.1016/j.ijsolstr.2011.09.005.

J. T. Engelder. Cataclasis and the Generation of Fault Gouge. *Geological Society of America Bulletin*, 85(10):1515, 1974. doi: 10.1130/0016-7606(1974)85<1515:CATGOF>2.0.CO;2.

S. Forest and E. Lorentz. Localization phenomena and regularization methods. In J. Besson, editor, *Local Approach to Fracture*, volume 1, pages 311–371. Ecole des Mines de ParisâĂŞLes Presses, 2004.

S. Forest, G. Cailletaud, and R. Sievert. A Cosserat theory for elastoviscoplastic single crystals at finite deformation, 1997.

J. Fourier. *Théorie analytique de la chaleur*. 1822. URL http://www.gabay-editeur.com/FOURIER-Theorie-analytique-de-la-chaleur-1822.

E. Fukuyama. *Introduction: Fault-zone properties and earthquake rupture dynamics*, volume 94. Elsevier Inc., 1 edition, 2009. ISBN 9780123744524. doi: 10.1016/S0074-6142(08)00001-6. URL http://dx.doi.org/10.1016/S0074-6142(08)00001-6.

W. Gan and C. Frohlich. Gas injection may have triggered earthquakes in the Cogdell oil field, Texas. *... of the National Academy of Sciences*, 2013. doi: 10.1073/pnas.1311316110/-/DCSupplemental.www.pnas.org/cgi/doi/10.1073/pnas.1311316110. URL http://www.pnas.org/content/110/47/18786.short.

D. I. Garagash. Seismic and aseismic slip pulses driven by thermal pressurization of pore fluid. *Journal of Geophysical Research: Solid Earth*, 117(4), 2012. ISSN 21699356. doi: 10.1029/2011JB008889.

D. I. Garagash and J. W. Rudnicki. Shear heating of a fluid-saturated slip-weakening dilatant fault zone: 1. Limiting regimes. *Journal of Geophysical Research*, 108(B22121): 1–19, 2003. ISSN 0148-0227. doi: 10.1029/2002JB002218.

D. Gaston, C. Newman, G. Hansen, and D. Lebrun-Grandié. MOOSE: A parallel computational framework for coupled systems of nonlinear equations. *Nuclear Engineering and Design*, 239(10):1768–1778, 2009. ISSN 00295493. doi: 10.1016/j.nucengdes.2009.05.021.

D. R. Gaston, J. W. Peterson, C. J. Permann, D. Andrs, A. E. Slaughter, and J. M. Miller. Continuous integration for concurrent computational framework and application development. *Journal of Open Research Software*, 2(1):1–6, 2014. doi: http://dx.doi.org/10.5334/jors.as. URL http://files.figshare.com/1193732/moose{_}wssspe13.pdf.

P. Germain. The Method of Virtual Power in Continuum Mechanics. Part 2: Microstructure. *SIAM Journal on Applied Mathematics*, 25(3):556–575, 1973a.

P. Germain. La méthodes des puissances virtuelles en mécanique des milmieux continus - 1. Théorie du second gradient. *Journal de Mecanique Theorique et Appliquee*, 12(2): 235–274, 1973b.

S. Ghabezloo and J. Sulem. Stress dependent thermal pressurization of a fluid-saturated rock. *Rock Mechanics and Rock Engineering*, 42(1):1–24, may 2009. ISSN 0723-2632. doi: 10.1007/s00603-008-0165-z.

G. K. Gilbert. A theory of the earthquakes of the Great Basin, with a practical application. *American Journal of Science*, s3-27(157):49–53, 1884. ISSN 0002-9599. doi: 10.2475/ajs.s3-27.157.49. URL http://www.ajsonline.org/content/s3-27/157/49.citation$\delimiter"026E30F$nhttp://www.biodiversitylibrary.org/item/119555{#}page/58/mode/1up.

M. Godio, I. Stefanou, K. Sab, and J. Sulem. Dynamic finite element formulation for Cosserat elastic plates. *International Journal for Numerical Methods in Engineering*, 101(13):992–1018, 2015. doi: 10.1002/nme.4833>. URL https://hal.archives-ouvertes.fr/hal-01114343.

M. Godio, I. Stefanou, K. Sab, and J. Sulem. Multisurface plasticity for Cosserat materials: plate element implementation and validation. *International Journal for Numerical Methods in Engineering*, 2016. ISSN 00295981. doi: 10.1002/nme.5219.

Y. Gu and T. fong Wong. Development of shear localization in simulated quartz gouge: Effect of cumulative slip and gouge particle size. *Pure and Applied Geophysics PAGEOPH*, 143(1-3):387–423, 1994. ISSN 00334553. doi: 10.1007/BF00874336.

J. Hadamard. *Leçons sur la propagation des ondes et les équations de l'hydrodynamique*. Paris: Librairie scientifique A. Hermann, 1903.

B. H. Hager. Oceanic plate motions driven by lithospheric thickening and subducted slabs. *Nature*, 276:156–159, 1978. ISSN 00280836. doi: 10.1038/276156a0.

S. A. Hall, M. Bornert, J. Desrues, N. Lenoir, Y. Pannier, G. Viggiani, and P. Bésuelle. Discrete and continuum analysis of localised deformation in sand using X-ray μCT and volumetric digital image correlation. *Géotechnique*, 60(5):315–322, 2010. ISSN 0016-8505. doi: 10.1680/geot.2010.60.5.315.

R. Han, T. Hirose, and T. Shimamoto. Strong velocity weakening and powder lubrication of simulated carbonate faults at seismic slip rates. *Journal of Geophysical Research: Solid Earth*, 115(3), 2010. ISSN 21699356. doi: 10.1029/2008JB006136.

R. Heermance, Z. K. Shipton, and J. P. Evans. Fault structure control on fault slip and ground motion during the 1999 rupture of the Chelungpu fault, Taiwan. *Bulletin of the Seismological Society of America*, 93(3):1034–1050, 2003. ISSN 00371106. doi: 10.1785/0120010230.

T. Hirono, T. Yokoyama, Y. Hamada, W. Tanikawa, T. Mishima, M. Ikehara, V. Famin, M. Tanimizu, W. Lin, W. Soh, and S. R. Song. A chemical kinetic approach to estimate dynamic shear stress during the 1999 Taiwan Chi-Chi earthquake. *Geophysical Research Letters*, 34(19), 2007. ISSN 00948276. doi: 10.1029/2007GL030743.

M. Hu, M. Veveakis, T. Poulet, and K. Regenauer-Lieb. The Role of Temperature in Shear Instability and Bifurcation of Internally Pressurized Deep Boreholes. *Rock Mechanics and Rock Engineering*, pages 1–15, 2017. ISSN 07232632. doi: 10.1007/s00603-017-1291-2. URL "http://dx.doi.org/10.1007/s00603-017-1291-2.

W. Huang and E. Bauer. Numerical investigations of shear localization in a micro-polar hypoplastic material. *International Journal for Numerical and Analytical Methods in Geomechanics*, 27(4):325–352, 2003. ISSN 03639061. doi: 10.1002/nag.275.

M. J. Ikari, D. M. Saffer, and C. J. Marone. Frictional and hydrologic properties of clay-rich fault gouge. *Journal of Geophysical Research: Solid Earth*, 114(5):1–18, 2009. ISSN 21699356. doi: 10.1029/2008JB006089.

M.-M. Iordache and K. William. Localized failure analysis in elastoplastic Cosserat continua. *Computer Methods in Applied Mechanics and Engineering*, 151(3-4):559–586, 1998. ISSN 00457825. doi: 10.1016/S0045-7825(97)00166-7. URL http://www.sciencedirect.com/science/article/pii/S0045782597001667.

K. A. Issen and J. W. Rudnicki. Conditions for compaction bands in porous rock. *Journal of Geophysical Research: Solid Earth*, 105(B9):21529, 2000. ISSN 0148-0227. doi: 10.1029/2000JB900185. URL http://doi.wiley.com/10.1029/2000JB900185.

M. Jirasek. Modeling of Localized Inelastic Deformations. In *Lecture notes of a short course given at the Czech Technical University in Prague (9/7-11/2015)*, pages 1–338, 2015.

H. Kanamori and E. E. Brodsky. The physics of earthquakes. *Reports on Progress in Physics*, 67(8):1429–1496, aug 2004. ISSN 0034-4885. doi: 10.1088/0034-4885/67/8/R03.

H. Kanamori and L. Rivera. Energy Partitioning During an Earthquake. In *Earthquakes: Radiated Energy and the Physics of Faulting*, pages 3–13. American Geophysical Union, 2006. ISBN 9781118666272. doi: 10.1029/170GM03.

A. R. Khoei, S. Yadegari, and S. O. R. Biabanaki. 3D finite element modeling of shear band localization via the micro-polar Cosserat continuum theory. *Computational Materials Science*, 49(4):720–733, 2010. ISSN 09270256. doi: 10.1016/j.commatsci.2010.06.015.

B. S. Kirk, J. W. Peterson, R. H. Stogner, and G. F. Carey. libMesh : a C++ library for parallel adaptive mesh refinement/coarsening simulations. *Engineering with Computers*, 22(3-4):237–254, 2006. ISSN 0177-0667. doi: 10.1007/s00366-006-0049-3. URL http://link.springer.com/10.1007/s00366-006-0049-3.

S. Kramer. *Geotechnical earthquake engineering*. 1996. URL https://scholar.google.fr/scholar?cluster=18184087303499408938{&}hl=fr{&}oi=scholarr{&}sa=X{&}ei=mHv9VPqjJuTP7Qbeq4GgDw{&}sqi=2{&}ved=0CB8QgAMoADAA{#}0.

H. W. Kuhn and A. Tucker. Nonlinear Programming. *Proceedings of the Second Symposium on Mathematical Statistics and Probability*, (x):481–492, 1951. ISSN 01605682. doi: 10.1007/BF01582292. URL http://projecteuclid.org/euclid.bsmsp/1200500249.

A. H. Lachenbruch. Frictional Heating, Fluid Pressure, and the Resistance to Fault Motion. *Journal of Geophysical Research: Solid Earth*, 85(10):6097–6112, 1980.

A. H. Lachenbruch and J. H. Sass. Heat flow and energetics of the San Andreas Fault Zone. *Journal of Geophysical Research B*, 85(B11):6185–6222, 1980.

J. Lemaitre, J.-L. Chaboche, A. Benallal, and R. Desmorat. *Mécanique des matériaux solides-3eme édition*. Dunod, 2009. ISBN 978-2100516230.

D. Lesniewska and D. M. Wood. Advances in Bifurcation and Degradation in Geomaterials. *Geomechanics and Geoengineering*, 11:353–358, 2011. doi: 10.1007/978-94-007-1421-2. URL http://www.springerlink.com/index/10.1007/978-94-007-1421-2.

M. Lesueur, M. Casadiego, M. Veveakis, and T. Poulet. Modelling fluid-microstructure interaction on elasto-visco-plastic digital rocks. *Geomechanics for Energy and the Environment*, 12:1–13, 2017. ISSN 23523808. doi: 10.1016/j.gete.2017.08.001. URL http://dx.doi.org/10.1016/j.gete.2017.08.001.

B. Loret and J. Prevost. Dynamic strain localization in fluid-saturated porous media. *Journal of engineering mechanics*, 117(4):907–922, 1991.

S. Losh, L. Eglinton, M. Schoell, and J. Wood. Vertical and Lateral Fluid Flow Related to a Large Growth Fault, South Eugene Island Block 330 Field, Offshore Louisiana. *AAPG Bulletin*, 83(2):244–276, 1999. URL http://archives.datapages.com/data/bulletns/1999/02feb/0244/0244.htm.

A. M. Lyapunov. *The General Problem of the Stability of Motion (in Russian)*. PhD thesis, University of Kharkov, Kharkov Mathematical Society, 1892.

A. M. Lyapunov. The general problem of the stability of motion. *International Journal of Control*, 55(3):531–773, 1992. ISSN 0020-7179.

J. Mandel. Conditions de Stabilité et Postulat de Drucker. In *International Union of theoretical and applied Mechanics. Rheology and Soil Mechanics Symposium Grenoble, April 1-8, 1964.*, pages 58–68, 1966.

M. T. Manzari. Application of micropolar plasticity to post failure analysis in geomechanics. *International Journal for Numerical and Analytical Methods in Geomechanics*, 28 (10):1011–1032, 2004. ISSN 03639061. doi: 10.1002/nag.356.

C. J. Marone. Laboratory-Derived Friction Laws and Their Application To Seismic Faulting. *Annual Review of Earth and Planetary Sciences*, 26(1):643–696, may 1998. ISSN 0084-6597. doi: 10.1146/annurev.earth.26.1.643. URL http://www.annualreviews.org/doi/abs/10.1146/annurev.earth.26.1.643.

C. J. Marone and C. H. Scholz. The depth of seismic faulting and the upper transition from stable to unstable slip regimes. *Geophysical Research Letters*, 15(6):621–624, 1988.

C. J. Marone and C. H. Scholz. Particle-size distribution and microstructures within simulated fault gouge. *Journal of Structural Geology*, 11(7):799–814, 1989. ISSN 01918141. doi: 10.1016/0191-8141(89)90099-0.

R. M. May. Simple mathematical models with very complicated dynamics. *Nature*, 261 (5552):459–467, 1976. URL http://www.ncbi.nlm.nih.gov/pubmed/1264226.

R. Mindlin. Micro-structure in linear elasticity. *Archive for Rational Mechanics and Analysis*, 16(1), 1964. ISSN 0003-9527. doi: 10.1007/BF00248490.

K. Mizoguchi, T. Hirose, T. Shimamoto, and E. Fukuyama. Reconstruction of seismic faulting by high-velocity friction experiments: An example of the 1995 Kobe earthquake. *Geophysical Research Letters*, 34(1), 2007. ISSN 00948276. doi: 10.1029/2006GL027931.

A. Molinari. Collective behaviour and spacing of adiabatic shear bands. *Journal of the Mechanics and Physics of Solids*, 45(9):1551–1575, 1997.

A. Molinari and R. J. Clifton. Analytical Characterization of Shear Localization in Thermoviscoplasitc. Technical report, Brown University, 1986.

A. Molinari and Y. M. Leroy. Structures in shear zones due to thermal effects. *Comptes Rendus de l'Académie des Sciences - Series IIB - Mechanics-Physics-Astronomy*, 313(1): 7–13, 1991.

L. G. J. Montési and G. Hirth. Grain size evolution and the rheology of ductile shear zones: From laboratory experiments to postseismic creep. *Earth and Planetary Science Letters*, 211(1-2):97–110, 2003. ISSN 0012821X. doi: 10.1016/S0012-821X(03)00196-1.

H.-B. Mühlhaus. Scherfugenanalyse bei granularem Material im Rahmen der Cosserat-Theorie. *Ingenieur-Archiv*, 56:389–399, 1986. doi: 10.1007/BF02570619.

H. B. Mühlhaus and I. Vardoulakis. The thickness of shear bands in granular materials. *Géotechnique*, 37(3):271–283, jan 1987. ISSN 0016-8505. doi: 10.1680/geot.1987.37.3.271. URL http://www.icevirtuallibrary.com/content/article/10.1680/geot.1987.37.3.271.

D. Muir Wood. Some observations of volumetric instabilities on soils. *International Journal of Solids and Structures*, 39(13-14):3429–3449, 2002. ISSN 00207683. doi: 10.1016/S0020-7683(02)00166-X.

R. Myers and A. Aydin. The evolution of faults formed by shearing across joint zones in sandstone. *Journal of Structural Geology*, 26(5):947–966, may 2004. ISSN 01918141. doi: 10.1016/j.jsg.2003.07.008.

A. Needleman. Material rate dependence and mesh sensitivity in localization problems. *Computer Methods in Applied Mechanics and Engineering*, 67(1):69–85, 1988. ISSN 00457825. doi: 10.1016/0045-7825(88)90069-2.

H. Noda, E. M. Dunham, and J. R. Rice. Earthquake ruptures with thermal weakening and the operation of major faults at low overall stress levels. *Journal of Geophysical Research: Solid Earth*, 114(7), 2009. ISSN 21699356. doi: 10.1029/2008JB006143.

M. Oda and H. Kazama. Microstructure of shear bands and its relation to the mechanisms of dilatancy and failure of dense granular soils. *Géotechnique*, 48(4):465–481, aug 1998. ISSN 0016-8505. doi: 10.1680/geot.1998.48.4.465.

J.-l. Pac. *Systèmes dynamiques*. Dunod edition, 2012. URL https://www.dunod.com/sciences-techniques/sciences-techniques-industrielles/genie-mecanique/master-et-doctorat/systemes-dynamiques.

V. Palciauskas and P. A. Domenico. Characterization of Drained and Undrained Response of Thermally Loaded Repository Rocks. *Water Resources Research*, 18(2):281–290, 1982.

P. C. Papanastasiou and I. Vardoulakis. Numerical treatment of progressive localization in relation to borehole stability. *International Journal for Numerical and Analytical Methods in Geomechanics*, 16(6):389–424, jun 1992. ISSN 0363-9061. doi: 10.1002/nag.1610160602. URL http://doi.wiley.com/10.1002/nag.1610160602.

P. C. Papanastasiou and A. Zervos. Numerical modelling of strain localization. In *ALERT Doctoral School 2016. Modelling of instabilities and bifurcation in Geomechanics*, pages 133–164. 2016.

M. Peters. *On the initiation of boudinage and folding instabilities in layered elasto-visco-plastic solids: Insights from natural microstructures and numerical simulations*. PhD thesis, 2016.

N. J. Phillips and J. C. White. Grain size-dependent strength of phyllosilicate-rich gouges in the shallow crust: Insights from the SAFOD site. *Journal of Geophysical Research: Solid Earth*, 122(7):5789–5812, 2017. ISSN 21699313. doi: 10.1002/2016JB013828. URL http://doi.wiley.com/10.1002/2016JB013828.

C. G. Pijaudier and Z. P. Bazant. Non local Damage Theory. *Journal of engineering mechanics*, 113(10):1512–1533, 1987. ISSN 0733-9399. doi: http://dx.doi.org/10.1061/(ASCE)0733-9399(1987)113:10(1512). URL http://dx.doi.org/10.1061/(ASCE)0733-9399(1987)113:10(1512).

J. D. Platt, J. W. Rudnicki, and J. R. Rice. Stability and localization of rapid shear in fluid-saturated fault gouge : 2 . Localized zone width and strength evolution. *Journal of Geophysical Research: Solid Earth*, 2014. doi: 10.1002/2013JB010711.Received.

J. D. Platt, N. Brantut, and J. R. Rice. Strain localization driven by thermal decomposition during seismic shear. *Journal of Geophysical Research: Solid Earth*, 120(6):4405–4433, 2015. ISSN 21699356. doi: 10.1002/2014JB011493.

T. Poulet and M. Veveakis. A viscoplastic approach for pore collapse in saturated soft rocks using REDBACK: An open-source parallel simulator for Rock mEchanics with Dissipative feedBACKs. *Computers and Geotechnics*, 74:211–221, 2016. ISSN 18737633. doi: 10.1016/j.compgeo.2015.12.015.

T. Poulet, M. Veveakis, M. Herwegh, T. Buckingham, and K. Regenauer-Lieb. Modeling episodic fluid-release events in the ductile carbonates of the Glarus thrust. *Geophysical Research Letters*, 41(20):7121–7128, 2014. ISSN 19448007. doi: 10.1002/2014GL061715.

T. Poulet, M. Paesold, and M. Veveakis. Multi-Physics Modelling of Fault Mechanics Using REDBACK: A Parallel Open-Source Simulator for Tightly Coupled Problems. *Rock Mechanics and Rock Engineering*, pages 1–17, mar 2016. ISSN 07232632. doi: 10.1007/s00603-016-0927-y.

I. Prigogine and G. Nicolis. *ï£ijï£ijï£ijï£ijBifurcation analysis: principles, applications and synthesis*. 1985. ISBN 9027714460. URL file:///Users/RB/Dropbox/Papers2/Unknown/2012,ï¿ijï¿ijï¿ijï¿ijBifurcations.pdf$\delimiter"026E30F$npapers2://publication/uuid/1CE1604E-CFC3-4B4F-B8F4-E41C82525BB8.

S. Rafini. *Comportement hydraulique des milieux failles*. PhD thesis, UQAM, 2008.

H. Rattez, I. Stefanou, and J. Sulem. Thermo-hydro mechanical couplings and strain localisation in 3D continua with microstructure . Part I : Theory and linear stability analysis. *submitted*, 2017.

H. F. Reid. The mechanism of the earthquake. In *The California Earthquake of April 18, 1906, Report of the State Earthquake Investigation Commision, Vol. 2*, pages 1–192. 1910.

M. Rempe. *Frictional behavior and microstructures of calcite-bearing fault gouges*. PhD thesis, university of padova, feb 2015. URL http://paduaresearch.cab.unipd.it/7843/1/Rempe{_}Marieke{_}thesis.pdf.

A. W. Rempel and J. R. Rice. Thermal pressurization and onset of melting in fault zones. *Journal of Geophysical Research: Solid Earth*, 111(9), 2006. ISSN 21699356. doi: 10.1029/2006JB004314.

J. R. Rice. On the stability of dilatant hardening for saturated rock masses. *Journal of Geophysical Research*, 80(11):1531–1536, apr 1975. ISSN 01480227. doi: 10.1029/JB080i011p01531. URL http://doi.wiley.com/10.1029/JB080i011p01531.

J. R. Rice. Fault Stress States, Pore Pressure Distributions, and the Weakness of the San Andreas Fault. *International Geophysics*, 51:475–503, 1992.

J. R. Rice. Flash heating at asperity contacts and rate-dependent friction. In *Eos Trans. AGU, 77(46), Fall Meet. Suppl.*, page F471, 1999.

J. R. Rice. Heating and weakening of faults during earthquake slip. *Journal of Geophysical Research*, 111(B5), 2006a. ISSN 0148-0227. doi: 10.1029/2005JB004006. URL http://www.agu.org/pubs/crossref/2006/2005JB004006.shtml.

J. R. Rice. Heating and weakening of faults during earthquake slip. *Journal of Geophysical Research: Solid Earth*, 111(5), 2006b. ISSN 21699356. doi: 10.1029/2005JB004006.

J. R. Rice and M. Cocco. Seismic fault rheology and earthquake dynamics. *Tectonic Faults: Agents of Change on a Dynamic Earth*, (January 2005):16–21, 2007.

J. R. Rice, J. W. Rudnicki, and J. D. Platt. Stability and localization of rapid shear in fluid-saturated fault gouge : 1 . Linearized stability analysis. *Journal of Geophysical Research*, pages 1–23, 2014. doi: 10.1002/2013JB010710.Received.

L. F. Richardson. The Approximate Arithmetical Solution by Finite Differences of Physical Problems Involving Differential Equations, with an Application to the Stresses in a Masonry Dam, 1911. ISSN 1364-503X.

W. Riedel. Zur Mechanik Geologischer Brucherscheinungen. *Zentral-blatt fur Mineralogie, Geologie und Paleontologie, B*, pages 354–368, 1929.

P. Rognon, T. Miller, and I. Einav. A circulation-based method for detecting vortices in granular materials. *Granular Matter*, 17(2):177–188, 2015. ISSN 14347636. doi: 10.1007/s10035-015-0549-1.

J. W. Rudnicki. Diffusive instabilities in dilating and compacting geomaterials. *Multiscale Deformation and Fracture in Materials and Structures*, pages 159–182, 2000. doi: 10.1007/0-306-46952-9_10.

J. W. Rudnicki and J. R. Rice. Conditions for the localization of deformation in pressure-sensitive dilatant materials. *Journal of the Mechanics and Physics of Solids*, 23(6):371–394, dec 1975a. ISSN 00225096. doi: 10.1016/0022-5096(75)90001-0. URL http://linkinghub.elsevier.com/retrieve/pii/0022509675900010.

J. W. Rudnicki and J. R. Rice. Conditions for the localization of deformation in pressure-sensitive dilatant materials. *Journal of the Mechanics and Physics of Solids*, 23(6):371–394, dec 1975b. ISSN 00225096. doi: 10.1016/0022-5096(75)90001-0.

A. Ruina. Slip instability and state variable friction laws. *Journal of Geophysical Research: Solid Earth*, 88(12):10,359 – 10,370, 1983. URL http://onlinelibrary.wiley.com/doi/10.1029/JB088iB12p10359/full.

A. Sakaguchi, F. Chester, D. Curewitz, O. Fabbri, D. Goldsby, G. Kimura, C. F. Li, Y. Masaki, E. J. Screaton, A. Tsutsumi, K. Ujiie, and A. Yamaguchi. Seismic slip propagation to the updip end of plate boundary subduction interface faults: Vitrinite reflectance geothermometry on integrated ocean drilling program nantro SEIZE cores. *Geology*, 39(4):395–398, 2011. ISSN 00917613. doi: 10.1130/G31642.1.

C. G. Sammis and Y. Ben-Zion. Mechanics of grain-size reduction in fault zones. *Journal of Geophysical Research: Solid Earth*, 113(2):1–12, 2008. ISSN 21699356. doi: 10.1029/2006JB004892.

C. G. Sammis, G. King, and R. L. Biegel. The kinematics of gouge deformation. *Pure and Applied Geophysics PAGEOPH*, 125(5):777–812, 1987. ISSN 0033-4553. doi: 10.1007/BF00878033. URL http://link.springer.com/10.1007/BF00878033.

J. E. Samuelson and C. J. Spiers. Fault friction and slip stability not affected by CO2 storage : Evidence from short-term laboratory experiments on North Sea reservoir sandstones and caprocks. *International Journal of Greenhouse Gas Control*, Volume 11(November 2012):78–90, 2012.

A. Schofield and C. Wroth. *Critical State Soil Mechanics*. 1968. ISBN 978-0641940484. doi: 10.1111/j.1475-2743.1987.tb00718.x.

C. H. Scholz. *The mechanics of earthquakes and faulting*. Cambridge, second edi edition, 2002. ISBN 978-0-521-65223-0.

D. Scott, C. J. Marone, and C. G. Sammis. the apparent friction of granular fault gouge in sheared layers. *Journal of Geophysical Research*, 99(84):7231–7246, 1994.

M. M. Scuderi, A. R. Niemeijer, C. Collettini, and C. J. Marone. Frictional properties and slip stability of active faults within carbonateâĂŞevaporite sequences: The role of dolomite and anhydrite. *Earth and Planetary Science Letters*, 369-370:220–232, may 2013. ISSN 0012821X. doi: 10.1016/j.epsl.2013.03.024.

M. M. Scuderi, B. M. Carpenter, and C. J. Marone. Physicochemical processes of frictional healing: Effects of water on stick-slip stress drop and friction of granular fault gouge. *Journal of Geophysical Research: Solid Earth*, 119:4090–4105, 2014. doi: 10.1002/2013JB010641.Received.

P. Segall and J. R. Rice. Does shear heating of pore fluid contribute to earthquake nucleation? *Journal of Geophysical Research: Solid Earth*, 111(9):1–17, 2006. ISSN 21699356. doi: 10.1029/2005JB004129.

E. Sharbati and R. Naghdabadi. Computational aspects of the Cosserat finite element analysis of localization phenomena. *Computational Materials Science*, 38(2):303–315, 2006. ISSN 09270256. doi: 10.1016/j.commatsci.2006.03.003.

Z. K. Shipton, A. Soden, J. D. Kirkpatrick, A. M. Bright, and R. J. Lunn. *How thick is a fault? Fault displacement thickness scaling revisited*. 2006. ISBN 978-0-87590-435-1. doi: 10.1029/170GM19.

R. H. Sibson. Interactions between Temperature and Pore-Fluid Pressure during Earthquake Faulting and a Mechanism for Partial or Total Stress Relief. *Nature*, 243:66–68, 1973. ISSN 0028-0836. doi: 10.1038/physci243066a0.

R. H. Sibson. Generation of Pseudotachylyte by Ancient Seismic Faulting. *Geophysical Journal of the Royal Astronomical Society*, 43(3):775–794, 1975. ISSN 1365246X. doi: 10.1111/j.1365-246X.1975.tb06195.x.

R. H. Sibson. Fluid flow accompanying faulting: Field evidence and models. *Earthquake prediction*, 4:593–603, 1981. doi: 10.1029/ME004p0593.

R. H. Sibson. Thickness of the seismic slip zone. *Bulletin of the Seismological Society of America*, 93(3):1169–1178, 2003. ISSN 00371106. doi: 10.1785/0120020061.

R. Sievert, S. Forest, and R. Trostel. Finite deformation Cosserat-type modelling of dissipative solids and its application to crystal plasticity. *J. de Physique IV*, 8:Pr8–357—-364, 1998. ISSN 1155-4339. doi: 10.1051/jp4:1998844.

J. C. Simo and R. L. Taylor. Consistent tangent operators for rate-independent elastoplasticity. *Computer Methods in Applied Mechanics and Engineering*, 48(1):101–118, 1985. ISSN 00457825. doi: 10.1016/0045-7825(85)90070-2.

F. Simões and J. Martins. Flutter instability in a non-associative elasticâĂŞplastic layer: analytical versus finite element results. *International Journal of Engineering Science*, 43 (1-2):189–208, jan 2005. ISSN 00207225. doi: 10.1016/j.ijengsci.2004.09.001.

D. Simpson. Seismicity changes associated with reservoir loading. *Engineering Geology*, 10(2446), 1976. URL http://www.sciencedirect.com/science/article/pii/0013795276900168.

T. Skalicky. LASPack Reference Manual. Technical report, 1995.

S. A. F. Smith, S. Nielsen, and G. Di Toro. Strain localization and the onset of dynamic weakening in calcite fault gouge. *Earth and Planetary Science Letters*, 413:25–36, 2015. ISSN 0012821X. doi: 10.1016/j.epsl.2014.12.043.

S. J. Steacy and C. G. Sammis. An Automaton for Fractal Patterns of Fragmentation. *Nature*, 353(6341):250–252, 1991. ISSN 0028-0836. doi: 10.1038/353250a0.

I. Stefanou and S. Alevizos. Fundamentals of bifurcation theory and stability analysis. In J. Sulem, I. Stefanou, E. Papamichos, and E. Veveakis, editors, *Modelling of instabilities and bifurcation in Geomechanics, 26th ALERT Doctoral School*. 2016. URL http://alertgeomaterials.eu/data/school/2016/2016{_}ALERT{_}schoolbook.pdf.

I. Stefanou, J. Sulem, and I. Vardoulakis. Homogenization of interlocking masonry structures using a generalized differential expansion technique. *International Journal of Solids and Structures*, 47(11):1522–1536, 2010. ISSN 00207683. doi: 10.1016/j.ijsolstr.2010.02.011.

I. Stefanou, J. Sulem, and H. Rattez. Cosserat approach to localization in geomaterials. In *Handbook of Nonlocal Continuum Mechanics for Materials and Structures*. Springer, 2017.

P. Steinmann and K. Willam. Localization within the Framework of Micropolar Elasto-Plasticity. In *60th Anniv. Volume Prof. H. Lippmann*, pages 296–313. 1991. ISBN 978-3-540-53988-9. doi: 10.1007/978-3-642-48890-0_24. URL http://dx.doi.org/10.1007/978-3-642-48890-0{_}24.

F. Storti, A. Billi, and F. Salvini. Particle size distributions in natural carbonate fault rocks : insights for non-self-similar cataclasis. *Earth and Planetary Science Letters*, 206: 173–186, 2003.

S. H. Strogatz. Nonlinear Dynamics and Chaos, 1994. ISSN 00319228. URL http://scholar.google.com/scholar?hl=en{&}btnG=Search{&}q=intitle:Nonlinear+Dynamics+and+Chaos:+With+Applications+to+Physics,+Biology,+Chemistry+and+Engineering{#}0.

J. Sulem and V. Famin. Thermal decomposition of carbonates in fault zones: Slip-weakening and temperature-limiting effects. *Journal of Geophysical Research*, 114 (B3):B03309, mar 2009a. ISSN 0148-0227. doi: 10.1029/2008JB006004. URL http://www.agu.org/pubs/crossref/2009/2008JB006004.shtml.

J. Sulem and V. Famin. Thermal decomposition of carbonates in fault zones: Slip-weakening and temperature-limiting effects. *Journal of Geophysical Research*, 114(B3): 1–14, 2009b. doi: 10.1029/2008JB006004.

J. Sulem and I. Stefanou. Multiphysics couplings and strain localization in geomaterials. In *ALERT Doctoral School 2016. Modelling of instabilities and bifurcation in Geomechanics*, pages 188–213. 2016. URL http://alertgeomaterials.eu/data/school/2016/2016{_}ALERT{_}schoolbook.pdf.

J. Sulem and I. Vardoulakis. Bifurcation analysis of the triaxial test on rock specimens. A theoretical model for shape and size effect. *Acta mechanica*, 83(3-4):195–212, 1990. ISSN 0001-5970. doi: 10.1007/BF01172981.

J. Sulem, I. Vardoulakis, H. Ouffroukh, M. Boulon, and J. Hans. Experimental characterization of the thermo-poro-mechanical properties of the Aegion Fault gouge. *Comptes Rendus Geoscience*, 336(4-5):455–466, mar 2004. ISSN 16310713. doi: 10.1016/j.crte.2003.12.009.

J. Sulem, I. Stefanou, and M. Veveakis. Stability analysis of undrained adiabatic shearing of a rock layer with Cosserat microstructure. *Granular Matter*, 13(3):261–268, feb 2011. ISSN 1434-5021. doi: 10.1007/s10035-010-0244-1.

B. Taylor. *Methodus Incrementorum Directa et Inversa*. 1715.

J. Tejchman. *Shear Localization in Granular Bodies with Micro-Polar Hypoplasticity*. Springer Series in Geomechanics and Geoengineering. Springer Berlin Heidelberg, Berlin, Heidelberg, 2008. ISBN 978-3-540-70554-3. doi: 10.1007/978-3-540-70555-0. URL http://link.springer.com/10.1007/978-3-540-70555-0.

T. Togo and T. Shimamoto. Energy partition for grain crushing in quartz gouge during subseismic to seismic fault motion: An experimental study. *Journal of Structural Geology*, 38:139–155, 2012. ISSN 01918141. doi: 10.1016/j.jsg.2011.12.014. URL http://dx.doi.org/10.1016/j.jsg.2011.12.014.

A. Tordesillas, J. F. Peters, and B. S. Gardiner. Shear band evolution and accumulated microstructural development in Cosserat media. *International Journal for Numerical and Analytical Methods in Geomechanics*, 28(10):981–1010, aug 2004. ISSN 0363-9061. doi: 10.1002/nag.343.

A. Tordesillas, S. Pucilowski, Q. Lin, J. F. Peters, and R. P. Behringer. Granular vortices: Identification, characterization and conditions for the localization of deformation. *Journal of the Mechanics and Physics of Solids*, 90:215–241, 2016. ISSN 00225096. doi: 10.1016/j.jmps.2016.02.032. URL http://dx.doi.org/10.1016/j.jmps.2016.02.032.

S. T. Tse and J. R. Rice. Crustal earthquake instability in relation to the depth variation of frictional slip properties. *Journal of Geophysical Research*, 91(B9):9452, 1986. ISSN 0148-0227. doi: 10.1029/JB091iB09p09452. URL http://doi.wiley.com/10.1029/JB091iB09p09452.

A. Tsutsumi and T. Shimamoto. High-velocity frictional properties of Gabbro. *Geophysical Research Letters*, 24(6):699–702, 1997.

R. Tung, T. Poulet, S. Alevizos, M. Veveakis, and K. Regenauer-Lieb. Shear heating in creeping faults changes the onset of convection. *Geophysical Journal International*, 211 (1):270–283, 2017.

K. Ujiie and A. Tsutsumi. High-velocity frictional properties of clay-rich fault gouge in a megasplay fault zone, Nankai subduction zone. *Geophysical Research Letters*, 37(24): 1–5, 2010. ISSN 00948276. doi: 10.1029/2010GL046002.

K. Ujiie, A. Tsutsumi, and J. Kameda. Reproduction of thermal pressurization and fluidization of clay-rich fault gouges by high-velocity friction experiments and implications for seismic slip in natural faults. *Geological Society, London, Special Publications*, 359(1):267–285, 2011. ISSN 0305-8719. doi: 10.1144/SP359.15. URL http://sp.lyellcollection.org/lookup/doi/10.1144/SP359.15.

P. Unterreiner. *Contribution à l'étude et à la modélisation numérique des sols cloués : application au calcul en déformation des ouvrages de soutènement*. PhD thesis, Ecole Nationale des Ponts et Chaussées, oct 1994.

P. Vannucchi and L. Leoni. Structural characterization of the Costa Rica decollement: Evidence for seismically-induced fluid pulsing. *Earth and Planetary Science Letters*, 262 (3-4):413–428, 2007. ISSN 0012821X. doi: 10.1016/j.epsl.2007.07.056.

I. Vardoulakis. Stability and bifurcation of undrained, plane rectilinear deformations on water-saturated granular soils. *International Journal for Numerical and Analytical Methods in Geomechanics*, 9(5):399–414, sep 1985. ISSN 0363-9061. doi: 10.1002/nag.1610090502. URL http://doi.wiley.com/10.1002/nag.1610090502.

I. Vardoulakis. Dynamic stability analysis of undrained simple shear on water-saturated granular soils. *International Journal for Numerical and Analytical Methods in Geomechanics*, 10(2):177–190, mar 1986. ISSN 0363-9061. doi: 10.1002/nag.1610100206. URL http://doi.wiley.com/10.1002/nag.1610100206.

I. Vardoulakis. Deformation of water-saturated sand : I. uniform undrained deformation and shear banding. *Géotechnique*, 46(3):441–456, 1996.

I. Vardoulakis. Lecture notes on Cosserat continuum mechanics with application to the mechanics of granular media, 2009. URL http://geolab.mechan.ntua.gr/teaching/lectnotes/CCM2009.pdf.

I. Vardoulakis and E. C. Aifantis. A gradient flow theory of plasticity for granular materials. *Acta Mechanica*, 87:197–217, 1991.

I. Vardoulakis and J. Sulem. *Bifurcation Analysis in Geomechanics*. Blackie, Glascow, 1995. ISBN 0203697030.

B. A. Verberne, C. J. Spiers, A. R. Niemeijer, J. H. P. Bresser, D. A. M. Winter, and O. Plümper. Frictional Properties and Microstructure of Calcite-Rich Fault Gouges Sheared at Sub-Seismic Sliding Velocities. *Pure and Applied Geophysics*, dec 2013. ISSN 0033-4553. doi: 10.1007/s00024-013-0760-0.

B. A. Verberne, C. J. Spiers, A. R. Niemeijer, J. H. P. De Bresser, D. A. M. De Winter, and O. Plümper. Frictional Properties and Microstructure of Calcite-Rich Fault Gouges Sheared at Sub-Seismic Sliding Velocities. *Pure and Applied Geophysics*, 171(10):2617–2640, 2014. ISSN 14209136. doi: 10.1007/s00024-013-0760-0.

E. Veveakis, S. Alevizos, and I. Vardoulakis. Chemical reaction capping of thermal instabilities during shear of frictional faults. *Journal of the Mechanics and Physics of Solids*, 58(9):1175–1194, 2010. ISSN 00225096. doi: 10.1016/j.jmps.2010.06.010.

M. Veveakis, J. Sulem, and I. Stefanou. Modeling of fault gouges with Cosserat Continuum Mechanics: Influence of thermal pressurization and chemical decomposition as coseismic weakening mechanisms. *Journal of Structural Geology*, 38:254–264, may 2012. ISSN 01918141. doi: 10.1016/j.jsg.2011.09.012.

M. Veveakis, I. Stefanou, and J. Sulem. Failure in shear bands for granular materials: thermo-hydro-chemo-mechanical effects. *Géotechnique Letters*, 3(April-June):31–36, may 2013. ISSN 2045-2543. doi: 10.1680/geolett.12.00063.

R. C. Viesca and D. I. Garagash. Ubiquitous weakening of faults due to thermal pressurization. *Nature Geoscience*, 8(11):875–879, 2015. ISSN 1752-0894. doi: 10.1038/ngeo2554. URL http://www.nature.com/doifinder/10.1038/ngeo2554.

D. J. Wald and T. H. Heaton. Spatial and Temporal Distribution of Slip for the 1992 Landers , California , Earthquake. *Bulletin of the Seismological Society of America*, 84 (3):668–691, 1994. ISSN 0037-1106. doi: 10.1785/0120000728.

W. Wang, L. Sluys, and R. de Borst. Interaction between material length scale and imperfection size for localisation phenomena in viscoplastic media. *European Journal of Mechanics - A/Solids*, 15(3):447–464, 1996. ISSN 0997-7538.

W. M. Wang, L. J. Sluys, and R. de Borst. Viscoplasticity for instabilities due to strain softening and strain-rate softening. *International Journal for Numerical Methods in Engineering*, 40(20):3839–3864, 1997. ISSN 0029-5981. doi: 10.1002/(SICI)1097-0207(19971030)40:20<3839::AID-NME245>3.0.CO;2-6.

C. A. Wibberley and T. Shimamoto. Internal structure and permeability of major strike-slip fault zones: the Median Tectonic Line in Mie Prefecture, Southwest Japan. *Journal of Structural Geology*, 25(1):59–78, 2003. ISSN 01918141. doi: 10.1016/S0191-8141(02)00014-7.

C. a. J. Wibberley. Initiation of basement thrust detachments by fault-zone reaction weakening. *Geological Society, London, Special Publications*, 245(1):347–372, 2005. ISSN 0305-8719. doi: 10.1144/GSL.SP.2005.245.01.17.

M. L. Wilkins. Calculation of elasto-plastic ïňĆow. 38(3):430–432, 1964.

O. C. Zienkiewicz and R. L. Taylor. *The finite element method, fourth edition; volume 1: basic formulation and linear problems*. 1994. ISBN 0070841748. URL http://trid.trb.org/view.aspx?id=1165636.

M. Zoback, S. Hickman, and W. Ellsworth. Scientific drilling into the San Andreas fault zone - An overview of SAFOD's first five years. *Scientific Drilling*, (1):14–28, 2011. ISSN 18168957. doi: 10.2204/iodp.sd.11.02.2011.

M. D. Zoback, L. T. Silver, T. Henyey, and W. Thatcher. The Cajon Pass scientific drilling experiment: overview of phase 1. *Geophysical Research Letters*, 15(9):933–936, 1988.